LCH Laboratoire de Constructions Hydrauliques
Laboratory of Hydraulic Constructions

ÉCOLE POLYTECHNIQUE
FÉDÉRALE DE LAUSANNE

Communication 35

Contractile floating barriers for confinement and recuperation of oil slicks

Azin Amini

Editeur : Prof. Dr A. Schleiss

Lausanne, 2007

Communications du Laboratoire de Constructions Hydrauliques ISSN 1661-1179
Ecole Polytechnique Fédérale de Lausanne
Editeur: Prof. Dr A. Schleiss

Preface

After the experience with several catastrophic accidents with tankers, oil spills are of major environmental concern in coastal regions. The transportation of oil slicks by wind and waves towards the coast can damage marine life and pollute the coastal environment severely over many years. Containment and physical removal is still the most efficient method for oil spill cleaning up. Floating oil barriers, as the main tool for oil spill response, are used to contain and displace oil spills on the sea surface. Thus specific areas can be protected against spreading of the slick.

In her research, Mrs. Dr. Azin Amini studied the behavior of a new anti-pollution system designed by Cavalli in 1999. With this system the oil spill is encircled by a contractible floating barriers made of very light material as Kevlar. The so created circular reservoir can then be subdivided into two or four circles, with the result that the oil layer thickness increases. This facilitates the pumping operation but also the displacing of the reservoir under high wave conditions.

Mrs. Dr. Azin Amini performed for the first time systematic laboratory tests with a flexible barrier in presence of sea waves and under towing conditions. This gave new insights in the behavior of flexible barriers. An innovative experimental set-up in a laboratory flume had to be developed, which allowed a free deformation of the barrier but without having leakage of the oil along the side walls of the flume. The systematic two-dimensional tests were carried out with rapeseed oil. In comparison, oil was also simulated by light expanded clay aggregates (LECA) which has never done before.

The initiation of containment failure could be assessed for rigid and flexible barriers due to the effect of towing of the reservoir and incident waves. Precise measurements using UVP and PIV techniques allowed new insights in the flow characteristics in the vicinity of the barrier.

Furthermore, the efficiency of a double barrier in oil slick containment, which is representative for a trapping reservoir, was also tested. Finally the results of the laboratory tests were compared with numerical simulations. Several empirical relationships could be derived which are very useful for the practical design of flexible barriers in presence of sea waves and under towing conditions.

We would like to thank Dr. Fangxin Fang, from Imperial College, United Kingdom for her support and guidance during the project and for her valuable comments also as member of the jury. We thank also the other members of the jury Prof. Alfred Johny Wüest of Eawag, and Prof. André Lejeune of Université de Liège, Belgium for their helpful suggestions. Finally we also thank gratefully the Swiss Petroleum Union for their financial support under grant No. 4'09'02.

Prof. Dr. Anton Schleiss

To my beloved sisters, Sheyma, Zahra & Yasaman

Contents

Abstract

Contractile floating barriers for confinement and recuperation of oil slicks

Marine oil spills can cause serious environmental damages to natural resources and to those whose sustenance depends upon these resources. Unfortunately experience shows that even the best efforts have not prevented occasional occurrences of major accidents on the sea. As long as massive oil spills are probable, special techniques and equipments will remain essential to facilitate spill cleanup in coastal regions.

Oil spill containment booms are the most commonly adopted techniques to collect and contain oil on the sea surface, or to protect specific areas against slick spreading. Recently, an anti-pollution boom called the Cavalli system, has been designed with the intention of preventing the spread of spilled oil by trapping it inside a flexible floating reservoir and improving the pumping operation by decreasing the reservoir surface, and consequently increasing the oil layer thickness.

Although flexible barriers have become increasingly common as a cleanup facility, there is no more than inadequate elaborate knowledge about their behavior. According to an extensive literature review, most of existing researches, either physical or numerical, have been done for rigid barriers.

The main motivation for introducing the present research project is to study the efficiency and operational limits of the Cavalli system. However, the objectives are not constrained to this particular case. The present investigation focuses on the behavior of flexible barriers containing spilled oil. Previous researches of containment booms, even for the case of rigid barriers, have been mainly carried out in calm water. Accordingly, the main concentration is devoted to the response of a flexible barrier in presence of sea waves.

Both experimental and numerical approaches were pursued to evaluate the efficiency limits and behavior of flexible barriers.

Two-dimensional experiments have been carried out in a laboratory flume 6.5 m long, 1.2 m deep, and 12 cm wide. Flexible and rigid barriers containing rapeseed oil were examined, with and without waves.

As the first step, the behavior of a flexible barrier in currents without waves was studied and compared to that of a rigid barrier. The key challenge was to contain the oil behind a flexible barrier that can freely deform in the water flow. This could be achieved using a slitted side skirt on the boom where it faces the lateral wall of the flume.

The failure mode observed for rapeseed oil was entrainment failure. The initial failure velocity of different experimental conditions was studied and an empirical relationship was suggested in order to assess the maximum permissible oil-water relative velocity as a function of barrier draft and oil characteristics. The geometrical charac-

teristics of the contained slick were examined and empirical equations were proposed to predict the slick length and headwave thickness as a function of contained oil volume.

The second and more significant step was to conduct experiments with a flexible floating barrier in presence of five different waves. The analysis focused on the relationship between the failure velocity and the wave parameters with an emphasis on the behavior of flexible barriers. Likewise, empirical equations were proposed for the prediction of the initial failure velocity and geometrical characteristics of the slick. A type of drainage failure, namely, surging drainage was observed in the presence of waves. It was shown that the wave steepness and oil layer thickness are the dominant parameters in such failure.

It was noticed that by decreasing the wave period or increasing the wave height, interfacial waves became more aggressive and consequently failure initiated at a lower velocity. Flexible barriers were more sensitive to the variations of wave characteristics. Applying appropriate time and length scales, a critical wave period of 6 s and wave height of 0.5 m were proposed for the prototype.

Accurate measurements of velocity profiles and flow patterns in the vicinity of barriers with different conditions by means of Ultrasonic Velocimetry Profiling (UVP) and Large-Scale Particle Image Velocimetry (LSPIV) methods provided a reasonable understanding of the hydrodynamics in the vicinity of the barrier. The characteristics of the headwave at the upstream end of the oil slick were deliberately compared to those of a gravity current. It was concluded that despite geometrical similarities, these two phenomena are quite diverse. Furthermore, the oil-water interface was traced by detecting the maximum ultrasonic echo intensity, and velocity profiles in water and oil phases were independently obtained.

To enhance the understanding of the mechanisms associated with oil containment failure, numerical simulations of multiphase flow were carried out using FLUENT code, applying the finite volume method (FVM). Comparisons between the obtained flow pattern and velocity field derived from numerical simulations and precise experimental measurements confirmed the capability of the numerical model to simulate the multiphase flow.

The turbulence wake downstream of rigid and flexible barriers was simulated with and without the presence of oil phase. The simulations revealed the effect of contained oil on flow pattern and consequently the drag force acting on the barrier.

Simulations of a full-scale barrier proposed a drag coefficient, C_d, of 1.90 for rigid barriers. Contrarily a constant value for the drag coefficient cannot be attributed to flexible barriers, since its deformations do not allow it to form similar shapes at different velocities.

Last but not least, comparing the drag force on a rigid barrier with that of a flexible barrier towed by the same velocity demonstrated the fact that the forces acting on the skirt could be appreciably reduced by allowing flexibility.

Keywords: Oil spill containment boom, flexible barrier, two-phase fluid, entrainment failure, interfacial instability, Cavalli system, headwave, UVP measurements, LSPIV measurements, wave steepness, surging drainage, numerical simulation, fluid-structure interaction, drag coefficient.

Résumé

Barrières flottantes contractiles pour le confinement et la récupération des nappes d'hydrocarbures

Les marées noires peuvent créer de graves dommages au milieu naturel marin et aux organismes vivant qui en dépendent. L'expérience montre cependant que malgré les efforts importants consentis pour leur prévention, les pollutions marines ne peuvent être définitivement empêchées. Aussi longtemps que le risque de pentes d'hydrocarbures existe, un équipement et des techniques spéciales de récupération et de stockage sont nécessaires.

La technique la plus couramment utilisée est la récupération et le stockage des nappes superficielles à l'aide de barrières flottantes. Celles-ci peuvent également être utilisées pour la protection des zones côtières contre la marée noire. Selon cette même idée, une barrière anti-pollution originale, appelée système Cavalli, a récemment été développée. Son principe est d'empêcher la diffusion des hydrocarbures déversés en les encerclant à l'intérieur d'un réservoir souple flottant puis de les épaissir en réduisant la surface confinée afin de faciliter l'opération de pompage de la nappe.

Bien que l'utilisation de barrières flexibles tend à se généraliser, la connaissance précise de leur fonctionnement fait encore défaut. Une revue de littérature étendue a montré que la plupart des recherches réalisées, de nature tant physique que numérique, ont considéré des barrières rigides.

Lors du lancement de ce projet de recherche, la principale motivation était d'étudier l'efficacité et les limites opérationnelles du système Cavalli sans toutefois se limiter à ce cas particulier. De manière élargie, la présente recherche se focalise sur le comportement des barrières flexibles contenant une couche d'hydrocarbures. Les précédentes recherches sur le sujet, concernant exclusivement les barrières rigides, ont été réalisées sur des plans d'eau calmes. Ici, une attention particulière a été portée sur le comportement d'une barrière flexible en présence non seulement de courant mais aussi de vagues.

Des approches à la fois expérimentale et numérique ont été entreprises pour évaluer le comportement limite et l'efficacité des barrières flexibles.

Des expériences bidimensionnelles ont été réalisées dans un canal d'essai de 6.5 m de longueur, 1.2 m de profondeur et 12 cm de largeur. Des barrières souples et rigides contenant de l'huile de colza ont été testées avec et sans vagues.

Dans une première étape, le comportement d'une barrière souple dans un courant sans vagues a été analysé et comparé à celui d'une barrière rigide. Le défi principal était alors de retenir l'huile derrière une barrière flexible, qui peut se déformer librement sous l'effet de l'écoulement. Pour ceci, une jupe fendue a été installée sur les deux bords latéraux de la barrière flexible, qui vient se plaquer sur les parois du canal d'essai pour éviter les fuites latérales.

La limite de fonctionnement de la barrière souple avec l'huile de colza est atteinte lorsque des pentes sont observées. La vitesse limite d'entraînement a été étudiée pour différentes conditions expérimentales. Une relation empirique est proposée pour l'estimation de la vitesse relative maximale entre l'huile et l'eau, en fonction des caractéristiques de la barrière et de l'huile. Les caractéristiques de la nappe contenue par la barrière ont été analysées et des équations sont également proposées pour prédire la longueur de la nappe et l'épaisseur du front en fonction du volume d'huile.

La seconde étape, la plus importante, concerne l'étude expérimentale d'une barrière souple en présence de vagues. Cinq vagues caractéristiques ont été testées et l'analyse a porté sur la relation entre la vitesse critique d'entraînement et les paramètres des vagues, en considérant également le comportement de la barrière souple. Là encore, des équations empiriques ont été développées pour la prédiction de la vitesse critique et des caractéristiques géométriques de la nappe. En présence de vagues, indépendamment de la vitesse critique d'entraînement d'huile, une limite de fonctionnement du système a été observée. Il a été démontré que les paramètres déterminants pour ce mode de rupture sont la cambrure des vagues et l'épaisseur de la nappe d'huile.

En diminuant la période des vagues, ou en augmentant leur hauteur, les vagues interfaciales deviennent plus agressives et la limite de fonctionnement est atteinte pour une vitesse d'entraînement plus faible. Les barrières flexibles sont alors plus sensibles aux caractéristiques des vagues. En appliquant des échelles de temps et de longueur appropriées, une période critique de 6 secondes et une hauteur de vague de 0.5 mètres sont proposées comme limites de fonctionnement pour le prototype.

Des mesures précises des profils de vitesses et du champ d'écoulement à proximité des barrières ont été réalisées pour différentes conditions expérimentales au moyen des techniques UVP et LSPIV. Ces mesures ont largement contribué à la bonne compréhension de l'hydrodynamique dans la zone proche de la barrière. Les caractéristiques du front à l'extrémité amont de la nappe d'huile ont été comparées à celles d'un courant de gravité. Malgré les similarités géométriques, cette analyse a montré que les deux phénomènes sont fondamentalement différents.

Pour améliorer la compréhension des mécanismes associés à la limite d'entraînement d'huile, des simulations numériques de l'écoulement multiphasique ont été réalisées à l'aide du code FLUENT utilisant la méthode des volumes finis (FVM). La comparaison des conditions d'écoulement et des champs de vitesses obtenus par simulation numérique, avec les résultats expérimentaux, confirme la capacité des modèles numériques à simuler les écoulements multiphasiques.

Le sillage de turbulence en aval de la barrière a été reproduit pour les barrières rigides et flexibles, avec et sans la présence de couche d'huile. Les simulations ont révélé l'influence de la présence d'huile sur les conditions d'écoulement et par conséquent sur la force de traînée agissant sur la barrière. Les simulations à l'échelle du prototype ont permis d'estimer un coefficient de traînée, $C_d = 1.90$ pour une barrière rigide. Pour des barrières souples, une valeur constante du coefficient de traînée ne peut être attribuée, en raison de la déformation de la jupe qui varie avec la vitesse.

Mots-clés: nappe d'hydrocarbure, barrière flexible, fluide multiphasique, limite d'entraînement, instabilités interfaciales, système Cavalli, mesures UVP, mesures LSPIV, cambrure de vague, drainage dû à la houle, simulation numérique, interaction fluide-structure, coefficient de traînée.

Zusammenfassung

Kontraktile schwimmende Ölschutzsperren für den Einschluss und die Beseitigung von Ölverschmutzungen

Maritime Ölverschmutzungen können schwere Ökoschäden verursachen und die Existenzgrundlagen all derjenigen gefährden, welche von den betroffenen Naturschätzen leben. Wie die Erfahrungen leider aufzeigen, können trotz riesiger Anstrengungen solche Unfälle auf See nicht vermieden werden. Solange ein Potenzial für massive Ölverschmutzungen vorhanden ist, sind spezielle Techniken und Ausrüstungen notwendig, welche die Säuberungsarbeiten in den Küstenregionen erleichtern.

Die Ölrückhaltesperre ist die am weitesten verbreitete Technik um das auf der Wasseroberfläche schwimmende Öl zu sammeln und einzugrenzen, oder um bestimmte Landstriche vor einem Ölteppich zu schützen. Neulich wurde das Cavalli System, eine Anti-Verschmutzungssperre, entworfen. Dieses soll die Ausbreitung des Ölteppichs verhindern, indem das Öl innerhalb eines beweglichen schwimmenden Ringes eingeschlossen wird. Gleichzeitig soll damit das Pumpvorgehen erleichtert werden, da die Ölschichtstärke hiermit vergrössert werden kann.

Obschon die beweglichen Schutzschwimmkörper immer häufiger für Säuberungsarbeiten verwendet werden, fehlen detaillierte Kenntnisse deren Verhalten. Ein ausgiebiges Literaturstudium zeigt, dass die meisten bisherigen physikalischen oder nummerischen Forschungsarbeiten im Bereich der starren Sperren getätigt wurden.

Die Untersuchungen der Effizienz und der betrieblichen Grenzen des Cavalli Systems waren die Hauptmotivation dieses Forschungsprojekts. Allerdings blieb die Studie nicht nur auf diesen speziellen Fall beschränkt. Die vorliegenden Nachforschungen konzentrieren sich auf das Verhalten beweglicher Ölschutzsperren. Die vorangehenden Studien über Schutzsperren, darin eingeschlossen diejenigen mit starren Vorrichtungen, wurden meist im ruhigen Wasser unternommen. Folglich wurde hier die grösste Aufmerksamkeit auf die Verhaltensweise beweglicher Schutzsperren bei Wellengang gerichtet.

Es wurden experimentelle und nummerische Annäherungen durchgeführt um die Grenzen der Funktionsfähigkeit und das Verhalten beweglicher Schutzsperren auszuloten.

Zwei-dimensionale Experimente wurden in einem 6.5 m langen, 1.2 m tiefen und 12 cm breiten Modellgerinne durchgeführt. Bewegliche und starre Rapsöl rückhaltende Sperren wurden ohne und mit Wellengang überprüft.

Als erster Schritt wurde das Verhalten einer beweglichen Sperre in einer Strömung ohne Wellengang untersucht und mit demjenigen einer starren Sperre verglichen. Die grösste Herausforderung galt dabei dem Rückhalt des Öls hinter der beweglichen Sperre, welche sich frei in der Strömung verformen konnte. Dieses Problem konnte mit einer flexiblen Schürze als seitliche Abdichtung überwunden werden. Der

festgestellte Versagensgrund des Systems ist das Mitreissen von Rapsöl. Die kritische Fliessgeschwindigkeit, welche zum Systemversagen führt, wurde bei Versuchen unter verschiedenen experimentellen Bedingungen eruiert. Daraufhin wurde eine empirische Beziehung entwickelt, welche die maximal erlaubte relative Öl-Wasser-Geschwindigkeit in Funktion der Sperrengeometrie und Öleigenschaften beschreibt. Die geometrischen Eigenschaften des eingegrenzten Ölteppichs wurden untersucht, und es wurden empirische Gleichungen aufgestellt, die die Ölteppichlänge und die Kopfwellenstärke als Funktion des umfassten Ölvolumens beschreiben.

Der zweite und wichtigere Schritt war es, die Versuche mit einer beweglichen Ölsperre bei fünf verschiedenen Wellengrössen durchzuführen. Bei der Auswertung wurde auf die Beziehung zwischen der kritischen Fliessgeschwindigkeit und den Wellenparametern ein Augenmerk gelegt, wobei besonders das Verhalten der Sperre umfassend untersucht wurde. Auch hier wurden empirische Gleichungen für die Vorhersage der kritischen Fliessgeschwindigkeit und der geometrischen Eigenschaften des Ölteppichs aufgestellt. Bei Wellengang wurde nebst dem Versagen des Mitreissens ein weiteres Auslaufversagen, das so genannte Untendurchschwappen, festgestellt. Es konnte gezeigt werden, dass die Steilheit der Welle sowie die Stärke der Ölschicht ausschlaggebende Versagensparameter waren.

Bei abnehmender Wellenperiode oder zunehmender Wellenhöhe wurden die Wellen an der Grenzfläche steiler, und folglich trat das Versagen bereits bei geringeren Fliessgeschwindigkeiten ein. Bewegliche Sperren waren empfindlicher gegenüber Veränderungen der Welleneigenschaften. Unter der Annahme angemessener Zeit- und Längengrössenordnungen werden eine kritische Wellenperiode von 6 s und eine kritische Wellenhöhe von 0.5 m für den Prototyp empfohlen.

Präzise Geschwindigkeitsprofilmessungen und Strömungsfeldaufnahmen mittels Ultraschall-Doppler-Geschwindigkeitsmessmethode (UVP) und large-scale particle image velocimetry (LSPIV) im Nahbereich der Sperre unter verschiedenen Bedingungen ergaben plausible Erkenntnisse über die Hydrodynamik im Bereich der Sperre. Die Eigenschaften der Kopfwelle am oberen Ende des Ölteppichs wurden detailliert mit denjenigen einer Dichteströmung verglichen. Es wurde abschliessend festgestellt, dass trotz geometrischer Ähnlichkeiten diese beiden Phänomene verschieden sind.

Um das Ölsperrenversagen besser zu verstehen wurden nummerische Simulationen mit einem Multi-Phasen-Modell durchgeführt. Dazu wurde das CFD Programm FLUENT verwendet, welches mit der Finiten Volumen Methode (FVM) arbeitet. Der Vergleich der nummerischen Simulationen und der präzisen Modellmessungen anhand der Strömungs- und Geschwindigkeitsfelder bestätigt die Plausibilität des nummerischen Modells bei Multi-Phasen- Strömungssimulationen.

Simulationen einer Sperre im Massstab 1:1 ergaben für starre Sperren einen Widerstandskoeffizienten von $C_d = 1.90$. Aufgrund der von der Fliessgeschwindigkeit abhängigen ungleichen Verformungen der beweglichen Sperre kann dieser kein konstanter Widerstandskoeffizient zugeordnet werden.

Der Vergleich zwischen der Widerstandskraft einer starren und einer mit derselben Geschwindigkeit gezogenen beweglichen Sperre zeigt, dass die auf die Schürze einwirkenden Kräfte durch deren Verformbarkeit stark vermindert werden können.

Schlüsselwörter: schwimmende Ölschutzsperre, bewegliche Sperre, Zwei-Phasen Fluid, Mitreissversagen, Grenzflächeninstabilität, Cavalli System, Kopfwelle, UVP Messungen, LSPIV Messungen, Wellensteilheit, Untendurchschwappen, Nummerische Simulation, Fluid-Struktur-Interaktion, Widerstandskoeffizient.

List of Symbols

Roman Symbols

Δh	difference between oil and water levels on both sides of the barrier
ΔL_s	difference of slick length at each velocity from initial slick length
$\Delta p(z)$	pressure difference at front and rear of the skirt at a point of depth z
Δx	displacement of barrier's end point due to wave effect
A	frontal profile
A_2	flow surface downstream the barrier
A_b	flow surface beneath the barrier
A_o	area of that part of float section, which is submerged in the oil
A_w	area of that part of float section, which is submerged in the water
B	ballast weight per unit length of the barrier
c	sound velocity in the fluid
C_d	drag coefficient
C_f	drag coefficient for a flexible body
C_f	oil-water friction coefficient
C_μ	empirical constant related to turbulent dissipation rate
D	barrier draft
d	water depth
d_b	distance between two parallel barriers
D_e	effective draft, vertical submergence depth of a flexible barrier
D_s	typical particle size

d_{50}	median grain size
d_{tr}	diameter of tracer particles
E	nondimensional parameter representing the solid phase
f	freeboard of the boom
F_d	drag force
F_h	headwave based Froude number
F_r	densimetric Froude number
g	acceleration due to gravity
H	wave height
h	global head loss
h	oil layer thickness
$h(x)$	oil thickness as a function of distance from upstream point
h_1	distance from float center to water surface
h_2	distance from float center to oil surface
H_i	instantaneous wave height
h_n	local head loss due to narrowing
h_s	head loss along the slick
h_w	local head loss due to widening
H_{rms}	root mean square wave height
I	turbulent intensity
I_U	increment of flow velocity comparing to the initial failure velocity
J	energy slope
K	number of measured waves during measure time by ultrasonic gauges
k	headwave thickness coefficient
k	turbulent kinetic energy
k_β	modification coefficient of shear stress due to slope effect
L	characteristic length
L	distance of two measurements points

L	wave length
l	length of barrier
l	turbulence length scale
L_0	wave length in deep water
L_i	wave length in intermediate water depth
L_s	length of contained oil slick
L_{in}	initial slick length in the beginning of each experiment
L_{max}	length of major axe of oil slick, if considered as an ellipse
L_{min}	length of minor axe of oil slick, if considered as an ellipse
L_{sw}	length of contained oil slick in presence of waves
Q	water discharge
q_E	oil loss rate per barrier width
r	radius of float
R_h	hydraulic radius
Re	Reynolds number
Re_p	particle Reynolds number
Re_{HD}	Reynolds number based on hydraulic radius of the flume
s	wave steepness
T	towing force
T	wave period
t	time after oil spill starts
T_a	tension in the boom induced by wind
t_h	thickness of headwave
T_w	tension in the barrier due to water currents without waves
t_{eq}	equivalent slick thickness
T_{tot}	total tension in the barrier
U	mean flow velocity
U_1	upstream velocity

U_2	downstream flow velocity
U_c	velocity of gravity current, or oil internal velocity at headwave
U_f	containment initial failure velocity
U_{KH}	Kelvin-Helmholtz instability threshold velocity
$U_{tr}(t)$	tracer's velocity at time t after change in flow velocity
U_{wind}	speed of wind
V	initial oil volume per unit length of the barrier
V_{oil}	total volume of spilled oil
w	channel width
W_{ref}	weight of water that can fill half of the float volume per unit length
W_{tot}	total weight of boom per unit length
We_{cr}	critical Weber number
X	horizontal parameter on Shields' diagram
x	distance from the slick upstream point
Y	vertical parameter on Shields' diagram
Y_{cr}	Critical value of modified shields' diagram
z	depth of specific point
z_1	upstream water depth
z_2	downstream water depth
z_b	water depth under the barrier

Greek Symbols

α	nondimensional parameter for flexible barrier deformation
α_d	maximum volume fraction (packing limit)
α_q	volume fraction of q^{th} material
β	inclination angle of UVP transducer
β	longitudinal slope angle
β	particulate loading

Δ	relative oil density, $(\rho_w - \rho_o)/\rho_w$
δ	relative oil thickness, t_{eq}/D
$\Delta\rho$	difference in water and oil densities, $\rho_w - \rho_o$
ϵ	turbulent dissipation rate
γ	specific weight
γ_s	specific weight of granules
κ	tracer response time
λ_L	length scaling factor
λ_T	time scaling factor
λ_U	velocity scaling factor
λ_c	wave length of capillary waves
μ	dynamic viscosity
ν	kinematic viscosity
$\Psi(E)$	threshold function in modified Shields' diagram
ρ	density
ρ_{tr}	density of tracer particles
σ_f	standard deviation of the filtered final wave signal
σ_{ow}	oil-water surface tension
τ	Shields parameter
τ	tension coefficient dependent on gap ratio
τ_0	shear stress
τ_b	modified shear stress
θ	rotation angle of the barrier in waves
υ_*	shear velocity
φ	reposing angle of grains
ς	entrainment parameter
ξ	displacement of a flexible barrier

ζ_w	coefficient of head loss

Subscripts

a	air
avr	average wave characteristics
m	model
max	maximum wave characteristics
o	oil
p	prototype
s	significant wave characteristics
w	water

List of Tables

List of Figures

Chapter 1

Introduction

This chapter provides a short introduction about oil spill causes, fate, and impacts. Furthermore, different remediation techniques and their efficiency, in general, and spill containment booms, in details, are discussed. A special kind of oil booms, called Cavalli system, is then introduced. Finally the main objectives of the research project are described and the methodology of the study is presented.

1.1 Oil spill problem

Oil spills are of major environmental concern in coastal regions. The movement of the oil slicks can pollute the coastal environment and damage marine life. A major oil spill can contaminate the shoreline, cause long-term damage to the aquatic environment for fishery and wildlife, and foul the harbor facilities and vessels. Toxic effects of spilled oil seriously threatens the environment.

The world's rapid economic development has caused a significant increase in fossil fuel consumption. The world production of crude oil is about three billion tonnes per year and 1.7 billion tonnes of it is transported by ship from producing and refining countries to the consuming countries. Most oil spills occur during extraction and transportation of oil and petroleum products.

Spilled oil will rapidly form a thin film over a wide region, through both natural spread phenomena and the influence of environmental action. The need to confine spilled oil to a small area, in relatively thick layers, as quickly as possible is a practical necessity.

1.1.1 Main causes of oil spills

A significant amount of oil is spilled into the sea from operational discharges of ships in the vicinity of marine oil platforms as well as from accidental tankers' collision and grounding. The cause of large amount oil spills (more than 700 tonnes) during the years from 1974 to 2004 is acquired from International Tanker Owners Pollution Federation (ITOPF) handbook (2006) and illustrated in Fig. 1.1.

Large quantities of oil have been released to the environment during the past

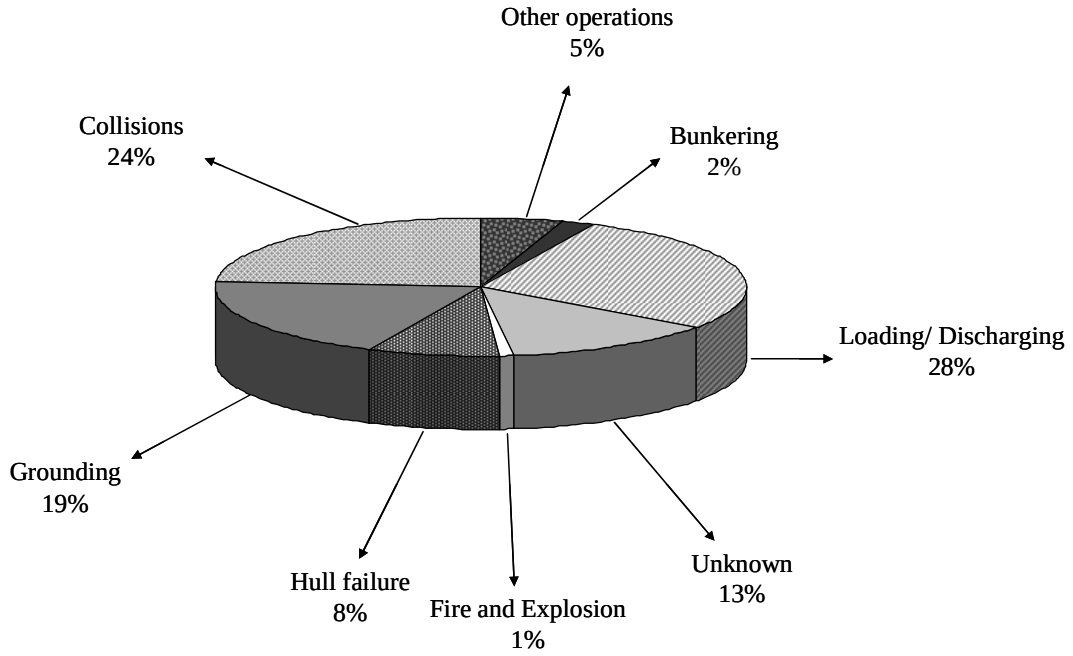

Figure 1.1: Cause of incidents with more than 700 tonnes spilled oil, from 1974 to 2004 (after ITOPF, 2006)

35 years mainly from oil tankers and oil producing platforms. The quantity of spilled oil during this period is presented in Fig. 1.2.

Although the statistics reported that the volume of spilled oil and the number of large spills are decreasing worldwide (that indicates the effectiveness of new technologies for prevention and response of oil spills), the need for more efficient devices in combating oil spills is evident. As an example, the Prestige incident in 2002 spewed 64'000 tonnes of oil over Spain, Portugal, and France coastlines and caused huge disasters to the coastal environment.

1.1.2 Fate of spilled oil

When oil is spilled at sea, it spreads and moves on the surface while undergoing a number of chemical and physical changes, collectively termed weathering. The trajectory and fate of spilled oil are governed by physical, chemical, and biological processes that depend on the oil properties, hydrodynamics, meteorological and environmental conditions. Some different involved processes are listed below:

- Spreading due to wind and the associated turbulence
- Advection and horizontal movement dependent on sea conditions
- Vertical dispersion and emulsification dependent on oil type, breaking wave energy and temperature
- Evaporation, oxidation and dissolution

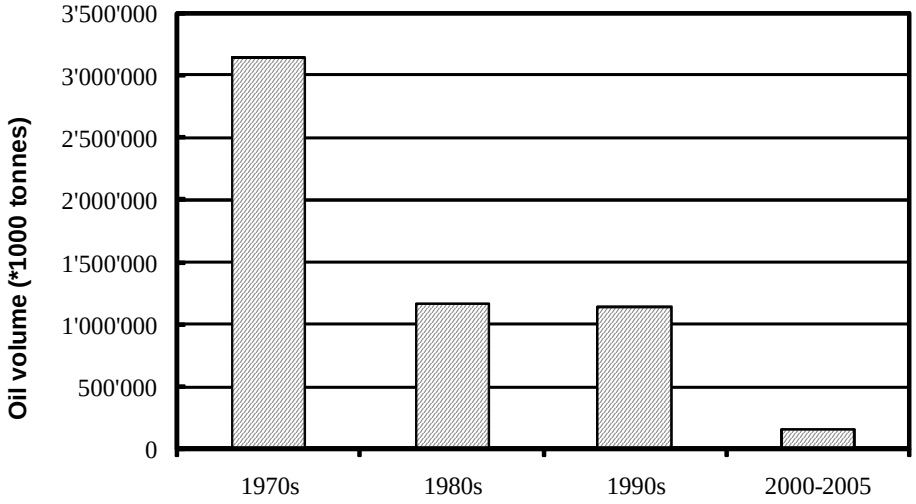

Figure 1.2: Quantity of spilled oil during the last 35 years (ITOPF, 2006)

- Shoreline deposition and re-entrainment into water
- Sedimentation and absorption of oil by sediment
- Biodegradation

1.1.3 Impacts of oil spills

Marine oil spills can cause serious damages to natural resources and to those whose livelihoods depend upon these resources. The nature and duration of any impacts will depend on a number of factors. These include the type and amount of oil and its behavior once spilled, the physical characteristics of the affected area, weather conditions and season, the type and effectiveness of the cleanup response, the biological and economic characteristics of the area, and their sensitivity to oil pollution.

Environmental impacts:
The environmental impacts on the ecosystem of the area exposed to danger can cause irretrievable damages. One liter of oil can pollute up to 10'000 liter of water. Seabirds are the most vulnerable users of open waters since they are easily harmed or killed by floating oil, while in the rivers fish are main victims. For example one liter of oil can kill over 1000 fish in a river. Somehow, shorelines are more than any other part of the marine environment exposed to the effect of oil as oil naturally tends to accumulate there.

Economic impacts:
Industries that rely on seawater for their normal operation, particularly power stations and desalination plants can be adversely affected by oil spills. An oil spill can also directly damage the boats and traps used for catching and cultivating marine species. Another economic impact is due to cleanup costs, which varies considerably from one incident to another. The type of oil, the

location of the spill and the characteristics of the affected area are generally the most important factors influencing the cleanup costs.

1.1.4 Remediation techniques and their efficiency limits

Unfortunately experience shows that even best efforts cannot prevent the occasional occurrence of major accidents at sea. Human error, mechanical failure, or environmental stress will cause maritime disasters. As long as the potential for massive oil spills exists, special techniques and equipments to facilitate spill cleanup in the coastal region will be required. Practically many competitive methods are available (Oil Spill Response Catalog, 2005), but they are mainly associated with adverse side effects:

In-situ burning:
In-situ burning is a controlled combustion of oil, which is considered as a cleaning method but a dangerous one and requires special authorizations. It has to be always used in conjunction with fire resistant booms. Moreover, before processing this operation, it is very important to pay attention to many parameters such as wind and current direction and velocities, water temperature, wave amplitude, oil type and so on. By this method the spilled oil cannot be recovered again. Another problem is that some components of fuel will remain in the water. Finally, burning the oil will cause air pollution that is undesirable specially in near coast regions.

Dispersing agents:
Dispersing agents are chemicals that contain compounds breaking oil into smaller droplets. These droplets are subjected to many natural processes that break them down further. The efficiency of such products depends on the oil type as well as on the rate at which the product is applied. Other factors like water salinity and temperature can influence dispersant efficiency.

Biological agents:
Oil biodegradation naturally occurs at a very low speed. Biological agents consist of enzymes or microorganisms and they can increase the biodegradation speed. Their function is also limited to a certain temperature range.

Sorbents:
Sorbents are materials that soak up liquids. The material of sorbent should be oil attractive and water repellent. The ideal sorbant absorbs oil quickly and retain it. Further, an effective sorbent material should absorb a large amount of oil per unit weight but very little water.

Mechanical barriers:
Containment and physical removal are recognized to be the most desirable methods of oil spill cleanup. Mechanical oil barriers, or "booms", are used to contain or divert oil spills on water and are key tools in oil spill response (Oebius, 1999).

They are the most commonly used techniques to collect and contain oil on the sea surface, or to protect specific areas against slick spreading. In recent years many different types of booms have been developed and studied in considerable detail both analytically and experimentally.

1.2 Oil spill containment booms

The first stage of an effective response is to deploy booms for limiting further spreading and concentrate the oil for recovery. Booms vary considerably in their design, but all normally incorporate the following features:

1. Freeboard to prevent or reduce splashover
2. Skirt to prevent or reduce escape of oil under the boom
3. Flotation by air or some buoyant material
4. Ballast to keep the boom upright in the water and to provide strength to withstand the effects of waves and currents.

There are many booms ranging from small lightweight models designed for manual deployment in harbors, to large robust units which usually need cranes and vessels to handle them and are designed for use in the open sea.

1.2.1 Different types of oil booms

Several classifications are applied to categorize the oil spill containment booms. The more general classification is due to the application of oil booms, where booms are categorized to calm water, protected water, and open water booms. Another classification is due to the deployment manner of the booms, which is explained and depicted by Oebius (1999) (Fig. 1.3).

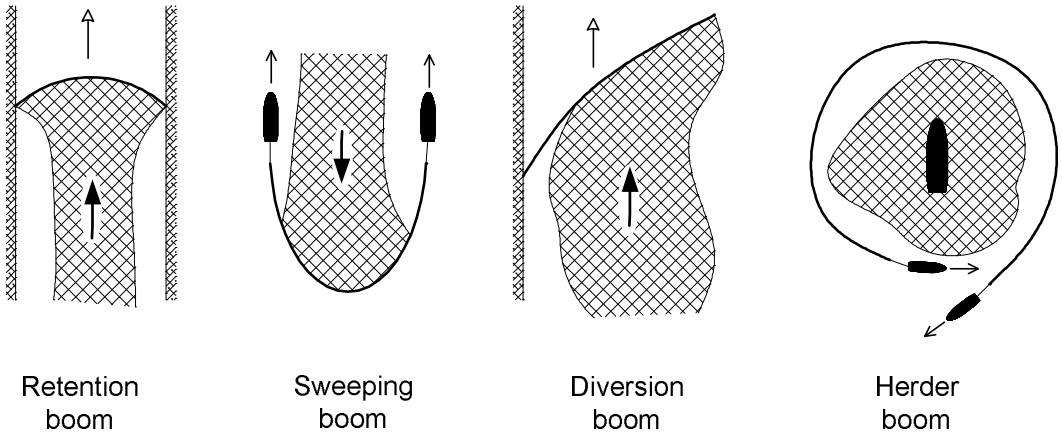

Figure 1.3: Classification of booms due to their deployment manner (after Oebius, 1999)

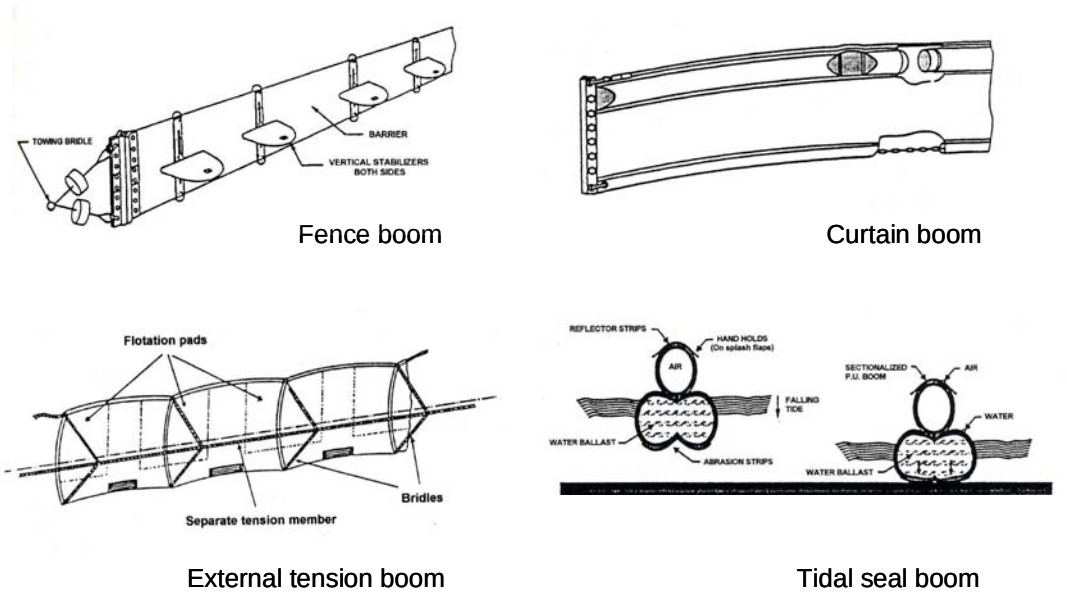

Figure 1.4: Different types of oil spill booms (Oil Spill Response Catalog, 2005)

Different types of booms are classified by the Oil Spill Response Catalog (2005) using their designations to help the user select products for contingency planning (Fig. 1.4).

1. *Fence booms* have a rigid or semi-rigid material as a vertical barrier.

2. *Curtain booms* have a flexible skirt that is held down by ballasting weights and are further identified according to their flotation:

   - Internal foam
   - External foam
   - Self-inflatable
   - Pressure-inflatable

3. *External tension booms* are slightly flexible and are controlled with an external tension bridle. They are only used for sweeping or in currents.

4. *Fire resistant booms* are used while conducting in-situ burning or if oil is already burning. They are made of fire resistant materials.

5. *Tidal seal booms* use air or foam for buoyancy and water as ballast. They float free at high tide and seal to the mud or sand at low tide. When grounded, the ballast seals the boom to the shoreline and prevents oil from moving along the intertidal zone.

6. *Special purpose booms*, e.g. "ice booms" or "sorbent booms", which are available for specialized use.

1.2.2 Efficiency of oil booms

The most important characteristic of a boom is its oil containment and deflection capability, determined by its behaviour in relation to water movement. It should be flexible to conform to wave motion yet sufficiently rigid to retain as much oil as possible. No boom is capable of containing oil against currents greater than 1 *knot* (0.5 m/s) irrespective of boom size or skirt depth. This factor limits the speed at which booms can be towed to 0.5 to 1 *knot* (0.25 to 0.5 m/s) (Cormark, 1999). Technically, an oil boom needs three principal characteristics to perform well:

1. **Bouyancy** is important to keep the boom afloat and to maintain adequate freeboard.

2. **Roll response** is rotation of the boom due to waves, wind, or current forces. Oil may be lost under a boom if the skirt is deflected excessively or has "rolled" from the vertical position.

3. **Heave response** is the ability of the boom to react to the vertical motion of water surface. A boom with good heave response is one that can closely follow the water surface as a wave passes. Flexible barriers are thus more effective than rigid ones.

Other important boom characteristics are strength, ease and speed of deployment, reliability, weight and cost.

1.2.3 Existing booms: dimensions and material properties

A wide range of oil booms exist nowadays on the market. The size of the boom depends on its application. For the open sea waters the boom depth varies between 60 to 150 cm, with freeboards from 30 to 130 cm. The length of the booms can reach easily up to 300 m (Oil Spill Response Catalog, 2005). Storage volume for containment booms can be a significant problem. Self-inflating and flatable booms generally require less storage volume than those with fixed floatation. Quick deployment by a small number of personnel is desirable. The self-inflating booms are often rolled on reels and they can be deployed by both helicopters and boats. Fig. 1.5 shows such a boom and its deployment methods.

The material used for the flexible skirt is of a significant importance for curtain booms. Existing skirts are made of different materials such as PVC coated polyester, urethane, vulcanized neoprene rubber, and Nitrile/Vinyl rubber impregnated high strength nylon cloth. The newest trend is using Kevlar sheets or Kevlar base fabric under urethane coating, that has a high chemical and mechanical resistance (Swedberg, 2003).

The ballast is usually made of galvanized steel chains. Furthermore, the ASTM standard can be used for design of boom connectors. Basically, a good connector is secure, strong, and prevents oil leaks (ASTM, 2004).

Figure 1.5: Self-inflating oil containment booms, helicopter and vessel deployable booms

1.3 Cavalli system

1.3.1 Main concept

A new anti-pollution system has been designed by Cavalli in 1999. The aim was to contain and clean up spilled oil. It can be used around or in close proximity to tankers and offshore platforms (Cavalli, 1999). The floating reservoir is made up of several self-inflating curtain booms, made of Kevlar with a ballast at the end point. Since the skirt is quiet flexible, the boom has very good roll and heave responses.

The concept of the Cavalli system is depicted in Fig. 1.6. First, oil spill is confined by a reservoir, with a herder boom system, avoiding its spreading over water surface (Fig. 1.6a). The reservoir can then be subdivided into two or four circles, using ropes, in order to increase the oil layer thickness (Fig. 1.6b and c). This improves the pumping operation by reducing the amount of water drawing up. The system can be deployed in the spill location by boats. It can also be permanently installed on tankers or platforms and be deployed around the slick immediately. Furthermore, the oil slick contained by booms can be towed to safe locations, i.g. near the coast, where the procedure of recovery is less influenced by wind and wave impacts.

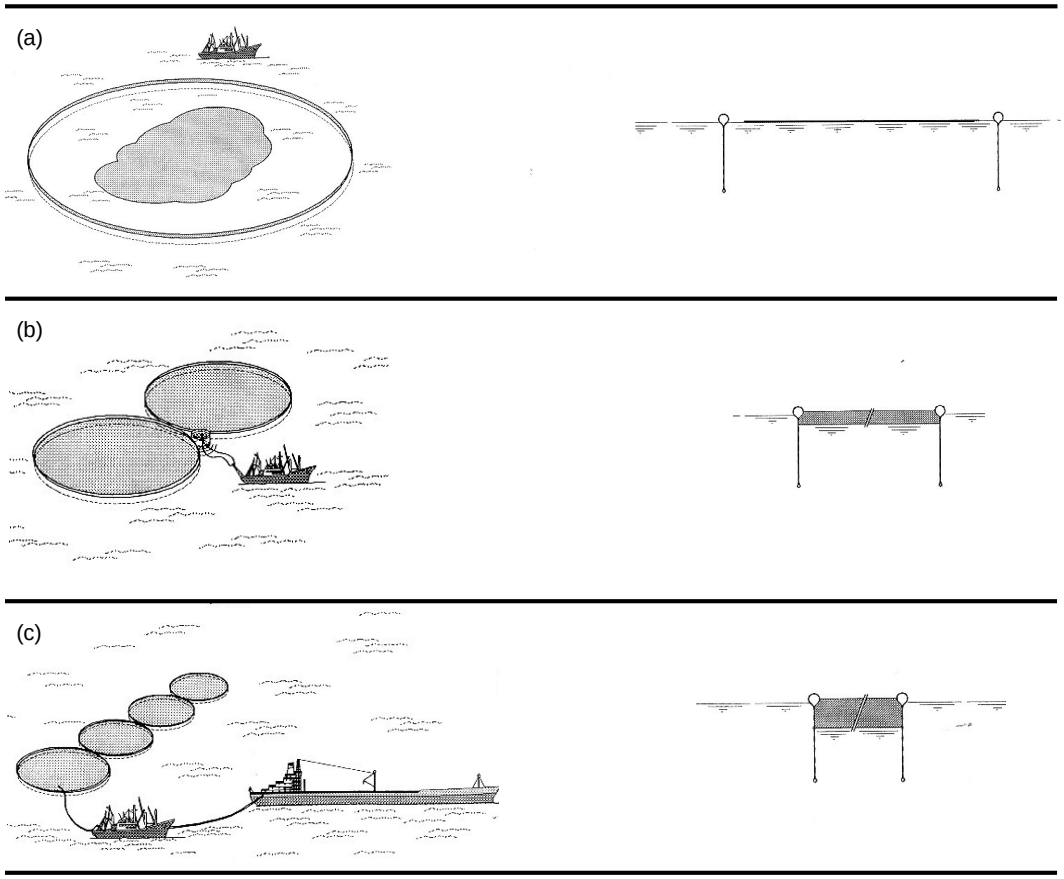

Figure 1.6: Cavalli oil containment system (Cavalli, 1999): (a) trapping oil by the reservoir; (b) increasing the oil layer thickness by dividing the reservoir into two smaller circles; (c) continuing to increase the oil layer thickness with a quadruple configuration

1.3.2 Previous study on Cavalli system

The application limits of single, double, and quadruple configurations of the Cavalli system were investigated at Laboratory of Hydraulic Constructions (LCH) by Sayah et al. (2004) and its efficiency under wave conditions has been confirmed. Experiments in both wave and towing tanks confirmed that the Cavalli contractile floating reservoir can be efficient for trapping oil spills (Fig. 1.7). The structural deformation and the oil loss rate was mainly influenced by the increase of wave steepness and towing velocity. The quadruple configuration was shown to be the most vulnerable one, which failed to contain the oil even for low velocities. The results of experiments performed under downscaled Mediterranean Sea and Atlantic Ocean waves were promising for effectiveness of the system under real wave conditions. The hydrostatic behavior of this system has been studied analytically by Amini et al. (2004).

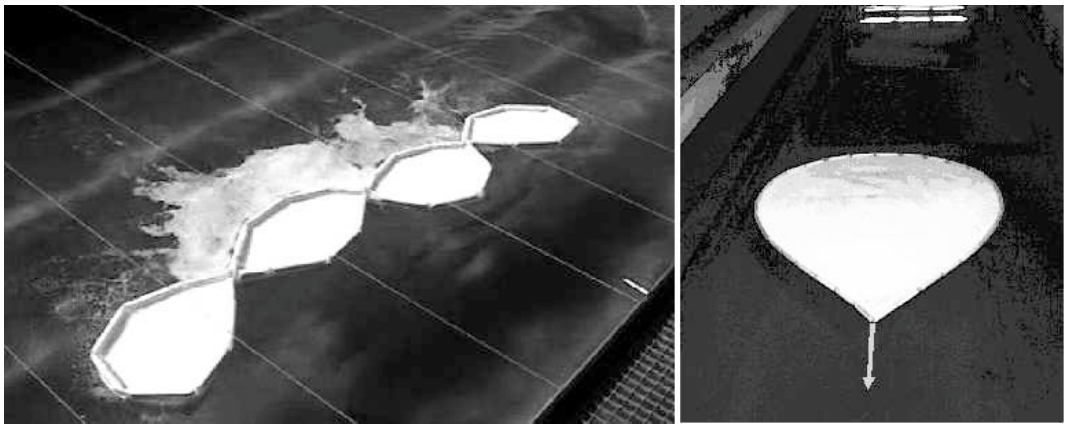

Figure 1.7: Background study on Cavalli system at LCH, left: quadruple configuration in a wave thank, right: single configuration in a towing tank (Sayah et al., 2004)

1.4 Scope and methodology of the study

Although the main motivation for launching the research project was to study the efficiency and operational limits of the Cavalli system, the objectives were not constrained to that particular case. The present investigation, however, focused on the behavior of flexible barriers in containing spilled oil. The main attention was given to the response of a flexible barrier in presence of waves.

Both experimental and numerical approaches are followed during the study. The experimental part is aimed to:

- Investigate the effect of a flexible barrier on initiation of failure and slick characteristics by performing two-dimensional test in a laboratory flume.
- Assess the initiation of failure for rigid and flexible barriers due to effect of incident waves.
- Precise measurements of the flow characteristics in the vicinity of the barrier, using UVP and PIV techniques.
- Study the capability of double barriers (representative for a trapping reservoir) to contain the oil slick.

To improve the understanding of the mechanisms associated with oil containment failure, numerical simulations are performed. The main objectives of numerical modeling are:

- Simulate the oil-water-air multiphase flow and geometrical characteristics of the oil slick.
- Evaluate the effect of a flexible barrier on flow hydrodynamics.
- Study the flow pattern and velocity field in the vicinity of different barriers.
- Investigate the oil containment by a trapping reservoir.

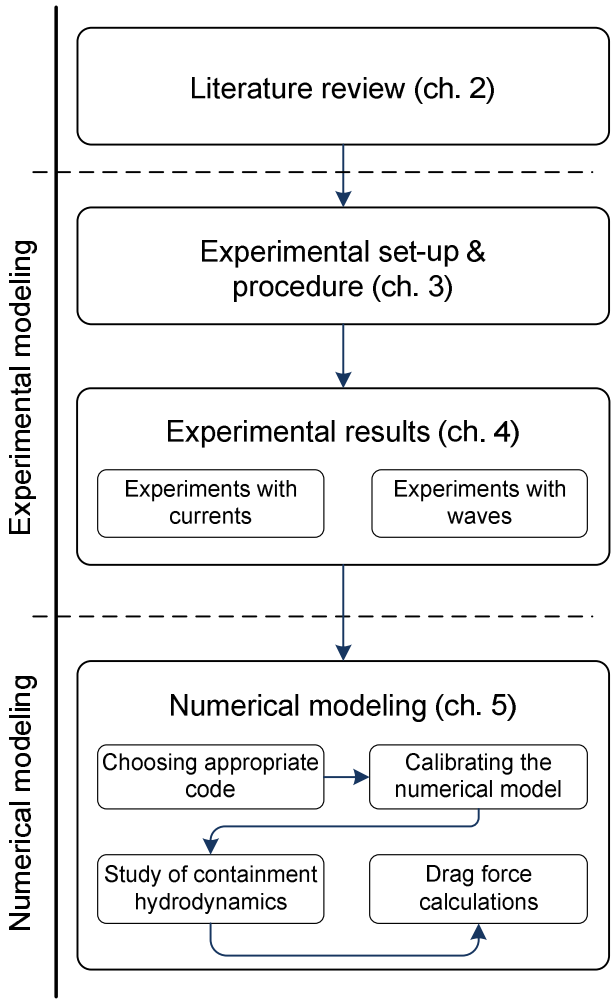

Figure 1.8: Methodology of the research project and structure of the chapters

– Estimate the drag force and compare results for rigid and flexible barriers.

The methodology of the research project and the structure of the present report is shown in Fig. 1.8. The main objectives of each chapter are described briefly:

– *Chapter 2* is dedicated to review the existing studies concerning oil spill problem. Different reported failure mechanisms are discussed in detail and the theoretical background is provided.

– *Chapter 3* explains the experimental set-up and the choice of experimental facilities and materials. In this chapter the characteristics of measuring instruments are described and their capabilities are discussed. Furthermore, the applied downscaling rules and laboratory effects are presented. The testing procedures for experiments with and without waves are stated at the end.

– *Chapter 4* presents the experimental observations, measurements, and results. Accordingly, it comprise the most important part of the report. The

results of experiments with rigid and flexible barriers, with and without waves, are demonstrated and comparisons are made.

– *Chapter 5* delineates the principles and results of numerical modeling. Preliminary simulations for choosing an appropriate numerical code are presented. After calibrating the model with experimental results, it is used for simulating multiphase flow in the vicinity of flexible and rigid barriers. Finally, acting forces on prototype are calculated and analyzed.

– *Chapter 6* summarizes the experimental and numerical results, suggests recommendations for a real case, and finally presents proposals for further research.

Chapter 2

Literature review on oil spill containment booms

In this chapter the background study on oil spill containment booms is reviewed. Most of the background research on containment booms has focused on limits of oil boom application. As a result, the failure mechanism has received special attention. Most of studies have investigated the involved parameters and physical or environmental conditions which lead to total or partial failure in containment and recuperation procedure. Hence, the main part of this chapter describes the investigations regarding principal failure mechanisms.

Moreover, some innovative boom configuration are presented briefly and oil spill trajectory prediction and fate models, as well as numerical models are summarized.

2.1 Failure mechanisms of containment booms

Containment booms can be highly successful in recuperating spilled oil. However, they do not perform well in every case. Several mechanisms can cause (a part of) the oil to be transferred underneath the barrier. Generally, there are seven basic modes of operating failure (Oil Spill Response Catalog, 2005; ITOPF, 2006):

- Splashover
- Submergence
- Planing failure
- Structural failure
- Entrainment failure
- Drainage failure
- Critical accumulation

Splashover occurs in choppy seas when oil splashes over the boom's free board. Submergence failure may happen when a boom is deployed or anchored in a fast current, or is being towed at a high velocity in still water. The tendency to submerge at a given velocity is determined by the ratio of boom's buoyancy to weight. A strong wind and strong current moving in opposite directions may cause a boom to heel flat on the water surface and the planing failure to happen. The most catastrophic failure mode is the structural one, that happens when the boom fails to stand the imposed hydrodynamic loads. Since the last three failure modes are more relative to the scope of this research project, they are discussed in more detail in Sec. 2.1.1, Sec. 2.1.2, and Sec. 2.1.3.

2.1.1 Entrainment failure

Entrainment failure occurs when a high relative oil-water velocity causes interfacial waves to form, and oil droplets to be entrained from the oil-water interface and pass beneath the barrier. For most oils with a viscosity in the order of less than 1000 cSt, droplet entrainment failure occurs at a lower velocity than does drainage failure, so the former failure mechanism dictates the speed limit for effective containment. Additionally, the drainage failure can be prevented using a barrier with a sufficiently deep draft, whereas the entrainment failure is independent of the draft and can not be avoided at velocities higher than a certain value.

A number of studies have been carried out on the problem of oil entrainment failure and instability of an oil layer over a water surface. Wicks (1969) carried out one of the earliest investigations and identified three different regions in an oil layer: the headwave region at the upstream end of the oil slick where the oil layer has maximum thickness, the middle region where the drag of the flowing water thickens the slick, and the near boom region that is influenced by a circulation cell formed behind the barrier (Fig. 2.1). He postulated that the headwave is analogous to a gravity current turned upside down. The so-called headwave region was emphasized because of its importance to entrainment failure, since the droplets are torn off the rear of the headwave and entrained into the water flow.

Wicks (1969) also recognized that oil droplet entrainment is a consequence

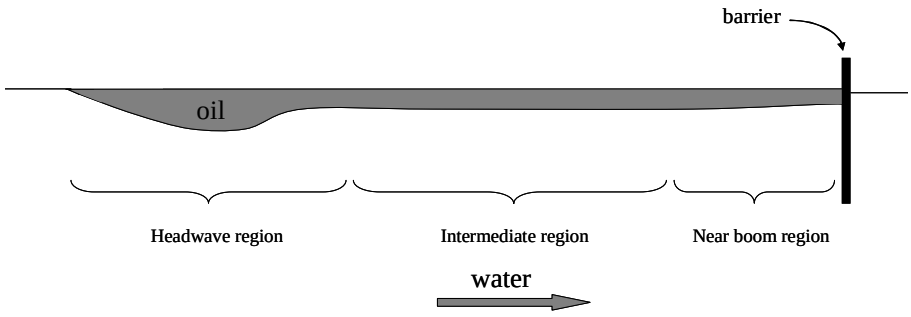

Figure 2.1: Shape of contained slick in case of entrainment failure, the three regions identified by Wicks (1969)

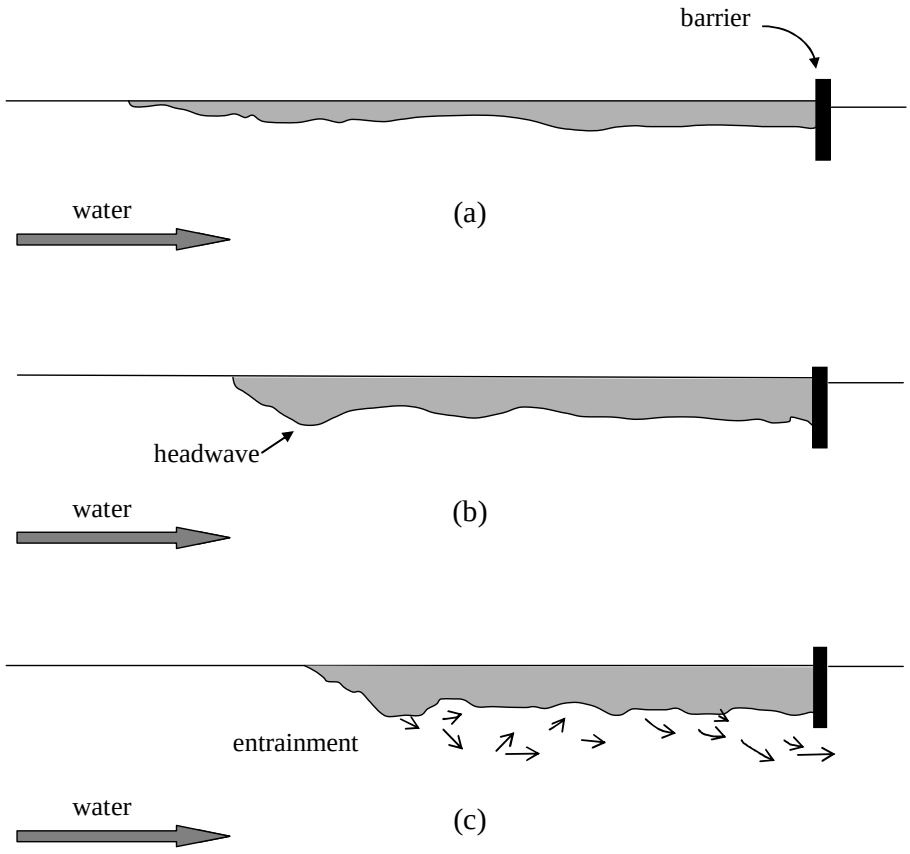

Figure 2.2: Oil slick profiles at different flow velocities: (a) low velocity (less than 15 cm/s); (b) intermediate velocity (between 15 to 25 cm/s); (c) above critical velocity (more than 25 cm/s) (after Agrawal and Hale, 1974)

of a Kelvin-Helmholtz instability at the oil-water interface. He attributed the velocity at which the oil droplets peal off the headwave to a critical Weber number, We_{cr} of about 14:

$$We_{cr} = \frac{\rho_w U^2}{\sigma_{ow} g(\rho_w - \rho_o)} = 14 \tag{2.1}$$

where σ_{ow} is the oil-water interfacial tension, U is the flow velocity, g is the gravity acceleration, and ρ_o and ρ_w are densities of oil and water respectively.

Doing experimental work, Agrawal and Hale (1974) found this critical Weber number to be rather 28.2, which is about two times the value suggested by Wicks (1969). The proposed oil slick profile at different current velocities and the initiation of headwave are shown in Fig. 2.2. Jones (1972) studied the instability at the interface that provokes wave formation. He reported that the waves begin to grow, and when a wave becomes steep enough, the interfacial tension forces cause the crest of the wave to break off and form a droplet which is then entrained into the flow. This interfacial instabilities can usually be explained by Kelvin-Helmholtz instability predictions.

Classical Kelvin-Helmholtz predictions deal with two semi-infinite inviscid fluids of different densities, each moving at a given uniform velocity. But oil

layer over water surface has a finite thickness and a certain viscosity. Jones (1972) tried to modify these predictions by determining the effect of the finite thickness of the oil. In his analysis, however, he neglected the interfacial tension of the air-oil interface as well as air density, and imposed a constant pressure boundary condition at surface. This made him conclude that thick layers are more stable than thin ones, which is not justifiable. It was explained later by Leibovich (1976) and Milgram and Van Houten (1978) that thin layers are more stable, since the oil-air tension has a stabilizing influence when the layer is thin.

To predict droplet formation at the headwave, Zalosh and Jenson (1975) modeled the oil-water and oil-air interfaces with a set of discrete vortices, whose circulation vary with time. The developed numerical model was able to simulate stable or unstable oil slick headwave at different water velocities. The model showed also that oil loss rates increase sharply with velocity.

Leibovich (1976) evaluated the possible mechanisms that may transfer energy to wave motions and hence allow for wave growth. One phenomenon that may promote droplet formation on the lee side of the headwave is the adverse pressure gradient that the water boundary layer confronts, and its consequent separation and eddy formation. Anyhow, Leibovich (1976) suggested a more elementary cause: the local current speed is greatest at the maximum thickness. He postulated that all the traveling waves which are found on the oil-water interface at velocities in excess of about 15 cm/s are Kelvin-Helmholtz waves whose amplitudes are limited by finite-amplitude effects similar to those analyzed by Drazin (1970)[1].

Leibovich (1976) concluded that below a minimum flow velocity ($U = 2.2U_{KH}$ or $We_{cr} \approx 20$), no droplets are shed from any part of the slick. Above this minimum velocity but below a second critical velocity ($U = 3.1U_{KH}$ or $We_{cr} \approx 40$), droplets can be formed only on the headwave. And above the second critical velocity, drops may be formed from any part of the slick. The parameter U_{KH} indicates the Kelvin-Helmholtz stability threshold velocity:

$$U_{KH} = \left(2\frac{\rho_w + \rho_o}{\rho_w \rho_o} \sqrt{\sigma_{ow} g(\rho_w - \rho_o)} \right)^{1/2} \tag{2.2}$$

In this equation σ_{ow} stands for the oil-water interfacial tension, and ρ_o and ρ_w for oil and water densities respectively. The instability corresponds then to a disturbance with capillary wavelength, λ:

$$\lambda_c = 2\pi \sqrt{\frac{\sigma_{ow}}{g(\rho_w - \rho_o)}} \tag{2.3}$$

An error has been found in these empirical values by Wilson (1977). The corrected velocity values are $1.55U_{KH}$ for droplet formation from headwave and $2.2U_{KH}$ for droplet formation at other locations on the interface.

[1]Drazin (1970) had studied the non-linear Kelvin-Helmholtz instability of two parallel horizontal streams of inviscid incompressible fluids under the gravity force theoretically. He showed that unstable waves may be stabilized by nonlinear terms ignored in the linear stability analysis of Kelvin-Helmholtz.

To point out the relative effects of dynamic pressure and frictional forces in determining the thickness distribution of an oil layer contained by a barrier, Milgram and Van Houten (1978) performed an experimental study. They suggested that viscosity of the oil plays a role in determining the critical velocity for droplet entrainment through its effect on the interfacial waves. They postulated that dynamic forces are not dominant in the headwave region and viscous stresses are more important than dynamic pressure forces.

Fannelop (1983) summarized the work of his pioneers and did an extensive investigation to clarify the capability of containment booms. The main aim of his study was to estimate the capacity of containment barriers. He discussed about loss mechanisms and loss rate for two-dimensional and three-dimensional barriers.

The study of droplet entrainment failure was later continued by Lee and Kang (1997). They proposed an empirical formula for threshold velocity for entrainment failure, U_f.

$$U_f = 1.98U_{KH} + 0.085\sqrt{g\Delta D} \tag{2.4}$$

in which

$$\Delta = \frac{\rho_w - \rho_o}{\rho_w} \tag{2.5}$$

In the above equation, the Kelvin-Helmholtz threshold velocity, U_{KH}, is calculated from Eq. 2.2 and D is the barrier's draft. This empirical equation is the only proposed equation taking into account the barrier draft, D. However, this is based on the assumption that the draft remains vertical, i. e. for a rigid barrier.

The controversial definition of failure velocity, brought about some discrepancy in critical velocity causing entrainment failure. Some researchers considered the velocity at which significant oil droplets were first formed at the headwave of a contained slick, while the others took into account the velocity at which the first droplet passes beneath the barrier. Anyhow, the reported failure velocities are between 25 to 35 cm/s.

2.1.2 Drainage failure

The second failure mechanism is called drainage failure and happens when oil plunges under the boom and escapes with the water. Cross and Hoult (1971) studied the drainage failure and described the form of an oil slick contained by a barrier in a current of finite depth. Three terms were considered in the equation of motion: inertia, pressure, and friction from the water flowing under the oil. The equilibrium of these forces was used to derive the equation for prediction of oil thickness. The proposed profile of contained oil thickness, $h(x)$, is shown in Fig. 2.3. The slick layer thickens with the square root of the distance in the down stream direction:

$$h(x) = \sqrt{\frac{C_f U^2}{g\Delta}}\, x^{1/2} \tag{2.6}$$

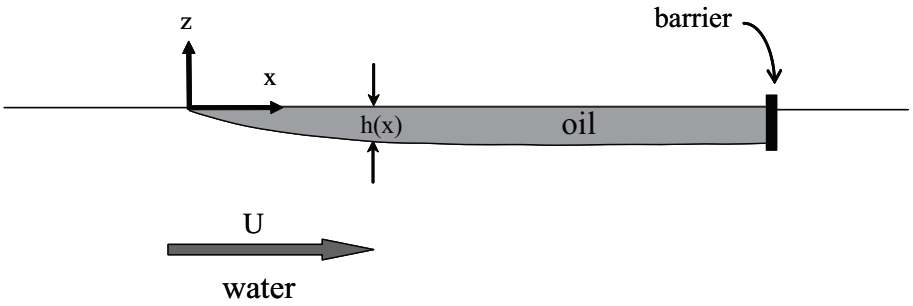

Figure 2.3: Profile of oil slick contained behind a barrier in case of drainage failure (after Cross and Hoult, 1971)

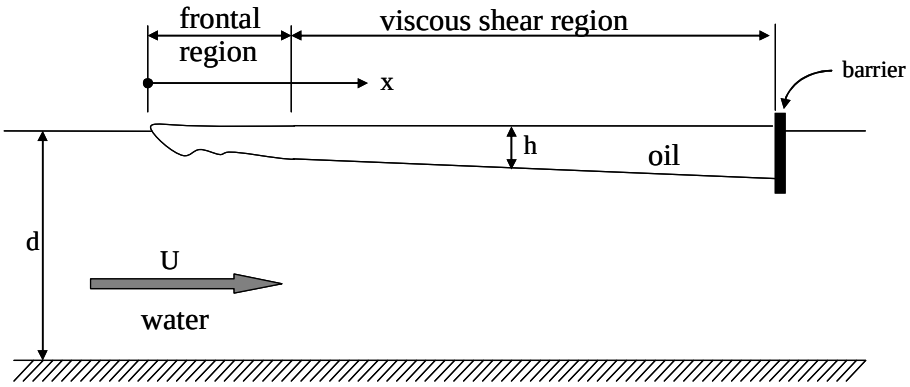

Figure 2.4: Schematic drawing of contained oil slick with frontal and viscose zones (after Wilkinson, 1973)

where C_f is the friction coefficient, Δ is the relative oil density derived from Eq. 2.5, and x is the distance from the slick upstream point as it is shown in Fig. 2.3. For low Reynolds numbers, it was assumed that C_f decreases with increasing x, while it is constant for higher Reynolds numbers. They assumed a typical value of C_f to be equal to 0.005.

Wilkinson (1972a) simplified the analysis by dividing the slick into two zones: the frontal zone in which dynamic forces are dominant, and a viscous shear zone in which viscous effects are dominant. These zones are presented in Fig. 2.4. For the frontal region, the equation proposed by Benjamin (1968) for gravity currents was used to calculate the thickness of oil, h:

$$h = \frac{U^2}{2\Delta g} \tag{2.7}$$

For the viscous shear zone, the interfacial slope is determined by solving the water and oil equilibrium equations together. The resulted profile is similar to the parabolic profile which had been presented by Cross and Hoult (1971). But, it is also affected by boundary stresses acting on the fluid flowing beneath the oil. The boundary friction on the flume was found to contribute by an amount of 15% to 20% to the friction coefficient (Wilkinson, 1972b).

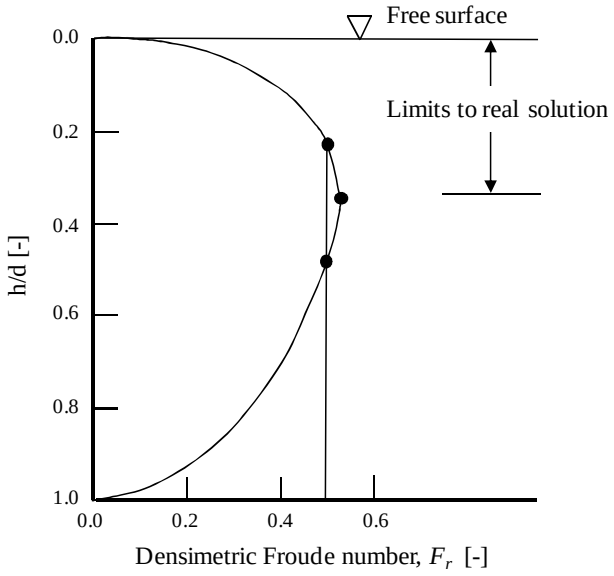

Figure 2.5: Ratio of slick thickness to water depth, h/d, as a function of densimetric Froude number (after Wilkinson, 1972b)

Knowing the oil thickness at the barrier, drainage failure can be prevented by increasing the barrier depth. However in the case of a turbulent oil-water interface, there is no equilibrium thickness and entrainment failure makes the retention of such a slick impossible. This critical velocity is dependent on the flow depth and oil density. An oil slick will not attain a stable thickness when the densimetric Froude number, F_r, is greater than a certain value.

$$F_r = \frac{U}{\sqrt{\Delta g d}} \tag{2.8}$$

where d is the water depth and Δ is calculated from Eq. 2.5. The effect of Froude number on the slick thickness is depicted in Fig. 2.5. For Froude numbers greater than approximately 0.5, the contained slick is unable to reach a dynamic equilibrium.

Later on, Wilkinson (1973) evaluated the limitations to volume and length of contained oil slicks. He implied that the limit of slick length contained by a barrier depends on the densimetric Froude number, F_r, upstream of the slick, as well as both interfacial and boundary roughness (correspondent to a Chezy coefficient). On other words, an increase in the boundary stress will result in a more rapid thickening and therefore a shorter slick.

Lau and Moir (1979) recognized that although the value of the interfacial friction coefficient, C_f, is of prior importance to calculate slick profile and volume. They studied the effect of oil property on magnitude of C_f. The interfacial shear stress was found to be larger for more viscous oils, probably because of a smaller circulation velocity in the oil and thus a larger relative velocity between the oil and the water. Therefor C_f increases for oils with higher viscosity. Furthermore, they have established criteria for the containment of oil slicks using a barrier in open channel flows considering the densimetric Froude number, F_r,

and the barrier's draft, D:

$$F_r \leq 0.5; \quad and \quad D \geq \frac{U^2}{2(\frac{\Delta}{1-\Delta})g} \tag{2.9}$$

Unlike earlier researchers, Fannelop (1983) expressed that the characterization 'inviscid' and 'viscous' regions should be avoided, as viscous stresses are important, and perhaps even dominant, everywhere along the oil-water interface.

Ertekin and Sundararaghavan (1994, 1995); Sundararaghavan and Ertekin (1997) studied the effect of viscosity on the instability of attached and detached flows in finite and infinite water depths. They developed a numerical model to simulate streamlines, velocity vectors, and vorticity contours in the vicinity of a rigid barrier.

As a summary, for oils with low viscosity ($\nu < 3'000\ cSt$) and at low velocities, the oil-water interface is smooth with a headwave on the upstream edge of the slick. By increasing the velocity, slow waves appear at interface. The slick becomes then shorter and thicker and a drainage failure happens if the oil thickness exceeds barrier draft. Hence, the drainage failure can be avoided using barriers with a deeper draft. If drainage failure does not (yet) occur, the gravity shear waves become unstable (Kelvin-Helmholtz instability) and droplet entrainment begins. In Sec. 2.1.3 the case of oils with higher viscosities is discussed.

2.1.3 Critical accumulation

For oils with higher viscosity or in case of water-oil emulsions, a third failure mechanism may occur, in which the whole oil volume accumulates behind the barrier and passes under the barrier suddenly, i.e. critical accumulation failure.

Earliest studies on the viscous effects of oil had illustrated the importance of this parameter and encouraged the researchers to do further investigations using high viscous oils. In real oil spills, the viscosity of slicked oil increases rapidly as a result of weathering and emulsification. Delvigne (1989) studied the effect of viscosity using a wide range of oil types and viscosities (ν between 12 to $36'000\ cSt$). He concluded that the oil viscosity is a principal parameter involved in the occurrence of any type of failure mode. His experiments indicated that the critical accumulation appears to occur for oil viscosities over $3'000\ cSt$ at relative oil-water velocity of $0.15\ m/s$. The critical velocity was found to be of the same order for oil with viscosity between 3'000 and 20'000 cSt, with a slight increase for more viscous oils, and independent of oil volume, barrier draft, water depth, and other oil properties. In critical accumulation, the oil remains a single mass due to the high viscosity and moves readily through the water. In Fig. 2.6 the deformation of headwave for critical accumulation is illustrated. The phenomenon is considered as an unstable growth of an interfacial wave to infinity.

High-viscosity oils and water-in-oil emulsifications are inherently non Newtonian fluids and their viscosity depends on applied shear rate. The oil emulsion

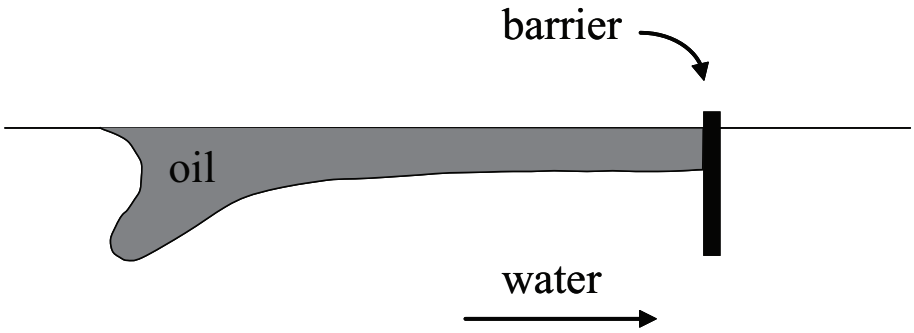

Figure 2.6: Deformation of the headwave at the onset of accumulation, (Delvigne, 1989)

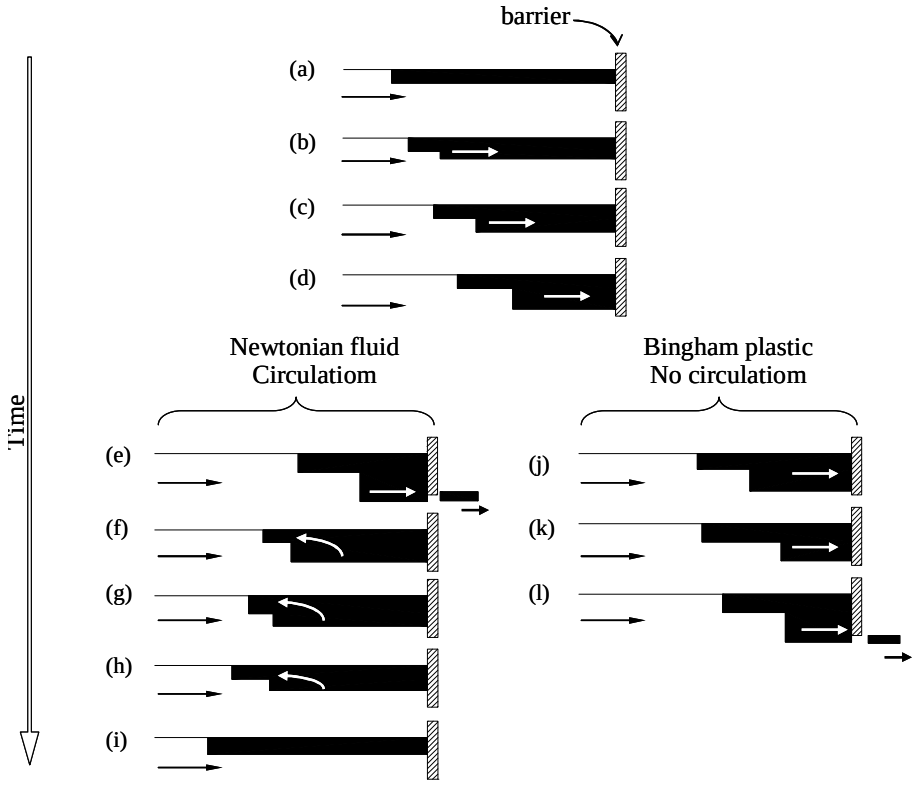

Figure 2.7: Typical oil slick behavior for a high-viscosity oil (after Johnston et al., 1993)

can form a rigid mass that resists deformation until the applied stress reaches a yield value. When this value is exceeded the emulsion starts to flow. Johnston et al. (1993) studied the surging behavior of contained slicks of viscous oils. They simplified the analysis by considering the oil having two behavior components: one that has pseudo-solid characteristics and another having the characteristics of a fluid. This decomposition of the flow field follows a Bingham plastic model that was suggested by Collins et al. (1976). Johnston et al. (1993) postulated that the critical accumulation failure is a result of the circulation in the oil which is insufficient to relieve the shear stress along the oil-water interface. Fig. 2.7 compares the reversal surge due to circulation in Newtonian

fluids with Bingham plastics. Differently from Delvigne (1989), they found the critical accumulation to occur for oils with viscosity more than 8'000 cSt.

2.2 Effect of waves and wind

Oil spill removal and control in open seas is seldom conducted in calm conditions. Therefore, the effects of waves and turbulence on the performance of oil spill equipment must be faced. Leibovich (1975a,b) presented the equations of motion for thin oil layers due to gravity, inertia, surface tension, and stresses imparted by wind and water waves. Kordyban (1982a,b, 1992) also made a major effort for taking waves and wind effects into account and implied that instability in presence of waves occurs much earlier than without waves. However, Lee et al. (1998) postulated that the waves may either increase or decrease the threshold velocity.

All existing studies are conducted with a fixed boom, while in practice the barrier is subjected to various motions in the presence of waves and wind, and follows the wave crest and trough. Performing experiments with a rigid fix barrier, Kordyban (1992) reported that the oil layer is thicker at the crest, and as the interface moves down, the thickness decreases significantly. It is minimum at the trough, but increase rather suddenly thereafter and reaches the bottom of boom. As the upward travel continues, the oil still escapes until the interface, eventually, returns to its normal shape as it is shown in 2.8. Kordyban (1982b) also examined the effect of the wind on the distribution of an oil layer on wavy water, since the waves exist usually in windy weather. It was found that the wind tends to decrease the difference between the oil layer thickness at the wave crest and the wave trough.

The most comprehensive investigation of oil spill containment barriers under various current, wave, and wind conditions was provided by Fang (1999) and

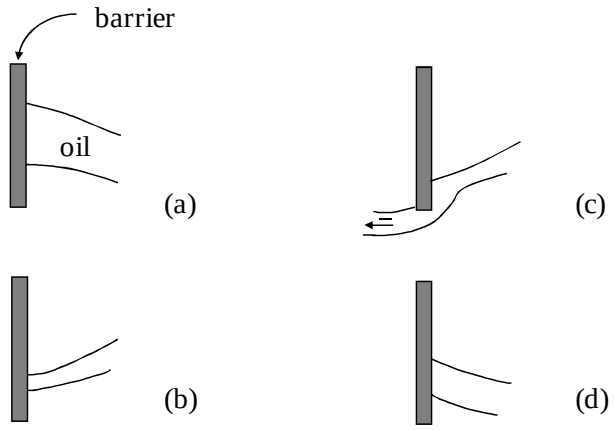

Figure 2.8: Schematic drawing of oil thickness change behind a rigid fix barrier in presence of waves (Kordyban, 1992): (a) near crest: maximum oil thickness; (b) near trough: minimum oil thickness; (c) sudden increase in oil thickness, oil escapes under the boom; (d) level rising

Fang and Johnston (2001a,b,c). They developed a local two-phase nonlinear hydrodynamic numerical model to simulate oil containment by a rigid fixed boom under open sea conditions. The results were compared with those obtained from experiments with different oils. The study approved that the failure mode is independent of wave characteristics and is just influenced by the oil viscosity. However, the initiation of failure can be considerably influenced as the wave hight or frequency increases. Furthermore, the velocity profiles in the region of oil slick were studied.

The efficiency of Cavalli system under open sea condition was the subject of some experimental investigations by Sayah et al. (2004). The generated waves in that work had the characteristics of downscaled Mediterranean waves as well as waves from Atlantic Ocean. It was shown that the increase of wave steepness may reduce the efficiency of containment system.

2.3 Forces and motion of oil barrier

The strength and seakeeping of oil control barriers were also subject of some research projects. Milgram (1971, 1973) formulated the tension in the barrier derived by water, T_w, implied on the barrier when it is moored in catenary shape in case of currents without waves by:

$$T_w = \frac{1}{2} l \rho_w U^2 D C_d \, \tau \tag{2.10}$$

where C_d is the drag coefficient (assumed to be 1.5), l is the barrier length and τ is a dimensionless tension parameter dependent of the opening ratio of the catenary shape as presented in Fig. 2.9. In presence of waves, Eq. 2.10 can be rewritten as follows (Oil Spill Response Catalog, 2005):

$$T_w = \frac{1}{2} l \rho_w \left(U + o.5\sqrt{H_s} \right)^2 D C_d \, \tau \tag{2.11}$$

where H_s is the significant wave height. The drag force induced by wind on the freeboard, T_a, can also be expressed as:

$$T_a = \frac{1}{2} l \rho_a (U_{wind})^2 f C_d \, \tau \tag{2.12}$$

where ρ_a is the density of air, U_{wind} the wind speed, and f is the boom freeboard. The total force applied on the barrier, T_{tot}, is then:

$$T_{tot} = T_w + T_a \tag{2.13}$$

Nash and Molsberry (1995), Cho and Cho (1995), and Van Dyck and Bruno (1995) stated the importance of wave conformance (heave response) and postulated that steep waves are the most difficult sea conditions for a floating boom to follow. The seakeeping characteristics of various booms in irregular waves and currents were investigated by Kim et al. (1997). In order to simplify the

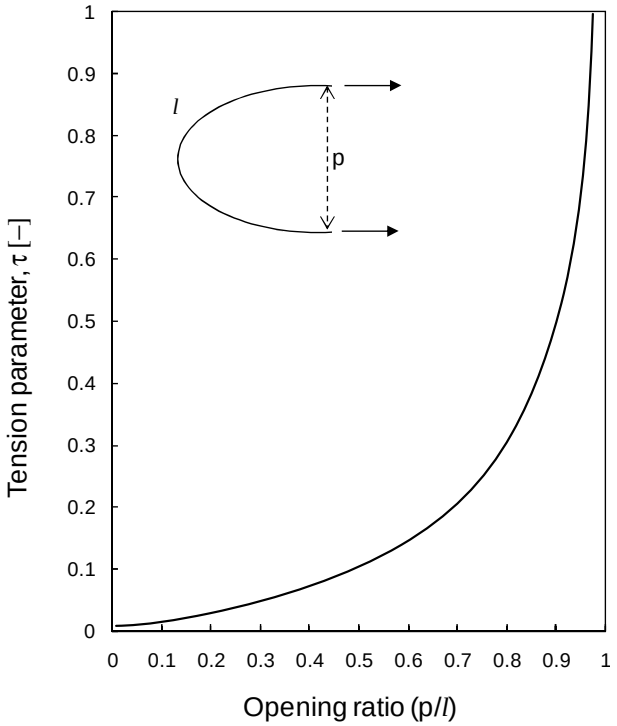

Figure 2.9: Tension coefficient, τ, as a function of barrier opening ratio, p/l (after Milgram, 1973)

problem, only rigid booms were examined and the influence of the oil slick on hydrodynamic performance of booms was assumed to be neglected.

The seakeeping performance of the boom is a function of boom geometry and buoyancy/weight ratio. High buoyancy/weight ratio booms are mostly effective against over-splashing failure even in high waves. The buoyancy/weight ratio near 20 is expected to have the best overall performance for all the sea conditions.

2.4 Non-conventional and tandem booms

The efficiency of single booms is limited to currents or towing velocities up to 0.3 m/s for oils with low viscosity (before entrainment failure occurs) and 0.15 m/s for oils with high viscosity (before critical accumulation occurs). This provoked the motivation for researchers to look for more efficient systems by changing the boom configuration. Delvigne (1984) examined the efficiency of a system with two parallel booms, i.e. tandem booms. The distance between two barriers should be designed in a way to provide the best oil slick protection. Lo (1996) had shown that a separation distance of 16 times the barrier draft could be rather suitable for confinement of both high and low viscosity oil slicks. Lee and Kang (1997) found this optimal separation distance to be eight times the boom draft while Lee et al. (1998) proposed a ratio of 10. However, they postulated that such a value may change for different oil types.

Lee et al. (2004) studied the flow characteristics between tandem fences by the Particle Image Velocimetry (PIV) method and assessed the effectiveness of tandem booms regarding the velocity field. They also examined tandem booms with non-identical fore and rear drafts.

Another innovative boom arrangement, combined of a ramp boom and three parallel booms of different drafts, was evaluated by Fang and Wong (2001) and it was shown that an optimal inclination angle of ramp boom and appropriate span between conventional booms can lead to an efficient containment system. Recently, Wong and Stewart (2003) tried to design a new barrier that can function efficiently in the presence of waves. They proposed three different rigid barrier with a sinusoidal cross section. This shape was found to perform better in turbulent conditions.

2.5 Oil spill trajectory and fate modeling

Applying an appropriate forecasting model will lead to convenient response and success in the cleanup operations. Rasmussen (1985) developed a numerical code that predicts weathering and transport of oil spills. To explore the combined influence of wind and shear currents, an accurate model was established by Tkalich and Chao (2001). A more complete model was developed by Tkalich et al. (2003) that simulates consequences of accidental oil spills on the water surface as well as the water column. The model predicts the oil slick thickness considering dissolution, emulsification and sedimentation processes.

Chao et al. (2001, 2003) developed two-dimensional and three-dimensional models for spill fate prediction. They suggested a diagram showing the average thickness of oil slick as a function of time, as represented in Fig. 2.10.

They used the equation proposed by Lehr (1984) to calculate the non-symmetrical spreading of oil slicks, which is based on the assumption that the oil slick spreads under the shape of an ellipse with the major axis (L_{max}) in the direction of the wind. The equation can be written as:

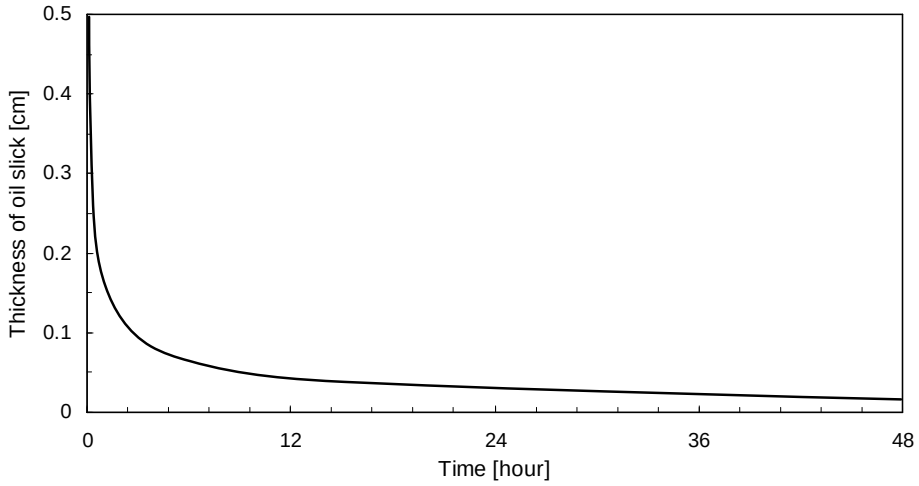

Figure 2.10: Thickness of the slicked oil as a function of time (Chao et al., 2003)

$$L_{min} = 53.76(\frac{\Delta\rho}{\rho_o})^{1/3} V_{oil}^{1/3} t^{1/4} \tag{2.14}$$

$$L_{max} = L_{min} + 0.95\, U_{wind}^{4/3}\, t^{3/4} \tag{2.15}$$

where L_{min} and L_{max} are respectively length of minor and major axes in meter, $\Delta\rho$ is the difference in oil and water densities, ρ_o the density of oil, V_{oil} total volume of the spilled oil in barrels, t the time in minutes, and U_{wind} the wind speed in knot.

The number of existing numerical and analytical models for forecasting oil spills fate and trajectory is enormous. A vast review on these models was presented by ASCE Task Committee (1996) and later by Sundararaghavan (2000).

2.6 Existing numerical models

As it was summarized in Sec. 2.5, the majority of numerical models are dedicated to modeling the spread of spilled oil on the surface of water, applying the physiochemical mechanisms of the spreading and developing hindcast models.

A few numbers of researchers have focused on numerical modeling of oil containment process. Badesha et al. (1993) applied Finite Element models to study the three-dimensional structural behavior of an oil spill boom. Brown et al. (1996), Goodman et al. (1996), and An et al. (1996) used the FLUENT code to simulate the oil-water flow in the vicinity of a containment boom. They simulated drainage and critical accumulation failure mechanisms successfully, however their model fails to simulate droplet entrainment failure. They showed that the presence of oil on the water surface behind a barrier modifies flow characteristics significantly.

Grilli et al. (2000a,b) developed a numerical code called "SlickMap" to predict the failure of viscose oil containment, i.e. critical accumulation failure mode. The model was calibrated by full scale experiments in OHMSETT[2]. He assumed that the slicked oil weathers and reaches very high viscosity so rapidly that the dominant failure mode is always the critical accumulation mode.

Recently, oil propagation along the free surface induced by wave and wind forces was incorporated by Fang and Johnston (2001a,b,c), and the interfacial waves and oil free surface waves under a number of hydrodynamic conditions were simulated. Furthermore, a friction-free model was established by Zhu and Strunin (2001, 2002) that quantitatively discussed the oil leakage from a floating barrier. Simple Fluid Structure Interaction (FSI) and multiphase models of oil containment booms were developed by Amini et al. (2005, 2006c).

As a summary, most of existing numerical models have been developed to simulate a special case of containment. Commercial CFD codes were also occasionally used and showed the capability of simulating multiphase problem of oil spill containment by rigid barriers.

[2]American national oil test facility in Sandy Hook, New Jersey

2.7 Anticipated contribution

Although the flexible barriers become more and more common as a cleanup facility, the knowledge about their behavior is lacking. As it was explained, almost all existing research, either physical or numerical, has been done for rigid barriers. Therefore, the present research is mainly focused on understanding the efficiency limits and behavior of flexible barriers.

As a first step, the behavior of a flexible barrier in currents without waves is investigated and compared to that of a rigid barrier. The key challenge is to contain the oil behind a flexible barrier that can freely deform in the water flow. The initial failure velocity at different experimental conditions is studied.

The second step, and the more important one, is to conduct experiments with a flexible floating barrier in presence of different waves. The analysis focus on the relationship between the failure velocity and the wave parameters with emphasis on the behavior of flexible barriers.

Since the Cavalli system is supposed to be deployed around the slick in the first hours of accident, when the oil slick is not yet weathered, it is assumed that it will contain a low-viscosity oil. This fact, in addition to pollution risks in the laboratory, are reasons to choose a low-viscosity oil for experiments. Therefore, special attention is given to entrainment failure mode and the investigations are concentrated on this failure mechanism.

Another aspect of the research project is to perform accurate velocity measurements in oil and water phases to derive the velocity profiles in each phase and to detect the oil-water interface.

Finally, a multiphase numerical model is developed to help in understanding the hydrodynamics of containment by flexible booms and to be used for assessment of acting forces on rigid and flexible barriers.

Chapter 3

Experimental set-up and procedure

This chapter outlines the experimental facilities and provides a detailed description of different aspects concerning experimental modeling. In the present study, the laboratory experiments were conducted under two-dimensional conditions, so the chapter starts with justifications for undertaking two-dimensional experiments. Then, the applied methodology for determination of experimental parameters and choice of experimental facilities are discussed. At the end, test programs and procedures are presented.

3.1 Why two-dimensional experiments?

Principally, physical experiments should be planned and executed in a way to detect practical limitations and find appropriate solutions to overcome these limitations. In case of oil spills, it is desirable to achieve the highest possible towing velocity, in order to collect as much oil as possible in the shortest possible time. Therefore, the parameter which was investigated in the present research was the maximum velocity or the initial failure velocity of the containment barrier. Now, two points should be considered regarding the choice of experimental modeling dimension:

- Doing full scale three dimensional experiments, Grilli et al. (2000a) stated that it is reasonable to assume that for both towed or fixed booms, the boom does not move and the water flows under the boom at a tow/flow velocity, U, equal to the relative boom-water velocity.

- A trapped slick, towed by barriers or exposed to currents, will have its maximum thickness along the centerline. The characteristic features along the centerline are generally assumed to be identical with those for a two dimensional barrier in a flume for the same physical conditions (Grilli et al., 2000b). It is also well-known that for each unstable three-dimensional wave component, there is a more unstable two-dimensional one (Squire, 1933). Hence, undertaking two-dimensional experiments instead of three-dimensional ones, generally overestimates the applied forces.

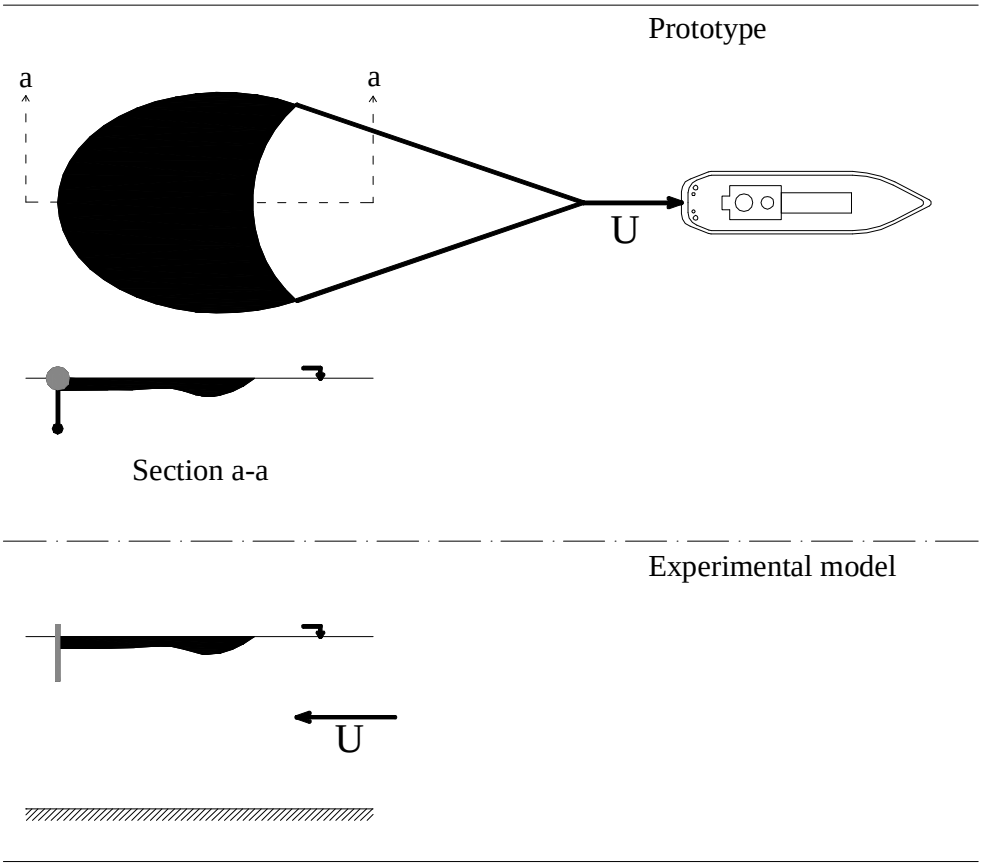

Figure 3.1: Schematic drawing of the prototype (top) and two-dimensional experimental model (bottom)

Following above mentioned points, in the present study experiments were carried out in a laboratory flume with flowing water and a fixed barrier. Fig. 3.1 illustrates the assumption applied to build up a two-dimensional model for simulating the three-dimensional problem.

3.2 Methodology of experimental study

Fig. 3.2 summarizes the methodology used to develop the experimental facilities and to carry out the experiments. The first step was to conduct preliminary experiments (Sec. 3.3). These experiments provided a better understanding of the problem and helped in detection and solving practical problems. Based on the results of preliminary experiments and downscaling rules, the experimental facilities were designed and fabricated (Sec. 3.4). Next step was to choose the scaling rule, that followed by considering laboratory and scale effects, presented in Sec. 3.5.

To chose experimental material and physical conditions, real oil spill cases and open-sea conditions were first studied. Thereby, involved parameters were selected regarding the model scale (Sec. 3.6). The last two sections (Sec. 3.7 and Sec. 3.8) describe the experimental program and procedures.

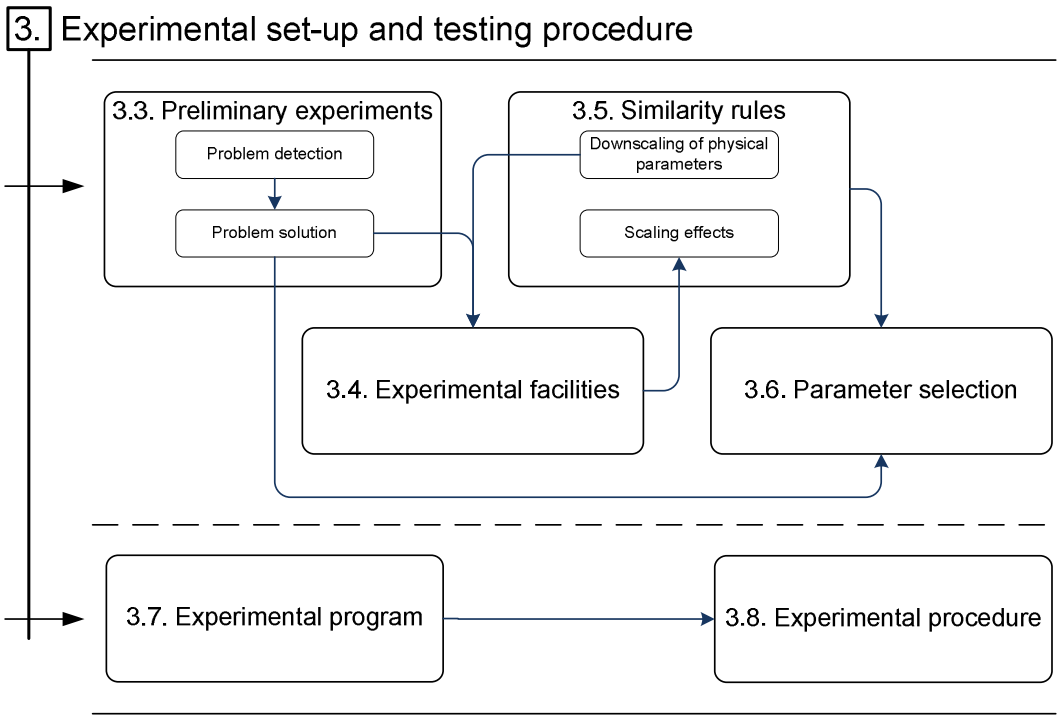

Figure 3.2: Methodology of the experimental study

3.3 Preliminary experiments

Preliminary experiments were undertaken in a 0.5 m wide, 13.85 m long and 0.8 m deep laboratory flume. For all experiments, the water depth was fixed at 0.6 m. A rigid barrier was located in the middle of the flume. Since the flume was connected to the main reservoir and circulation of Laboratory of Hydraulic Constructions (LCH), no pollution was permitted. Hence, the oil was substituted by polymer particles (Eraclene MP 90), the material which was previously used by Sayah et al. (2004) to perform three-dimensional experiments in the wave and towing tanks (Sec. 1.3.2). Fig. 3.3 shows an example of preliminary experiments with polymers at an average water flow velocity of 15 cm/s.

3.3.1 Problem detection

During the preliminary experiments, several problems were noticed:

1. Presence of a pair of vortices with opposite rotation directions at both corners of the flume upstream of the rigid barrier caused the contained material to be drained away and led to significant amount of material loss in a very short time interval (Fig. 3.4).

2. Polymer particles, with a density of 0.96 gr/cm^3, were easily torn off the slick and were carried beneath the barrier with flowing water, due to the fact that the buoyancy force compared to the weight was not enough to

keep them on the water surface. Lack of internal connections between the granules also caused random behavior of the contained slick.

3. Using the main reservoir of the laboratory and lack of efficient cleaning facilities prevented conducting experiments with real oil.

The first point have been mentioned by previous researchers, but was never studied in detail. To remove this effect, several experiments where conducted with different channel widths. For this purpose, the channel width in the vicinity of the barrier were reduced locally using PVC walls. It was observed that with a narrower channel, the vortices do not have enough space to form.

Regarding the second point, several materials, such as hot colored water and clay aggregates were examined to replace the polymer particles. It was concluded that, for a non-viscose material or a liquid of low viscosity, the density should be less than that of polymer particles (0.96 gr/cm^3) in order to avoid the rapid leakage of material.

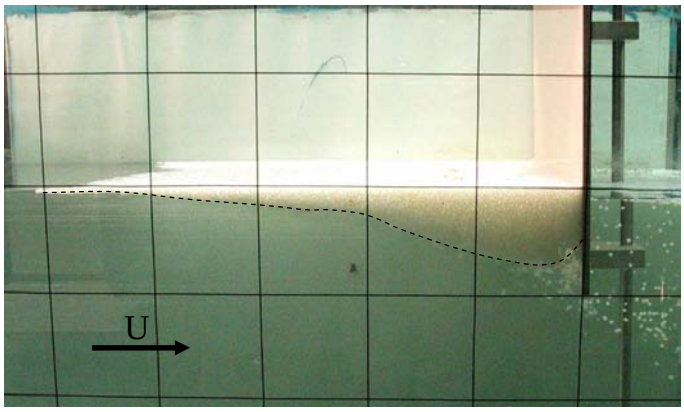

Figure 3.3: Preliminary experiments with polymer particles; water is flowing from left to right at a mean flow velocity of 15 cm/s

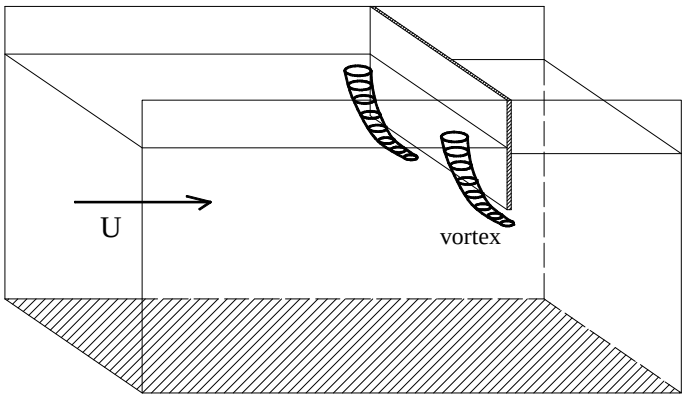

Figure 3.4: Pair of vortices forming at corners upstream the barrier in a wide flume

3.3.2 Problem solution

Considering the above-mentioned disadvantages, some modifications were made on the final test facilities:

1. To provide conditions without noticeable vortex influences, the channel width was reduced to 12 cm.

2. Polymer particles were replaced by a liquid vegetative oil for quantitative experiments, and LECA (Light Expanded Clay Aggregate) with a density of 0.71 gr/cm^3 for qualitative ones, as it will be explained in detail in Sec. 3.6

3. A closed water circuit, isolated from the main reservoir, was made to prevent risk of water pollution and permit the use of oil. Additionally, absorbent pads were supplied to facilitate the flume clean-up after each test.

3.4 Description of experimental facility

The schematic representation and some photos of the final experimental facility and its different parts are illustrated in Fig. 3.5 and Fig. 3.6 respectively. Detailed description of each element is discussed below.

3.4.1 Laboratory flume

Experiments were conducted in a 12 cm wide, 6.5 m long, and 1.2 m deep laboratory flume which was reinforced by metallic bars (each 50 cm). The system consisted of a flume, a pump , an inlet tank (1 in Fig. 3.5) and a storage tank (2 in Fig. 3.5) which were connected to each other by a 15 cm diameter pipes. A flowmeter ($\mp$ 0.1 lit/s precision) was used to observe and control the discharge (3 in Fig. 3.5). At the outlet of the flume a rectangular weir was used to adjust the water depth (4 in Fig. 3.5). For all experiments the water depth was fixed at 90 cm ($\mp$ 1 mm). The channel wall was made of PVC on one side and Plexiglas on the other side, providing the possibility to observe the process directly and make photographic evidence of the tests. To increase the visibility, a florescent light was placed at the bottom of the flume in the middle part, where the barrier was located. In order to establish uniform flow in the flume, a perforated pipe was used to enter the water in the inlet tank (5 in Fig. 3.5). The pipe was covered by a foam layer to achieve more uniform flow as it is shown in Fig. 3.7. By intrusion of air bubbles into the water, the pipe provided an adequate seeding for UVP measurements as well. At entrance of the flume, a floating wooden plate was placed over the water surface to stabilize the surface.

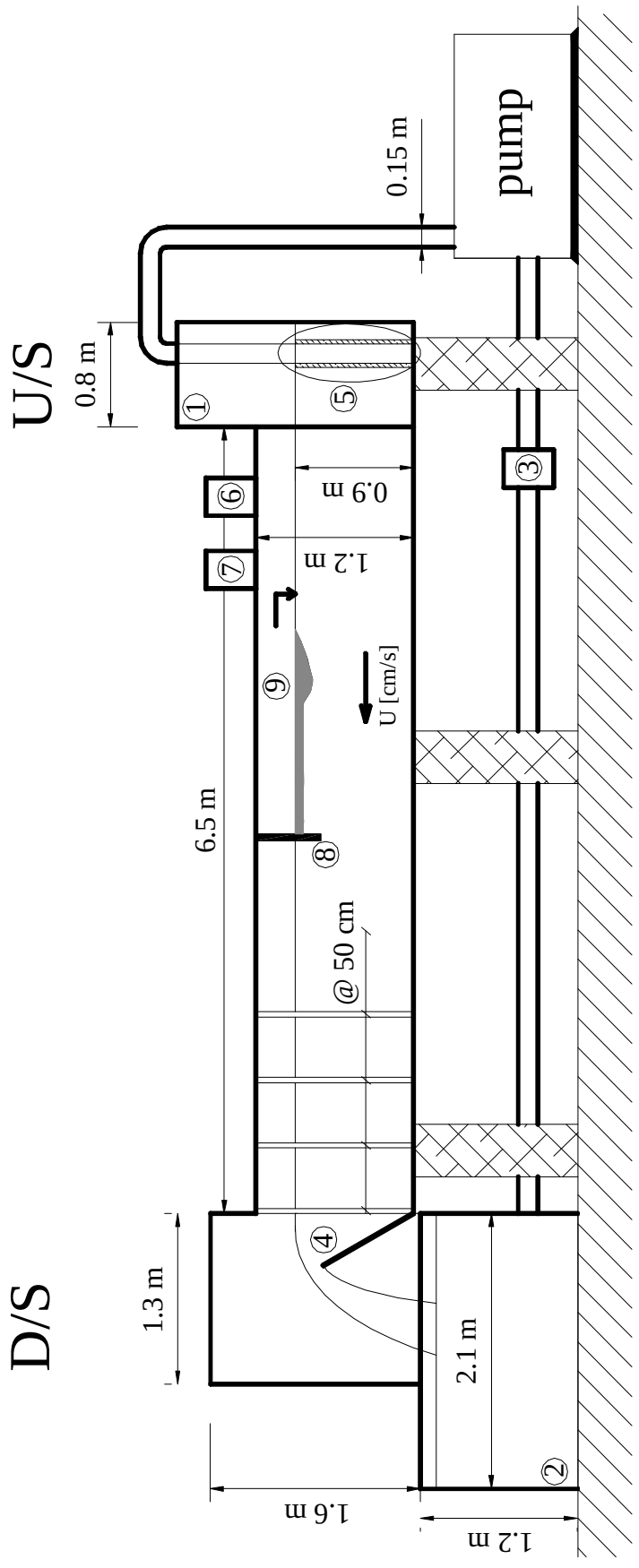

Figure 3.5: Schematic drawing of experimental flume and closed water circuit: (1) inlet tank; (2) storage tank; (3) flowmeter for controlling discharge; (4) rectangular weir for fixing water level; (5) perforated inlet pipe; (6) wave generator; (7) instrument for intrusion tracing particles for PIV measurements; (8) barrier; (9) oil slick contained upstream of the barrier

Figure 3.6: Photos of different part of the experimental facilities: (a) laboratory flume; (b) tracer distributer for PIV measurements; (c) pump; (d) flowmeter; (e) wave generator

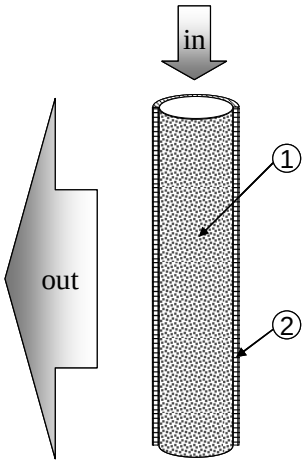

Figure 3.7: Inlet of the flume: (1) perforated pipe, (2) foam layer

3.4.2 Wave generator

For experiments conducted in presence of waves, a pneumatic wave generator was utilized to generate monochromatic unidirectional waves (6 in Fig. 3.5). Waves were generated by periodic air pressure applied uniformly over the water surface and their crests were always perpendicular to the channel side walls. The periodicity was produced by a metallic arm connected from one side to a rotating disk (Fig. 3.6e) and from the other side to a wind piston. The generated wave had the same frequency as the motor axes rotation. The arm length could be changed by sliding its end over the rail fixed on the disk, applying changes on the generated wave height.

3.4.3 Rigid and flexible barriers

Experiments were carried out with both rigid and flexible barriers. The rigid barrier was simply a PVC plate fixed in the middle of the flume (8 in Fig. 3.5).

Two different types of flexible barrier where fabricated for experiments with LECA granules and oil.

For experiments with LECA granules, a flexible barrier made up of small plastic bars was used. The plastic bars provide stiffness to the barrier in the third direction to achieve a perfectly two-dimensional condition. They were glued to a flexible skirt and could form a curved shape easily (Fig. 3.8a). At the end point of the skirt, the ballast weight could be changed using different metallic bars. Rubberized horsehair was used to guaranty the tightness of the barrier.

However, fabricating a flexible barrier that can deform under flow conditions, and at the same time, is tight enough so that oil can be contained behind it without leakage from the sides, was found to be a rather complex issue. This could be overcome using the barrier, shown in Fig. 3.8b, d, and e. On both sides of this barrier, a slitted tissue guarantees the tightness of the barrier (Fig. 3.8b and 3.8c).

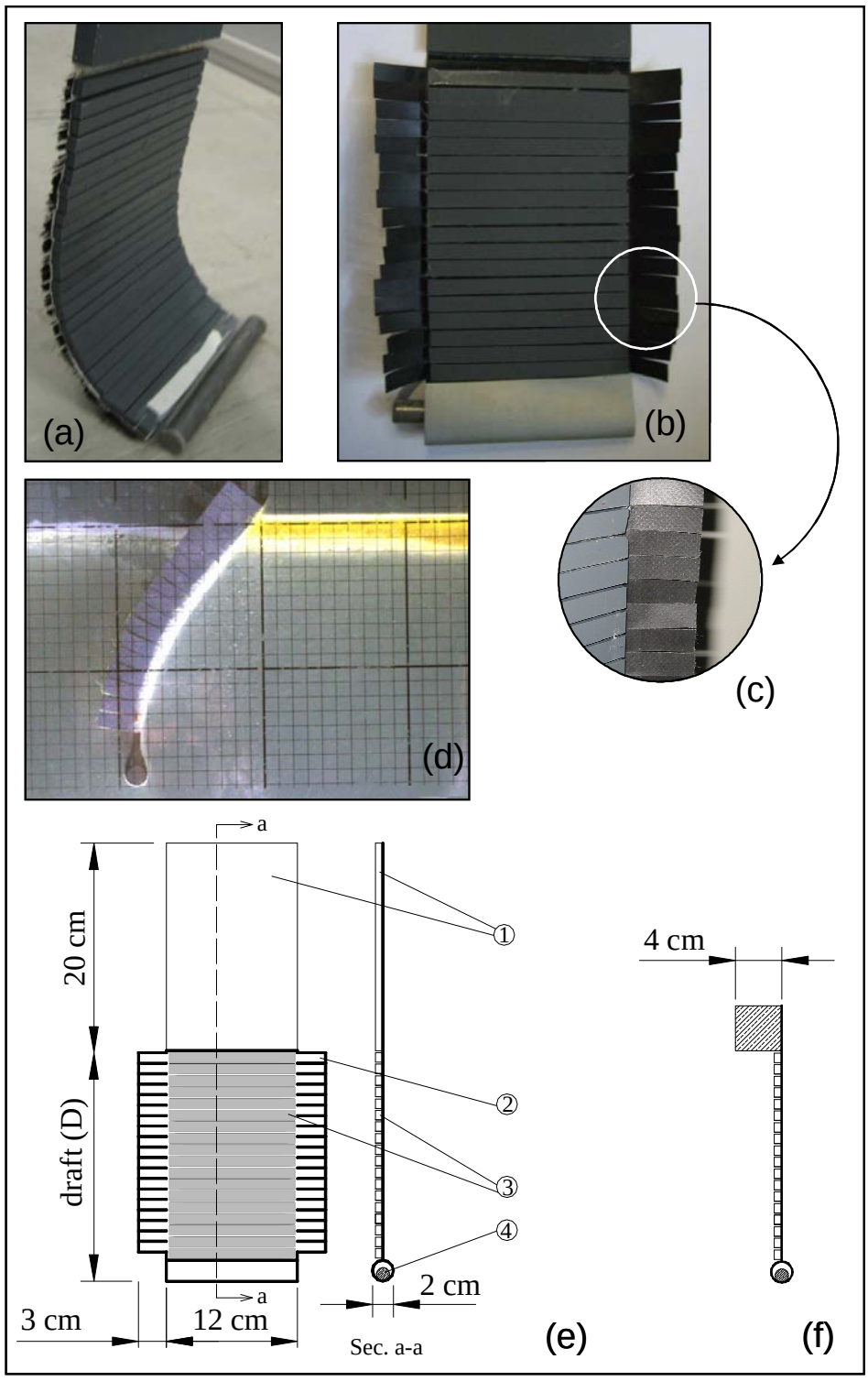

Figure 3.8: Details and different parts of the flexible barrier: (a) flexible barrier for experiments with LECA; (b) flexible barrier for experiments with oil; (c) slitted tissue providing the tightness of the barrier; (d) flexible barrier exposed to water flow during an experiment with oil; (e) scheme of the flexible barrier used for tests without waves: 1) rigid plate for supporting the barrier, 2) slitted tissue, 3) plastic bars, 4) changeable ballast; (f) scheme of the flexible barrier, used for tests with waves

For experiments in presence of waves, it was important that the barrier follows the surface movements and stays floating over the water surface. To achieve floating conditions, the barrier was connected to a cubic floating element at the top (Fig. 3.8f), which allows the displacement of barrier due to waves. The floating barrier was connected to the side walls by a rope at each side.

3.4.4 Measurement devices

3.4.4.1 Velocity profile measurements

Velocity measurements are used in various fields of research. In hydraulics, different velocity measurement methods exist (spinner, Pitot-tube, electromagnetic field, laser technology (LDA), Particle Imaging Velocimetry (PIV), and Ultrasonic Velocity Profiling (UVP)). The UVP measurement technique was developed by Takeda (1995) to measure an instantaneous velocity profile of liquid flows, using Doppler shift frequency in echoes reflected at small particles flowing with the liquid. The principles of UVP operation and the related theoretical explanations are presented in the manual provided by Met-Flow (2005). The UVP method was used to study the flow mapping of turbidity currents in a laboratory flume by De Cesare and Schleiss (1999) and De Cesare (1999). They showed the capability of such an instrument to detect the interface between the turbidity current and the ambient clear water.

The applicability of the UVP method to the flow with large fluctuation both in the velocity and orientation of gas-liquid interface was confirmed by Nakamura et al. (1998). Furthermore, the capability of this method to detect the interface of a two-phase flow was verified by Amini et al. (2006b).

In the present study, a nonintrusive velocity measurement method was needed which does not disturb the flow. The selected method was thus UVP. As it is illustrated in Fig. 3.9, the ultrasonic transducer was installed on the top of the oil, inclined with an angle of 20° looking upstream. The flow was not disturbed by the transducer as it just touched the oil surface. The UVP measurements provide the possibility to have an on-line velocity profile in both fluids. The main measurement parameters are listed in Table 3.1. Particles needed for the reflecting echo were provided by a perforated pipe covered by a foam layer as it was explained before (see Fig. 3.7).

Measurements were done along the oil slick at every 10 *cm* by moving the transducers from one point to another as it is illustrated in Fig. 3.9c.

3.4.4.2 Velocity field measurements

The velocity field was investigated using the nonintrusive method of Large-Scale Particle Image Velocimetry (LSPIV). LSPIV is an extension of conventional PIV method for velocity measurements in large-scale flows and the image and data-processing algorithms are similar to those used in conventional PIV. The PIV measurements were previously used to investigate the velocity and vorticity under a breaking wave by Chang and Liu (1998) and to study the flow characteristics between tandem boom by Lee et al. (2004). Recently, LSPIV method was

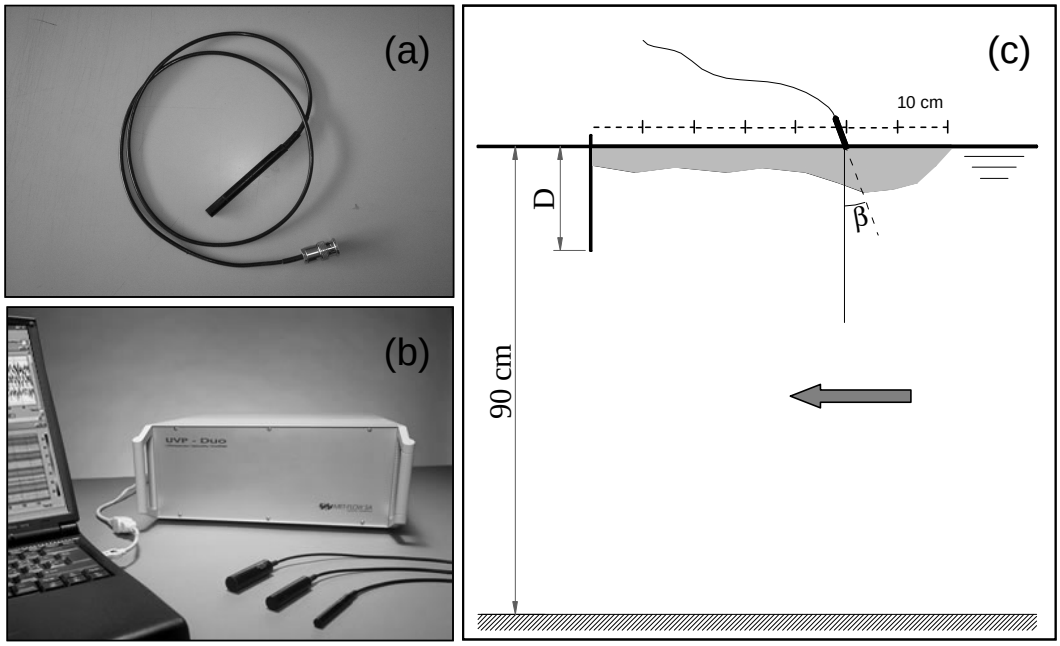

Figure 3.9: UVP instruments: (a) ultrasonic transducer (UVP probe); (b) main unit (Met-Flow); (c) schematic drawing of the UVP experimental setup

Table 3.1: Main parameters of UVP measurement

Parameter	**Value**
Number of channels	600
Number of profiles	512
Sampling period $[ms]$	100
Window start $[mm]$	3.7
Window end $[mm]$	446.96
Channel distance $[mm]$	0.74
Channel width $[mm]$	0.74
Frequency $[Hz]$	2
Cycles / Repetitions / Noise level	2 / 64 / 4

used by Kantoush et al. (2006) for horizontal surface velocity measurements of different shaped shallow reservoirs at LCH. However, its capability for vertical velocity measurement was not verified.

To achieve appropriate results, adjustments were required for illumination, seeding, and post-processing of the recorded images. In the present study, a digital video camera (SMX-150, monochrome, 1.2 megapixels), connected to a computer, was used to record images. It was fixed perpendicular to the flume wall at a distance of 2.2 m from the wall and covered an area of 0.88 by 1.17 m. The measurement device and setup is shown in Fig. 3.10.

During the experiments, seeding was provided by a distributer, as shown in Fig. 3.6b, located at upstream of the barrier (7 in Fig. 3.5). To find an appropriate seeding several particles were examined. A summary of their properties is presented in Table 3.2. The PIV accuracy depends on the ability of the particles to follow the flow fluctuations. When a particle is placed inside the flow or when the flow has a velocity oscillation, a time lag is required until the particle velocity is equal to the flow velocity. Therefore, fluid mechanical properties of the particles have to be checked in order to avoid large discrepancies between fluid and particle motion. The tracers ability to follow the flow streamlines was evaluated by determining the settling velocity of the particle under gravity.

The best seeding was found to be the Grilon AZ 3 (EMS-Chemie, Switzerland) polymer particles. The particles had an average diameter of 2.4 mm and a specific weight of 1.07 gr/cm^3. Hollow cylindrical shape particles allowed the water to pass through it and keep it moving with the same velocity as water.

To illuminate the measuring area three external lights and one neon light at bottom of the flume were used. The backside wall of the flume was painted with a black color to provide an adequate contrast with white particles and to

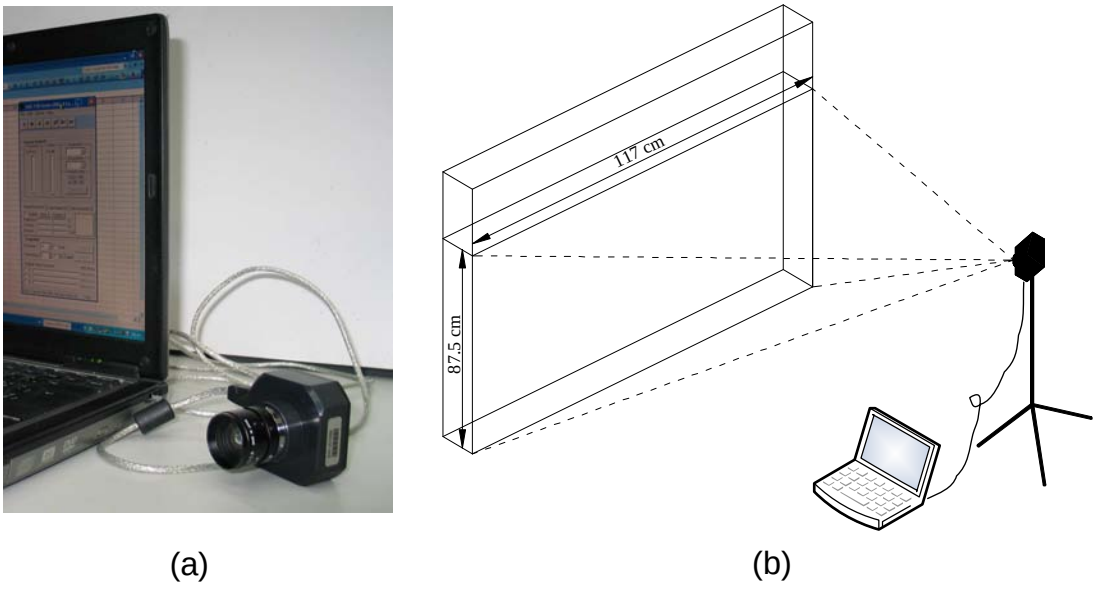

Figure 3.10: LSPIV instruments: (a) SMX-150 digital video camera; (b) schematic drawing of the LSPIV experimental setup

Table 3.2: Main properties of examined seeding particles for LSPIV measurements

Polymer material	Color	Density $[gr/cm^3]$	Mean diameter $[mm]$
Grilamid L16-LM	semi-transparent white	1.01	2.6
Grilon TSS/4	semi-transparent white	1.13	2.7
Grilon AZ 3	opaque white	1.07	2.4

improve images.

Finally for treating the results, the field of view was divided into several sub-areas, known as interrogation areas (IA). In each IA, a cross-correlation algorithm was applied in order to compute the shift Δx of the particles during the time Δt between two images.

3.4.4.3 Wave characteristics measurements

The characteristics of waves were measured simultaneously by three ultrasonic gauges at 40 *cm* above the water level. Two gauges were located on the upstream side of the barrier at distances of 10 and 70 *cm* from the barrier. One other gauge was situated on the downstream side at a distance of 120 *cm* from the barrier. The wave gauge is an ultrasonic analog cylindrical sensor with 3 *cm* diameter and 7 *cm* height (Baumer Electric, Switzerland). The sonic frequency is 230 kHz and the sensing range is 10 to 70 *cm*, with resolution of less than 0.3 *mm*. A computer located beside the flume received the three signals from the gauges. The raw data in volts were then saved using the LabView signal processing software. Using calibrating values, the volt signal was transformed into a distance signal.

As it was stipulated by Oppenheim et al. (1983), in order to build an exact representation of a band limited signal, sampling frequency has to be at least two times higher than the frequency of original signal. The sampling frequency of each ultrasonic wave gauge was fixed at 20 Hz, which was adequate for measuring maximum generated wave frequency (1.7 Hz). The acquisition time was fixed to 2 *min*, which was sufficient for monochromatic unidirectional waves.

3.5 Similarity rules

3.5.1 Downscaling of containment failure

It is generally accepted that there are different scaling rules that need to be considered for different oil containment failure modes (Delvigne, 1989). According to comprising experiments of Delvigne (1991) on scaling oil droplet formation, geometric downscaling used for small-scale laboratory experiments is unnec-

essary when modeling the generation of droplets from interfacial instabilities. However, the flow and advection, excluding droplet formation and droplet splitting can be modeled at a reduced scale by applying Froude similarity rules.

Critical accumulation is caused by oil-water interfacial instability and it is also independent of geometry of the barrier and specially the draft. As in droplet entrainment, all involved parameters are simulated at full scale. Since the drainage failure depends on barrier draft and shape, it can be scaled down according to Froude and densimetric Froude numbers. It was shown in Chapter 2, that the Weber number was also used by some researchers to scale down the oil droplets being torn from the oil slick. Delvigne (1991) showed the phenomenon to be independent of it. As a result, the down-scaling law has to be chosen considering the purpose of the particular case.

The formation of droplets is caused by unstable increasing waves (Kelvin-Helmholtz instability) on the interface. These interfacial waves and instabilities are influenced only by three oil parameters: density difference between oil and water, $\Delta\rho$, viscosity, ν, and interfacial tension, σ_{ow}. Hence, using real oil permits doing full scale experiments to model droplet entrainment failure.

In the present study, the main part of experiments were conducted with the rapeseed oil, where the dominant failure mode is entrainment failure. Therefore, no downscaling was applied and experiments were considered full scale. Moreover, for experiments in presence of wave, or experiments with LECA where failure was similar to drainage failure Froude similarities were applied.

3.5.2 Downscaling of waves

To investigate the relationship between oil containment failure and wave parameters, Froude similarity rule could be considered. Principally, Froude number is mainly used for free surface flows in channels and basins, for which the ratio between inertial and gravity forces should be conserved:

$$F_r = \sqrt{\frac{inertial\ force}{gravity\ force}} = \sqrt{\frac{\rho L^2 U^2}{\rho L^3 g}} = \frac{U}{\sqrt{gL}} \tag{3.1}$$

where U is the flow velocity, L is the characteristic length , i.e. the boom's draft, ρ_w water density and g the gravity acceleration. The Froude number should be the same in the model (subscribed m) as in the prototype (subscribed p), as follows:

$$\left(\frac{U}{\sqrt{gL}}\right)_p = \left(\frac{U}{\sqrt{gL}}\right)_m \tag{3.2}$$

Yalin (1971) delineated scale factor for length (λ_L), time (λ_T), and velocities (λ_U) as follows:

$$\lambda_L = \frac{L_m}{L_p} \tag{3.3a}$$

$$\lambda_T = \frac{T_m}{T_p} \tag{3.3b}$$

$$\lambda_U = \frac{U_m}{U_p} \tag{3.3c}$$

By replacing Eq. 3.3 in Eq. 3.2, the scale factors of time and velocity could be expressed as a function of λ_L:

$$\lambda_T = \sqrt{\lambda_L} \tag{3.4a}$$

$$\lambda_U = \sqrt{\lambda_L} \tag{3.4b}$$

3.5.3 Laboratory and scale effects

Comparing the model boundary conditions with those of real-life ones, the laboratory effects should be considered in order to modify and/or justify the experimental results.

Since the flow is considered as deep flow, the first parameter to be verified was the influence of the flume bottom. It was stipulated by Delvigne (1984) and later on confirmed by Fang and Johnston (2001a) that the water depth needs to be more than four times the barrier draft to be considered deep and the influence of bottom boundary on containment to be ignored. Water depth in this study was fixed at 90 cm, while the maximum barrier draft is 20 cm. Therefore, neglecting the bottom effect seems justified.

Other boundary conditions were imposed during experiments with waves. Fig. 3.11 clarifies these effects based on the actual set-up of the flume during the experiments. When the barrier was not present in the model, the wave reflected on the outlet weir (B) could be considered as a laboratory effect. Additionally, waves reflected on the longitudinal side walls were laboratory effects which perturb the assumption of two-dimensional conditions. To prevent surface reflection, a perforated inclined plate was installed at the outlet of the flume. It functions as a damper and absorbs the incident wave energy significantly (m in Fig. 3.11). Three-dimensional effects were found to be negligible since the incident perpendicular waves were measured at the longitudinal central axis of the flume (n-n line).

Using a rigid fixed barrier instead of a floating one could also lead to some unwished model effects. The reflected waves on rigid barrier caused standing waves upstream of the barrier (C). This effect could be mostly eliminated using a floating barrier that follows the water surface.

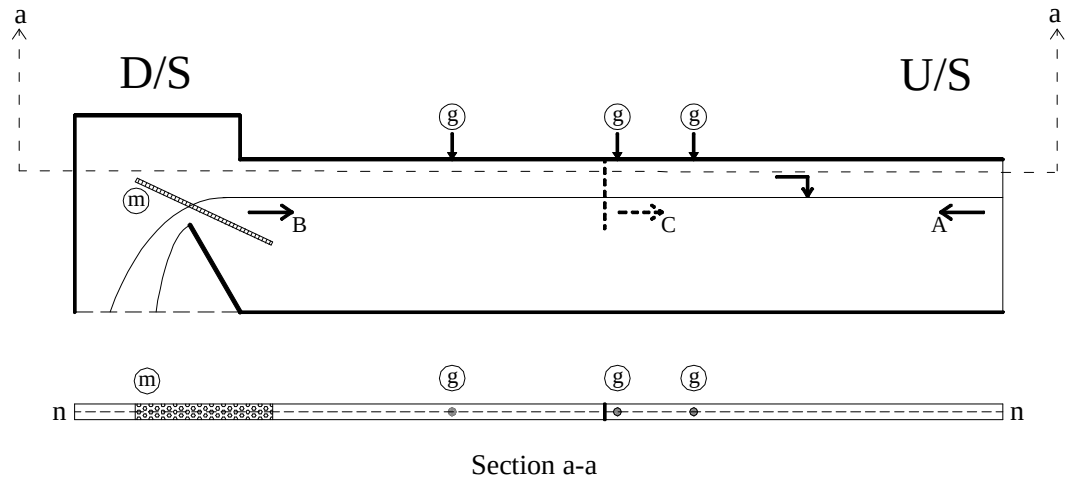

Figure 3.11: Schematic drawing of boundary conditions and laboratory effects; A: generated waves; B: reflected waves on outlet weir; C: reflected waves on a rigid fixed barrier; g: gauges for wave measurements; m: damper for absorbing wave energy; n-n: central axis of the flume

3.6 Selection of experimental parameters

The aim of this section is to evaluate the physics of involved natural components in an oil spill incident. Water and oil are the main contributing elements that can affect the slick spread and consequently the containment procedure. Waves and wind can influence the containment efficiency. To achieve reliable results, experimental materials and applied physical conditions should be representative for real cases.

3.6.1 Selection of materials

3.6.1.1 Sea water and experimental water properties

Principally, water properties do not affect the spill containment by mechanical barriers. However, its salinity and temperature are important when using chemical or biological agents, likewise while performing in-situ burning. The spread and weathering process of slicked oil can also be influenced by water properties. The density of water intervenes in stability and failure equations, since the fluid density difference ($\Delta\rho = \rho_w - \rho_o$) or relative oil density ($\Delta = 1 - \Delta\rho/\rho_w$) can affect both thickness and spreading forces as well as the growth of interfacial Kelvin-Helmholtz waves.

In this study, the water density is assumed to be equal to 1 gr/cm^3, which is an acceptable value for density of water at experimental temperature (15 to 20 °C).

3.6.1.2 Slicked oil characteristics

The main properties which affect the behavior of spilled oil at sea are specific gravity (its density relative to pure water often expressed as °API), distillation

characteristics (its volatility), viscosity (its resistance to flow), and pour point (the temperature below which it will not flow).

Oil is a mixture of hundreds of hydrocarbons, whose individual chemical properties vary widely. The properties of the oil as a whole depend on the properties of the individual constituents. Allen and Dale (1997) provided a classification system for describing and quantifying floating oil slicks and studied the spill area as a function of oil volume based on the oil thickness for each classified oil. Since the interactions between the various weathering processes are not well understood, reliance is often placed on empirical models based upon the properties of different oil types. For this purpose, it is convenient to classify the most commonly transported oils into four main groups, roughly according to their specific gravity (ITOPF, 2006):

Group I oils (non-persistent) tend to dissipate completely through evaporation within a few hours and do not normally form emulsions.

Group II oils can loose up to 40% by volume through evaporation, because of their tendency to form viscous emulsions.

Group III is like group II but there is an initial volume increase as well as a curtailment of natural dispersion.

Group IV oils are very persistent due to their lack of volatile material and high viscosity, which precludes both evaporation and dispersion.

The list of oils and their properties in each classified group is shown in Appendix A. An important parameter to be known before an appropriate response, is the remaining volume of spilled oil at a certain time after the accident which differs for each of the above mentioned group and is presented in ITOPF Handbook.

As it was discussed in Chapter 2, the mode of containment failure, depends on oil's viscosity. To assess the viscosity and consequently the failure mode, Delvigne (1989) quantified the increase of the viscosity :

- For most fresh crude oils and oil products the viscosity is less than 1'000 cSt.
- Emulsification takes place often within a few hours after the spill and results in a viscosity on the order of 1'000 cSt.
- The continual weathering of oil slicks during some days increases viscosity to the order of 10'000 cSt.
- In the long term, almost solid tar balls are formed.

This preceding classification helped to choose an appropriate oil for the present study. The Cavalli system is supposed to be carried by oil tankers and be deployed around the slick during the first hours after the accident, when the oil is not yet weathered or emulsified. Therefore, it can be assumed that the Cavalli system will mainly deal with oils having a relatively low viscosity.

3.6.1.3 Rapeseed oil

The main part of the experiments were carried out using refined *rapeseed* (or *colza*) oil. Rapeseed oil is of vegetable origin and is obtained from crushed

rapeseed by pressing or extraction. It is a light yellow to brownish yellow oil. Rapeseed oil is nowadays used in the manufacture of biodiesel for powering motor vehicles as green energy. Its viscosity is 88.8[1] cSt (mm^2/s) at room temperature (about 85 times the viscosity of water) with a density of 0.91 gr/cm^3. The interfacial tension of rapeseed oil and water is 30 mN/m. The oil's yellow color with help of the bottom light in the flume allowed following the trace of oil droplets in the water flow. To remove the oil and clean the flume after each test, oil sorbent pads (HP 156, 3M) were used.

To validate the experimental results, some supplementary experiments were undertaken using an oil with high viscosity. For this purpose, residue oil diluted with cracked gas oil was used. Its viscosity was 2400 cSt with a density of 0.96 gr/cm^3.

3.6.1.4 Light Expanded Clay Aggregates (LECA)

Apart from oil experiments, some tests were undertaken using LECA (Light Expanded Clay Aggregate) as substitute material. The aim was to study the influence of a flexible barrier on the drainage failure qualitatively. Rapeseed oil has a low viscosity and the dominant failure in containment of such an oil is droplet entrainment. To study the effect of a flexible barrier on the drainage failure, a more viscous oil than rapeseed oil was needed. Due to the risk of water and equipment pollution, LECA granules were used to study the drainage failure qualitatively.

LECA consists of small, lightweight, bloated particles of burnt clay with high porosity. LECA it light and has thermal insulation properties. This material is principally used as a thermal-insulation material in houses. The diameter of LECA granules is in the range of 8 to 16 mm with a mean density of 0.71 gr/cm^3. The particle size distribution is shown in Fig. 3.12.

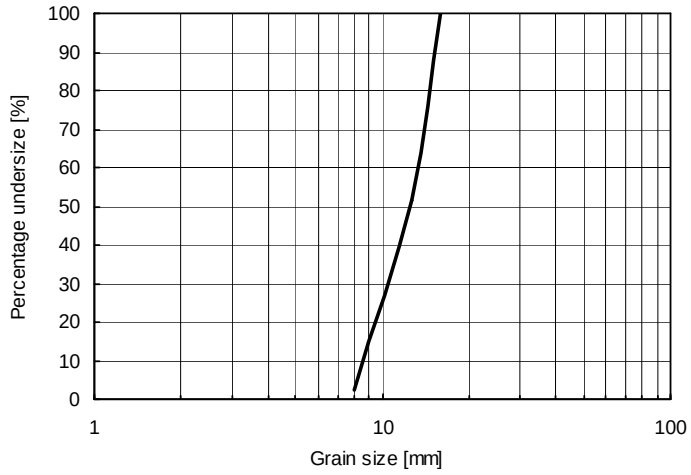

Figure 3.12: Particle size distribution of LECA granules[2]; grain diameter 8 to 16 mm; d_{50} =12.5 mm

[1]Measured at "Material Science and Engineering" department of EPFL.
[2]Measured at "Traffic Facilities Laboratory" of EPFL.

3.6.2 Selection of physical conditions

3.6.2.1 Wave characteristics in oceans and open seas

Wave characteristics have a significant influence on recovery operations in the open sea. Since wave conditions can vary considerably from one to another place, it seems logic to choose some selective points and use the corresponding wave parameters for experimental and numerical models. The real wave characteristics for three places in the Atlantic Ocean, Mediterranean Sea, and Persian Gulf are summarized in Table 3.3. The presented wave parameters are illustrated in Fig. 3.13. The characteristics of the real waves are later compared to the experimentally generated waves.

Table 3.3: Real wave characteristics in Atlantic Ocean, Mediterranean Sea (Sayah et al., 2004), and Persian Gulf (Maraghei et al., 2002)

	Atlantic Ocean, Ouessant	**Mediterranean Sea,** Sete	**Persian Gulf** Khowr-e-Musa
Local water depth $[m]$	110	32	17
Latitude/ Longitude	48 31 42 N	43 19 42 N	29 56 07 N
	05 49 03 W	0.3 39 33 E	49 11 05 E
Significant wave:			
Wave height, $H_s[m]$	2.40	0.50	-
Wave period, $T_s[s]$	10.00	4.50	-
Wave length, $L_s[m]$	156.29	31.65	-
Wave steepness $[-]$	0.0153	0.0095	-
Mean wave:			
Wave height, $H_{avr}[m]$	1.50	0.30	0.13
Wave period, $T_{avr}[s]$	7.50	3.50	4.66
Wave length, $L_{avr}[m]$	87.91	19.15	33.90
Wave steepness $[-]$	0.0171	0.0156	0.0038
Maximum wave:			
Wave height, $H_{max}[m]$	3.60	0.80	0.80
Wave period, $T_{max}[s]$	14.00	9.00	10.40
Wave length, $L_{max}[m]$	306.33	126.59	120.10
Wave steepness $[-]$	0.0117	0.0063	0.0067

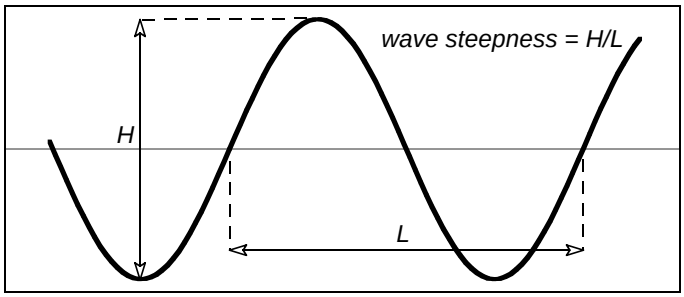

Figure 3.13: Illustration of wave parameters

3.6.2.2 Experimental waves: Description and calculation

Defining appropriate length, time, and velocity scale factors, the generated waves should be compared to the real case. The analysis procedure elaborated for wave measurements is based on data acquisition using LabView, and data analysis using MatLab. Sayah (2006) developed a code to calculate and analyze the wave characteristics using the registered signals from wave gauges.

For this purpose, non filtered results (raw signals) are saved in a three column matrix, each one corresponding to the complete signal provided by a single wave gauge.

Whilst measuring the water level, the ultrasonic beam could be reflected away from the gauge depending on the steepness of the measured wave. When the incoming signal is not entirely captured, the measured distance could tend to infinity. Such values, commonly called the outliers, should be filtered before the calculation of the characteristics of sinusoidal wave signal.

The calculation of wave height is based on the filtered wave signal. A statistical approach is used based on the calculation of the standard deviation of the filtered final wave signal, σ_f (Kamphuis, 2000):

$$\sigma_f = \sqrt{\frac{1}{K}\sum_{i=1}^{K} H_i^2} \tag{3.5}$$

where H_i is the instantaneous wave height calculated from difference of instantaneous and mean water levels, and K is the number of measured waves between time t_1 and t_2. The wave height corresponds to the root mean square of height, H_{rms}, values and is expressed as:

$$H_{rms} = 2\sqrt{2}\,\sigma_f \tag{3.6}$$

The average wave height, H_{avr}, can then be calculated:

$$H_{avr} = \frac{\sqrt{\pi}}{2} H_{rms} = 2\sqrt{2\pi}\,\sigma_f \tag{3.7}$$

The wave frequency is calculated using the FFT function (Fast Fourier Transform). The wave length (L) is obtained from following equations:

– For deep water, where $d/L_0 > 1/2$:

$$L_0 = \frac{gT^2}{2\pi} \tag{3.8}$$

– For intermediate depth, where $1/20 < d/L_0 < 1/2$:

$$L_i = L_0 \, tanh(\frac{2\pi d}{L_i}) \tag{3.9}$$

It was observed during the experiments that for same mechanical condition of wave generator, the wave height changes slightly from one experiment to the other and increases with increasing mean flow velocity. In order to determine a representative average wave height, a mean height value at different velocities was calculated. Since the calculated value of wave height would be later used to characterize the failure containment velocities, the mean value of H_{avr} was averaged only on measured values in the range of velocity failure. Corresponding graphs are shown in Appendix B. Calculated wave characteristics are presented in Table 3.4.

Table 3.4: Average waves characteristics in the model

		Wave 1	**Wave 2**	**Wave 3**	**Wave 4**	**Wave 5**
Wave height, H_{avr}	$[cm]$	0.59	1.72	2.36	3.47	5.33
Wave period, T_{avr}	$[\ s\ ]$	1.71	1.35	1.35	0.95	0.95
Wave length, L_{avr}	$[cm]$	402.95	274.39	274.39	140.27	140.27
Wave steepness, s	$[-]$	0.0015	0.0063	0.0086	0.0247	0.0380

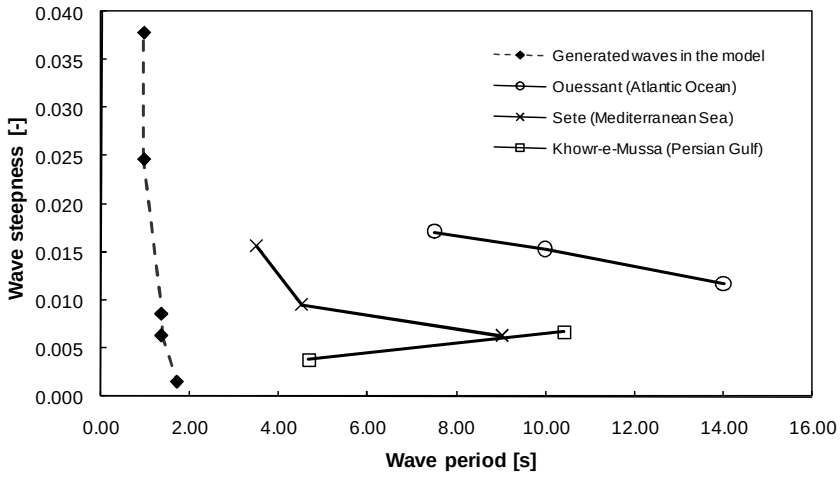

Figure 3.14: Comparison of waves generated in the model and real waves at Atlantic Ocean, Mediterranean Sea and Persian Gulf

The comparison of laboratory generated wave characteristics with real waves can be seen in Fig. 3.14. This Figure provides the steepness of waves according to the wave period for experimental and real waves. The mean value for average wave period of real waves, $(\overline{T}_{avr})_p$, is equal to 5.22 s. For experimental waves, the mean value of average wave period, $(\overline{T}_{avr})_m$, is equal to 1.34 s. The time scale, λ_T is thus equal to 3.89. After applying the time scale ratio as described in Eq. 3.4a, a geometric model scale of λ_L=1:15 is justified.

3.6.2.3 Wind effects

In reality, it is rare that the waves exist in nature in the absence of wind. It is well known that the wind affects the water surface both by shear forces and by presence of normal pressure variations (Kordyban, 1982b).

The effect of wind on containment failure is beyond the scope of this study. However, influence of wind on spill can be introduced as an additional flow velocity (Fang and Johnston, 2001c). The developed numerical model in the present study (see Chapter 5), consisting of three phases, has the ability to model the wind numerically.

3.7 Experimental program

3.7.1 Experiments with oil

Experiments with oil were carried out in absence or presence of waves, to quantitatively investigate the oil containment process. Experimental conditions for oil tests without waves are presented in Table 3.5. As the first step, experiments with a vertical rigid barrier were performed (OR1 to OR5). Three supplementary tests were then carried out with rigid curved barriers (ORc1 to ORc3). A flexible barrier with different ballast weights was also used to contain oil slicks with different volumes (OF1 to OF9). Obtained results are presented in Sec. 4.1.

Experimental conditions for oil tests with waves are presented in Table 3.6. Each series of experiments was undertaken in presence of different waves described in Table 3.4. Two series of tests were carried out with a rigid barrier (SR1 and SR2), and six series with flexible ones (SF1 to SF6). The results are presented in Sec. 4.2.

Since the concept of the Cavalli system is based on a trapped slick, some experiments were carried out with oil trapped between two parallel rigid barriers as shown in Fig. 3.15 schematically. The experimental conditions are presented in Table 3.7 and the results are discussed in Sec. 4.1.7.

In reality, the distance to draft ratio (d_b/D) for the single configuration of Cavalli system is much higher than the values tested here. However, the results of these experiments will help to better understand the operational limits in case of a high volume slick with small spread area, or in case of double and quadruple configurations.

Table 3.5: Experimental conditions for oil tests with rigid and flexible barriers without waves, velocity range: 10 to 35 cm/s

Group	**Test number**	**Oil volume** $[m^3/m]$	**Barrier draft** $[cm]$	**Ballast weight** $[kg/m]$
Rigid	OR1	10	10	-
barrier	OR2	10	20	-
	OR3	20	10	-
	OR4	20	20	-
	OR5	15	15	-
	ORc1	10	10	-
	ORc2	20	10	-
	ORc3	20	20	-
Flexible	OF1	10	10	0.6
barrier	OF2	10	10	1.5
	OF3	10	20	0.6
	OF4	10	20	1.5
	OF5	20	10	0.6
	OF6	20	10	1.5
	OF7	20	20	0.6
	OF8	20	20	1.5
	OF9	15	15	1.05

3.7.2 Experiments with LECA

LECA tests aimed at providing a qualitative comprehension of the effect of a flexible barrier on containment processes. The considered parameters are LECA volume per unit length, barrier draft, and ballast weight per barrier width for experiments with flexible barrier.

Experimental conditions for LECA tests are presented in Table 3.8. Doing experiments with both rigid (LR1 to LR6) and flexible (LF1 to LF12) barriers in the same conditions allows comparing the results and verifying the influence of the barrier flexibility. The results are presented in Sec. 4.3.

Table 3.6: Experimental conditions for oil tests with rigid and flexible barriers with waves, velocity range: 10 to 35 cm/s

Group	**Test Series**	**Oil Volume** $[m^3/m]$	**Barrier Draft** $[cm]$	**Ballast Weight** $[kg/m]$
Rigid	SR1	20	10	-
barrier	SR2	20	20	-
Flexible	SF1	20	10	0.6
barrier	SF2	20	10	1.5
	SF3	20	20	0.6
	SF4	20	20	1.5
	SF5	30	10	0.6
	SF6	30	20	0.6

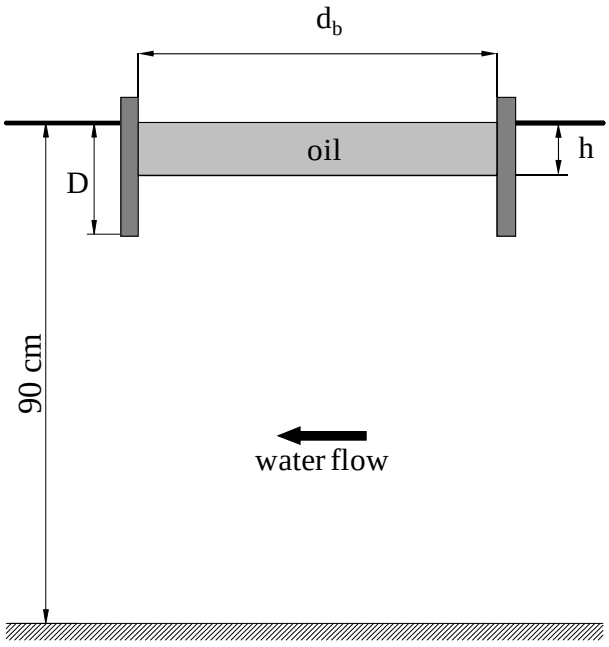

Figure 3.15: Schematic drawing of trapped oil tests; d_b is the distance between two barriers, h is the oil layer thickness, and D the barrier draft

Table 3.7: Experimental conditions for trapped oil tests, $D = 10\ cm$, velocity range: 10 to 55 cm/s

Test number	d_b/D [-]	h/D [-]
ORD1	6	0.2
ORD2	6	0.5
ORD3	6	0.7
ORD4	12	0.2
ORD5	12	0.5
ORD6	12	0.7

Table 3.8: Experimental conditions for LECA tests with rigid and flexible barriers, velocity range: 20 to 50 cm/s

Group	**Test number**	**LECA volume** $[m^3/m]$	**Barrier draft** $[cm]$	**Ballast weight** $[kg/m]$
Rigid	LR1	20	10	-
barrier	LR2	20	15	-
	LR3	20	20	-
	LR4	40	10	-
	LR5	40	15	-
	LR6	40	20	-
Flexible	LF1	20	10	0.6
barrier	LF2	20	10	1.5
	LF3	20	15	0.6
	LF4	20	15	1.5
	LF5	20	20	0.6
	LF6	20	20	1.5
	LF7	40	10	0.6
	LF8	40	10	1.5
	LF9	40	15	0.6
	LF10	40	15	1.5
	LF11	40	20	0.6
	LF12	40	20	1.5

3.8 Experimental procedures

All experiments were carried out in almost a similar way. The concept is to pour a certain volume of the material (oil or LECA) upstream the barrier at a low flow velocity and increase the velocity, step by step, while the water level is kept constant to 90 cm. For each step, some measurements and observations were made. This continued till failure took place. For LECA tests, experiments were carried out even after the failure, and at each velocity the escaped LECA volume was measured. The experimental procedures are described step below.

3.8.1 Experiments with oil

1. With the flow set at 10 cm/s, oil was poured below the water surface to prevent droplet formation and penetration into the flowing water.
2. The water flow was slowly increased (2 cm/s till 24 cm/s and 1 cm/s after it).
3. After the oil slick had stabilized, three steps were followed:
   - The contained material shape was observed and its length and thickness at different points were measured.
   - A photo was taken.
   - For tests with a flexible barrier, the skirt deformation was evaluated.
4. Steps 2 and 3 were repeated until oil droplets were observed to escape under the skirt and failure happened.

In presence of waves, the same above mentioned steps were followed. In the beginning, after pouring the oil over water surface, the desired wave was generated. During the experiment and after each velocity increase, the waves characteristics were measured using the three gauges as it was described before.

The trapped oil tests were also conducted in the same way as oil tests without waves. The only difference was that the velocity increment was 5 cm/s at each step.

3.8.2 Experiments with LECA

1. A mean flow velocity (20 cm/s) was established in the flume.
2. Certain volume of granules is poured on the water surface upstream of the barrier, under the form of a single layer.
3. A small increment of velocity (2 cm/s) was made.
4. After achieving a stable condition:
   - The volume of escaped material was measured.

- The contained material shape was observed and its length and thickness at different points were measured.
- A photo was taken.
- For tests with a flexible barrier, the skirt deformation was evaluated.

5. Steps 3 and 4 were repeated till a small volume of material was left behind the barrier and the rate of leakage of granules became very low.

Chapter 4

Experimental results and analysis

In this chapter, experimental observations and results are presented and discussed. The main part of the chapter outlines the experiments with oil, and relating measurements. The results of LECA experiments, however, are discussed in a separated section.

Entrainment failure receives particular attention, where drainage failure is also elucidated. Physical interpretation of the results is provided based on background studies, although some relationships are proposed for new concepts. The most important aspect of the analysis is to feature the effect of a flexible barrier on containment efficiency, which had not yet been revealed previously.

In the first section, the results of oil experiments without waves are discussed and the effects of initial oil volume as well as barrier's geometry on failure are investigated. The second section is dedicated to the effect of wave characteristics on the threshold failure velocity; where the third section comprises the results of LECA experiments. The two first sections deal mainly with entrainment failure, whereas the third section investigates drainage failure qualitatively.

The last two sections present the results of precise velocity measurements using PIV and UVP devices at oil-water interface and in the vicinity of the barrier.

4.1 Experiments with oil in the absence of waves

A first series of oil experiments were carried out in presence of currents in the laboratory flume, but without waves. The response of flexible and rigid barriers were examined for different experimental conditions presented in 3.7.1. In this section, general observations of slick shape evolution and its characteristics are presented and the effect of involved parameters on containment efficiency are discussed.

4.1.1 General observations

The evolution of the slick shape upstream the barrier, due to increase of flow velocity, was subjected to some observations and measurements. The fluctuations at oil-water interface started at a mean flow velocity of about 12 cm/s. The Kelvin-Helmholtz threshold instability velocity, U_{KH}, for rapeseed oil and water was calculated to be 14.7 cm/s using Eq. 2.2. As it was explained by Hogan and Ayyaswamy (1985), the threshold velocity could be smaller than in the classical KH instability by factor $\sqrt{\rho_o/(\rho_w + \rho_o)}$ because of important viscosity contrast of the two fluids. Multiplying this latter factor to the classical KH instability velocity yields a velocity of 10.8 cm/s for the instability initiations, which is in a good agreement with the observed threshold velocity of instability.

For low flow velocities (< 18 cm/s) the oil slick formed a monotonous layer over the water surface. At a flow velocity of about 18 cm/s, a small headwave was formed at the upstream end of the slick, that approached the barrier by increasing the flow velocity and consequently decrease of the slick length. Geometrical characteristics of a contained oil slick are depicted in Fig. 4.1. The interfacial waves became more significant at the headwave and propagated toward the barrier.

At higher flow velocities, the interfacial waves broke up on the headwave, causing droplets to be shed into the flowing water. The velocity at which droplets started to form was 24 to 26 cm/s in the present study. This is in quit good agreement with the value predicted by Wilson (1977) who proposed a minimum flow velocity of $1.55U_{KH} = 22.8$ for droplet shedding from the headwave.

Before reaching the failure velocity, the droplets detached and immediately rejoined the slick. At initial failure velocity, U_f, a part of detached droplets passed beneath the barrier, while the other part coalesced the slick. By increasing the flow velocity, a bigger part of droplets passed the barrier and loss rate increased. The evolution of the oil slick shape for a flexible barrier with a 10 cm draft and mean flow velocities from 18 to 30 cm/s is shown in Fig. 4.2. As it can be seen, the length of slick decreased by increasing the mean flow velocity while its thickness, particularly at the headwave, increased.

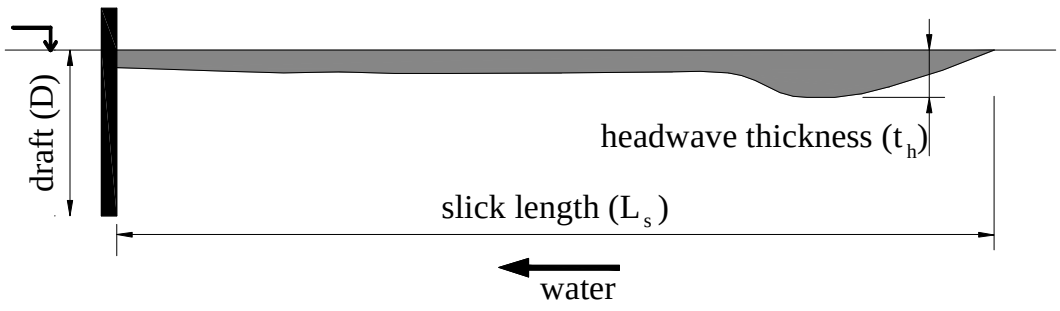

Figure 4.1: Geometrical characteristics of the contained oil slick

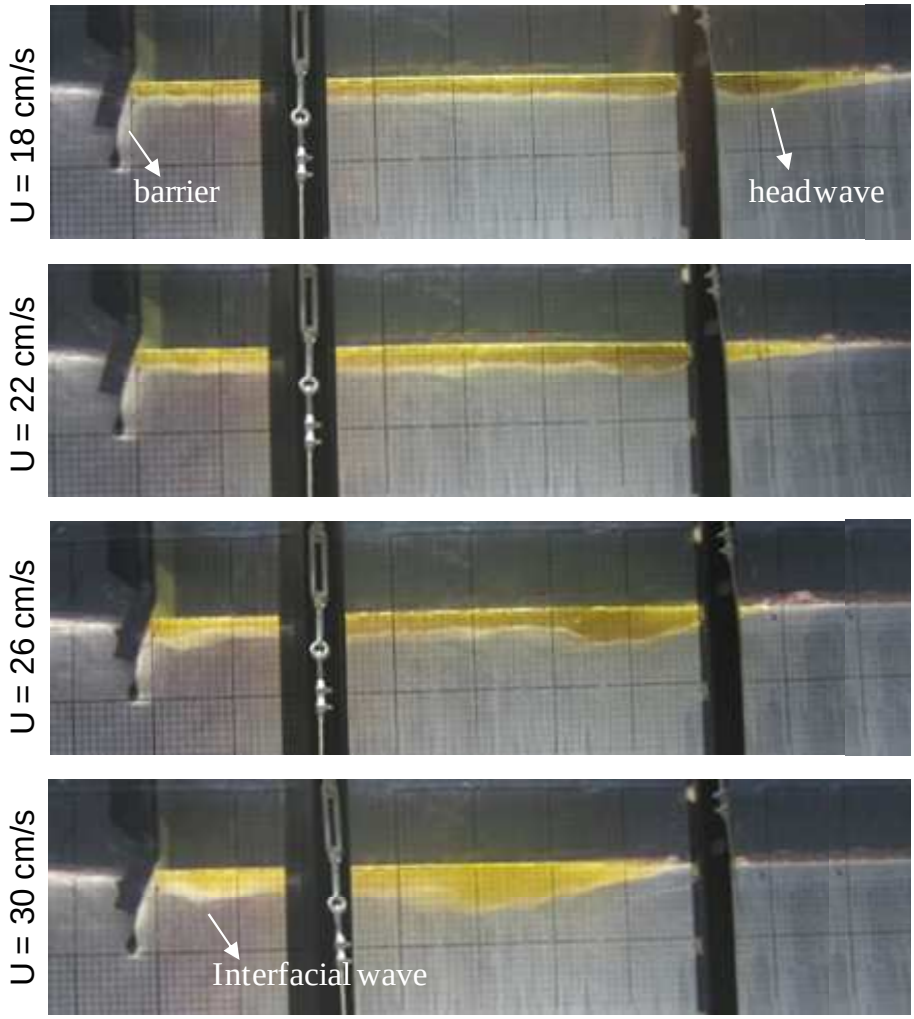

Figure 4.2: Slick shape evolution by increasing mean flow velocity, U, for a flexible barrier with 10 cm draft and 1.5 kg/m ballast weight; water is flowing from right to left; main grid spacing is 10 cm

4.1.2 Slick length and thickness

Fig. 4.3 to Fig. 4.5 depict the slick length, L_s (as defined in Fig. 4.1), and equivalent slick thickness, t_h, as a function of flow velocity for rigid and flexible barriers with different drafts and initial oil volumes. The equivalent slick thickness, t_{eq} is defined as the volume of retained oil divided by the plan view area of the slick:

$$t_{eq} = \frac{V}{L_s} \tag{4.1}$$

where V is the initial oil volume per unit length of the barrier $[m^3/m]$, and L_s is the oil slick length.

The effect of experimental parameters on slick length was investigated. The results of rigid and flexible barriers are presented separately in order to verify the effect of a flexible barrier.

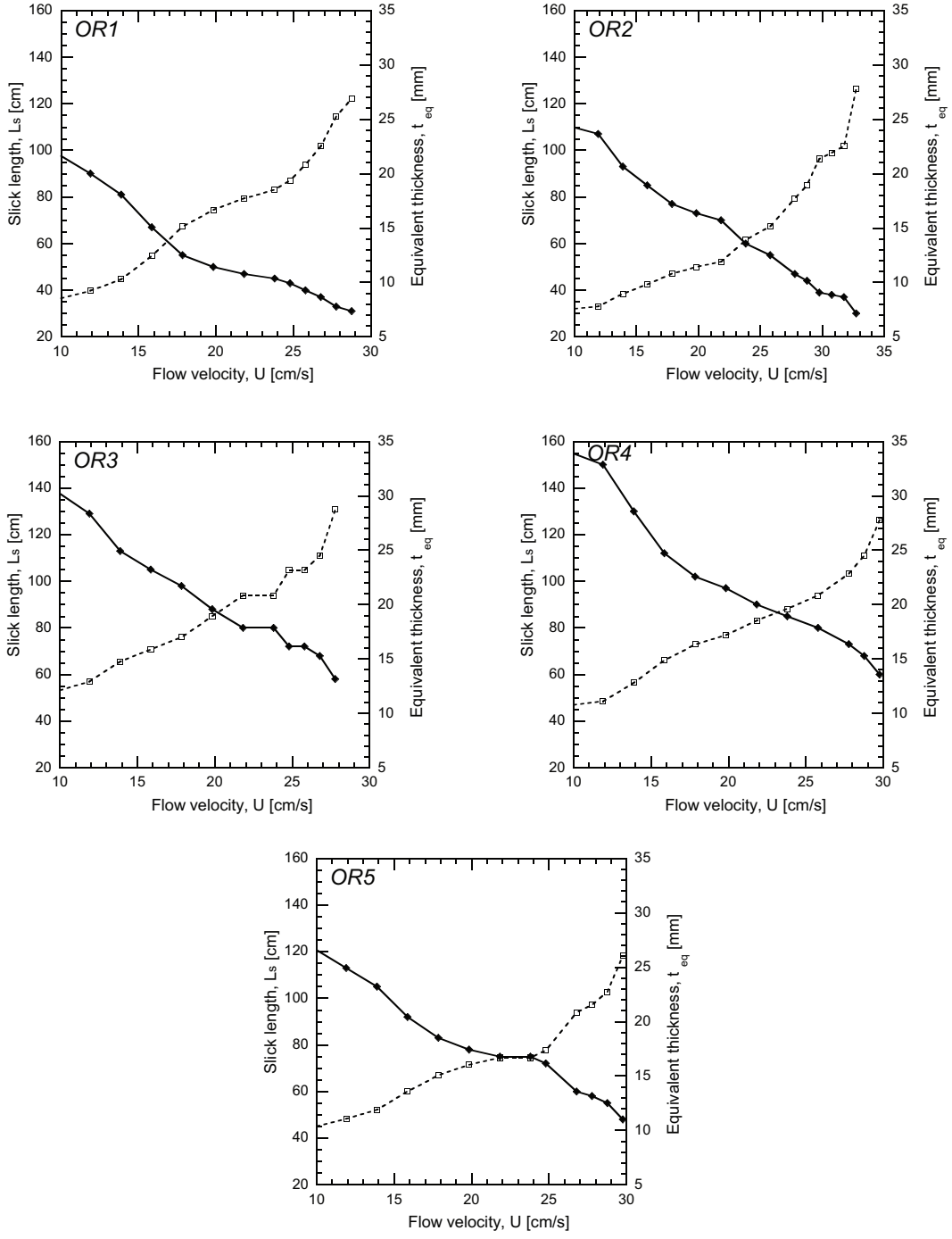

Figure 4.3: Length of slick, L_s, (solid line) and equivalent slick thickness, t_h, (dashed line) for experiments with rigid barrier, OR1 to OR5 (see Table 3.5)

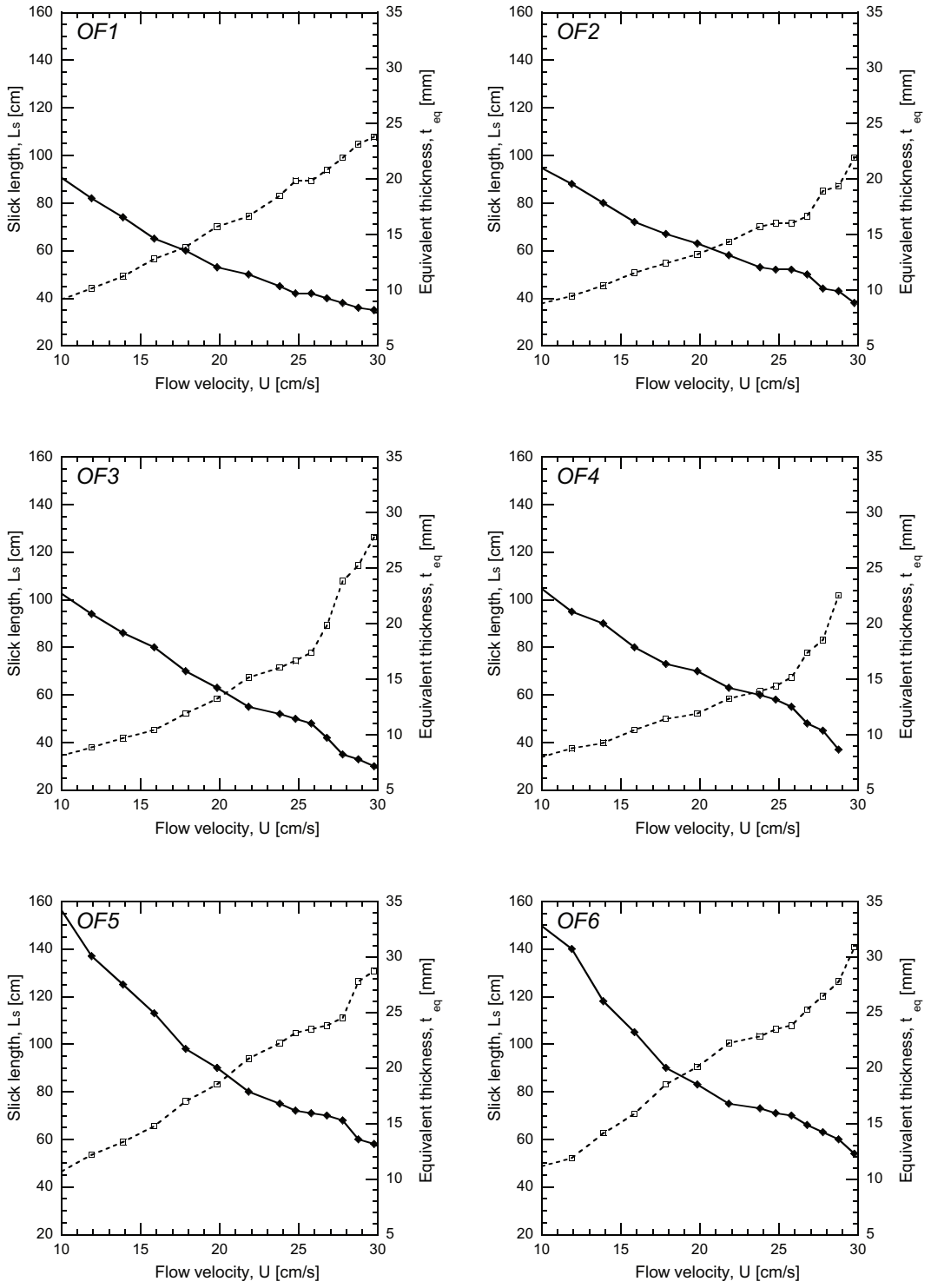

Figure 4.4: Length of slick, L_s, (solid line) and equivalent slick thickness, t_h, (dashed line) for experiments with flexible barrier, OF1 to OF6 (see Table 3.5)

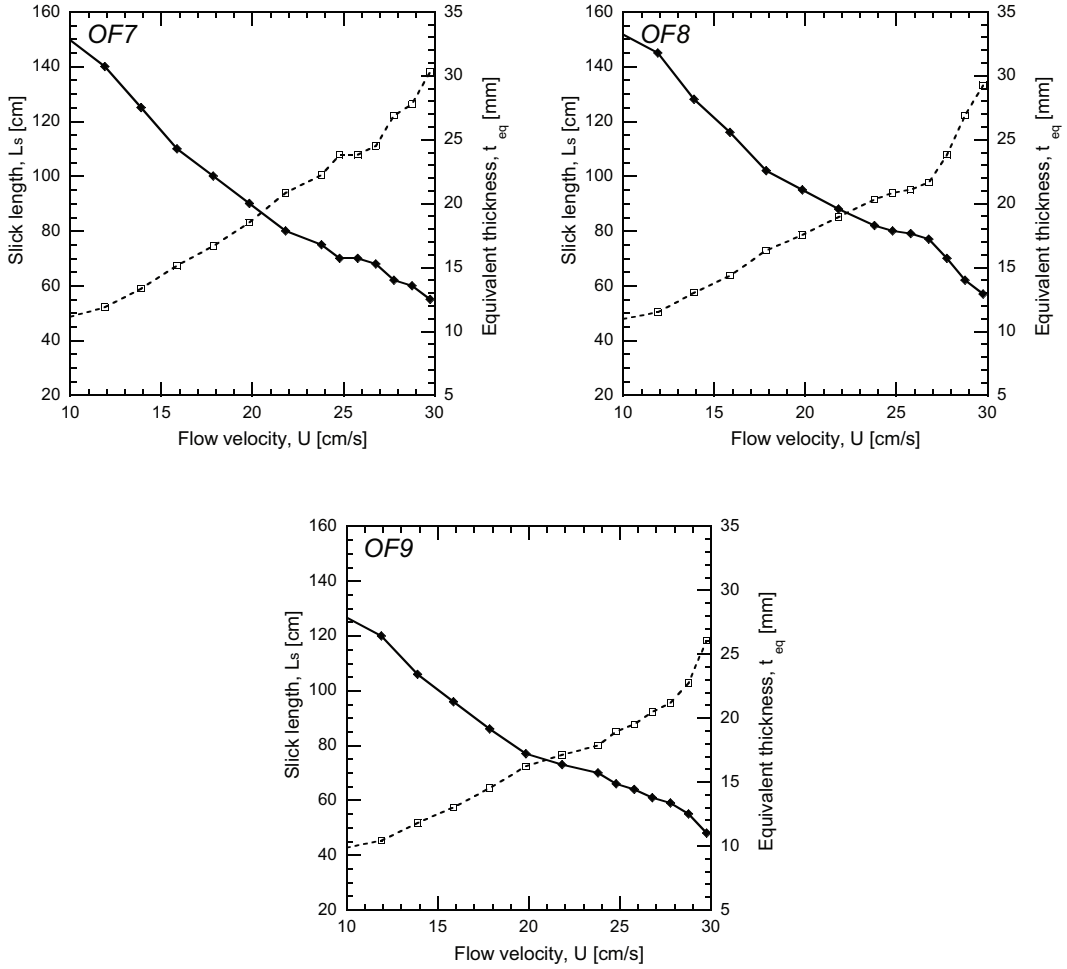

Figure 4.5: Length of slick, L_s, (solid line) and equivalent slick thickness, t_h, (dashed line) for experiments with flexible barrier, OF7 to OF9 (see Table 3.5)

Influence of the initial oil volume

The slick length upstream of the barrier was found to depend mainly on the slick volume. To investigate the influence of the initial oil volume the following points were considered:

– Fig. 4.6 demonstrates the measured slick length as a function of flow velocity for all experiments. Each series of points corresponds to experiments with the same oil volumes but for different barrier drafts and/or ballast weights (OR1 to OR5 and OF1 to OF9 in Table 3.5). It is shown that the slick length reduces with increasing the mean flow velocity; however, this reduction is less considerable at higher velocities. This can be confirmed by the decay rate of slick length, shown in Fig. 4.7. In both Fig. 4.6 and Fig. 4.7, it can be noticed that after a certain velocity of about 27 cm/s which is shown by hatches, the rate of length decay increases. The reason is the initiation of droplet detachment and entrainment into the flowing water after such a velocity. It can also be seen in Fig. 4.7 that the slick length decreases to about 50% of its initial length, by increasing the mean flow velocity from 10 to 27 cm/s.

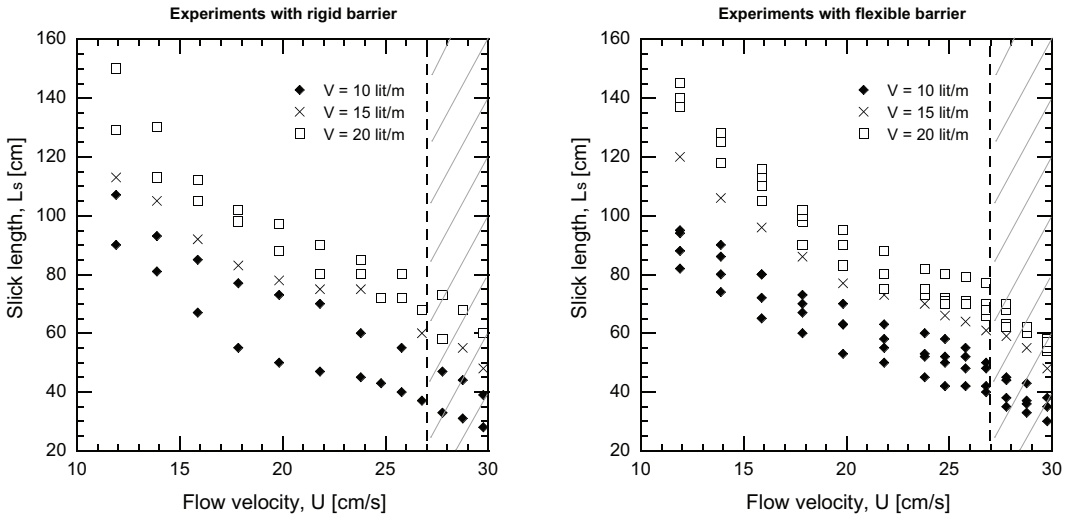

Figure 4.6: Length of oil slick, L_s as a function of flow velocity, U, for three initial oil slick volumes, V; the hatched area shows the initiation of droplet entrainment, where the slick length decreases more for a certain increment of flow velocity

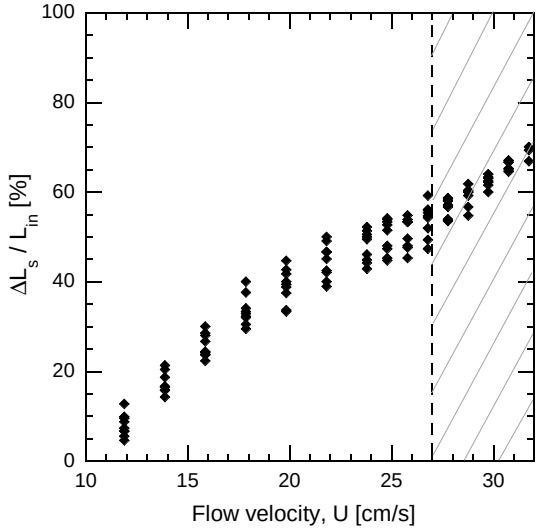

Figure 4.7: Decay rate of oil slick length, $\Delta L_s/L_{in}$, for both rigid and flexible barriers, ΔL_s is the difference of slick length at each velocity from the initial length at mean flow velocity of 10 cm/s (L_{in}); the hatched part shows the initiation of droplet detachment, where the decay rate increased due to droplet entrainment

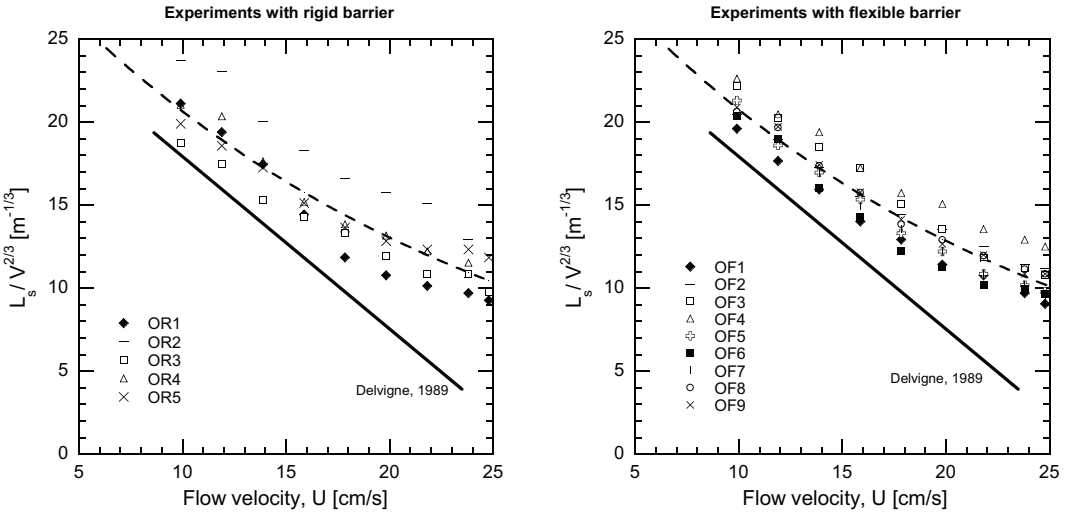

Figure 4.8: Obtained results compared to those presented by Delvigne (1989); dashed lines show exponential fittings to data

- To compare the obtained results with those of other research works, the reported results by Delvigne (1989) for oils with low viscosity, (ν changing from 350 to 1260 cSt) were used. As it was shown by Di Pietro and Cox (1980), the slick length at a certain velocity depends on characteristics of both spreading and ambient fluids, such as their viscosity, density, and interfacial tension. Since the oil used in the present study is not the same as what Delvigne (1989) used, the comparison between results of the present research project and existing ones, can just be used to verify the order of magnitude of agreement. This comparison is shown in Fig. 4.8 for rigid and flexible barriers separately. At a certain velocity, increasing the oil volume will cause increase of both oil length and thickness. Delvigne (1989) reported the proportionality of the slick length L_s with $V^{2/3}$. Obtained results in the present study showed a logarithmic fitting instead of a linear one proposed by Delvigne (1989).

- To verify the influence of oil volume on slick length, a supplementary experiment with an initial oil volume of 30 lit/m was carried out. The obtained slick length was compared to that of systematic experiments with initial oil volume of 10 and 20 lit/m. Fig. 4.9 illustrates the increase of slick length and maximum thickness by increasing its volume at a constant flow velocity of 20 cm/s. The slick length was 40 cm for an oil volume of 10 lit/m. By doubling the oil volume, the length increased to 60 cm (1.5 times the initial length), while tripling the volume led to a slick with 75 cm length (1.87 times the initial length). This shows a logarithmic relationship between oil volume and slick length.

Influence of the barrier draft

At upstream side of the barrier, i.e. near boom region, a small circulation cell is formed, that is extended less than one time the barrier draft (see Chapter 5.3). The only part of slick whose thickness and consequently its length was affected

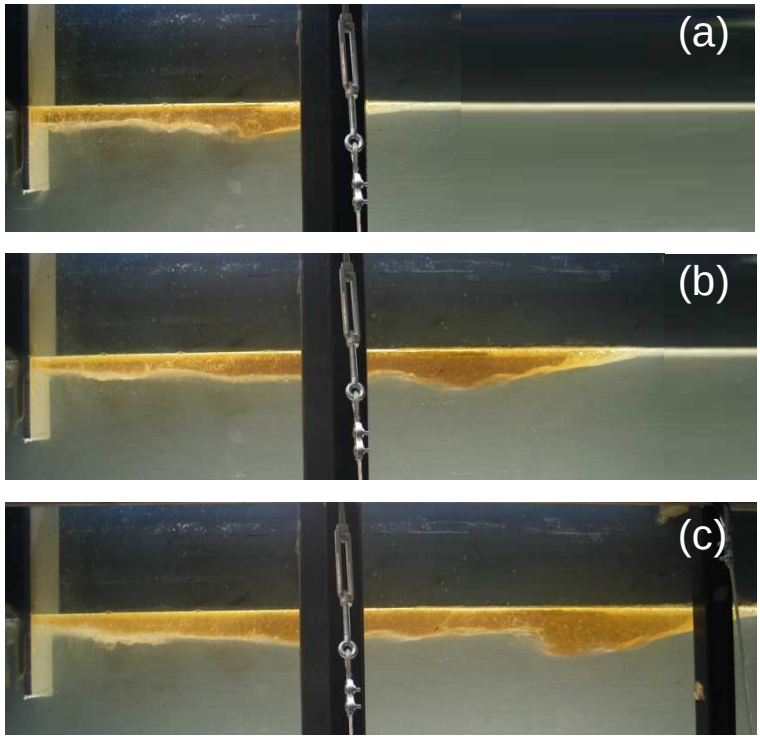

Figure 4.9: Contained oil by a rigid barrier with 10 cm draft, D; at mean flow velocity, U, of 20 cm/s; initial oil volume, V, is: (a) 10 lit/m, (b) 20 lit/m, (c) 30 lit/m

by the barrier draft or shape was the near-boom region. This part contains a small volume of the slick compared to the other parts. This region was observed to be extended about one times the draft upstream of the boom. Hence, the barrier's geometry did not affect the slick length significantly.

Influence of the barrier type and ballast weight

As it can be seen in Fig. 4.6 and Fig. 4.8 the results for rigid and flexible barriers are rather similar. It approved that the barrier type has no significant effect on slick length. Consequently, changing the ballast weight for a flexible barrier does not influence the slick length.

Based on the above mentioned points, an empirical relationship comprising involved parameters was established[1]. In the proposed equation the effect of initial oil volume, V, mean flow velocity, U, and the barrier draft, D, are considered:

$$L_s = V^{2/3}[-11.7 \ln U - \frac{2}{\sqrt{D}}] \; ; \; (R^2 = 0.96) \tag{4.2}$$

The equation gives the value of slick length, L_s, in m, where initial oil volume, V, is in m^3/m, mean flow velocity, U, is in m/s, and barrier draft, D, in m. It should be noticed that Eq. 4.2 is only valid for rapeseed oil, or

[1]Proposed empirical equations in this study were developed using a genetic programing tool: Evolutionary Polynomial Regression-EPR (Giustolisti and Savic, 2003).

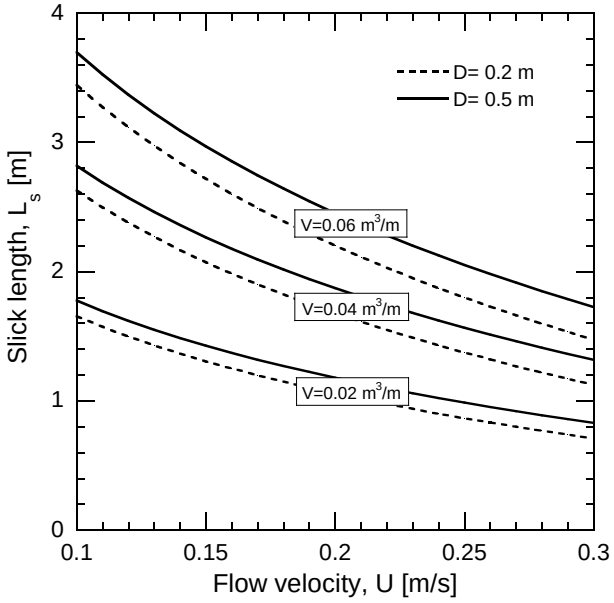

Figure 4.10: Prediction curves for slick length, L_s, as a function of mean flow velocity, U, for barriers with 0.2 and 0.5 m draft, D, using Eq. 4.2

oils with similar characteristics and for mean flow velocities less than 30 cm/s. The prediction curves for L_s for three different initial oil volumes contained by barriers with 20 and 50 cm draft are presented in Fig. 4.10.

4.1.3 Headwave thickness

The instability at oil-water interface starts from the headwave. Therefore, it is important to investigate the characteristics of the slick headwave. The measured headwave thicknesses (t_h in Fig. 4.1) are presented in Fig. 4.11. The barrier type (flexible or rigid) and its draft were shown to have no influence on the headwave thickness. The increase of flow velocity caused the increase of headwave thickness with a linear trend. Considering results of experiments with both rigid and flexible barriers, the following equation was obtained using genetic programming (EPR) to calculate the headwave thickness, t_h, for rapeseed oil at different velocities, U, as a function of initial oil volume per unit length of the barrier, V:

$$t_h = 1.4\sqrt{V}U \ ; \ (R^2 = 0.95) \tag{4.3}$$

The equation gives the thickness in m, where oil volume is given in m^3/m and the mean flow velocity is in m/s.

Fig. 4.12 shows the proportion of headwave thickness to the equivalent thickness of the slick. As shown in this figure, the headwave thickness varied between 1.5 to 2.5 times the equivalent thickness.

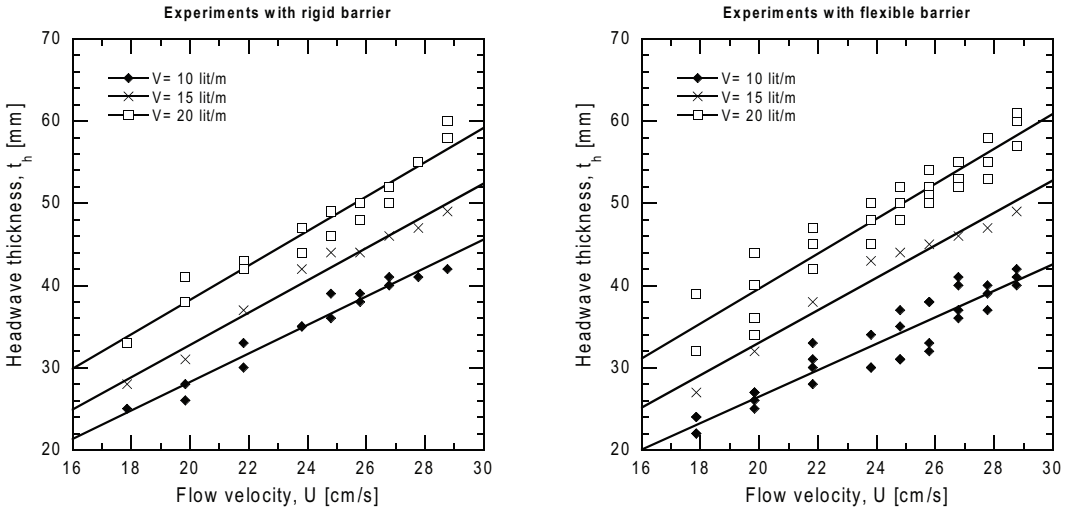

Figure 4.11: Headwave thickness as a function of mean flow velocity, U; lines show linear fitting to data

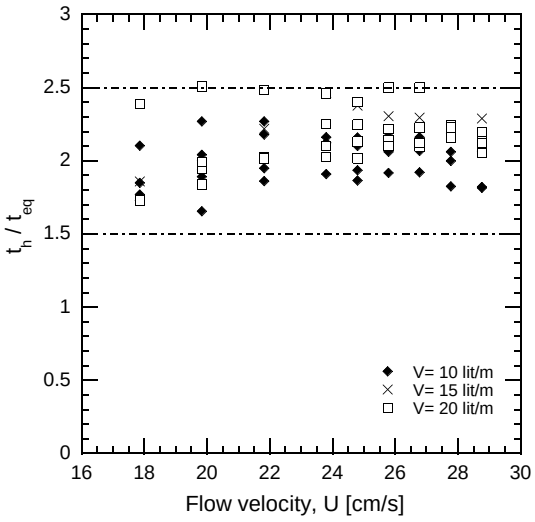

Figure 4.12: Ratio of headwave thickness, t_h, to the equivalent slick thickness, t_{eq}, as a function of mean flow velocity

4.1.4 Initial failure velocity

A subjective definition of boom failure velocity has caused significant variety in failure velocities reported by researchers. It is generally stated that loss initiates for oil booms at a flow velocity of 0.5 to 1 *knot* (25 to 50 cm/s) (Cormark, 1999). In this study, the failure velocity was defined as the velocity at which oil droplets start to be transferred underneath the barrier. For droplet entrainment failure, this velocity was observed to vary slightly with different barrier characteristics (Fig. 4.13). For a rigid barrier, the initial failure velocity, U_f, was in the range of 29 to 33 cm/s, while for a flexible barrier it varied between 30 and 33 cm/s.

The initial failure velocity is somehow dependent on the barrier draft and it increases slightly by increasing the draft. Lee and Kang (1997) proposed an

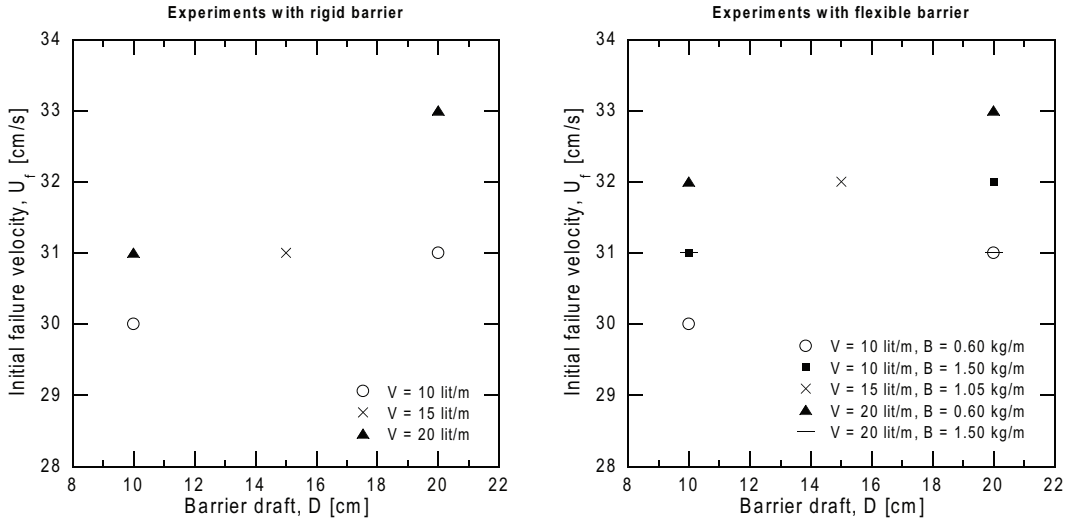

Figure 4.13: Initial failure velocity, U_f, for experiment with rigid and flexible barriers

empirical equation to predict the initiation of entrainment failure, U_f:

$$U_f = aU_{KH} + b\sqrt{g\Delta D} \tag{4.4}$$

in which, U_{KH} is the Kelvin-Helmholtz instability threshold velocity derived from Eq. 2.2, Δ is relative oil density calculated from Eq. 2.5, and a and b are empirical parameters found to be 1.98 and 0.085 respectively for rigid barriers by Lee and Kang (1997).

Analysis of results of the present study including flexible barriers using the least square method gave the same value for a. However, for b a value of 0.08 best fitted the data. Therefore, the initial failure velocity for flexible barriers can be calculated as:

$$U_f = 1.98U_{KH} + 0.08\sqrt{g\Delta D} \tag{4.5}$$

The initial failure velocity was nearly the same for rigid and flexible barriers, because the droplet detachment starts at headwave and depends on the local oil-water relative velocity there. A flexible barrier does not change significantly the velocity field at headwave location (detailed explanation and velocity field comparison is shown in Chapter 5).

Although Lee and Kang (1997) suggested that with a larger volume of oil the separated droplet has more chance to reattach the slick and entrainment starts at a lower velocity, they did not introduce the oil volume into the Eq. 4.4. In the present study, the initial failure velocity was slightly increased by increasing the oil volume in some experiments but it was not always the case. Hence, the effect of oil volume is not considered in Eq. 4.5. Increasing the oil volume will cause the increase of both slick length and thickness. Therefore, although increasing the oil volume may cause the headwave to be placed further from the barrier, it also make the headwave thickness to increase. Droplets shed from a thicker headwave have a bigger chance to be carried by the ambient flow. Hence, it is

reasonable that increasing the oil volume, does not influence the initiation of entrainment failure.

4.1.5 Loss rate

The total time required for cleaning up and recuperation operations following oil spill is rather long for most accidents. Hence, even small loss rates may compromise the cleanup procedure, as it will continue for a long time. Accordingly, many investigations considered the initial failure velocity rather than the loss rate and tried to determine so-called no leak conditions (Fannelop, 1983).

The rate of droplet shedding is affected by several parameters. Since the droplets are entrained into the flowing water mostly from the headwave, the distance of the headwave to the barrier may influence the loss rate. In a slick with a headwave close to the barrier, the generated droplets have less chance to rejoin the slick before passing underneath the barrier. A longer draft can also make some droplets to coalesce with the slick after colliding it. Another dominating parameter is the density of oil that influences the penetration depth of the droplets into the passing water and the buoyancy forces causing it to be brought up. Some researchers stated that the interfacial tension of oil can also affect the loss rate (Agrawal and Hale, 1974; Leibovich, 1976). But it was pointed out by Delvigne (1989) that, by lowering the interfacial tension to 20 % of the initial value by adding surfactant, the entrained droplets were considerably smaller but more numerous and neither the failure velocity nor the loss rate did change.

Zalosh and Jenson (1975) showed by numerical simulations that the loss rate increases sharply with velocity. Moreover, a simple entrainment loss relation has been suggested by Lindenmuth et al. (1970) for cases were the headwave was so close to the barrier that all formed droplets were lost:

$$q_E = \varsigma \, U \, t_h \tag{4.6}$$

where q_E is the oil loss rate (m^3/s per meter of barrier length), t_h the headwave thickness, and ς the entrainment parameter. This parameter is unknown but assumed by Lindenmuth et al. (1970) to be mainly dependent on the headwave Froude number:

$$F_h = \frac{U_c}{\sqrt{g \, \Delta \, t_h}} \tag{4.7}$$

where U_c is the oil internal velocity in the headwave. Eq. 4.6 only considers the oil slick and not the draft.

The present experiments showed a difference in loss rate for barriers with different drafts. Even if the loss initiates at similar flow velocities, the loss rate is higher and increases more by increasing the flow velocity in case of a barrier with a shorter draft (Fig. 4.14).

Instead of relating the loss rate to the headwave characteristics, it would be more useful if one presents an equation that relates the loss rate to the oil volume and barrier draft. In the present study an exponential trend seemed

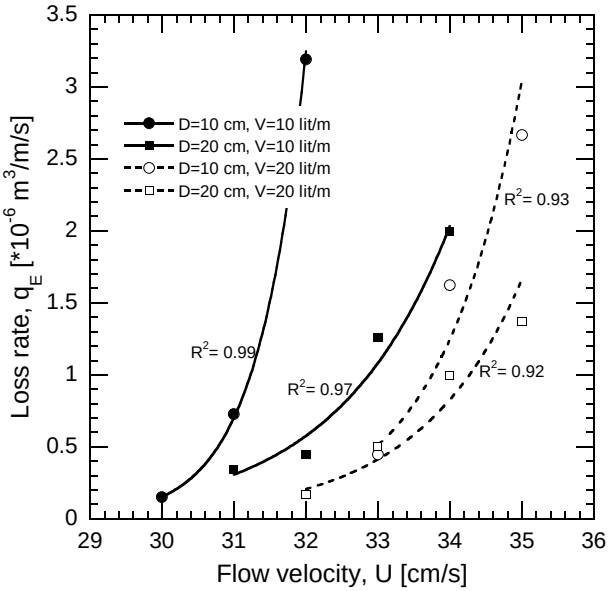

Figure 4.14: Loss rate as a function of flow velocity for a flexible barrier with 0.6 kg/m ballast weight containing 10 lit/m oil, curves show exponential fitting to data

to better fit the data. Accordingly, Eq. 4.8 was proposed using the genetic programming (EPR):

$$q_E = 122.79\, D\, V^{2/3} \exp\left(22.65\, I_U\right) + \frac{2.43\, I_U}{D^3\, V^{7/3}} - 0.74\ ;\ (R^2 = 0.89) \qquad (4.8)$$

where q_E is the loss rate in $cm^3/m/s$, I_U is the increment of the flow velocity in m/s comparing to the initial failure velocity, V is the initial oil volume in m^3/m and D is the barrier draft in m. Since the entrainment phenomenon was modeled at full scale, the equation can be used directly for the prototype.

4.1.6 Experiments with rigid curved barriers

Experiments OF1 to OF9, with a flexible barrier, were representative for first mode of skirt deformation, where the bottom point of the boom is free to displace. But another mode can also be considered, where the bottom point is horizontally fixed by the tensile rope and can also move in vertical direction. To study another mode of skirt deformation for Cavalli system, some experiments were undertaken with curved rigid barriers (ORc1 to ORc3 in Table 3.5). Two modes of barrier deformation are presented schematically in Fig. 4.15. Due to practical problems, instead of performing experiments with a flexible barrier whose end point is fixed in the horizontal direction, predefined deformed shapes were considered and rigid curved barriers with 10 and 20 cm draft were fabricated. An example of experiments with curved rigid barrier with 20 cm draft is shown in Fig. 4.15.

As it is presented in Table 4.1, the initial failure velocity and slick shape evolution was the same as in other experiments. This was expected since the

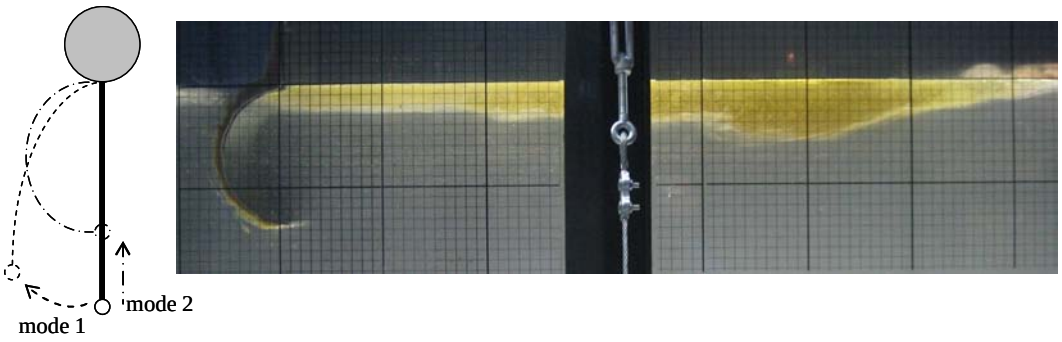

Figure 4.15: Second mode of barrier deformation; left: deformation modes of a flexible barrier; right: experiment ORc3, for a curved barrier with 20 cm draft

Table 4.1: Initial failure velocity for experiments with rigid curved barrier

Test No.	**Draft** $[cm]$	**Oil volume** $[lit/m]$	**Initial failure velocity** $[cm/s]$
ORc1	10	10	30
ORc2	20	10	32
ORc3	20	20	31

barrier shape can only affect the near boom region and has no significant effect on local velocities at headwave where entrainment occurs.

4.1.7 Trapped oil experiments

Experiments with double barriers were aimed to simulate oil slick captured by the Cavalli system for double and quadruple configurations (ORD1 to ORD6 in Table 3.7).

The flow pattern and streamlines passing parallel barriers, derived form numerical modeling are presented in Sec. 5.3. However to discuss the results of experiments, results presented by other researchers were reviewed. Ertekin and Sundararaghavan (1995) have studied the flow passing a single oil boom and showed the streamlines for such a case. They revealed that a stagnation point is located downstream of the barrier at a distance of about 4 times the barrier draft, for a barrier draft more than one third of the flow depth. Lee and Kang (1997) found this stagnation point to be situated at a distance of 8 times the boom draft for deep waters.

Using a colored tracer, it was observed that the turbulence wake downstream of a rigid barrier has an extension of about 6 to 8 times the barrier draft. The turbulence wake of the upstream barrier caused fluctuations in oil-water interface, which surge towards the downstream barrier and make a part of the

oil to pass beneath the barrier, with each crest of interfacial waves. Fig. 4.16 shows the slick shape of trapped oil slick during three seconds. The wake had considerable influence on the containment of trapped oil when the ratio of the distance between two barriers and the draft (d_b/D) was high, and led to a lower initial failure, as illustrated in Fig. 4.17.

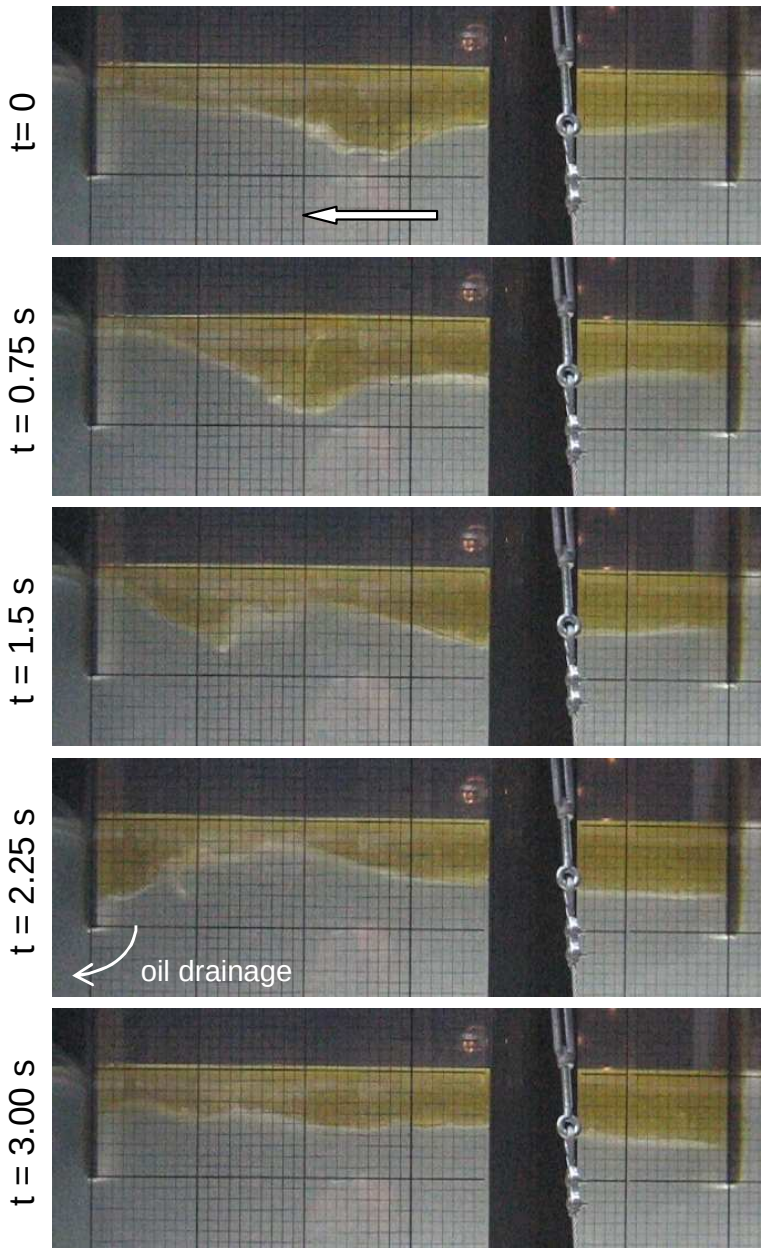

Figure 4.16: Interfacial waves for trapped oil slick with d_b/D equal to 6 and h/D equal to 0.5; water is flowing from right to left with mean flow velocity of 45 cm/s; main grid spacing is 10 cm

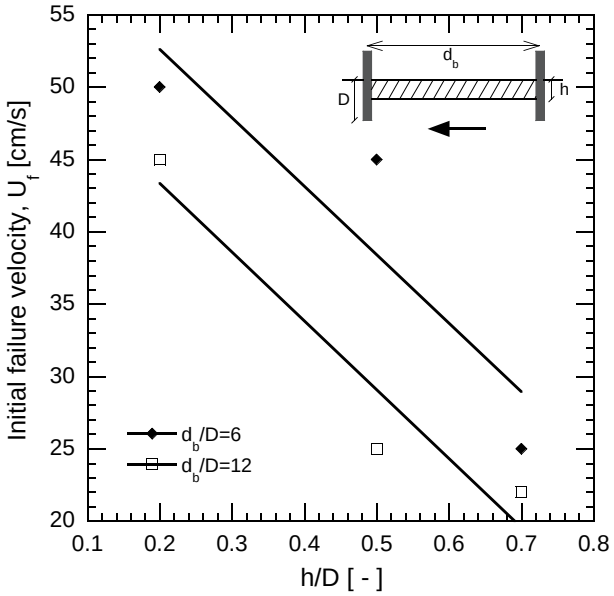

Figure 4.17: Initial failure velocity for a slick trapped between two parallel barriers; lines show linear fitting to data

As it is shown in Fig. 4.17 a trapping barrier can protect the oil slick inside and increase the initial failure velocity to more than 45 cm/s. For example if the ratio of distance to draft, d_b/D, is no more than 6 even for a slick with thickness of 50% the barriers draft, the flow velocity can reach 45 cm/s before failure initiates. Hence, in the case of using Cavalli system in a small slick and/or by dividing the reservoir into smaller circles, the towing velocity can be increased by up to 50%.

4.1.8 Experiments with a more viscous oil

Residue oil diluted with cracked gas oil (density 0.96 gr/cm^3 and viscosity 2400 cSt), was used to compare obtained results from experiments with rapeseed oil with that of a more viscous oil. The initial oil volume was 10 lit/m and the barrier draft was 15 cm. Fig. 4.18 shows the evolution of slick with increase of mean flow velocity. Same as experiments with rapeseed oil, slicked oil accumulated at the upstream end of the slick and formed a headwave. By increasing the flow velocity, the accumulated part approached the barrier. Unfortunately, the oil weathered very quickly and formed a very light foam over water surface (density of 0.31 gr/cm^3) and the experiment could not be continued.

4.1.9 Conclusions regarding experiments without waves

Experiments without waves were helpful to investigate the low-viscous oil containment procedure in calm water and provided the data to be compared with results of experiments with wave.

The geometrical characteristics of the slick were subject of some analysis. The slick length depends mainly on the contained oil volume. Two empirical

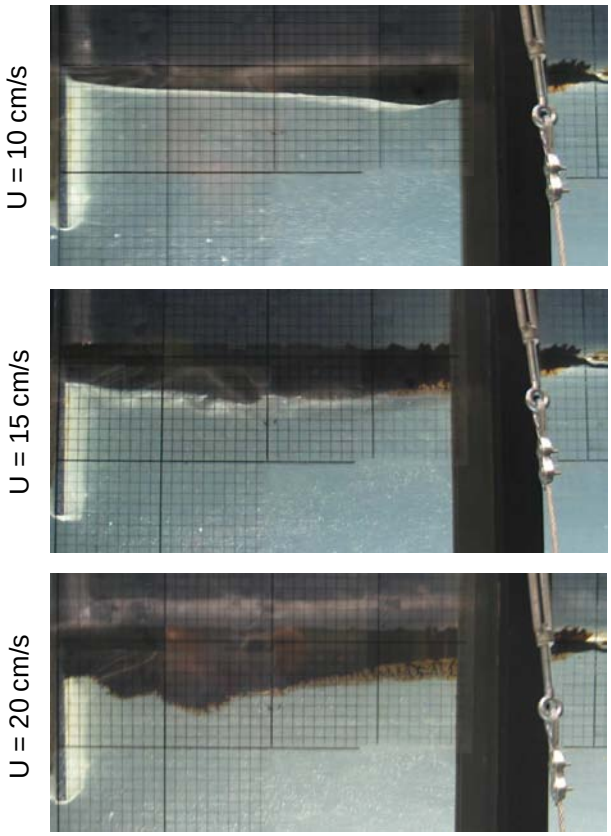

Figure 4.18: Experiments with residue oil diluted with cracked gas oil

equations were proposed for predicting the slick length (Eq. 4.2), and headwave thickness (Eq. 4.3) as a function of flow velocity considering the oil volume and barrier draft.

The failure of rigid and flexible oil containment barriers was shown to initiate at a flow velocity of 31±2 cm/s. The observed failure mechanism was droplet entrainment failure, as was expected for an oil slick with a viscosity of only 89 cSt. Containment failure velocity was found to be nearly independent of barrier's flexibility, but very slightly dependent on the barrier draft. Eq. 4.5 was proposed to predict initiation of failure for flexible barriers as a function of barrier draft and contained oil characteristics.

Once the failure initiated, the loss rate increased exponentially with flow velocity. The loss rate was higher and increases more by increasing the flow velocity in case of a barrier with a shorter barrier draft. Thereby the initial failure velocity was more critical in case of a barrier with smaller draft. Eq. 4.8 was proposed to predict the loss rate as a function of velocity increment.

Experiments with oil trapped between two rigid barriers revealed that the oil layer is influenced by the turbulence wake formed downstream of the first barrier. Induced fluctuations made a surging motion in the oil layer, which led to oil leakage underneath the barrier. However, if the diameter is not more than 6 times the barrier draft, a trapping reservoir could increase the initial failure velocity by up to 50%.

4.2 Experiments with oil in presence of waves

Second series of oil experiments were undertaken in presence of both currents and waves in the laboratory flume. Characteristics of experimental waves and testing conditions are presented in Sec. 3.6.2.2 and Sec. 3.7.1 respectively. The present section focuses on the effect of different wave characteristics on containment efficiency as well as deformation of the flexible barrier.

4.2.1 General observations

The evolution of slick form and shape were mostly the same for experiments with and without waves. However, the waves changed the containment limits and conditions. On the one hand, in presence of waves a thicker and shorter slick formed upstream of the barrier. On the other hand, waves provoked instabilities in the oil-water interface and consequently reduced the initial failure velocity. Like experiments without waves, the failure mode was entrainment failure. Nevertheless, for some experiments another mode of failure was observed, which was similar to drainage failure. It happened when the crest of interfacial waves reached the barrier bottom and a part of contained oil passed beneath the barrier. This phenomenon is discussed in detail in Sec. 4.2.6.

Fig. 4.19 to Fig. 4.23 demonstrate the evolution of slick shape with increasing the flow velocity, for a flexible barrier with 20 cm draft (SF3), in presence of five different experimental waves (see wave characteristics in Table 3.4). As it can be seen, the slick length could decrease considerably due to effect of waves. Moreover, the headwave thickness was increased and interfacial waves with large height were formed.

At lower flow velocities, it was observed that the oil thickness was minimum at the wave trough and maximum at the wave crest as it was reported by Kordyban (1992). However at higher flow velocities, the interfacial waves, approaching the barrier, made it difficult to observe such a phenomenon.

4.2.2 Initial failure velocity

The velocity at which entrainment failure initiates was measured and is presented in Fig. 4.24, for rigid barriers as well as flexible ones with different ballast weights. The figure summarizes the failure velocities of experiments with 20 lit/m initial oil volume (SR1, SR2, and SF1 to SF4 in Table 3.6). The results of experiments with no wave are also presented. The experimental series SF5 and SF6 with initial oil volume of 30 lit/m were not included. The initial failure velocity did not change significantly for barriers with different types (rigid or flexible), or with different ballast weights in case of a flexible barrier.

As it can be seen, the initial failure drops down considerably after wave 3. For waves 1 to 3 which were relatively weak, the failure initiates at velocities close to experiments with no wave. However, stronger waves can reduce the initial failure velocity significantly. The effect of wave parameters on failure initiation is explained in more detail in following sections.

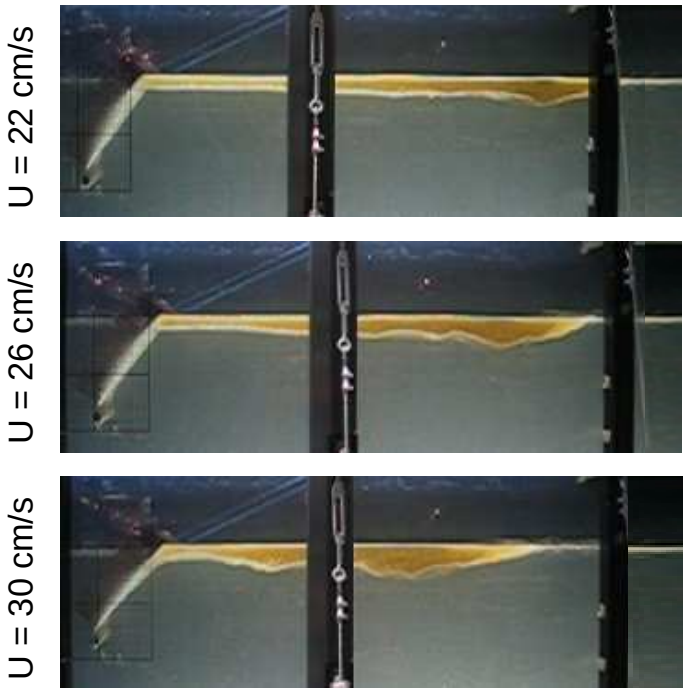

Figure 4.19: Slick shape evolution by increasing the mean flow velocity, U, for a flexible barrier with 20 cm draft and 0.6 kg/m ballast weight in presence of wave 1 (see Table 3.4); water is flowing from right to left

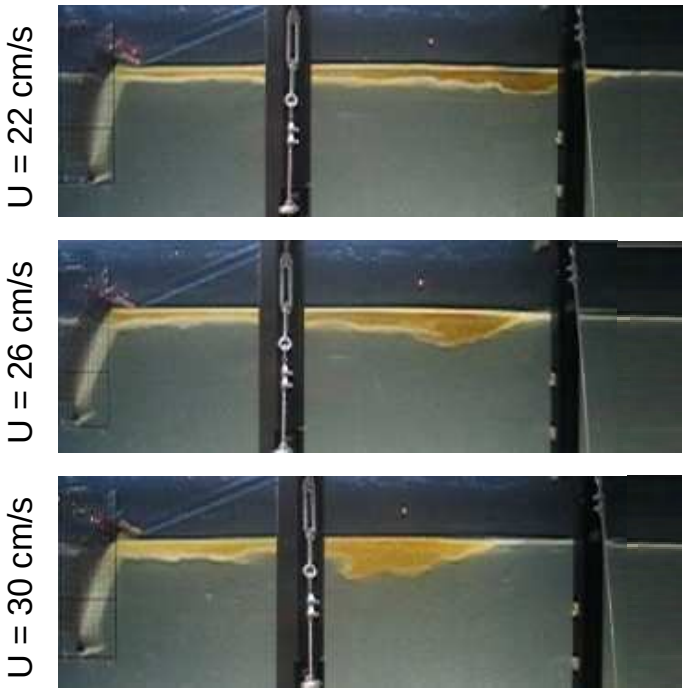

Figure 4.20: Slick shape evolution by increasing the mean flow velocity, U, for a flexible barrier with 20 cm draft and 0.6 kg/m ballast weight in presence of wave 2 (see Table 3.4); water is flowing from right to left

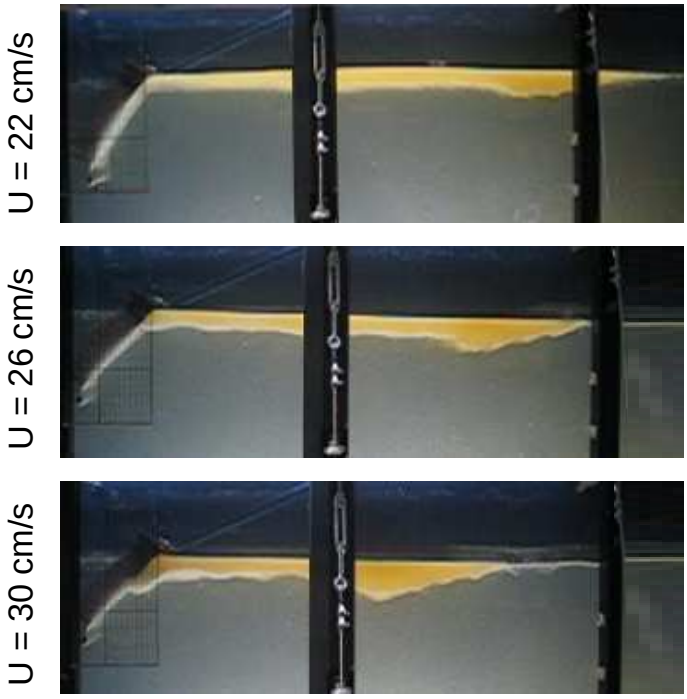

Figure 4.21: Slick shape evolution by increasing the mean flow velocity, U, for a flexible barrier with 20 cm draft and 0.6 kg/m ballast weight in presence of wave 3 (see Table 3.4); water is flowing from right to left

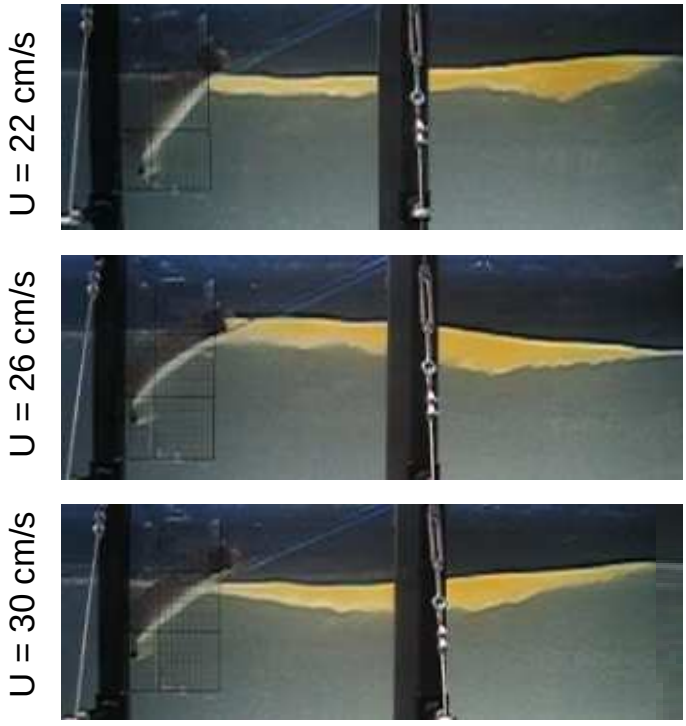

Figure 4.22: Slick shape evolution by increasing the mean flow velocity, U, for a flexible barrier with 20 cm draft and 0.6 kg/m ballast weight in presence of wave 4 (see Table 3.4); water is flowing from right to left

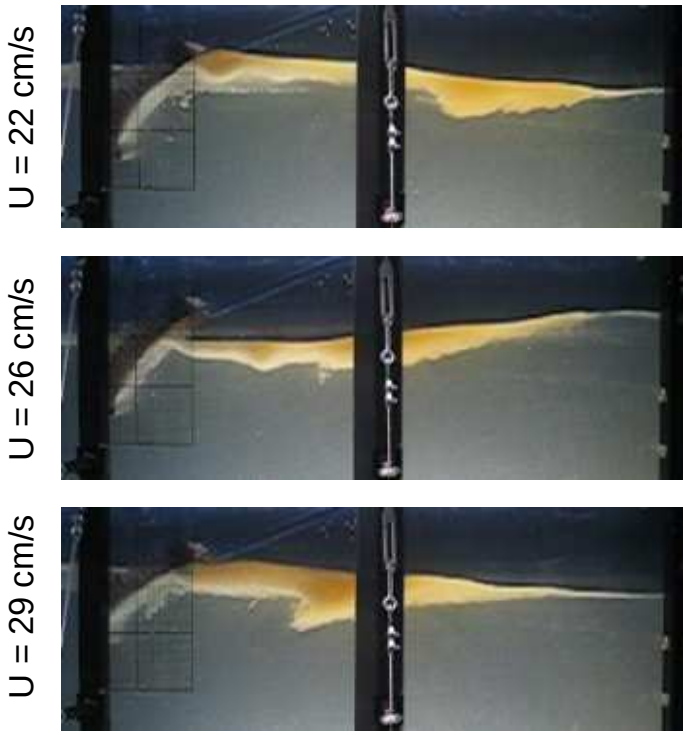

Figure 4.23: Slick shape evolution by increasing the mean flow velocity, U, for a flexible barrier with 20 cm draft and 0.6 kg/m ballast weight in presence of wave 5 (see Table 3.4); water is flowing from right to left

4.2.2.1 Effect of experimental parameters on failure initiation

According to the results of conducted tests, the main parameters influencing the initiation of failure were the characteristics of waves. Hence, the wave parameters receive the most attention in the following discussion. However, the effect of barrier draft and oil volume are also discussed.

Influence of wave height

To investigate the effect of wave height on failure velocity, experimental results for each wave height were classified. The initial failure velocities are presented in Fig. 4.25 where results of rigid and flexible barriers are illustrated separately. For wave height equal to zero the initial failure velocity for experiments without waves is included.

Increase of the wave height reduced the initial failure velocity. However for small wave heights, this reduction was not noticeable. Influence of wave height was more significant for barriers with 10 cm draft than barriers with 20 cm draft, and for flexible barriers comparing to rigid ones. No significant decrease of initial failure velocity was observed for wave heights up to 3.47 cm. As it was explained in Sec. 3.6.2.2, in presence of waves the geometric model scale, λ_L, equal to 15 was defined based on Froude similarity rule. Applying this scale factor, it can be concluded that for a prototype with dimension 15 times the experimental barrier, the effect of wave height on initial failure reduction stars at a wave height of about 0.52 m.

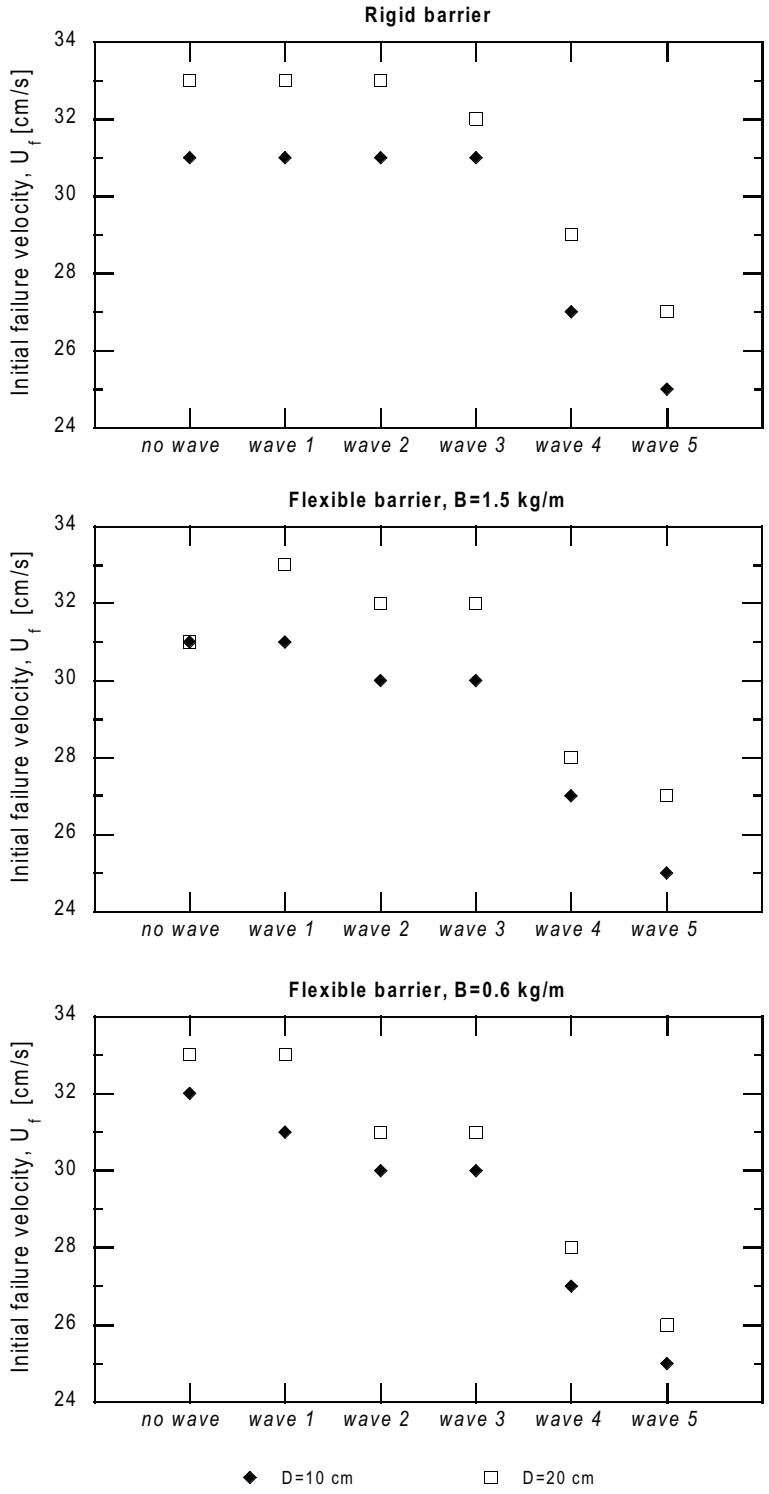

Figure 4.24: Initial failure velocity for rigid and flexible barriers due to different waves (see Table 3.4); D is the barrier draft and B is the ballast weight

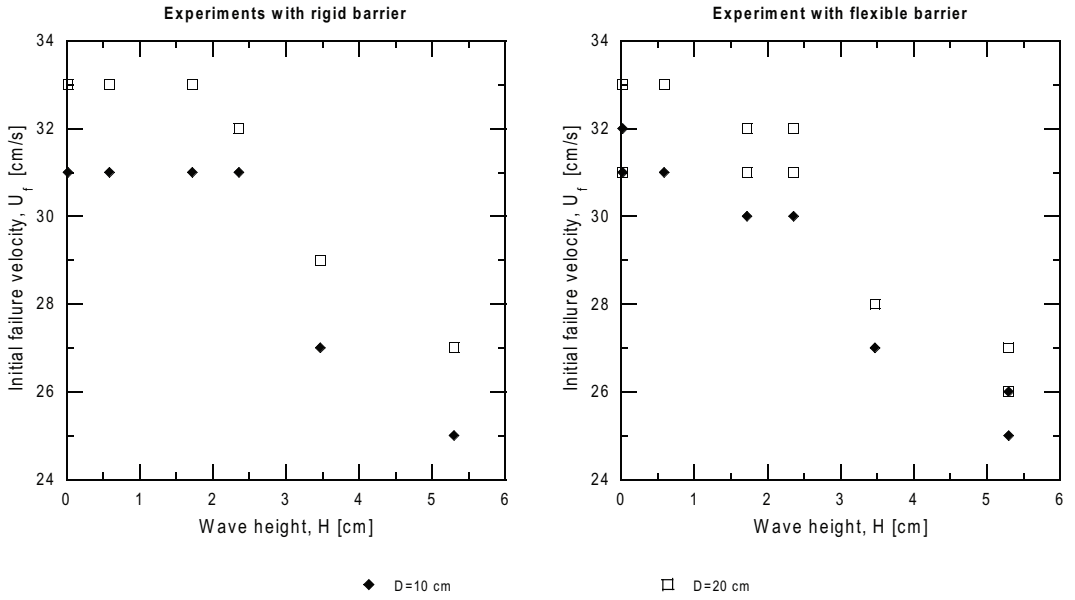

Figure 4.25: Initial failure velocities for experiments with rigid and flexible barriers with two different drafts, D, in presence of waves with different heights, H; initial oil volume, V, is 20 lit/m

Influence of wave period

To study the effect of wave period on failure velocity, classifications were made for experiments with different wave periods and results are shown in Fig. 4.26. By decreasing the wave period (increasing the frequency), interfacial waves became more aggressive and consequently failure initiated at a lower velocity as it can be seen in the figure. As it was observed for wave height variations, shorter and flexible barriers were more sensitive to variations of wave period. A significant reduction of the initial failure velocity could be observed for wave periods below 1.35 s. Applying the time scale, $\lambda_T = \sqrt{15}$, a critical wave period of 5.8 s can be proposed for the prototype.

Influence of wave steepness

A representative parameter to assess the effects of waves on containment process is the wave steepness, s, which is defined as the ratio of wave height to wave length. Fig. 4.27 shows the effect of wave steepness on failure velocity for rigid and flexible barriers separately, where the results of experiments with no wave are also included (wave steepness equal to zero). Data show a good fitting to linear trend lines. For experiments with a rigid barrier, wave steepness less than 0.01 could not affect the failure initiation, whereas flexible barriers were more sensitive to the presence of waves and even waves with steepness less than 0.01 could cause a decrease in initial failure velocity.

Influence of barrier draft

As it is shown in Fig. 4.27, in the presence of waves the barrier draft could somehow influence the failure initiation. The initial failure velocity was higher for barriers with a deeper draft.

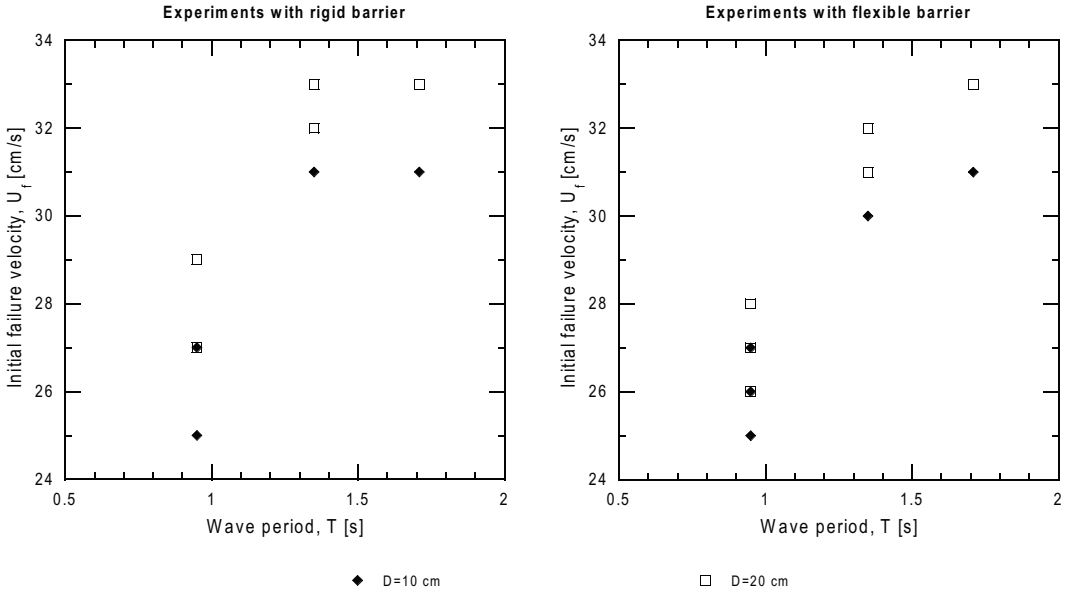

Figure 4.26: Initial failure velocities for experiments with rigid and flexible barriers with two different drafts, D, in presence of waves with different periods; initial oil volume, V, is 20 lit/m

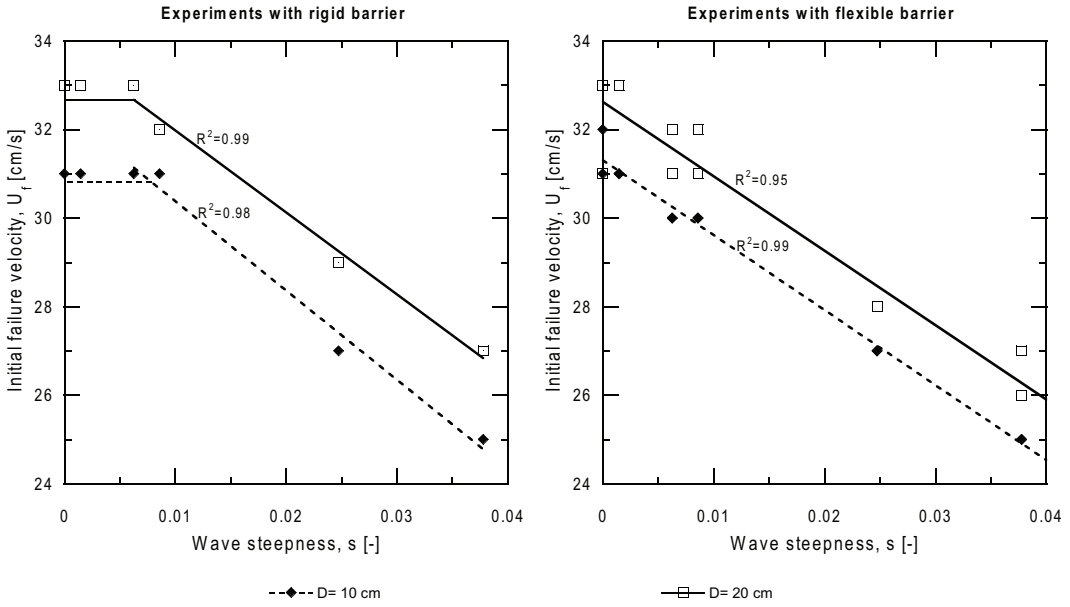

Figure 4.27: Effect of wave steepness on failure velocity for experiments with rigid and flexible barriers with two different drafts, D; initial oil volume, V, is 20 lit/m; lines present linear fitting to data

As it can be seen in Fig. 4.24 to Fig. 4.27, in presence of waves the failure initiates in almost all cases in a lower velocity for a barrier with a shorter draft. The influence of barrier draft on the initial failure velocity is the same as the experiments without waves and the difference of initial velocities for barriers with 10 and 20 cm draft is no more than 2 cm/s.

Influence of initial oil volume

Comparing the results of experiments SF5 and SF6 with initial oil volume of 30 lit/m, to experiments SF1 and SF3 having the same conditions with initial oil volume of 20 lit/m, shows unnoticeable effect of initial oil volume on initiation of entrainment failure, as presented in Table 4.2. As in case of experiments without waves, no matter how large is the oil volume and where the headwave is placed, the droplet detachment initiates at a certain velocity depending on oil characteristics. Effect of oil volume on drainage failure is discussed in Sec. 4.2.6.

Table 4.2: Initial failure velocity for experiments with flexible barrier ($B = 0.6\,kg/m$) containing different oil volumes

Test No.	**Draft**	**Initial oil volume**	**Initial failure velocity**				
	$[cm]$	$[lit/m]$	$[cm/s]$				
			$W1$	$W2$	$W3$	$W4$	$W5$
SF1	10	20	31	30	30	27	26
SF3	20	20	33	31	31	28	25
SF5	10	30	31	30	29	28	25
SF6	20	30	32	31	31	29	26

4.2.2.2 Prediction of failure initiation

Effect of different wave parameters, barrier draft, and oil slick volume on failure was discussed. It was shown that the wave steepness, representing both wave height and period, is an effective parameter on failure initiation and consequently an appropriate parameter to predict it. Another involved parameter was the barrier draft. Based on the above mentioned discussion and using the least square method, Eq. 4.9 is proposed to predict the initial failure velocity, U_f, for flexible barriers.

$$U_f = 1.98U_{KH} + 0.08\sqrt{gD\Delta} - \frac{5}{3}s \;;(R^2 = 0.95) \tag{4.9}$$

This equation gives the failure velocity, U_f, in m/s, where the draft, D, is introduced in m. For a rigid barrier at wave steepness less than 0.01, the failure velocity is the same as the case without wave and can be calculated using Eq. 4.5. This equation can be applied to predict the initiation of failure

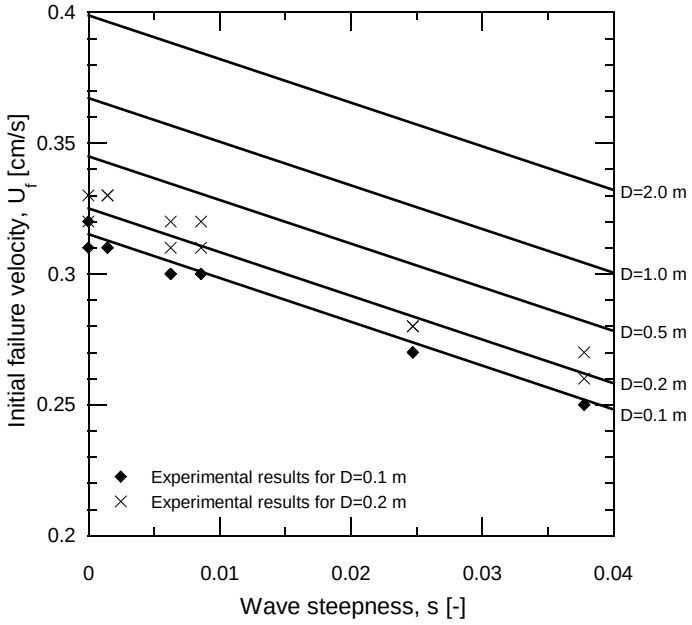

Figure 4.28: Prediction of failure velocity, U_f, for barriers with different drafts, D, as a function of wave steepness, s, using Eq. 4.9; points represent measured failure velocities during the experiments with rigid and flexible barriers

for a prototype. The prediction graphs for barriers with different drafts are shown in Fig. 4.28. The figure includes the experimental results as well.

4.2.3 Slick length

Waves affect the slick length significantly by pushing the slick to accumulate behind the barrier. To investigate this effect, slick length was measured for experiments with a barrier with 10 cm draft and 0.6 kg/m ballast weight, containing 20 lit/m oil (SF1). At a certain velocity and with no waves, the slick length, L_s, was measured. Afterward, a certain wave was established and the slick length was again measured in presence of the wave (L_{sw}). The percentage of slick length decay due to waves effect are shown in Fig. 4.29. Same measurement process was repeated for all five experimental waves. As expected for stronger waves, the decay rate was more significant at a certain velocity, and increased more rapidly by increasing the flow velocity. The data show an exponential trend. Eq. 4.10 is proposed to predict the slick length decay by increasing velocity for waves with different steepness.

$$\frac{\Delta L}{L_s} = 19.35\,\sqrt{s}\exp\left(7.56U\right)\,;(R^2 = 0.92) \tag{4.10}$$

where $\Delta L = L_s - L_{sw}$ and U is the mean flow velocity in m/s. The slick length without waves, L_s, can be calculated as a function of oil volume and barrier draft using Eq. 4.2. Fig. 4.30 illustrates the predicted slick length decay at different flow velocities as a function of wave steepness.

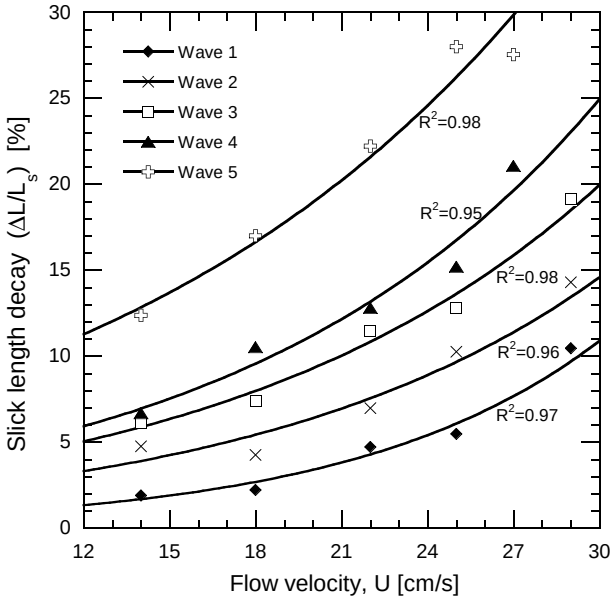

Figure 4.29: Slick length decay, $\Delta L/L_s$, caused by experimental waves (see Table 3.4), curves show exponential fitting to data

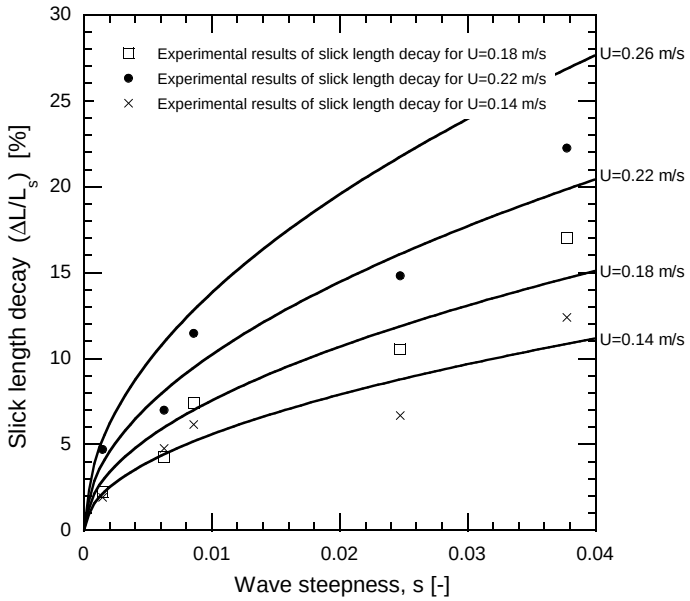

Figure 4.30: Prediction of slick length decay, $\Delta L/L_s$, as a function of wave steepness, s, using Eq. 4.10; the slick length without waves, L_s, can be calculated by Eq. 4.2; points represent experimental measurements

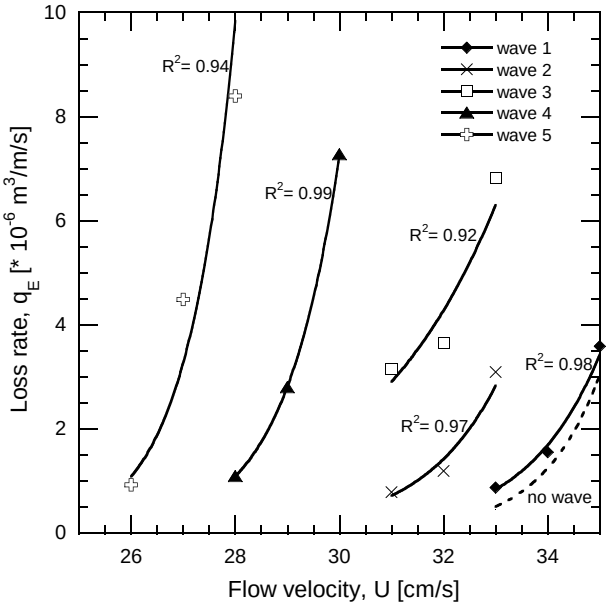

Figure 4.31: Influence of different waves on oil loss rate, for a flexible barrier with 10 cm draft, 0.6 kg/m ballast weight, and 20 lit/m initial oil volume; dashed line shows the loss rate for the same barrier and initial oil volume with no waves (extracted from Fig. 4.14); curves show exponential fitting to data

4.2.4 Loss rate

In absence of waves, it was shown in Sec. 4.1.5 that a longer draft can change the loss rate considerably. In presence of waves, for a flexible barrier with 20 cm draft and 1.5 kg/m ballast weight, the loss rate was measured. Results are shown in Fig. 4.31, and for each wave an exponential fitting is illustrated.

It can be noticed that the loss rate increased more rapidly for experiments with stronger waves. In the case of an aggressive wave such as *waves 4* and *5*, the loss rate augmented very rapidly after initiation of failure. It can also be seen that the loss rate was almost the same for experiments without waves (dashed line in Fig. 4.31) and for experiments with weak waves (*waves 1* and *2*).

4.2.5 Barrier roll and deformation due to wave effects

When no wave exists, the flowing water deforms the barrier to a stable position. It was observed during the experiments that if the barrier is floating freely over the water surface, it just moves up and down following the waves, without deformation in the barrier. However, for conducting experiments with oil it was needed to have a tight barrier with lateral constrains to avoid oil leakage from the sides. Therefore, the barrier was partially constrained and the presence of waves caused the barrier to roll around its stable position.

The barrier rotated with the same frequency and in the same phase as the progressive water waves. At wave crest, because of the high hydrostatic pressure, the barrier had the maximum deviation from vertical position, whereas at wave

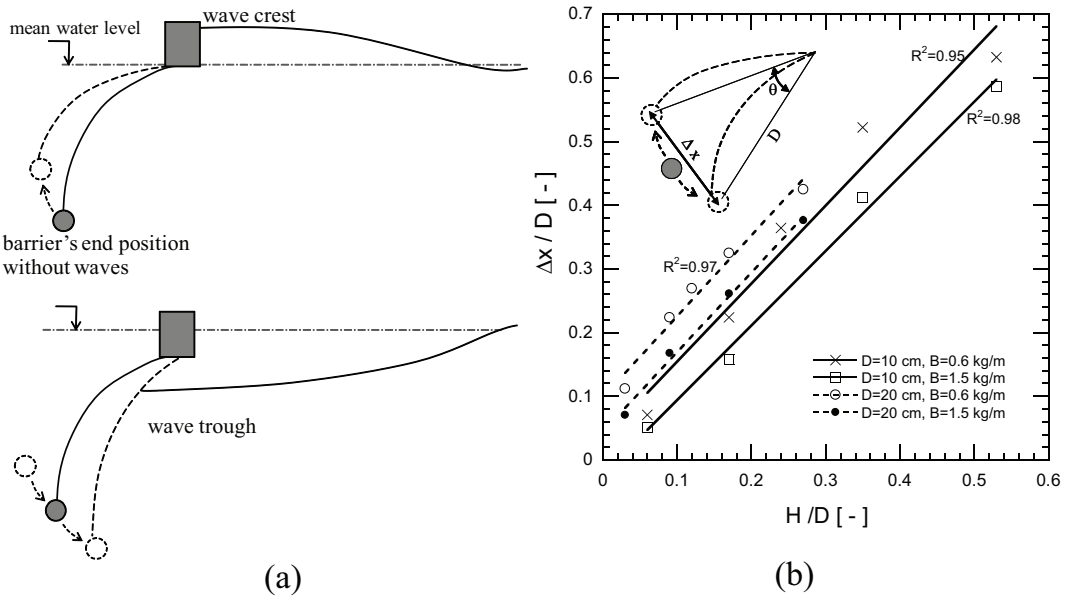

Figure 4.32: Barrier's roll due to wave effect: (a) Schematic drawing of the barriers deformation which goes far from the vertical position at wave crest and approaches the vertical position at wave trough; the barrier goes up and down but it cannot follow the water level freely; (b) effect of wave height on the roll angle ($\theta \approx \Delta x/D$); D and H are the barrier draft and wave height respectively; lines show linear fitting to data

trough, the low pressure caused the barrier to approach the vertical position (see Fig. 4.32a). The ratio of total displacement of the barrier end point, to the barrier draft, $\Delta x/D$, as a function of the ratio of wave height to the barrier draft, H/D, is shown in Fig. 4.32b. Data show a linear trend. The roll angle ($\approx \Delta x/D$) was less for a barrier with heavier ballast weight.

For a real case, the lateral motion of the barrier is also partially constrained, due to three-dimensional behavior of the barrier. Therefore, assuming that the barrier has the same degree of freedom as the present experimental conditions, it can be imagined that if the ratio of wave height to barrier draft is high (more than 0.5), the barrier can go through large rotations (displacement of end point more than 40% of the boom draft) due to wave effects.

4.2.6 Surging drainage failure

The surging drainage failure occurred when waves caused increase of oil layer thickness and interfacial wave height, and consequently led to occasional drainage under the barrier. A sequence of photos with 0.2 s interval, presented in Fig. 4.33 show this phenomenon. Velocities at which the surging drainage failure initiates are summarized for different experimental series and waves in Table 4.3.

It was previously shown by Fang (1999) that the influence of waves on velocity patterns is most profound near the bottom of the barrier, and large wave heights and frequencies increase the fluctuations in velocities near the bottom of the barrier, which triggered the oil to drain. As a result, the effect of waves became more crucial, when the oil layer thickness was more and the oil water interface was located closer to the bottom of the barrier.

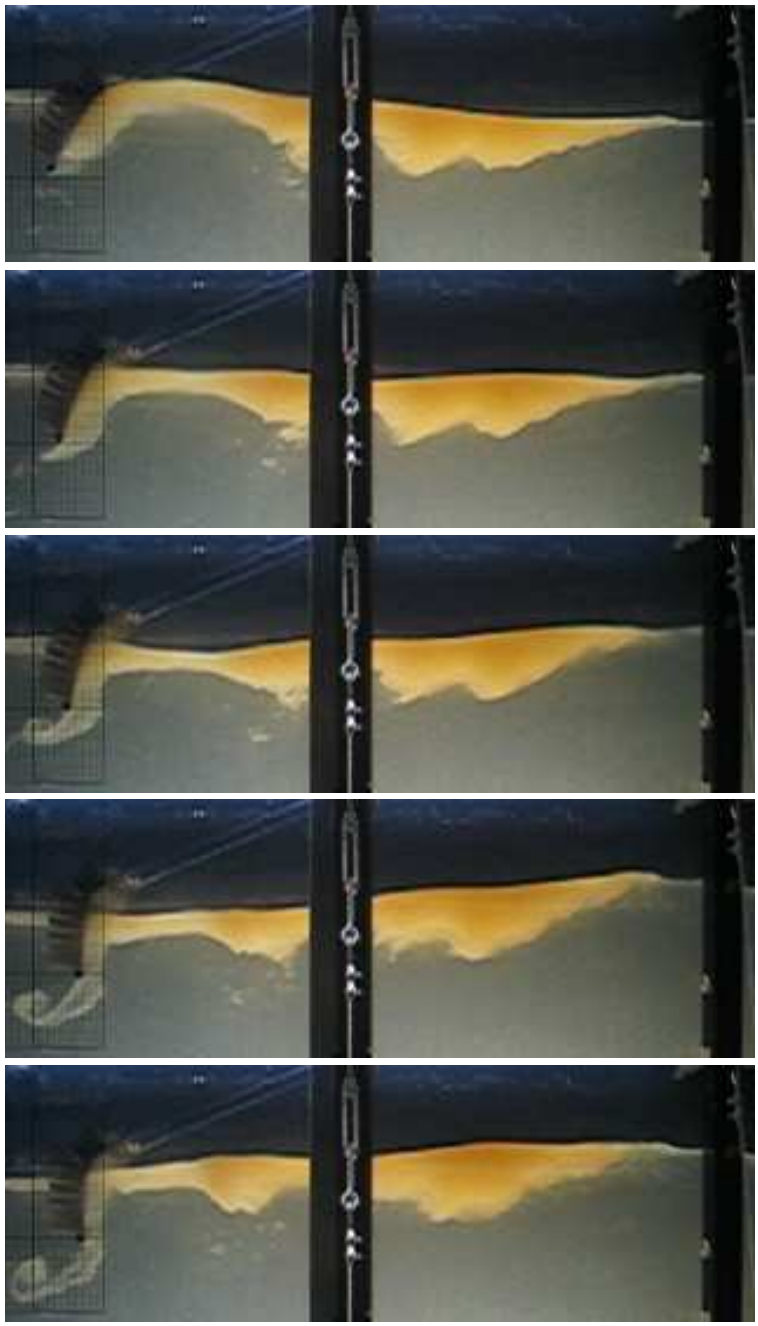

Figure 4.33: Surging drainage failure for a flexible barrier with 10 cm draft (SF5); mean flow velocity is 20 cm/s; photo sequence is 0.1 s

Table 4.3: Velocity at which surging drainage failure initiates for different experimental waves [cm/s]

	Test Series	Wave 1	Wave 2	Wave 3	Wave 4	Wave 5
V=20 lit/m	*SF1*	-	-	29	-	22
	SF2	-	31	-	26	24
	SR1	-	-	33	26	25
V=30 lit/m	*SF5*	-	30	27	24	20
	SF6	-	32	31	-	27

Therefore, a key factor in occurrence of drainage failure, is the oil thickness. The equivalent thickness, t_{eq}, previously defined in Eq. 4.1, was used to study the effect of the oil thickness and consequently oil volume. Another effective factor was the barrier depth. In fact, what provokes the drainage failure, is a high ratio of the equivalent thickness, t_{eq}, to the barrier draft, D. This ratio, called relative oil thickness, δ, is defined as:

$$\delta = \frac{t_{eq}}{D} \tag{4.11}$$

The higher δ, the lower needed wave height to initiate drainage failure. Fig. 4.34 illustrates the ratio of wave height to the barrier draft and the relative oil thickness, δ, for cases that the surging drainage failure was observed. A power curve was found to better fit the threshold values for δ, bellow which no failure occurs. As a results, the drainage happened when the wave height to draft ratio, H/D, was more than $0.0015\delta^{17/4}$. It can be seen that by increasing the relative oil thickness, δ, the drainage can happen for lower wave height to draft ratios.

Since the wave height to draft ratio, D/H, and relative oil thickness, δ, are both dimensionless parameters, the results can be directly used for prototype. As a rough estimation, for an oil layer thickness more than 25% barrier draft, the surging drainage can happen at relatively low wave height to barrier ratio, even for a waveheight equal to 10% the barrier draft.

4.2.7 Conclusions regarding experiments in presence of waves

Experiments in presence of waves were performed to evaluate the effect of waves on containment process, particularly for a flexible barrier. The observed failure mode was mainly entrainment failure. However, a surging drainage failure was observed to happen in case of more aggressive waves.

Effect of different wave parameters on initiation of failure was studied. Increase of wave height reduces the initial failure velocity. However, for small wave

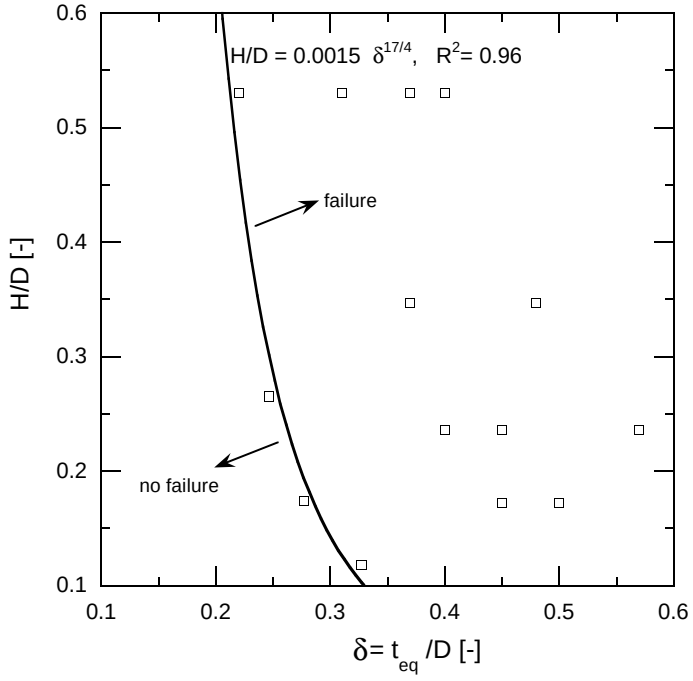

Figure 4.34: Wave height to barrier draft ratio, H/D, at which the surging drainage failure initiates versus relative oil thickness, δ; the points show the experimental results; the line shows the threshold value for relative oil thickness, δ

heights this reduction was not noticeable. For a prototype with dimensions 15 times the experimental barrier, the effect of wave height on initial failure reduction starts at a wave height of about 0.5 m.

By decreasing the wave period (increasing the frequency), interfacial waves became more aggressive and consequently failure initiated at a lower velocity as it can be seen in the figure. As for wave height variations, shorter and flexible barriers were more sensitive to variations of wave period. Applying the time scale, a critical wave period of about 6 s can be proposed for the prototype.

It was found that the wave steepness is a representative parameter to reveal the effect of waves, since it includes the effect of both wave height and period. For experiments with a rigid barrier, wave steepness less than 0.01 could not affect the failure initiation, whereas flexible barriers were more sensitive to presence of waves and even waves with steepness less than 0.01 cause a decrease in initial failure velocity.

The main parameters influencing the failure initiation were barrier draft and wave steepness. Consequently, Eq. 4.9 was proposed to predict the failure initiation, as a function of these two parameters.

Waves affect the slick length significantly by pushing the slick to accumulate behind the barrier. For stronger waves the decay rate was more significant at a certain velocity, and increases more rapidly by increasing the flow velocity. Eq. 4.10 was proposed to predict the slick length decay by increasing velocity for different waves.

Once the failure started, the effect of wave steepness on loss rate was found to be significant. The loss rate increased very rapidly by increasing the mean flow velocity for waves with higher steepness ($s > 0.01$).

Finally, a surging drainage failure was the subject of some investigations. This kind of failure could happen when the relative oil thickness to the draft was more than $0.0015\delta^{17/4}$. As a rough estimation for the prototype, for an oil layer thickness of more than 25% barrier draft, the surging drainage can occur at relatively low wave height to barrier ratio, even about 0.1.

4.3 Experiments with LECA

Experiments with LECA were aimed at qualitative investigations of the drainage failure. Amini et al. (2006a) studied the LECA containment by rigid and flexible barriers. Generally, suspensions have to be treated as non-Newtonian fluids, whose rheological properties are influenced by a lot of variables (Zapryanov and Tabakova, 1999). Therefore, a constant viscosity cannot be attributed to slick of LECA granules. However its general behavior at different flow velocities is qualitatively representative for drainage failure. Experimental conditions and procedure were explained in Sec. 3.7.2 and Sec. 3.8.2, respectively.

The results of experiments with LECA granules were also subject of a shear stress analysis. The idea was to use the Shields' modified curve for predicting the LECA granules movement. Shields' diagram is commonly used to define the initiation of motion in sediment transportation. Contrary to the case of sediment transportation, for LECA granules contained by a barrier, the particles are suspending over water surface. Therefore, some modifications had to be applied to Shield' diagram to become applicable for prediction of motion in LECA granules. The applied method as well as results are presented in Appendix C. It was shown that with appropriate assumptions, Shields' diagram is capable in predicting the movement initiation in suspended granules.

4.3.1 Slick geometry: Comparison with oil experiments

The LECA slick geometry during an experiment is shown schematically in Fig. 4.35. Firstly, LECA was poured on the water surface as a layer with uniform thickness (Fig. 4.35a). By increasing the flow velocity, a local thickening occurred and approached the barrier (Fig. 4.35b to d). At higher velocities, accumulated granules reached the barrier and the slick form a triangle behind it (Fig. 4.35e). This caused a continuous leakage of granulates whereby a partial failure occurred. After loosing some amount of LECA, the slick became stable under a parabolic shape and no more leakage happened (Fig. 4.35f). Increase of flow velocity would cause again a triangular shape (Fig. 4.35g) and the transport of material to the downstream side of the barrier. This process continued until the contained volume became too small that granules can not be picked up by the flowing water (Fig. 4.35h).

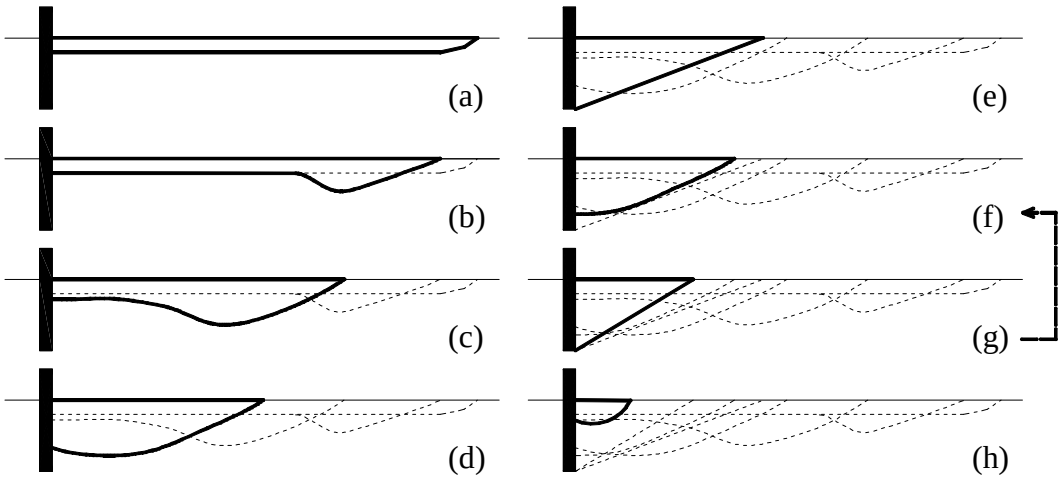

Figure 4.35: Evolution of LECA slick shape by increasing the flow velocity; Experiment starts at (a); at each step flow velocity increases until (g); the shape can alter several times from (f) to (g) and vice versa; finally a small volume of granules remains behind the barrier (h)

4.3.2 Effect of flexible barrier on containment efficiency

At a given flow velocity, a flexible barrier contained less material than a rigid one. In other words, the velocity at which the barrier fails to function was lower for a flexible barrier than for a rigid one.

Fig. 4.36 illustrates an example of a rigid and two flexible barriers with different ballast weights, containing a slick with 40 lit/m initial volume at three different velocities. The failure starts at a lower velocity for a flexible barrier than a rigid one. Accordingly, a flexible barrier with a lighter ballast starts to fail at a lower velocity than that with a heavier ballast.

Fig. 4.37 illustrates an overview of the results of all 18 experiments (see Table 3.8 for experimental conditions). As can be seen, the velocity at which 50 % of material passed the barrier was always higher for a rigid barrier than for a flexible one. For a flexible barrier, the capacity of the barrier to contain LECA granules decreased by reducing the ballast weight.

The loss percentage as a function of the mean flow velocity is shown for different tests in Fig. 4.38. Data show a logarithmic trend. Trend lines are continued to cross the x-axis. These crossing points can be representative for the velocity at which the failure initiated. For all the cases, the failure initiates at lowest velocity for the flaxible barrier with 0.6 kg/m ballast, then for the flexible barrier with 1.5 kg/m ballast, and finally for the rigid barrier. As it can be seen, the results are scattered and the LECA granules showed a rather random behavior.

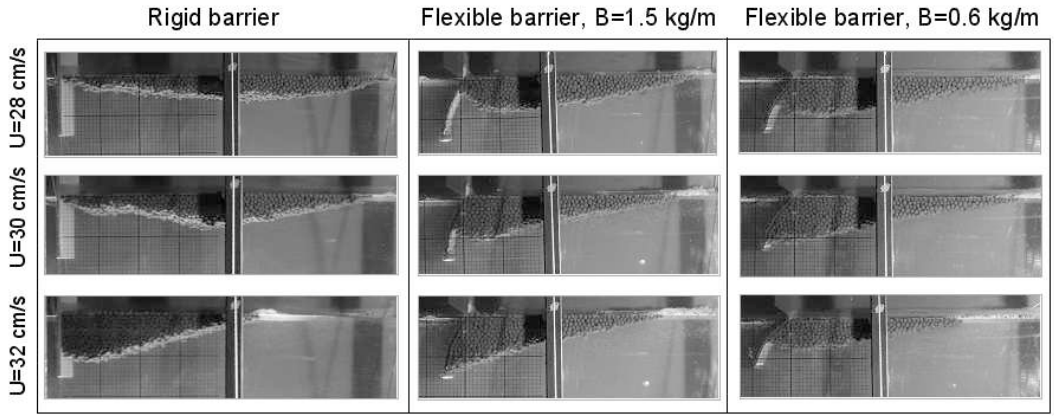

Figure 4.36: Experiments with similar conditions, for a rigid barrier (left column), a flexible barrier with 1.5 kg/m ballast weight (middle column) and a flexible barrier with a 0.6 kg/m ballast weight (right column); for all experiments the draft is 15 cm and the initial LECA volume is 40 lit/m; water is flowing from right to left

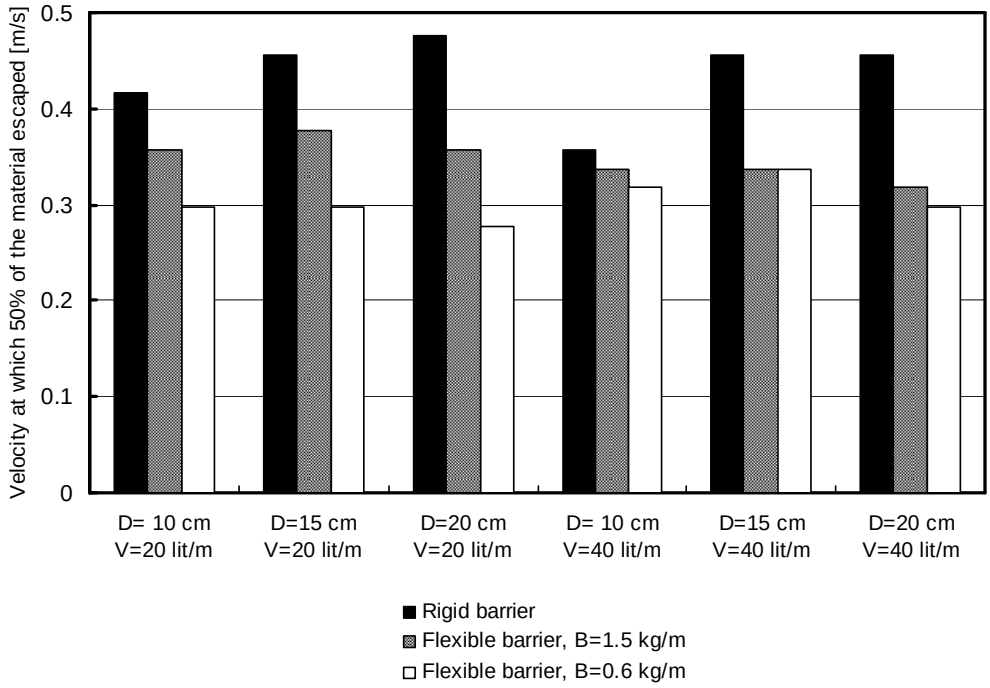

Figure 4.37: Velocity at which 50 % of LECA granules escaped, for barriers with different drafts, D, and initial volume of LECA, V

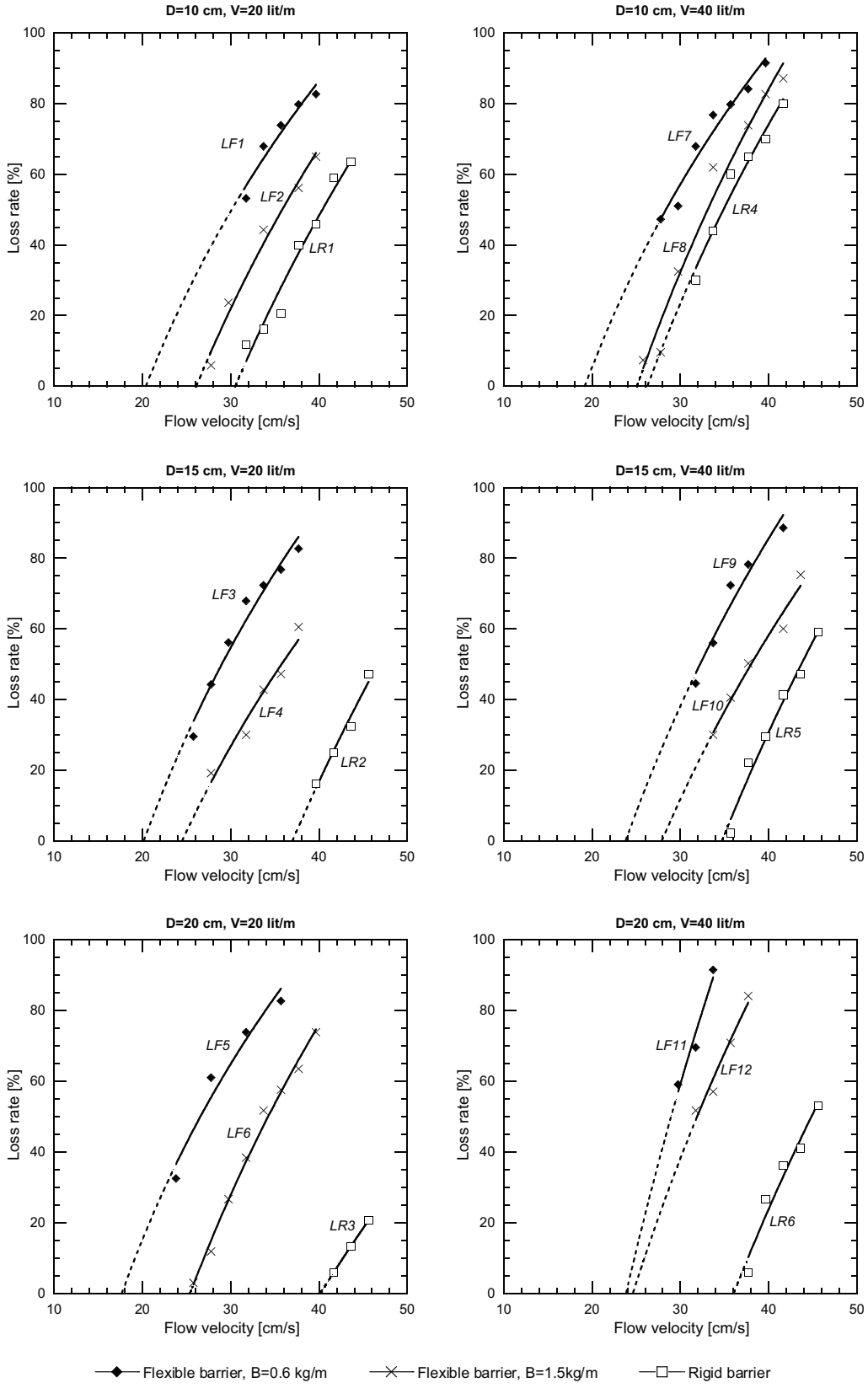

Figure 4.38: Percentage of loss as a function of mean flow velocity for rigid barriers (LR1 to LR6) and flexible ones (LF1 to LF12) (see Table 3.8); lines show logarithmic fitting to data

4.3.3 Effect of contained material on barrier deformation

The effect of contained material on the behavior of the barrier can be studied considering the deformed shape of the flexible barrier during experiments with different initial volumes of LECA.

Fig. 4.39 illustrates an example in which the barrier was subjected to a flow velocity of 0.3 m/s. The horizontal displacement from vertical position of the end point is shown for three different experiments, first without LECA, then with initial LECA volume of 20 lit/m and finally with initial LECA volume of 40 lit/m. It reveals that an increase of the contained volume decreases the deformation of the barrier up to 40%.

The reason of this change in deformation can be explained using the study presented by Lee and Kang (1997). They used the formula stated by Berteaux (1976) and showed that the deformed shape of a two-dimensional thin membrane subjected to a current of velocity, U, in the x-direction is determined by the following equation:

$$\Delta p(z) = \frac{B\frac{d^2\xi}{dz^2}}{(1+\xi^2)^{\frac{3}{2}}} \tag{4.12}$$

where $\Delta p(z)$ is the pressure difference between the front and the rear sides of the barrier, B is the ballast weight per unit length of barrier, $\xi(z)$ is the displacement of the skirt of draft D in the direction of x, and z is the vertical distance from the water surface. They also found from a dimensional analysis that $\xi(z)/D$ is a function of a non-dimensional parameter, α:

$$\alpha = \frac{\rho_w U^2 D}{2B} \tag{4.13}$$

which represents the ratio of the transverse dynamic pressure force to the vertical weight, B. $d(.)/dz$ denotes derivative of the parameter with respect to z. Fig. 4.40 shows the computed and experimental deformed shape of the barrier for different values of α. For some values of α, the shape of barrier subjected to pure water given by Eq. 4.12 is shown in solid lines. For the same values of α, the experimental deformed shape of a flexible barrier containing slicks with

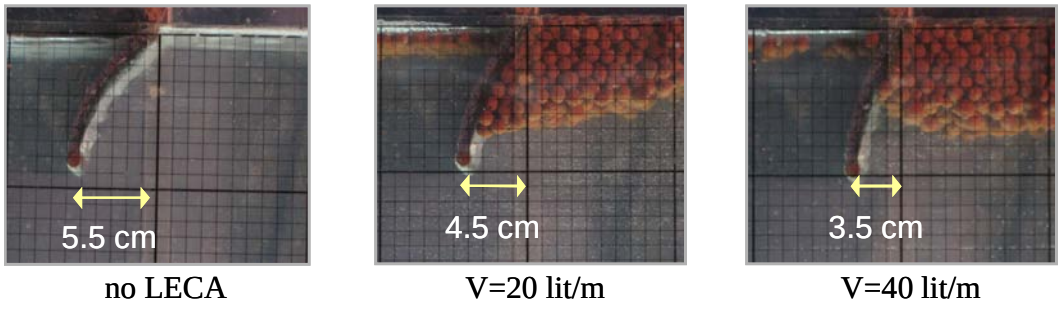

Figure 4.39: Displacement of the barrier from vertical position for a flexible barrier containing LECA slick with different volumes at mean velocity of 30 cm/s; water is flowing from right to left

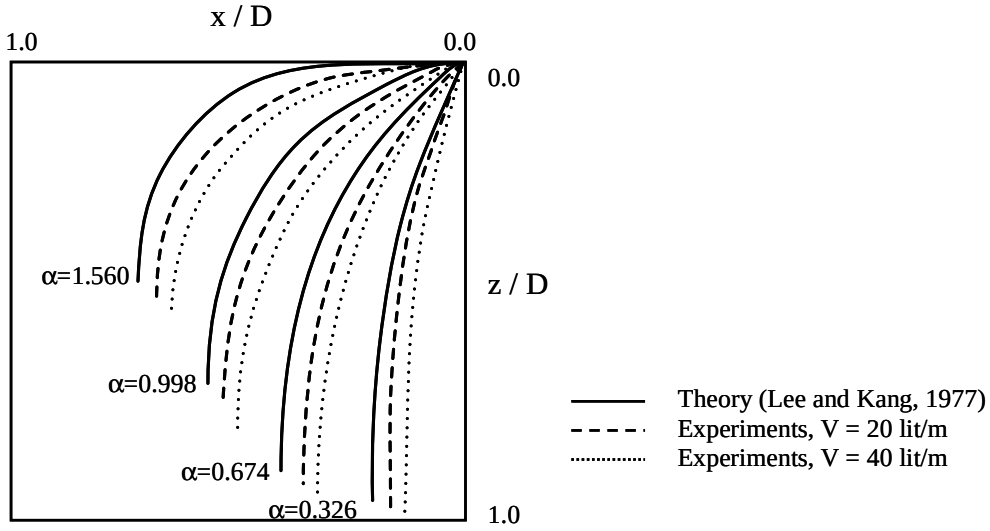

Figure 4.40: Deformed shape of flexible barrier; water is flowing from right to left

initial volume of 20 lit/m and 40 lit/m are represented by dashed and doted lines respectively. Presence of LECA granules behind the barrier could change the pressure field in the vicinity of the barrier and consequently the distributed load of p in Eq. 4.12. As a result, less pressure lead to a smaller deformation in the flexible barrier. In Sec. 5.5 the effect of contained material on the pressure field is investigated in more details.

4.3.4 Effect of barrier type on containment efficiency

Fig. 4.41 shows an example of experiment with a rigid barrier of 10 cm draft, compared to an experiment with the same conditions but with a flexible barrier of 15 cm draft. It is shown that even if the vertical submergence depth of a flexible barrier, called effective draft, D_e, was identical to draft of a rigid barrier, it contained less material than the rigid one.

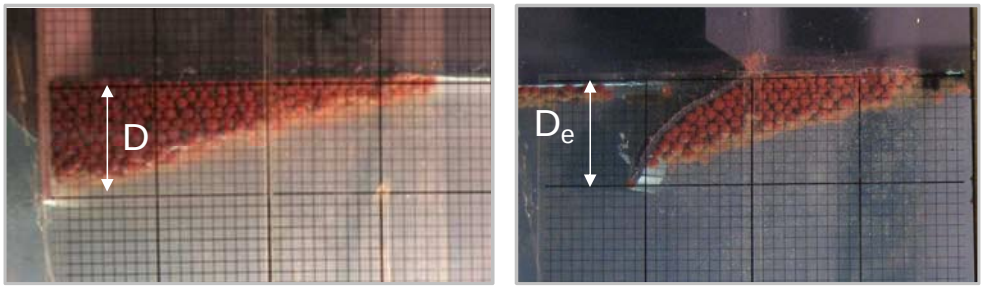

Figure 4.41: Effect of barrier type (rigid/flexible) on containment efficiency; experiment with 32 cm/s mean flow velocity; left: rigid barrier with 10 cm draft; right: flexible barrier with 15 cm draft and 10 cm effective draft; water is flowing from right to left

4.3.5 Conclusions regarding LECA experiments

LECA experiments provided qualitative understanding of drainage failure. In drainage failure, a barrier fails to function when the contained material accumulates upstream of the barrier and its depth exceed the barrier draft. Therefore, the occurrence and rate of drainage failure is highly dependent on the barrier characteristics and the effect of barrier flexibility is emphasized in case of drainage failure.

Accordingly, LECA experiments were important due to their role in investigating the effect of a flexible barrier. It was shown that at a certain velocity, a flexible barrier can contain less material than a rigid one. Additionally, the presence of contained material could influence the pressure distribution on the barrier and consequently its deformation. The obtained results concerning the barrier flexibility, highlighted the necessity of conducting experiments that are aimed to study drainage failure with flexible barriers, since it could modify the results significantly.

4.4 Analysis of velocity profiles and interface instabilities (UVP measurements)

As it was described in Sec. 3.4.4, UVP measurements were conducted for selected experimental conditions, i.e. experiments OR3, OR4, OF7, and OF8 (see Table 3.5), in order to study the velocity profiles in water and oil phases and detect their interface. Measurements were made for mean flow velocities of 15, 20 and 25 cm/s. The inclined measuring distance was 52 cm from water surface, i.e. vertical distance of 40 cm. The obtained results are discussed in the present section.

4.4.1 Velocity profiles in oil and water layers

The velocity profile at each measuring point, as an average over the measuring time (51 s), illustrates the horizontal component of flow velocity. An example of superposed horizontal velocity vectors and velocity fields for a rigid barrier with 10 cm draft (OR3) and mean flow velocity of 20 cm/s are presented in Fig. 4.42. Velocities are compared for the same experimental conditions with and without oil. The oil slick shape is also added to the figure for the experiment with oil. Oil slick thickness was measured visually during the experiments and also it has been derived from the detected interface by UVP measurements as will be discussed in Sec. 4.4.3. Appendix D includes measurement results of all test.

To achieve realistic conclusions, the laboratory effects should be considered before going for further analysis.

1. Despite all efforts for providing a uniform velocity in the flume, the flow was sheared and not completely uniform. The measured velocities in the upper part were about 20% higher compared to the mean flow velocity (Fig. 4.42a).

2. The measured velocity profiles at low flow velocities were disturbed due to the ultrasonic reflection at the oil-water interface. Fig. 4.43a illustrates this phenomenon for experiment OR3 at mean flow velocity of 15 cm/s. As it is shown, the reflect of ultrasonic pulse lead to a multiple echo in oil layer. At lower velocities, where oil surface is not yet fluctuating, this effect is amplified and influenced the measured profiles noticeably (Fig. 4.43b). Hence for achieving realistic results a modified profile, as shown in Fig. 4.43c, should be considered.

3. The velocity magnitude was calculated based on the speed of sound in water ($c_w = 1483\ m/s$). Principally, the velocity in oil should be modified by being divided to the speed of sound in oil which is $c_o = 1445\ m/s$. However, since the difference is not considerable, the error was neglected.

Regarding the above mentioned points, and considering the results shown in the Appendix D, different zones in Fig. 4.42 were studied and following points were extracted:

1. Presence of oil over water surface influences the horizontal velocity field considerably. This influence becomes more significant at higher flow velocities.

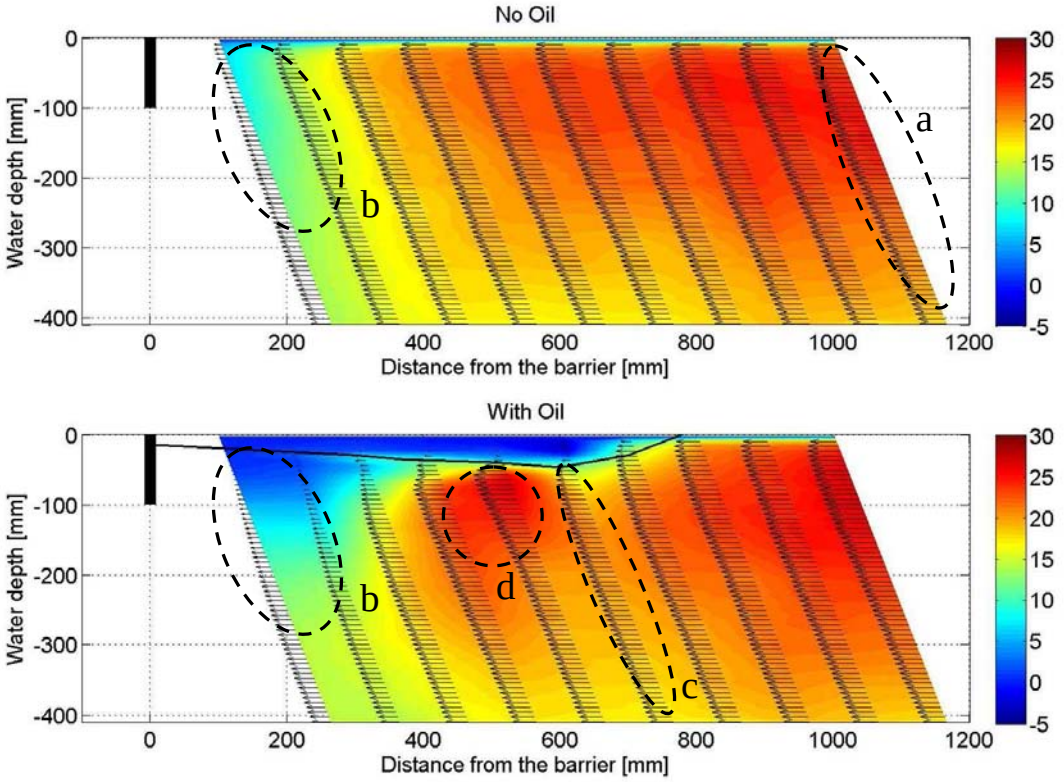

Figure 4.42: Example of horizontal velocity vectors and velocity field for a rigid barrier with 10 cm draft and mean flow velocity of 20 cm/s; velocities are presented in cm/s

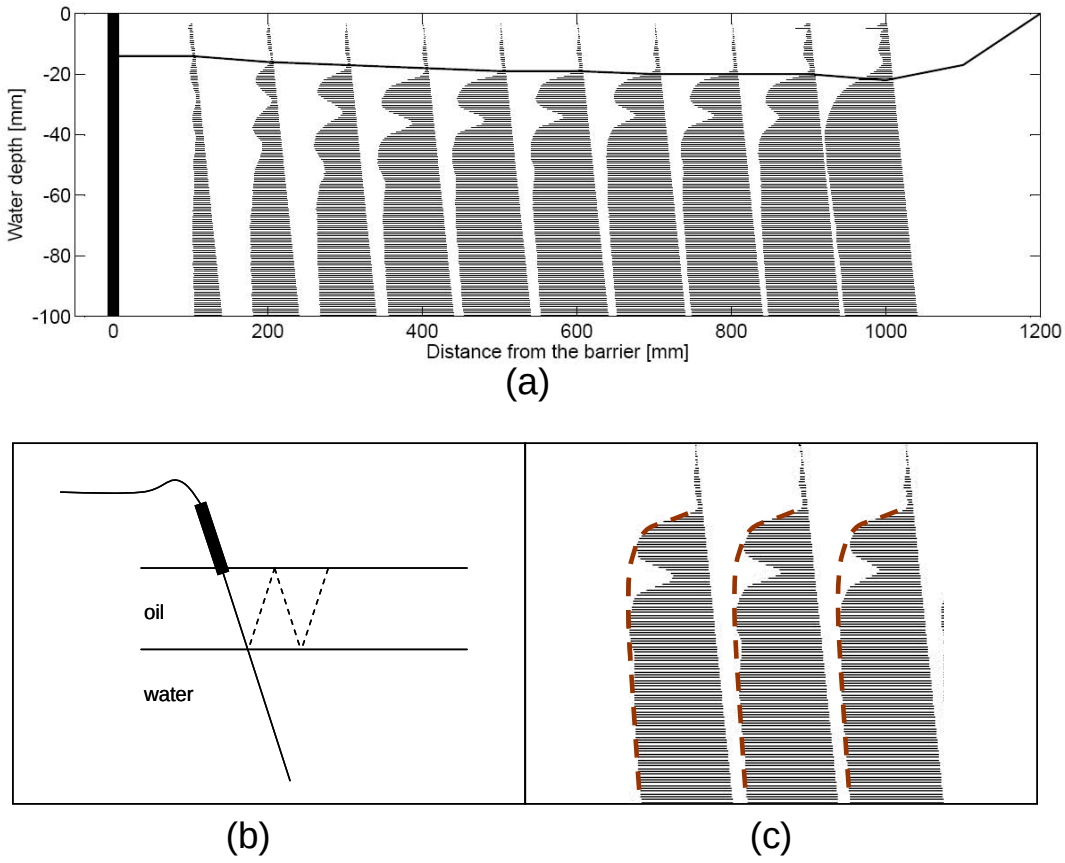

Figure 4.43: Laboratory effects on velocity profiles due to multiple echo (for experiment OR3): (a) disturbed velocity profiles by effect of multiple echo; (b) schematic explanation for the problem; (c) modified profiles in dashed line

2. At near boom region, where the vertical velocity increases, the horizontal velocity diminishes. The diminution is seen to be more significant in case of experiments with oil (Fig. 4.42b). The reason can be explained due to the effect of headwave, which causes the streamlines to detach from the surface earlier.

3. In the vicinity of the headwave, the horizontal component of velocity becomes weak, as the vertical component should increase (Fig. 4.42c).

4. The maximum value of horizontal velocity was observed to happen after the headwave (Fig. 4.42d). This phenomenon is quite similar to the case of a gravity current in a sheared ambient flow and is discussed in detail in Sec. 4.4.2.

5. Velocity field in the vicinity of the boom (Fig. 4.42b) was influenced by the barrier draft. However, it was less influenced by the barrier type (rigid or flexible) and even less by the ballast weight.

4.4.2 Analogy and difference of oil slick with gravity currents

Many investigators, amongst them Wicks (1969) and more recently Simpson (1997), have noticed the analogy between the headwave region of a contained oil slick and the frontal part of a gravity current turned upside down. However, Milgram and Van Houten (1978) have described that the headwave in contained oil slicks substantially differs from that of gravity currents. They implied that there are two important differences between the oil layer and the gravity current: the existence of a free surface above the oil, and a shear stress at the oil-water interface. This fact is the subject of detailed discussions in this section. The characteristics of gravity currents presented by several research studies are explained first. Then a comparison between gravity currents with contained slick headwave is made.

In an early study, Von Karman (1940) proposed a theoretical model for head of density currents in which the angle between the bottom and the front interface is about 60°. Based on this model, Benjamin (1968) continued to study the phenomenon and postulated that headwave rises to a bit more the mean height of the interface and on the rearward side of which there is a highly turbulent zone suggestive of some kind of wave breaking process. In the model, he proposed a nose shape part at the front of the head. Simpson (1972) studied the effect of the lower boundary layer and stipulated that, within the head, the lower boundary controls the detailed form of the structure. An empirical dependence of nose height on Reynolds number was also established.

More focused on mixing, Britter and Simpson (1978) suggested that this mixing occur through Kelvin-Helmholtz instability. Later on, Simpson and Britter (1979) found the motion behind the head of a gravity current as a complex three dimensional flow which is result of gravitational and shear instabilities at the head. To verify the effect of velocity profile (sheared or uniform) on gravity currents, Xu (1992) developed a two-phase model. It was confirmed that the depth of the density current and the vertically averaged frontal slope increase with the positive inflow shear. He also postulated that the turbulence at the head is due to a hydraulic jump. Contrary to the suggestion of Von Karman (1940), Xu and Moncrieff (1994) implied that when the inflow shear is sufficiently strong, the interface will become locally steeper than 60° at middepth of the density current.

Recently, Shin et al. (2004) investigated the gravity currents produced by lock exchange. They studied a surface gravity current, with fresh water as the less dense fluid and a solution of sodium chloride as the denser fluid (Fig. 4.44). The gravity current had a deep head with billows and mixing occurred at the rearward side. Immediately at the rear of the head the gravity current was shallower than both the head and also the current further behind. The mixing region was confined to within one or two head heights of the front, after which the edge of the current is stable and there is no appreciable mixing. They proposed a front/headwave Froude number of 1 rather that the previously accepted value of $\sqrt{2}$. This number is defined as $F_h = U_c/\sqrt{g\ \Delta\ t_h}$ in Eq. 4.7, where U_c

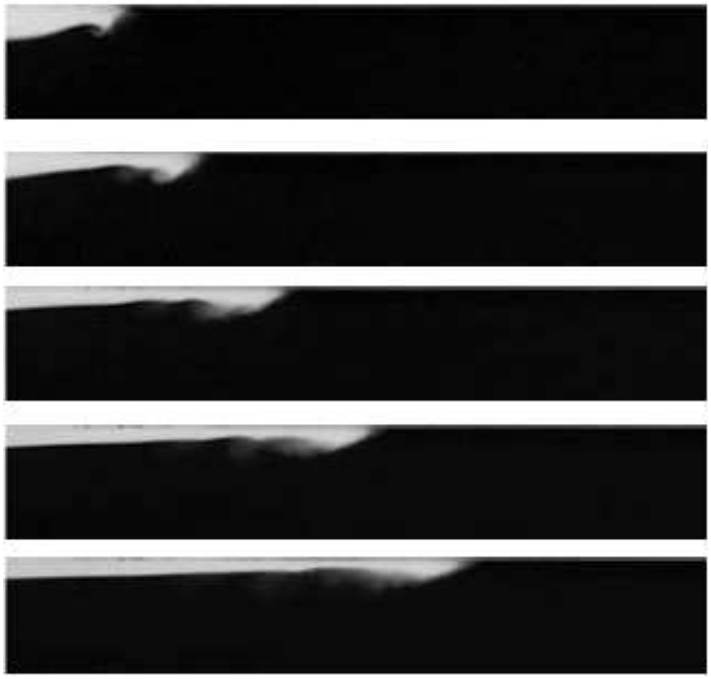

Figure 4.44: A surface gravity current produced by lock exchange; photos are taken at 1 s intervals, (Shin et al., 2004)

is the gravity current velocity (or oil internal velocity in present study) and t_h is the thickness of headwave.

Apart from geometrical analogy, a similar aspect in oil slick and gravity currents is the fact that the horizontal velocity component reaches its maximum value after the headwave or current front. Fig. 4.45a illustrates a schematic representation of a model of gravity current with a shear inflow presented by Xu (1992). In his model, the energy loss and generation of negative vorticity, that can exist due to dissipation by breaking of the interface and turbulence generation, was taken into account in the formulations for the outflow. In the present study with oil, similar to the Xu (1992) model, the ambient flow is sheared (Fig. 4.45b). Hence, the same zone with maximum velocity was observed at rearward side of the headwave (zone d in Fig. 4.42).

The dissimilarities between slick headwave and frontal zone of a gravity current are listed below:

- The angle between the bottom and front interface is 60° or more in the case of a gravity current, but in the present research the measured angle was about 45°.

- A gravity current has a nose at its front, which was not the case in an oil slick. This can be explained due to effect of lower boundary friction for a gravity current, that does not exist for an oil slick with free surface. It can be imagined that in presence of wind or surface contamination a nose forms at headwave of an oil slick.

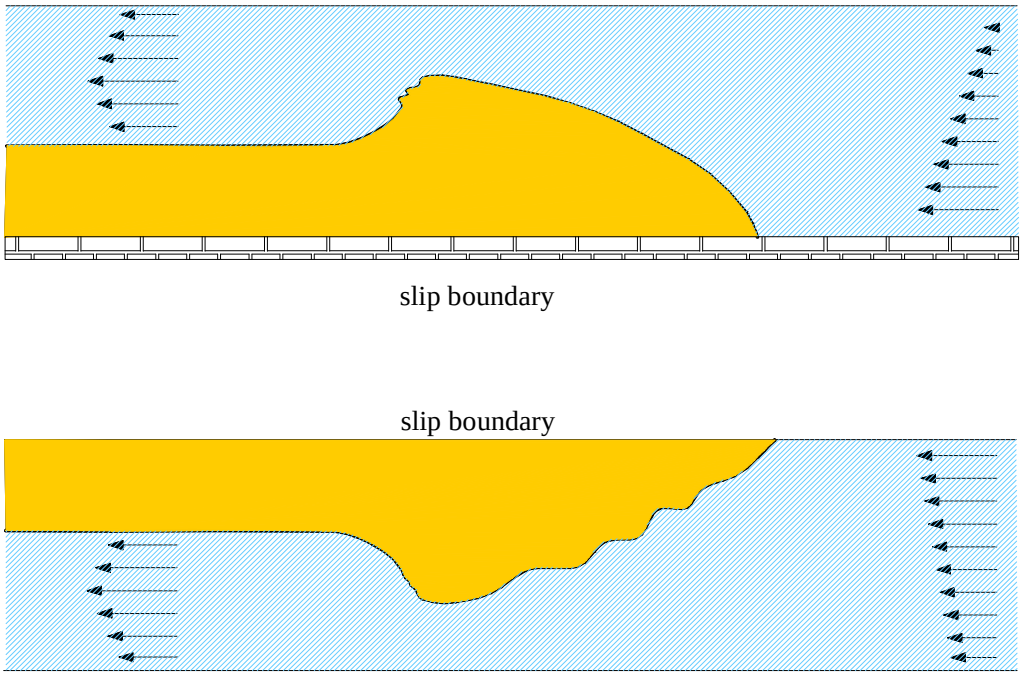

Figure 4.45: Comparison of head in gravity currents and observed headwave in the present study; dashed line shows the zone with maximum horizontal velocity after the head: (a) model presented by Xu (1992) for a gravity current in shear ambient flow; (b) observed headwave of oil slick with fluctuations in the front side

– The front Froude number is proposed to be 1 to $\sqrt{2}$ for a gravity current (Shin et al., 2004), which means that the head is super-critical, and the mixing at the rearward side is due to hydraulic jump. However the headwave Froude number was of a lower order for oil slick (0.15 to 0.25) and the head was sub-critical. The breaking interfacial waves were due to Kelvin-Helmholtz instability.

– The flow in a contained oil slick was laminar ($Re \approx 50$), contrary to gravity currents which are turbulent flows.

– For gravity currents, billows are formed on the rear side of the head, while in an oil headwave, they were seen forming at frontward side (Fig. 4.46).

– Oil and water formed an inmiscible interface, that caused separated phases, whereas in gravity currents, the interface is miscible and the fluids can mix together easier, and make a mixture at rearward side of the head.

As a results, it can be concluded that even there are similarities between gravity currents and headwave of oil slicks, the phenomena are quite different.

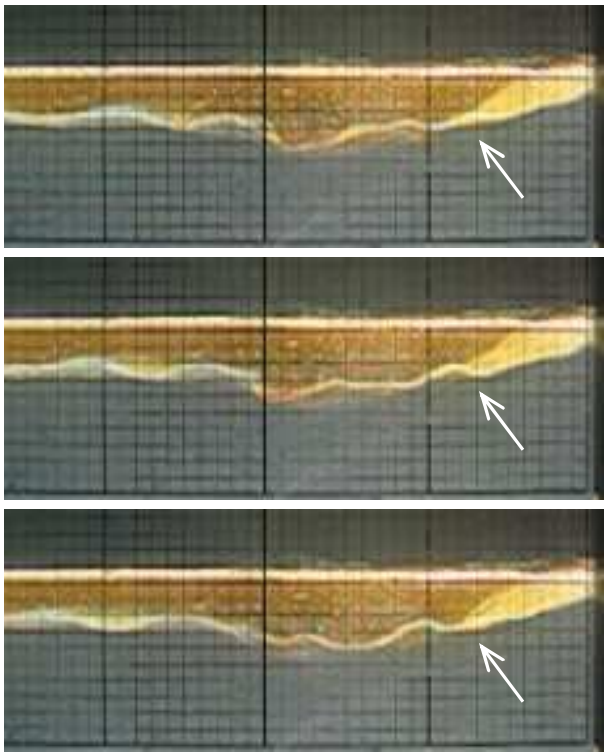

Figure 4.46: Interfacial waves forming at frontward side of the oil slick headwave, sequence of pictures is 0.4 s

4.4.3 Interface detection and velocity profile in oil and water layers

Investigation of interfacial fluctuations and detecting the position of the oil-water interface requires a precise measure. UVP measurements were for the first time applied to detect oil-water interface by Amini et al. (2006b). The idea is that the ultrasonic echo has its maximum value at oil-water interface. To verify this idea, the oscillations at the rearward side of the slick headwave, where interfacial waves were more regular, were studied. At other parts of the slick the local reflection of waves provoked irregularity in fluctuations. The power spectrum for the points in the vicinity of the observed interface were studied. Power spectrum gives the portion of signal power falling within certain frequency and its peak corresponds to most occurred frequency. Fig. 4.47 illustrates the power spectrum in the vicinity of an observed interfacial point, with its peak being at the frequency of 2.62 Hz. In that case the location of interface was visualized to vary between 3.2 to 4.8 cm from the UVP transducer. Hence, a spatial average of the power spectrum over the region where oscillation was observed, was taken. This averaging might cancel the random noise appearing in the spectrum and more clear peak structure can be obtained. The average value for the spectrum, corresponding to points located in the oscillation amplitude, was 2.53 Hz, which mean that the period of oscillations was about 0.4 s. The sequential photos of the same experiment showed the period of about 0.4 s for interfacial wave at the considered point (see Fig. 4.46).

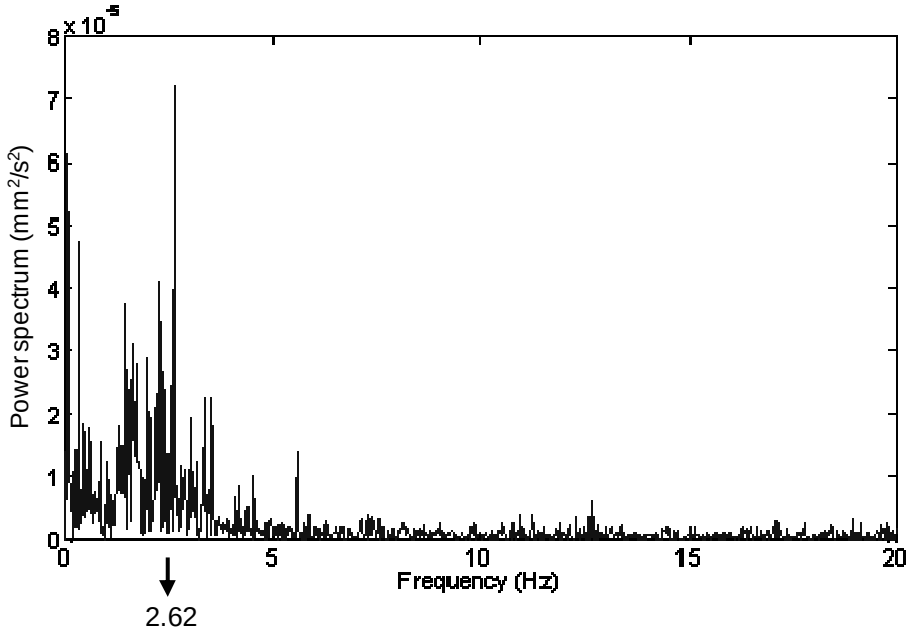

Figure 4.47: Power spectrum in the vicinity of the observed interface

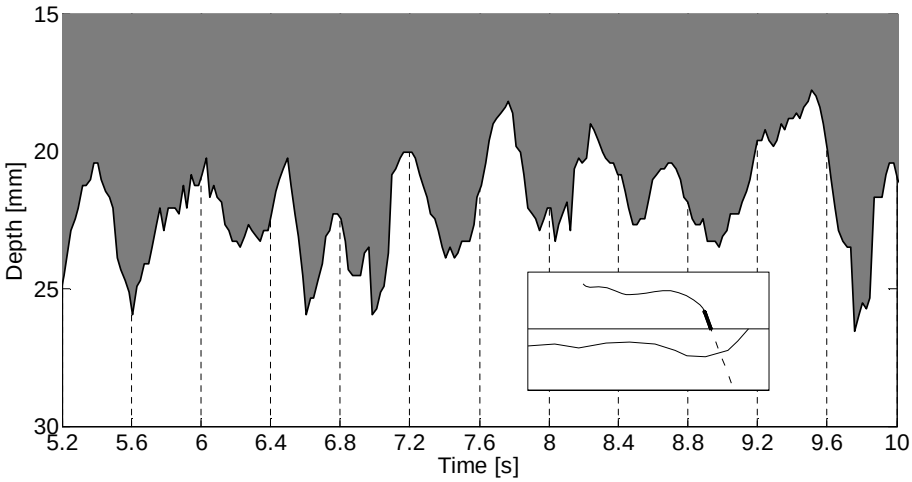

Figure 4.48: Oil-water interfacial derived from echo intensity at rearward side of the slick headwave

Accordingly, the oil-water interface could be detected by finding the location of the maximum echo intensity. Fig. 4.48 shows the derived oil-water interface for a duration of about 5 s. The period of 0.4 s (frequency of 2.5 Hz) seems to match appropriately as the period of fluctuations. The values were smoothened with moving average method in order to remove the noise.

The interface obtained from ultrasonic echo, can also be used for measuring oil depth. As an example Fig. 4.49 illustrates the oil-water oscillations at points with different distance from the barrier for the experiment OR3 at mean flow velocity of 25 cm/s. The oil thickness at each point can be derived from the

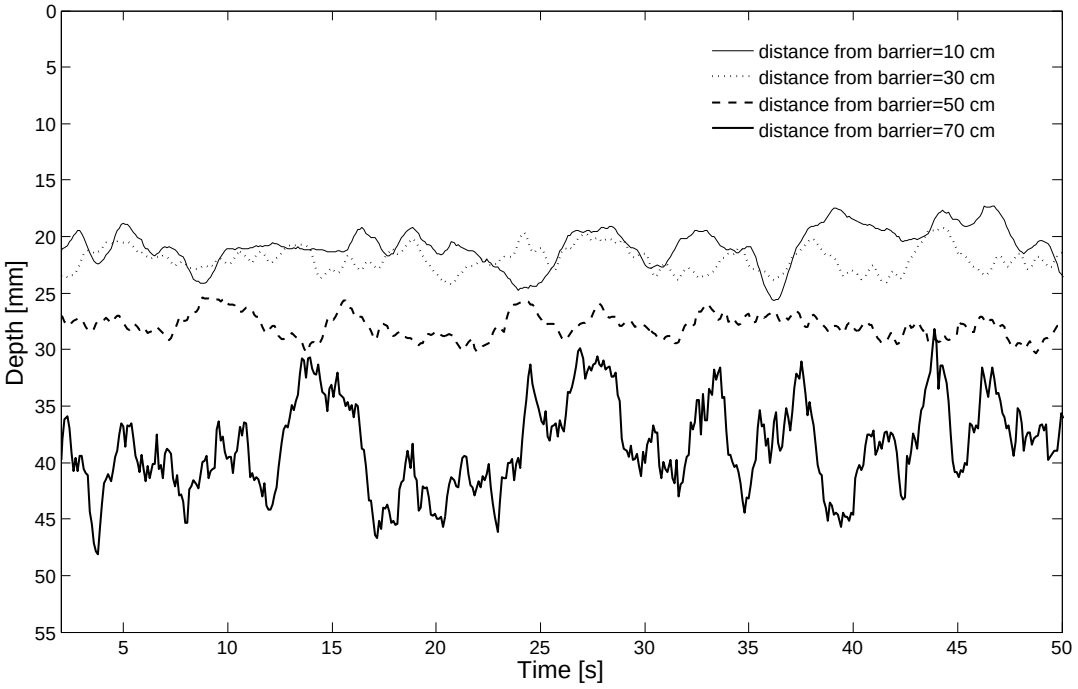

Figure 4.49: Oil thickness at points of different distance from the barrier; experiment with a rigid barrier of 20 cm draft at mean flow velocity of 25 cm/s

average value of interface position.

Once the interface location is found, the velocity profiles in oil and water phases can be obtained separately. To obtain the velocity profile in oil and water, the interface position is detected during a certain time and the measured instantaneous velocity profile is shifted to achieve a constant position of interface. The mean values of velocity in oil and water phases are then calculated. As it can be seen in Fig. 4.50 the boundary layer locates in the water since it is less viscose and energy dissipation is less.

4.4.4 Interface instability

The classical problem of Kelvin Helmholtz (KH) instability is described in various text books (e. g., Chandrasekhar, 1961; Drazin and Reid, 2004). KH instability can occur when velocity shear is present within a continuous fluid or when there is sufficient velocity difference across the interface between two fluids. A well known example is the generation of waves on oceans by the wind. In general, instability occurs when there is some disturbance of the equilibrium of the external forces, inertia and viscous stresses, in a fluid. External forces of interest are buoyancy in fluids of different density, surface tension, magnetohydrdynamic forces, etc.

The waves traveling along the interface between two fluids, whose dynamics are dominated by the effects of surface tension, are called as capillary waves. The wavelength of such waves was previously defined as $\lambda_c = 2\pi\sqrt{\sigma_{ow}/g(\rho_w - \rho_o)}$ in Eq. 2.3, where σ_{ow} is the oil-water interfacial tension. Leibovich (1976) and Delvigne (1991) attributed the same wave length to KH instabilities at oil-water

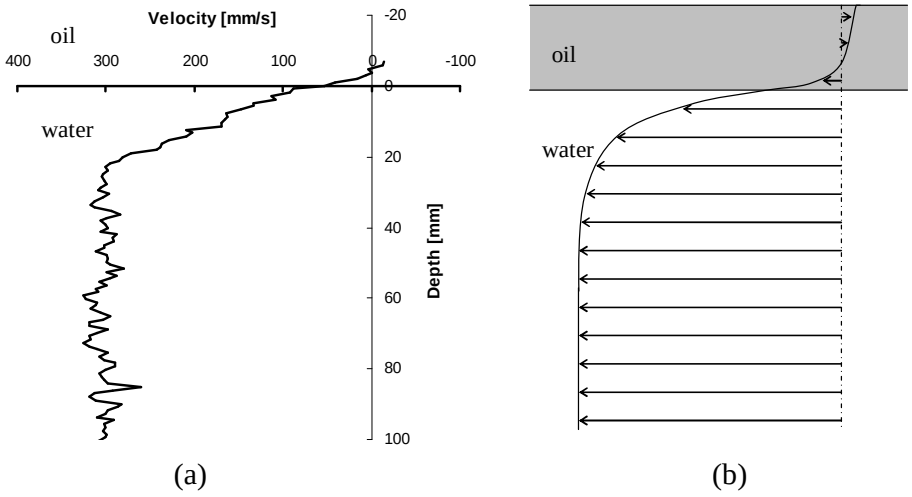

Figure 4.50: Velocity profile in oil and water phases: (a) measured profile, averaged over 100 profiles; (b) proposed profile in oil-water two-phase fluid

interface.

Replacing the interfacial tension between water and rapeseed oil (30 mN/m) in the latter equation, the value of 3.7 cm is achieved for the interfacial wave lengths. As it can be seen in Fig. 4.46, observed wavelength during the present experiments was about 4 cm which is in a good agreement with the calculated capillary wavelength.

4.4.5 Conclusions regarding UVP measurements

UVP measurements provided precise results of horizontal velocity in oil-water two-phase fluid. The obtained results were useful to evaluate the physics of oil slick, particularly the headwave region. The characteristic of the headwave at upstream end of the oil slick were compared, in detail, to those of a gravity current. It was concluded that despite geometrical similarities, these two phenomena are quite different.

Comparison between results of measurements with and without oil slick confirmed the noticeable influence of oil on velocity field behind the barrier.

The capability of UVP measurements in detecting the oil-water interface was approved and it was shown that the location of maximum ultrasonic echo intensity can be representative for the interface. The velocity profiles in each phase were derived and it was revealed that the boundary layer is located in the water, since it is less viscose and the energy dissipation is less in water.

4.5 Velocity field behind a barrier (LSPIV measurements)

4.5.1 Velocity measurements

The velocity fields behind the barriers with different configuration were investigated by means of LSPIV measurements as it was explained in Sec. 3.4.4. Measurements were carried out for rigid and flexible barriers with 10 and 20 cm draft at a mean flow velocity of 20 ∓ 1 cm/s. The measured velocity fields and streamlines are presented in Appendix E. An example is shown in Fig. 4.51 to Fig. 4.53 for flow passing a rigid barrier with 20 cm draft. Fig. 4.51 illustrates the velocity field and vectors, where Fig. 4.52 and Fig. 4.53 show streamlines and horizontal and vertical components of the flow velocity respectively.

Before analyzing the results, the laboratory effects should be considered:

1. As it can be seen in Fig. 4.51, the two reinforced bars located in the observation window disturbed the measurement in two bands. Although interpolation was made to obtain missing data, lack of data for these two regions caused local inaccuracy in results.

2. In the left bottom of the observing window, there was lack of appropriate illumination, thus a shadow zone could be observed in the results at this area (Fig. 4.51a).

3. Presence of the barrier caused some tracer particles to accumulate behind it (Fig. 4.51b) and to prevent them follow the flow. As a result, the obtained velocity for that region is underestimated.

4. As it was shown by UVP measurements, despite efforts for achieving a uniform flow, the flow is not completely uniform (Fig. 4.51c).

5. To find an appropriate seeding particle, several materials were examined (see Table 3.2) and the Grilon AZ 3 particle was selected as the best. However, seeding particles did not have the same size, which made some part of them to ascend to the surface (Fig. 4.52a) and another part to descend to the bottom (Fig. 4.52b) and lead to incorrect patterns in streamlines.

Despite above mentioned problems and shortcomings, LSPIV measurements provided interesting results about velocity field and stream lines in the vicinity of the barrier:

1. As it is shown in Fig. 4.51d, the flow accelerated beneath the barrier. For the rigid barrier with 10 cm draft the influenced water depth is about seven times the barrier draft.

2. The maximum velocity measured beneath the barrier (d in Fig. 4.51) had a higher velocity in case of a rigid barrier than a flexible one. The values of velocity magnitude for each barrier were used to calibrate the numerical model, as it is explained in Sec. 5.3.

3. The turbulence wake downstream of the barrier was partially captured. The wake is deeper for rigid barriers in comparison to flexible ones.

4. At the upstream side of the barrier, the barrier showed to have influence on the stream lines in the close proximity to it (Fig. 4.52c). The influenced area was extended about one time the barrier draft on the upstream for the rigid barriers and even less for flexible ones. This explains the reason of the independency of the entrainment failure velocity to the barrier draft or type as it was discussed in Sec. 4.1. Moreover, it describes why the slick length was being slightly influenced by the barriers draft or type.

5. Horizontal velocity field illustrated in Fig. 4.53 shows similar velocity distribution in the vicinity of the barrier, to the results of UVP measurements. At upstream of the barrier flow accelerates in the vertical direction to pass the barrier and makes the horizontal component to decrease

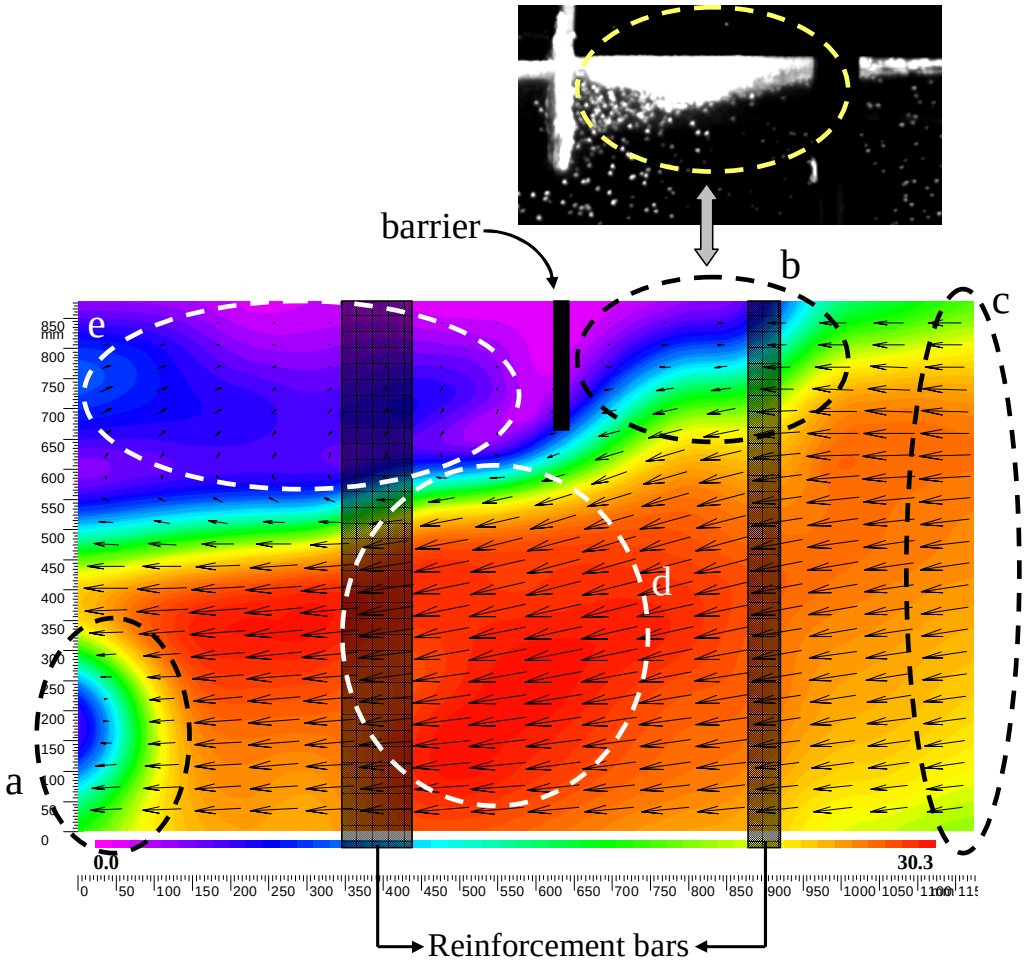

Figure 4.51: Contours of velocity magnitude and velocity vectors derived from LSPIV measurements in the vicinity of a barrier with 20 cm draft and mean flow velocity of 20 cm/s; dark bands show the location of reinforcement bars of the laboratory flume ; velocity magnitude is presented in cm/s

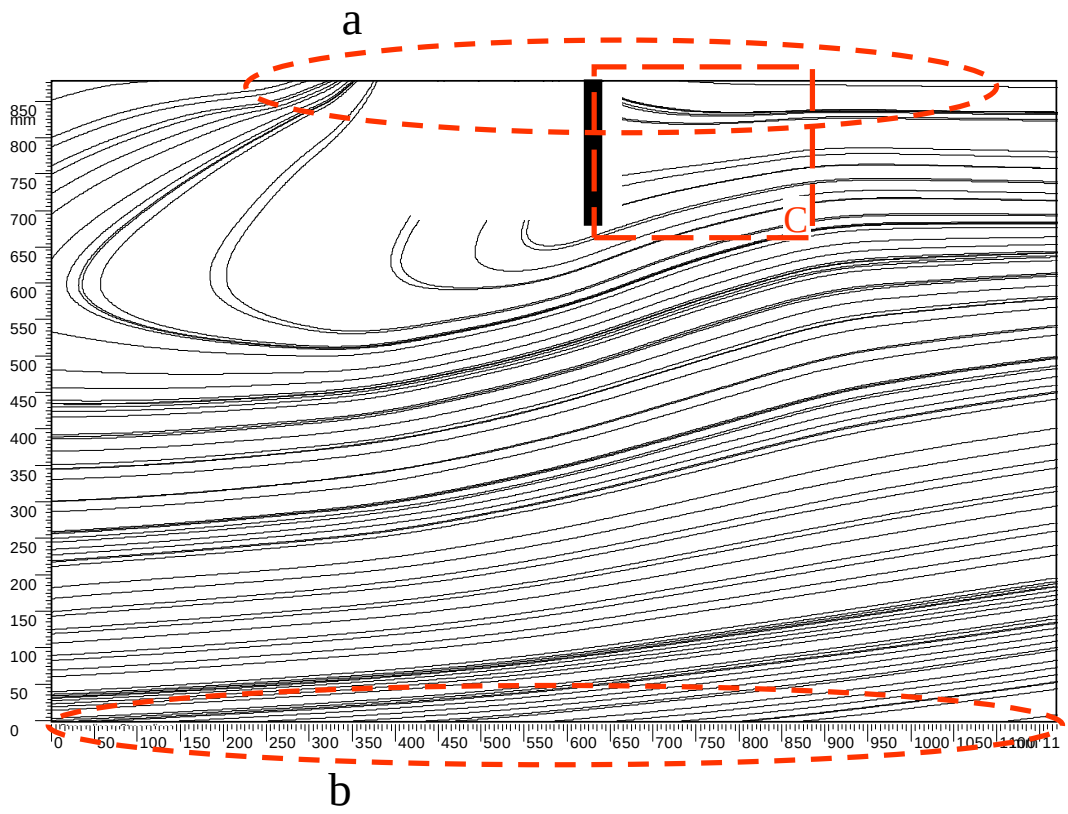

Figure 4.52: Streamlines derived from LSPIV measurements in the vicinity of a barrier with 20 cm draft and mean flow velocity of 20 cm/s

(Fig. 4.53a). In deeper parts the horizontal velocity augments due to narrowing effect of the barrier (Fig. 4.53b).

6. The flow passing the barrier made high vertical velocities beneath the barrier near the bottom of it on upstream side (Fig. 4.53c), which could take the detached oil droplets with.

4.5.2 LSPIV measurements in presence of waves

One of the foreseen goals of LSPIV measurements was to investigate the velocity field in the vicinity of the barrier in presence of waves. Eq. 4.14 was used in order to have an evaluation of the tracer capacity (Raffel et al., 1998). It allows the calculation of the time which is needed for the tracer from the moment a change is made in the flow velocity to the moment that its velocity, $U_{tr}(t)$, is equal to flow velocity, U:

$$U_{tr}(t) = U[1 - \exp(-\frac{t}{\kappa})] \tag{4.14}$$

where κ is the particle's relaxation time or tracer response time, and is obtained from Eq. 4.15:

$$\kappa = d_{tr}^2 \frac{\rho_{tr}}{18\mu} \tag{4.15}$$

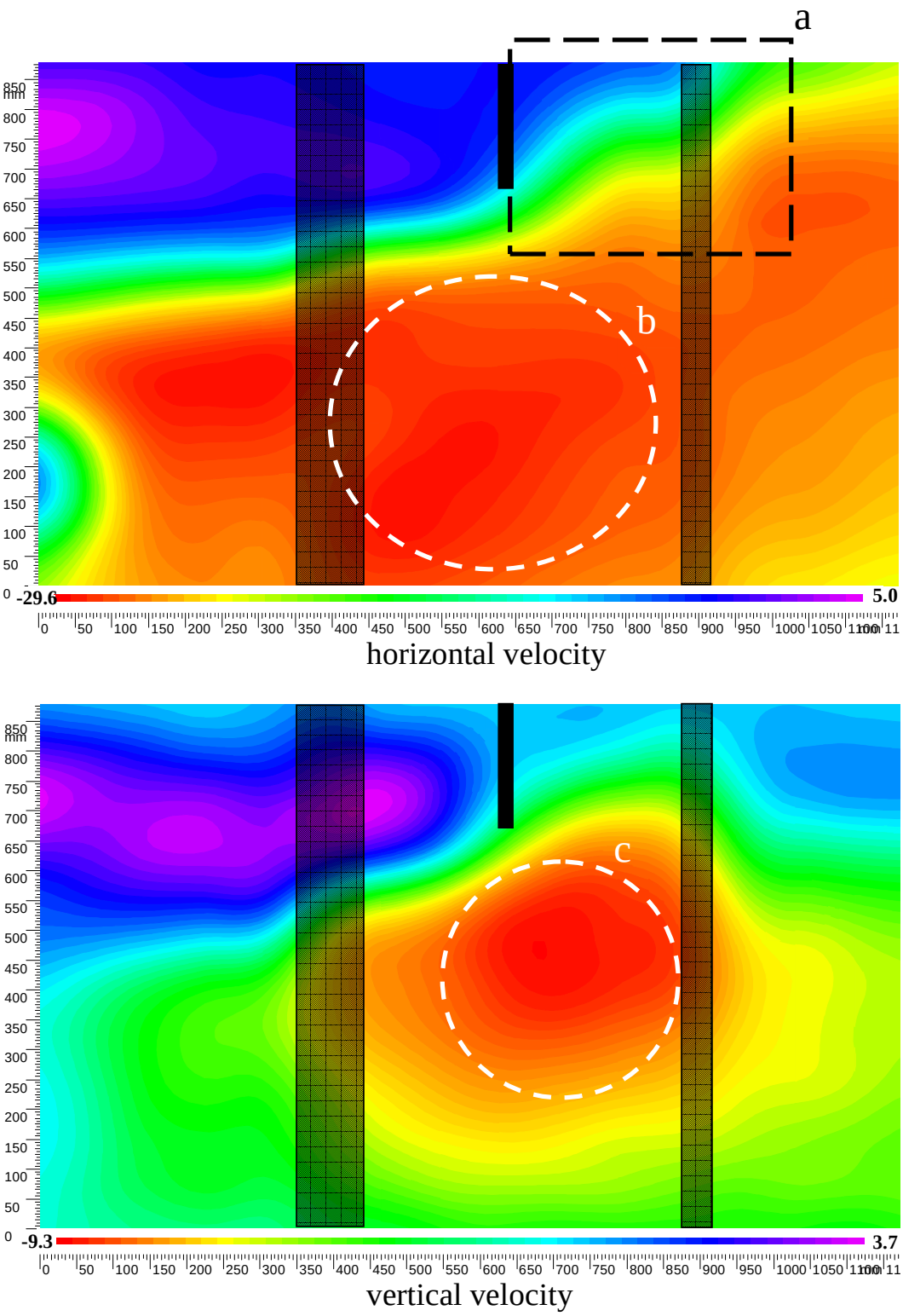

Figure 4.53: Contours of horizontal (top) and vertical (bottom) velocity components in the vicinity of a barrier with 20 cm draft and mean flow velocity of 20 cm/s; dark bands show the location of reinforcement bars ; velocity magnitude is presented in cm/s

In this latter equation d_{tr} and ρ_{tr} stand for tracer diameter and density respectively, and μ for the dynamic viscosity of the flowing fluid.

Calculations showed that the time required by the tracer to follow the flow is about 6 s which is more than three times the maximum experimental wave period ($1.7s$). Therefore, the particles could not be used to investigate velocity fields in presence of waves.

4.5.3 Conclusions regarding LSPIV measurements

Measurements by means of LSPIV method helped in evaluation of velocity fields and flow patterns behind barriers with different conditions. Practical shortcomings prevented complete study of velocity components. However, the obtained results provided better understanding of flow characteristics in the vicinity of the barrier.

It was shown that with a rigid barrier the zone of maximum velocity beneath the barrier was deeper and velocity magnitude was higher, in comparison to a flexible barrier with the same draft. The turbulence wake downstream of the barrier was also deeper for a rigid barrier.

The velocity vectors upstream of the barrier deviated from horizontal direction at distance about one time the barrier draft for rigid barriers and even less for flexible barriers.

The flow passing the barrier made high vertical velocities on upstream side, beneath the barrier near the bottom of it where it could take the detached oil droplets with.

The main achievement of LSPIV measurements was to provide the velocity field for barriers with different types and drafts which could be used later to calibrate the numerical model, as it is explained in detail in Sec. 5.3.

The device was not able to measure velocities in presence of waves, as well as in experiments with oil. For a further investigation in both oil and water fluids, a more precise PIV method, e.g. using a laser sheet, is recommended.

Chapter 5

Numerical modeling

The purpose of this chapter is to describe the conditions and results of the numerical models. Numerical models tend to provide better understanding of containment hydrodynamics in the vicinity of rigid and flexible barriers. Single and double barriers were simulated and the flow characteristics were compared. The models where used to compute the forces acting on the barriers and provided the possibility to compare drag force on flexible and rigid barriers.

5.1 Methodology of numerical study

To start with numerical simulations, preliminary studies were done in which two different commercial codes, ANSYS and FLUENT, were applied to simulate the barrier and flow around it.

After choosing the more appropriate code, simulations were carried out to model the conducted experiments in the laboratory flume. The results of numerical simulations, with and without oil, were compared to experiments and the numerical model was calibrated.

Finally, the model was used to simulate real conditions and to calculate the acting forces on the barrier.

5.2 Preliminary simulations

Preliminary simulations were conducted in two steps. As the first step, the Finite Element code, ANSYS (ANSYS, 2007), was used to model the interaction between fluid and the (rigid or flexible) barrier. Finite element method has been used for structural analysis since long time. However, its application to fluid modeling and CFD problems is still increasing. Implementing ANSYS code provided the possibility to solve fluid and structure considering the interactive forces[1].

The second step was to model the multiphase flow, using a robust CFD code, FLUENT (FLUENT, 2007). This code was used to model experiments with LECA granules. The model was calibrated by results of experimental

[1]The work was realized with help of *ANSYS Inc.* society (www.cadfem.ch).

modeling. FLUENT uses the Finite Volume method to solve the fluid and hence it gives more reliable results for the fluid comparing to FE codes specially for three-dimensional problems.

5.2.1 Fluid-Structure Interaction (FSI) model

For FSI model, the ANSYS code was used. The aim was to develop a fluid-structure interaction (FSI) analysis of a boom exposed to water flow, to verify the influence of a flexible barrier on pressure and velocity fields in the vicinity of the barrier.

5.2.1.1 Numerical model characteristics

To account for fluid-structure interaction, a sequential coupled-field analysis was employed for a 2D section. In this method, sequences of uncoupled analysis are conducted so that the boundary condition and/or load in each sequence are taken from the results of the analysis of the former sequence analysis. Therefore, after a number of iterations, the change in the flow conditions and updated geometry will be below a small-prescribed tolerance and the system approaches the equilibrium condition.

When the flow is established, it applies a pressure load to the barrier. This pressure deforms the boom and consequently results to modification of the flow pattern. This is an interactive behavior between the fluid and the barrier and the degree of coupling is significantly high as the boom can undergo large deformations and subsequently affect the flow.

To come to a convenient method, a coupling algorithm was required to solve the system for the fluid-structure interaction. This further, demands proper formulation of fluid and structure to simulate each physical domain realistically. The fluid is assumed to be governed by Navier-Stokes (NS) equations. When finite element is used for fluid problems, special attention is required for discretisation of the convection terms in the NS equations. One of the recommended methods is the Streamline Upwind Petrov-Galerkin (SUPG) scheme. This method has proved its efficiency for fluid problems and therefore was employed in the present study.

5.2.1.2 Mesh generation and modeling conditions

Since the flexible barrier undergoes large deformations, it was necessary to have a mesh updating (remeshing) in each iteration of the FSI. Therefore, the mesh generation should be compatible for this remeshing and result mapping in each step. The barrier was therefore modeled with solid beam elements. However, since the skirt is very thin, the moment of inertia of the section was very small and therefore the bending resistance of the barrier was negligible and it only indicated membrane stiffness due to stress stiffening phenomenon. The number of divisions for the skirt was selected in a way that it can be capable to deform due to probable modes of the barrier curvature, including large deformation and rotation.

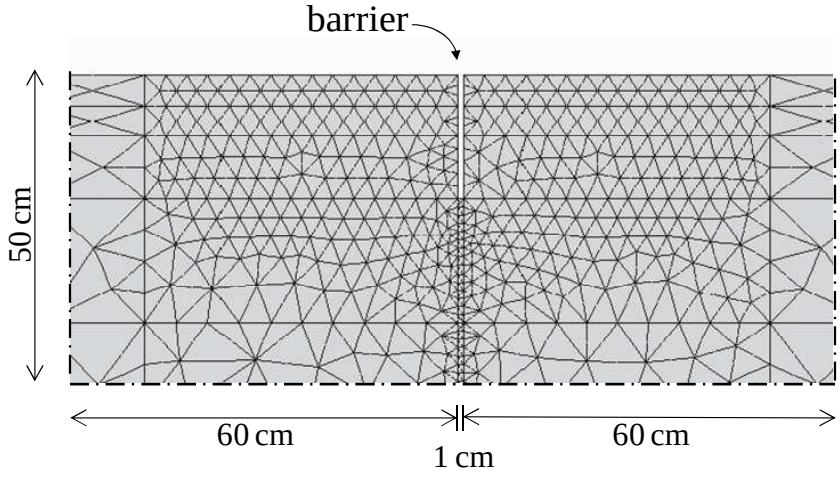

Figure 5.1: Initial mesh before Fluid-Structure Interaction (FSI) analysis in the vicinity of the boom

The FSI analysis included a time integration approach for the solution of the transient equations. In each time increment, FSI iterations are conducted with mesh updating so that the loading, transferred from flow to the structure and vice versa, goes under a prescribed tolerance.

The dimensions and conditions of model were identical to the preliminary physical model, i.e. a laboratory flume with 0.6 m depth, 6 m length, and the barrier draft was 20 cm. At the end point of the barrier a vertical force of 2 kg/m was applied which represents the linear ballast weight. The initial mesh in the near boom region is shown in Fig. 5.1. The mesh was built up of 5'326 triangular cells and was finer in the region close to the barrier. It became coarser by getting away from the barrier.

The system was analyzed once for a rigid barrier without considering the Fluid-Structure Interaction (FSI) and then for a flexible barrier using FSI. For the latter, the deformation of system was investigated with a free bottom point (first mode of deformation) as well as a horizontally attached bottom point allowing only vertical movement of the bottom point (second mode of deformation) as it was explained in Sec. 4.1.6. The deformed mesh at the end of FSI analyses are shown in Fig. 5.2.

5.2.1.3 Boundary conditions

Following conditions were set at each boundary of the model:

- **Free-surface:** The normal velocity component and the horizontal shear stress were set to zero.
- **Bottom:** The normal velocity component was set to zero.
- **Inlet:** The velocity was uniform with a magnitude of 40 cm/s.
- **Outlet:** The pressure was set to zero.
- **Barrier:** The normal velocity was set to zero.

5.2.1.4 Results of the Fluid-Structure Interaction model

In Figs. 5.3 and 5.4 the pressure and velocity fields, in the vicinity of rigid and flexible barriers are illustrated. The preliminary numerical study indicated that a flexible barrier could change the pressure and velocity fields in the vicinity of the barrier. The highest hydrodynamic pressure occurred in the case of a flexible barrier horizontally fixed at the bottom point (second mode of deformation) as the fluid is trapped inside barrier and imposes higher forces to the barrier. Whereas the minimum pressure corresponded to the case of a flexible barrier with a free end point, that can easily deform due to imposed forces.

The maximum pressure was the same for the rigid barrier and the flexible barrier with horizontally fixed end point. For the flexible barrier with free end point the maximum pressure was about 30% less comparing to the case of the rigid barrier and the attached flexible barrier. The applied force on the barrier was 44.2 N per unit length of the barrier for rigid barrier, and 30.6 and 55.1 N for flexible barriers of first and second mode of deformation respectively.

The velocities were approximately of the same magnitude for all three cases. The region with high velocity was more extended in case of a rigid barrier.

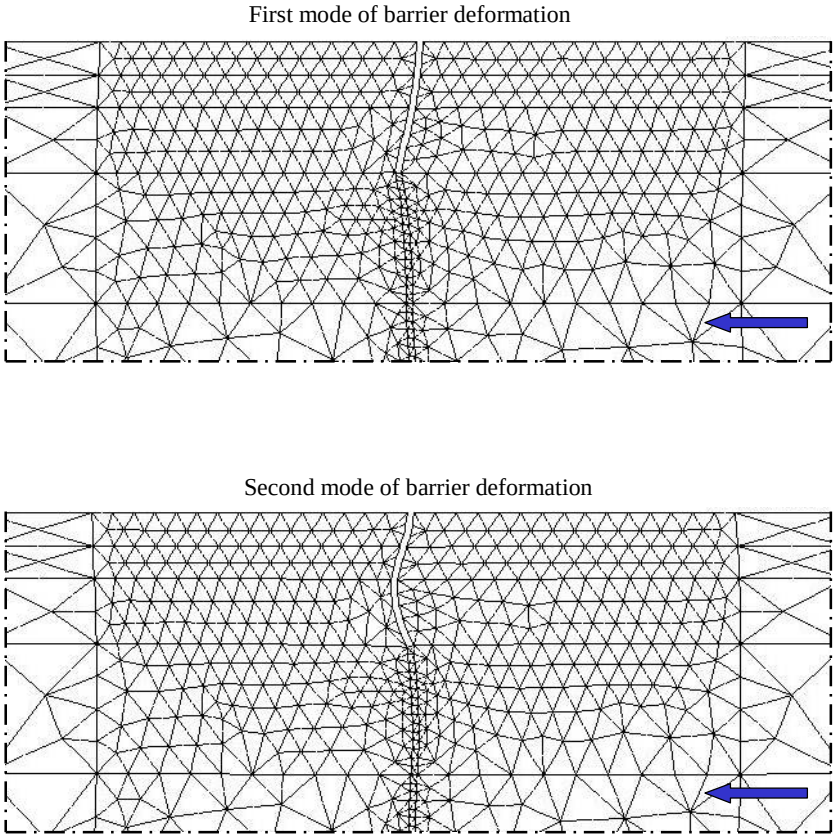

Figure 5.2: Deformed mesh in the vicinity of the barrier after FSI analysis of a flexible barrier for first (top) and second (bottom) modes of the boom deformation; water is flowing from right to left

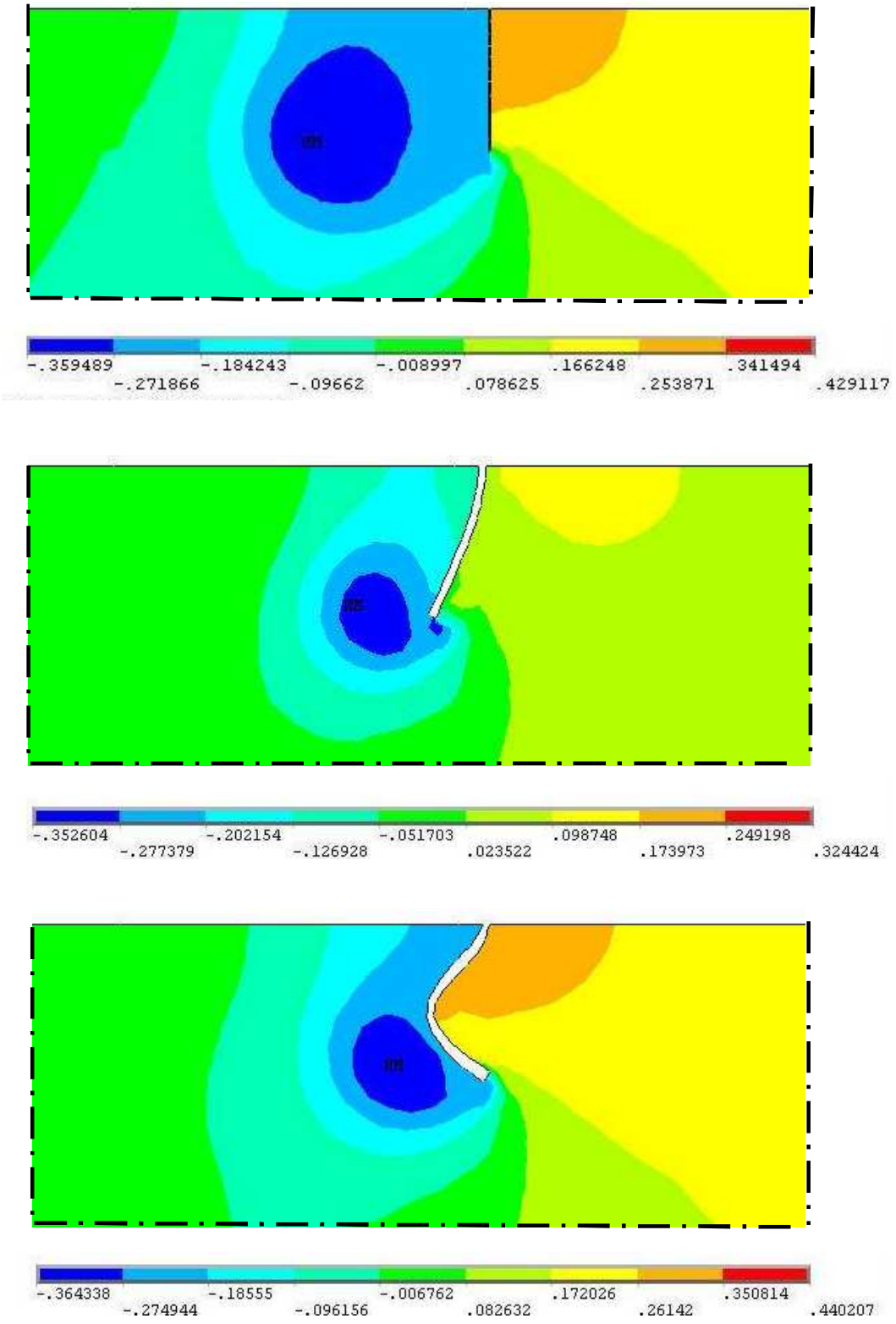

Figure 5.3: Pressure field in the vicinity of rigid and flexible barriers in kPa; water is flowing from right to left

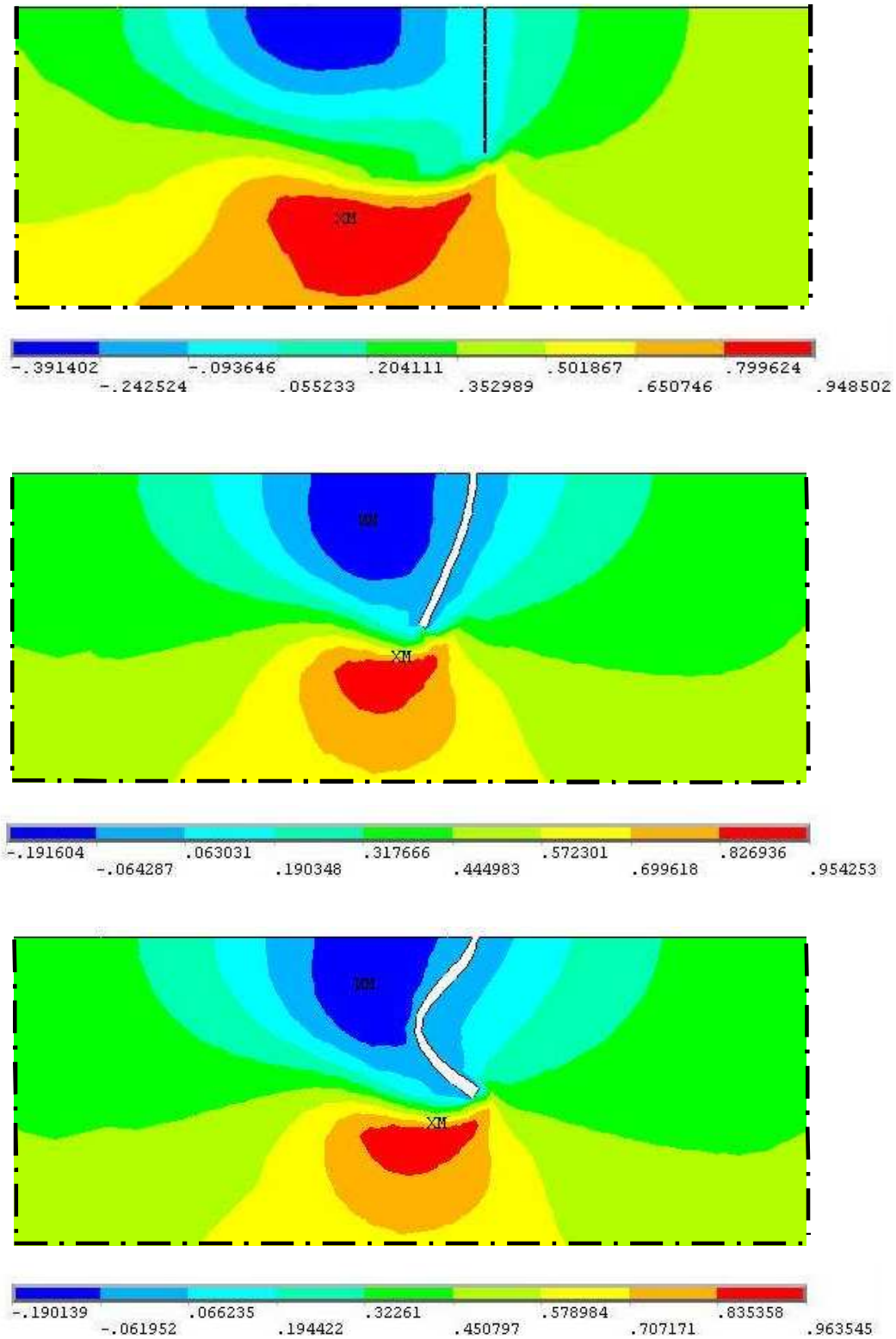

Figure 5.4: Contours of velocity magnitude of rigid and flexible barriers in m/s; water is flowing from right to left

5.2.2 Multiphase model

The first attempt to simulate multiphase flow was to model the containment of LECA granules by rigid barriers in the laboratory flume. A two-dimensional two-phase model was developed using FLUENT (v6.3) code[2]. FLUENT uses the Finite Volume Method (FVM), a special finite difference formulation, to solve the governing equations for a fluid. It provides the capability to use different physical models such as incompressible or compressible, inviscid or viscous, laminar or turbulent, etc.

5.2.2.1 Numerical model characteristics

The Finite Volume Method (FVM) is one of the most versatile discretization techniques used in CFD. The formulation and background theory of FVM is described in various text books such as that of Versteeg and Malalasekera (2007). Based on the control volume formulation, the first step in the FVM is to divide the domain into a number of control volumes, where the variable of interest is located at the centroid of the control volume. The next step is to integrate the differential form of the governing equations over each control volume. Interpolation profiles are then assumed in order to describe the variation of the concerned variable between cell centroids. The resulting equation is called the discretization equation. In this manner, the discretization equation expresses the conservation principle for the variable inside the control volume.

The most compelling feature of the FVM is that the resulting solution satisfies the conservation of quantities such as mass, momentum, energy, and species for any control volume as well as for the whole computational domain and for any number of control volumes.

5.2.2.2 Mesh generation and modeling conditions

The geometry definition and grid generation was done using GAMBIT, the preprocessor bundled with FLUENT. The model was defined parametrically to allow parametric studies.

For modeling the fluid, 13'720 quadrilateral shape computational cells were used. The boom was modeled by two adjacent but distinct edges. An study was made to choose an appropriate model for multiphase problem of LECA granules in water as it is described in Sec. 5.2.2.3. The turbulence was modeled using the standard $k - \epsilon$ model.

Successful computations of turbulent flows require some consideration during the mesh generation. Since turbulence plays a dominant role in the transport of mean momentum and other parameters, one must ascertain that turbulence quantities in complex turbulent flows are properly resolved. It is therefore recommended that the regions where the mean flow changes rapidly and forms shear layers, were resolved with sufficiently fine meshes. As a result, in the near boom region local refinement was applied to the mesh to catch high gradient of

[2]Calculations were launched on "Pleiades" cluster at EPFL.

velocity or phase volume fraction fields. The near-wall mesh can be checked in FLUENT by plotting the values of y^+.

For standard wall functions, each wall-adjacent cell's centroid should be located within the log-law layer, 30< y^+ <300, in order to satisfy the logarithmic profile assumption and to solve the boundary layer. A y^+ value close to the lower bound ($y^+ \approx 30$) is most desirable. After checking the y^+ value, FLUENT is capable to refine the mesh locally in regions where y^+ is high.

Six different models were built up, where each run represented one of the tests LR1 to LR6 (see Table 3.8). The initial LECA volume and barrier draft were changed for each individual run due to the corresponding experimental test. Each model was launched for three different mean flow velocities: 20, 25 and 30 cm/s.

5.2.2.3 Multiphase model selection

Several approaches were developed to simulate the transportation of granular material (or bubbles and droplets) in a fluid flow. The phenomenon is generally categorized as liquid-solid flows and there are a number of formulations for the solution.

Generally, there are two approaches in modeling the multiphase flows which are Lagrangian and Eulerian formulations. In the Lagrangian approach, motion of the particles is determined by a steady Lagrangian frame, where in an Eulerian approach the granular phase is treated as another continuum.

In the Lagrangian formulation, the fluid flow is first solved and then by knowing the flow velocity field, applied forces to the particles are determined. Then by using the equation of motion for the particles (in the Lagrangian frame) the incremental movement of the particle in each time step is calculated. This approach ignores any interaction between the fluid flow and the particles flow and assumes that the motion of the particles has no effect on the fluid flow. This approach can fail for high concentration (particulate loading) of the granular dispersed phase where the flow is influenced by motion of the particles.

In the Eulerian formulation, the dispersed phase (granular material) is assumed to be the same as the carrier phase (water) and similar governing equations are solved for it. In this method a set of new variables, α_q s, are introduced in the equations (for each phase denoted by q) which indicates the fraction of the q^{th} phase in a control volume. All properties of the fluid are averaged among the phases based on each phase volume fraction. Therefore, for each dispersed phase a new advection equation is introduced which is associated with volume fraction of that phase.

FLUENT introduces "discrete phase model" for the Lagrangian approach and "mixture" and "general Eulerian model" based on the Eulerian approach (FLUENT, 2007). For the case under study, the particle phase volume fraction was high and therefore the approximate distance between particles was quite low. Hence, use of "discrete phase models" was not appropriate for this case and mixture or Eulerian model shall be used.

To select between "general Eulerian" and "mixture model" another param-

eter had to be examined. This parameter is the particulate loading, β, which is defined as:

$$\beta = 0.706\frac{\alpha_d}{1-\alpha_d} \tag{5.1}$$

In which α_d is the maximum volume fraction (packing limit) of LECA and was measured experimentally to be 0.7. Applying the value of α_d in Eq. 5.1 gave an approximate amount of 1.7 for β . The particulate loading, β, was considered to be high and therefore, the " mixture model" could not properly model the particles behavior. As a conclusion, considering the high particulate loading of the LECA granules, "general Eulerian" formulation may properly approximate the system behavior.

The "Eulerian model" is the most complex multiphase model in FLUENT. It solves the momentum and continuity equations for each phase. Coupling is achieved through the pressure and interphase exchange coefficients. The manner in which this coupling is handled depends upon the type of phases involved; granular (fluid-solid) flows are handled differently than non-granular(fluid-fluid) flows. For granular flows, the properties are obtained from application of kinetic theory. Momentum exchange between the phases is also dependent upon the type of mixture being modeled.

To change from a single-phase model, where a single set of conservation equations for momentum, continuity and (optionally) energy is solved, to a multiphase model, additional sets of conservation equations must be introduced. Further to introducing additional sets of conservation equations, the original set must also be modified. The modifications involve, among other things, the introduction of the volume fractions $\alpha_1, \alpha_2, ..., \alpha_n$ for the multiple phases, as well as mechanisms for the exchange of momentum, heat, and mass between the phases. Details about the Eulerian multiphase model are presented in the manual of FLUENT.

5.2.2.4 Boundary conditions

Following conditions were set at each boundary of the model:

- **Free-surface:** Slip wall condition was applied and the shear stress was set to zero.

- **Bottom:** No-slip wall condition was applied.

- **Inlet:** The velocity distribution was horizontal and linear, decreasing along the depth. The LECA particles were introduced into the model as a portion of the inlet edges, over water surface. Volume of LECA per unit length of barrier was prescribed and using the internal programming service of FLUENT, User Defined Function (UDF), the transient boundary condition at the inlet for phase volume fraction and inlet velocity profile was programmed.

  FLUENT requires specification of transported turbulence quantities, when the flow enters the domain. The value of turbulent kinetic energy, k, and

the turbulent dissipation rate, ϵ, were estimated by Eqs. 5.2 to 5.4, as follows:

$$k = \frac{3}{2}(U\ I)^2 \tag{5.2}$$

In the equation, U and I stand for the mean flow velocity and turbulence intensity respectively. The turbulence intensity can be calculated as:

$$I = 0.16(Re_{HD})^{-1/8} \tag{5.3}$$

where Re_{HD} is the Reynolds number based on hydraulic radius of the flume. The vale of turbulent dissipation rate was estimated as:

$$\epsilon = C_{\mu}^{3/4}\frac{k^{3/2}}{l} \tag{5.4}$$

where C_{μ} is an empirical constant equal to 0.09 and l is the turbulence length scale, which is a physical quantity related to the size of the large eddies that contain the energy in turbulent flows. In the present model, the turbulence obtains its characteristics length from the barrier which is an obstacle for the flow.

- **Outlet:** The "outflow" boundary condition was defined, i.e. the required information was extrapolated from the interior and the same discharge as was entered from the inlet, went out of the model.

- **Barrier:** No-slip wall condition was applied.

5.2.2.5 Results of the multiphase model

Evolution of the slick shape during the run time of numerical model was very similar to that of experiments. The LECA layer over water surface accumulated behind the barrier and after a while a part of it was escaped beneath the barrier.

Examples of shape evolution for two different loss levels are illustrated in Figs. 5.5 and 5.6. The shape evolution in experimental and numerical models were in quite good agreement, although the thickness and length of the LECA slick were not always the same.

The velocity contours and vectors in water and LECA granules are shown in Fig. 5.7. Velocity vectors show an internal circulation inside LECA slick. The same circulation was observed during the experiments. Velocity vectors in the LECA-water interfacial layer indicate high shear velocities.

Developing an internal program (UDF), the volume fraction of the granular phase was determined downstream of the barrier by a loop over cells at each side of the boom. The amount of lost LECA from the barrier was calculated from the difference between the volumes in two sides. The evolution of slick shape and the loss percentage was then compared for experimental and numerical tests.

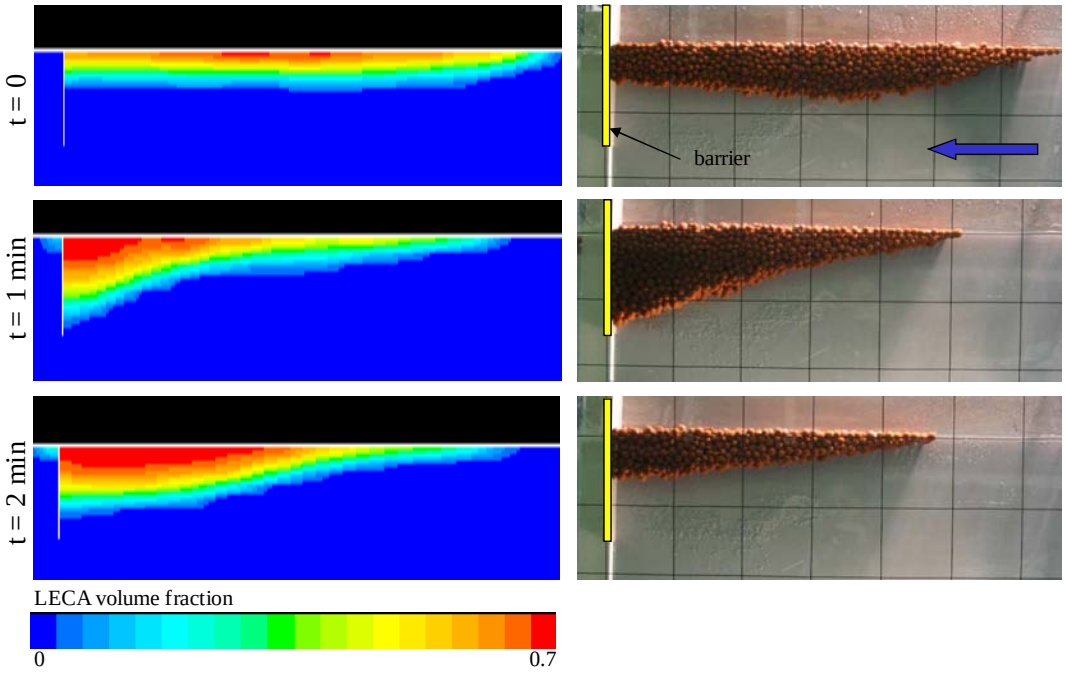

Figure 5.5: Evolution of LECA slick shape during experimental (right) and numerical (left) modeling for $U = 25\ cm/s$, $V = 40\ lit/m$, and $D = 15\ cm$; loss percentage less than 50%

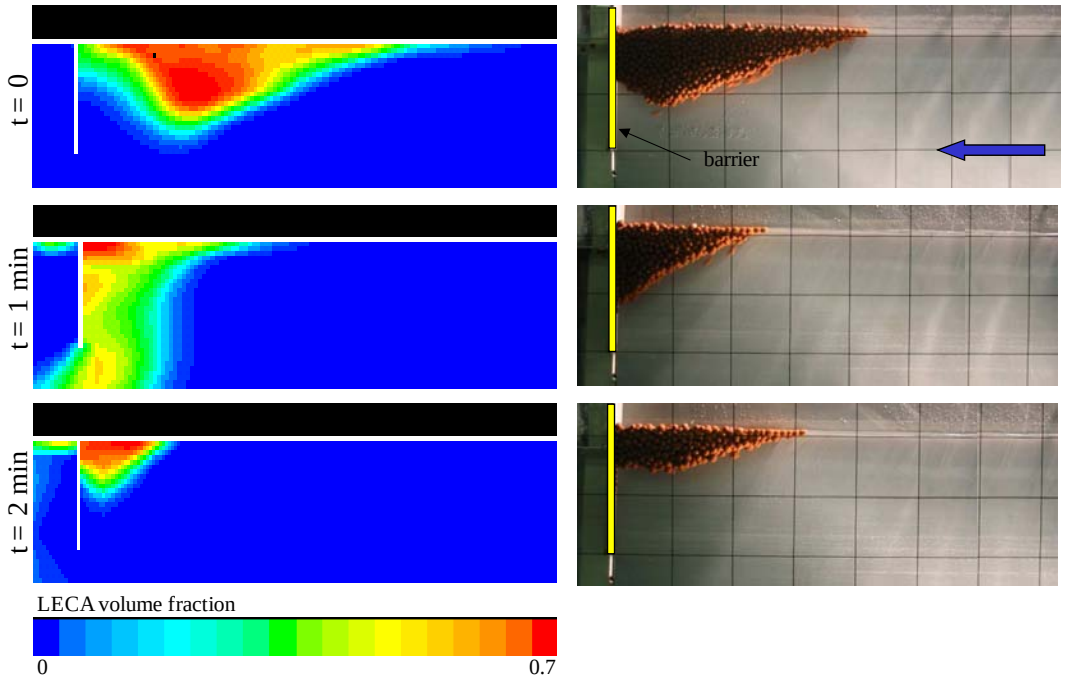

Figure 5.6: Evolution of LECA slick shape during experimental (right) and numerical (left) modeling $U = 35\ cm/s$, $V = 40\ lit/m$, and $D = 20\ cm$; loss percentage more than 50%

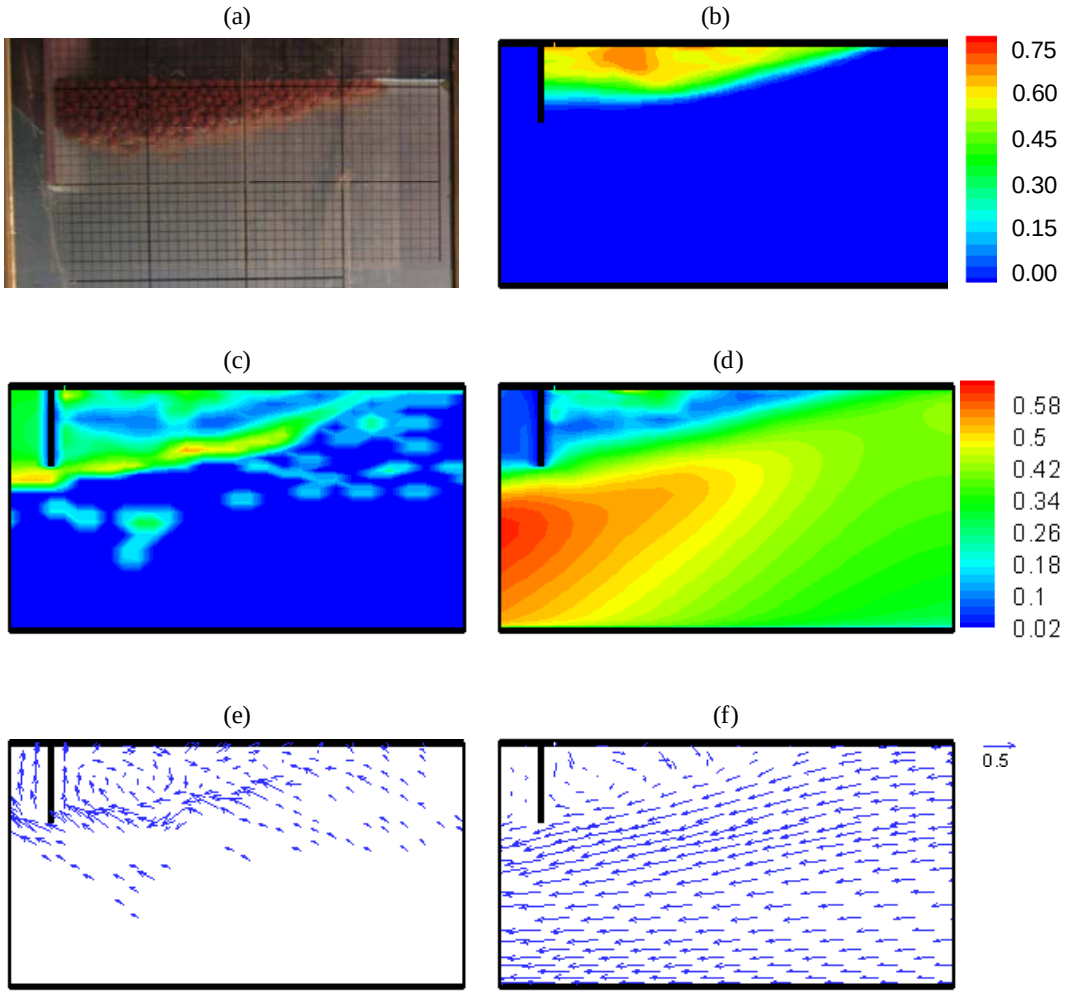

Figure 5.7: Detailed flow characteristics in the LECA slick with mean flow velocity, U, of 0.35 m/s, initial oil volume, V equal to 40 lit/m, and draft of 20 cm: (a) LECA slick shape from experiments; (b) LECA volume fraction; (c) contours of velocity magnitude in LECA; (d) contours of velocity magnitude in water; (e) velocity vectors in LECA; (f) velocity vectors in water; velocities in m/s

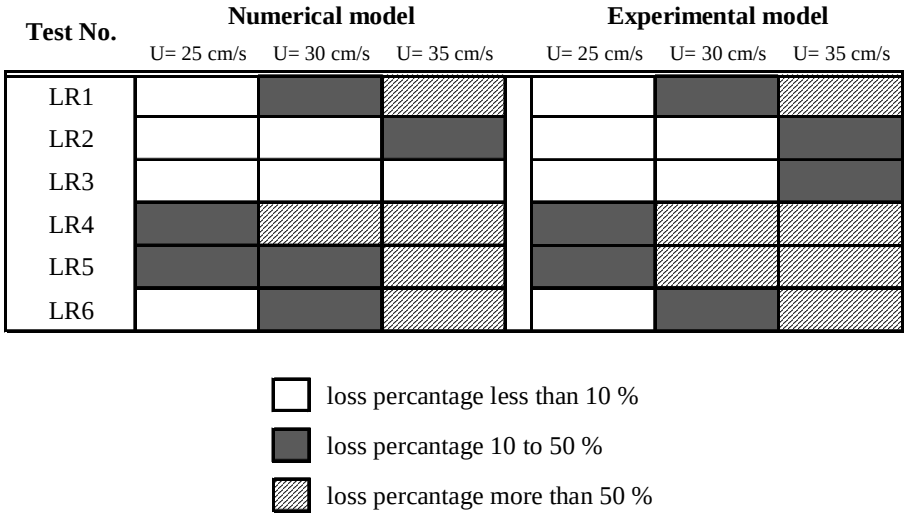

Figure 5.8: Comparison of LECA granules loss between numerical and experimental results at different mean velocities

Fig. 5.8 shows the range of percentage of LECA granules loss for both numerical and experimental models at different flow velocities. The figure shows that numerical model was capable to simulate the two-phase fluid behavior appropriately and the percentage of loss in numerical models was in good agreement with that of experiments.

5.2.3 Conclusions regarding the preliminary simulations

Preliminary simulations approved the capability of commercial codes in modeling the oil slick containment barriers. Since the hydraulic aspects of the study are more important than its structural ones, it was decided to continue the simulations with FLUENT, which applies FVM and is more reliable for fluid modeling. The most important advantage of FLUENT code was the possibility of modeling multiphase flows, which is crucial item in oil-water models of oil containment barriers.

5.3 Numerical model of barrier without oil

The numerical models of the barrier, with same size as experiments in the laboratory flume, without oil were performed to calibrate the model with the results of UVP and LSPIV measurements and to describe the details of the flow field in the vicinity of rigid and flexible barriers with different drafts. Additionally, the flow field around double barriers was simulated.

A double precision, steady, one-phase model was used for simulations. The standard $k - \epsilon$ model was applied for the turbulence.

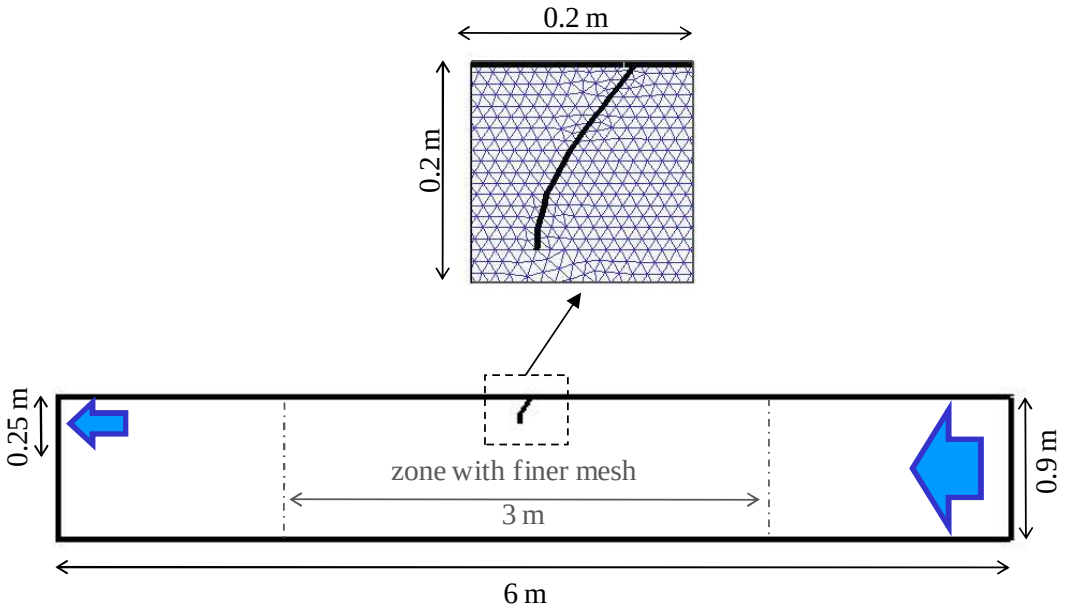

Figure 5.9: Geometry of the numerical model built up for down-scaled simulations and the mesh in the region close to the barrier

5.3.1 Mesh generation and modeling conditions

The mesh was generated using GAMBIT, for single and double barrier configurations. To model the flexible barriers, predefined shapes, derived from experiments, was applied. Simulations of single barrier were carried out for rigid and flexible barriers with 10 and 20 *cm* draft.

For modeling rigid and flexible double barriers, the draft was 10 *cm* and three cases with barrier distance of 60, 120, and 180 *cm* were modeled. The mean flow velocity was 20 cm/s for both single and double barriers.

The fluid was modeled with 61'862 triangular shape computational cells. In the middle part of the flume, where the barrier locates, the mesh was finer and it became gradually coarser at the edges. The boom was modeled by two adjacent but distinct edges. A 6 *m* long, 0.9 *m* deep flume was modeled (same as laboratory flume) and the barrier was located at the middle of it. Fang and Johnston (2001b) suggested that, when the distance between the upstream boundary and the boom exceeds 15 times the boom draft, the change in pressure over this distance becomes insignificant. In the present models, the upstream distance was 15 to 30 time the boom draft which remain in acceptable range.

In the experimental model, the water level was maintained using a weir at the outlet of the flume, thus in the numerical model the same opening was considered. The geometry of the model and the mesh in barrier region is shown in Fig. 5.9.

5.3.2 Boundary conditions

Following conditions were set at each boundary of the model:

– **Free-surface:** Slip wall condition with no shear was considered.

- **Bottom:** No-slip wall condition was considered.
- **Inlet:** The horizontal velocity distribution was linear decreasing along the depth. To obtain a mean flow velocity of 20 cm/s the top velocity was set to 25 cm/s, where bottom velocity was 15 cm/s. The velocity distribution is derived from LSPIV measurements.
- **Outlet:** The "outflow" boundary condition is defined, i.e. FLUENT extrapolates the required information from the interior and the same discharge, as was entered from the inlet, goes out of the model.
- **Barrier:** No-slip wall condition was applied.

5.3.3 Results of models without oil

The results of numerical simulations of models without oil were compared to experimental results of horizontal velocity measurements with UVP instrument and was used to calibrate the numerical model. An example for a rigid barrier with 10 cm draft is shown in Fig. 5.10 and as it can be seen, the result are in a very good agreement.

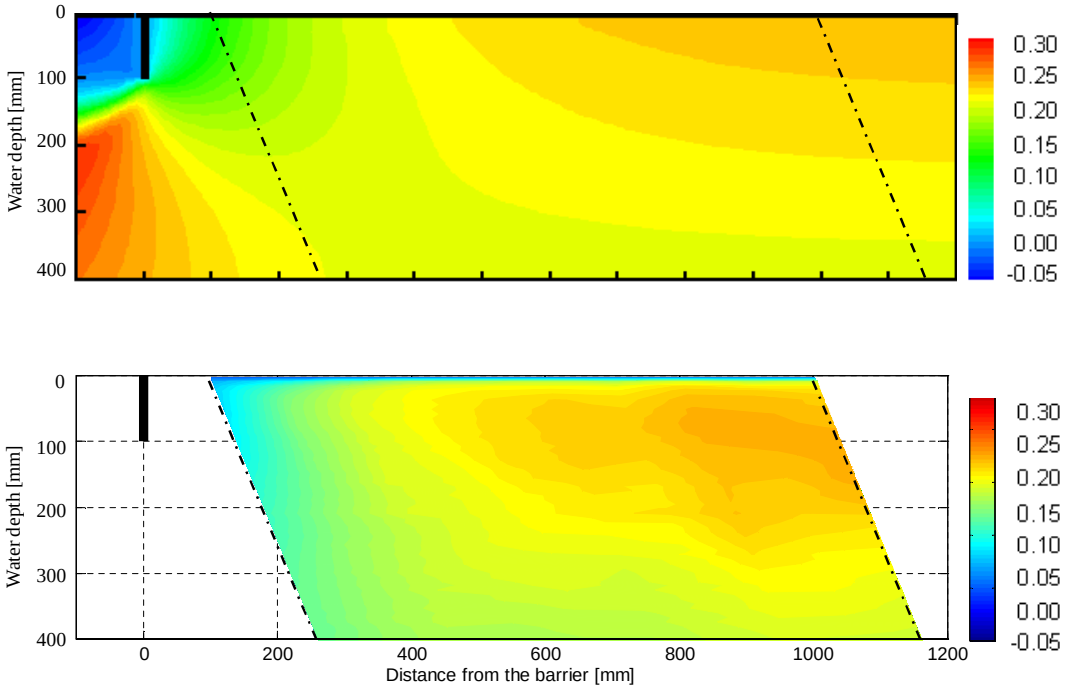

Figure 5.10: Comparison between horizontal velocity derived from numerical results (top) and experimental UVP measurements (bottom) for a rigid barrier with 10 cm draft; velocities in m/s

5.3.3.1 Simulation of flow passing a single barrier

The simulations provided the possibility to compare the velocity fields in the vicinity of different barriers. The velocity contours in the region close to a single barrier are shown in Fig. 5.11. A zone with high velocity was formed beneath the barrier. Evidently, the velocity magnitude in this zone is higher for barriers with 20 cm draft in comparison with those of $10cm$ draft and for rigid barriers comparing to flexible barriers with the same draft.

Fig. 5.12 illustrates the streamlines for the same region of flow. In this figure, the turbulence wakes downstream of the barrier are shown very well. As in high-Reynolds-number flows passing an obstacle, the flow pattern is characterized by a separated boundary layer which divides the wake, from the rest of fluid. The distance of the stagnation point downstream of the barrier varies from case to case. For rigid barriers it locates in a distance about 8 to 10 times the barrier draft; whereas for the flexible barriers, the distance is 6 to 8 times the barrier draft.

A circulation cell is formed upstream of the barrier which is very small in case of flexible barriers. Fig. 5.13 shows the velocity vectors in the close proximity of the barrier, it indicates that the flow approaching the barrier deviates upstream of the barrier at a distance equal to one time the barrier draft for rigid barriers and less for flexible barriers.

5.3.3.2 Simulation of flow passing two parallel barriers

The velocity field in the vicinity of two parallel barriers is illustrated in Fig. 5.14. The streamlines and velocity vectors are also shown in Fig. 5.15 and Fig. 5.16 respectively.

The velocity magnitude is very low in the area between barriers when the barriers are close to each other (Fig. 5.15a). By increasing the distance of barriers, the velocity of flow between them increases. For the case with barriers at distance equal to 12 times the barrier draft (Fig. 5.15b), the velocity magnitude is rather high in the zone between barriers.

The wake of the first barrier is influenced by the second barrier and it is extended more than a case with single barrier. In other words, as it was seen in Fig. 5.12a, the wake of a single rigid barrier is extended to a distance of 8 to 10 times the barrier draft. However, the presence of the second barrier influences the wake of the first one and as it can be seen in Fig. 5.15b no stagnation point exists between two barriers at a distance of 12 times the barrier draft. Hence, the wake of the first barrier forms a circulation cell between two barriers.

For the case with barriers at distance equal to 18 times the barrier draft (Fig. 5.15c), the streamlines have the possibility to rejoin the surface upstream of the second barrier. In other words, the second barrier is out of the wake of the first one, and the wake of the first barrier is not influenced by the second barrier. Fig. 5.17 illustrates the streamlines in the vicinity of double flexible barriers. The wake of the first barrier is less extended comparing to double rigid barriers. Even for a distance of 12 times the barrier draft, a stagnation point exists between two barriers.

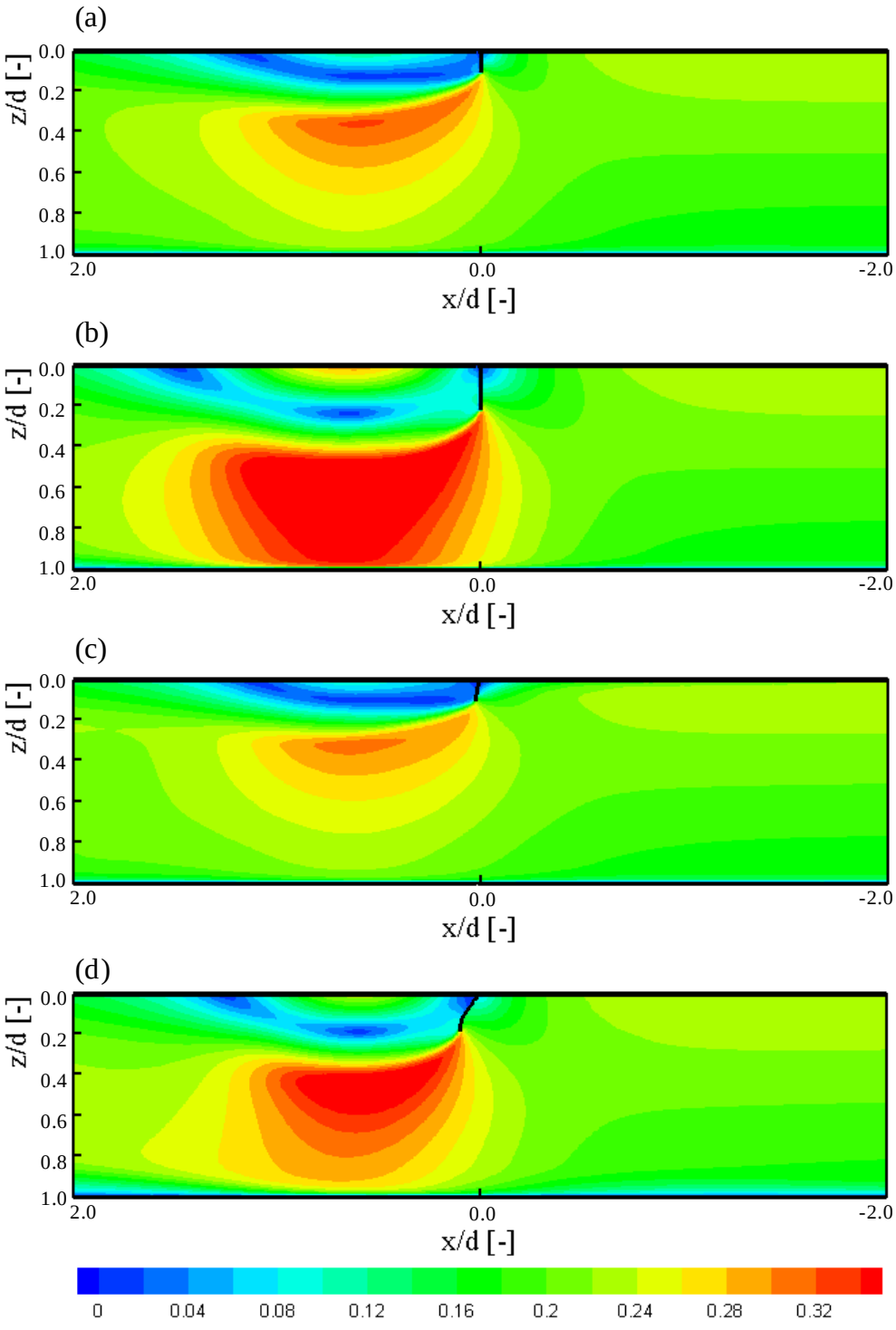

Figure 5.11: Contours of velocity magnitude in the vicinity of different barriers: (a) rigid barrier with 10 *cm* draft; (b) rigid barrier with 20 *cm* draft; (c) flexible barrier with 10 *cm* draft; (d) flexible barrier with 20 *cm* draft; mean flow velocity is 20 cm/s; velocities in m/s

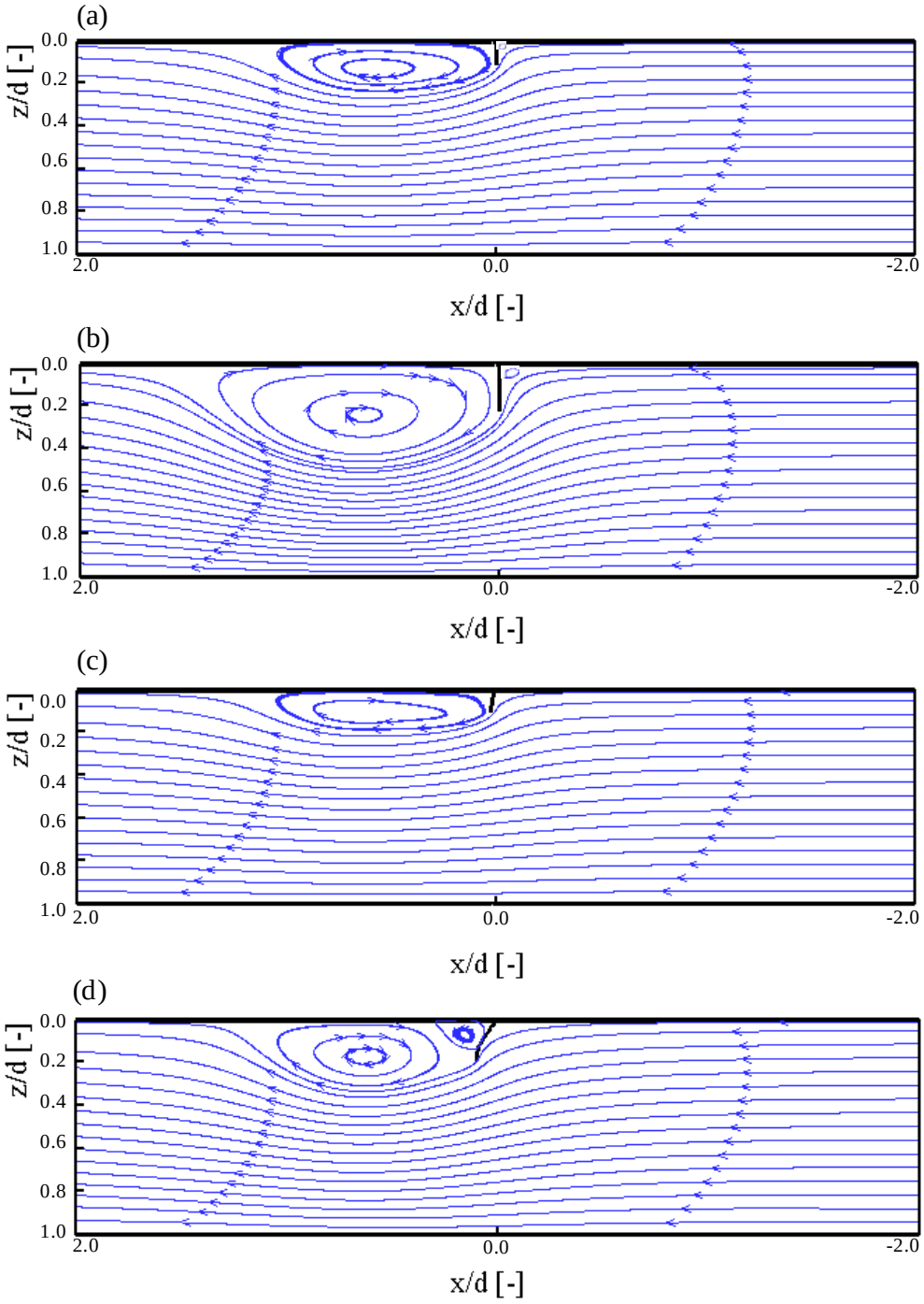

Figure 5.12: Streamlines in the vicinity of different barriers: (a) rigid barrier with 10 *cm* draft, (b) rigid barrier with 20 *cm* draft (c) flexible barrier with 10 *cm* draft, (d) flexible barrier with 20 *cm* draft; mean flow velocity is 20 cm/s

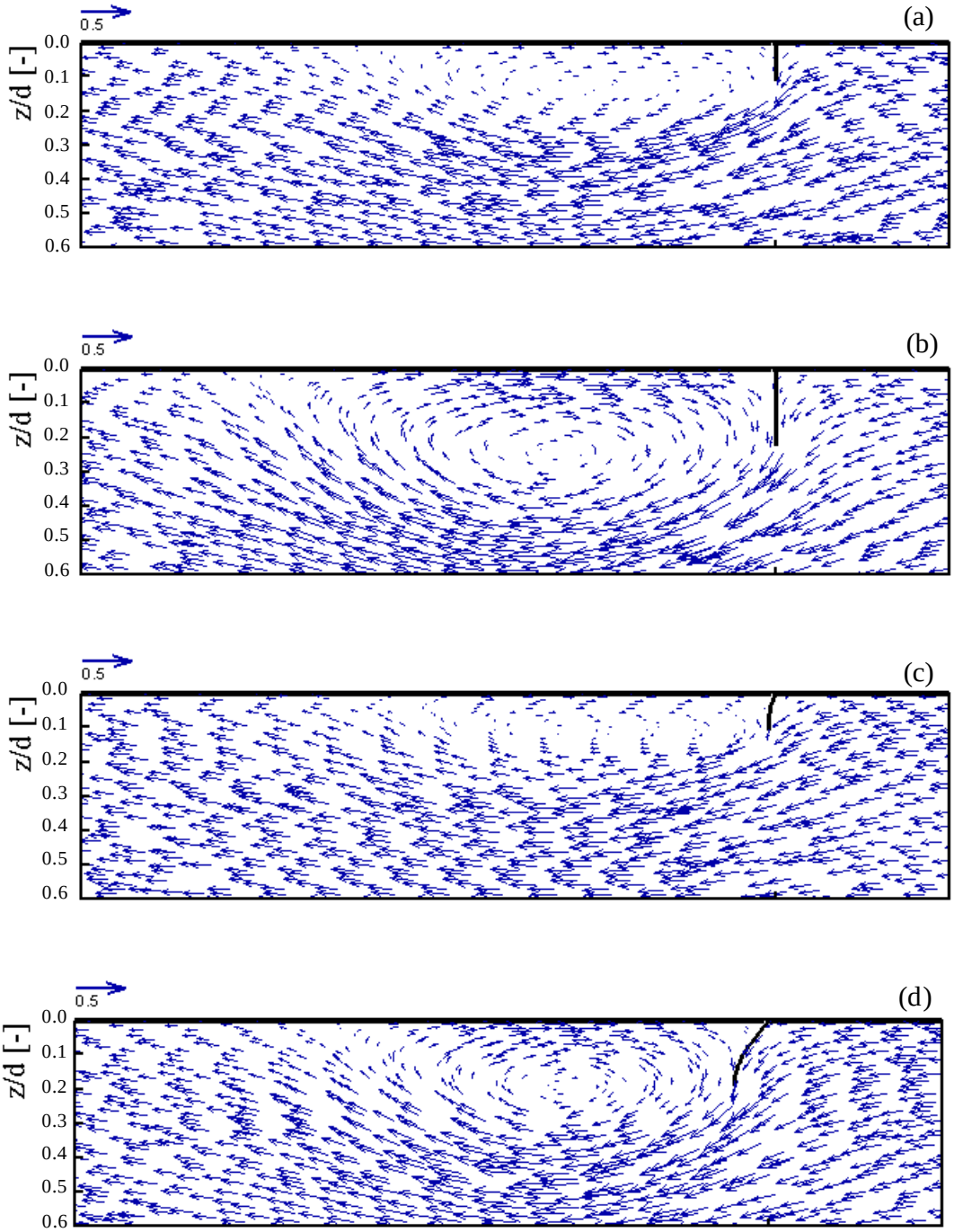

Figure 5.13: Velocity vectors in the close proximity of the barrier for different barriers: (a) rigid barrier with 10 *cm* draft; (b) rigid barrier with 20 *cm* draft; (c) flexible barrier with 10 *cm* draft; (d) flexible barrier with 20 *cm* draft; mean flow velocity is 20 cm/s

Hence, it can be concluded that in a closed reservoir such as Cavalli system, if the ratio of reservoir diameter to the barrier draft is small, maximum 6, it can protect the surrounded slick and withstand higher towing velocities, as it was also shown for experimental models in Fig. 4.17.

On the other hand, if two parallel barriers are used as tandem booms, as was proposed by Delvigne (1984) and others, the distance between two barriers should be more than 12 times the barrier draft, to give the opportunity to escaped oil droplet to ascend to the surface and be contained behind the second barrier.

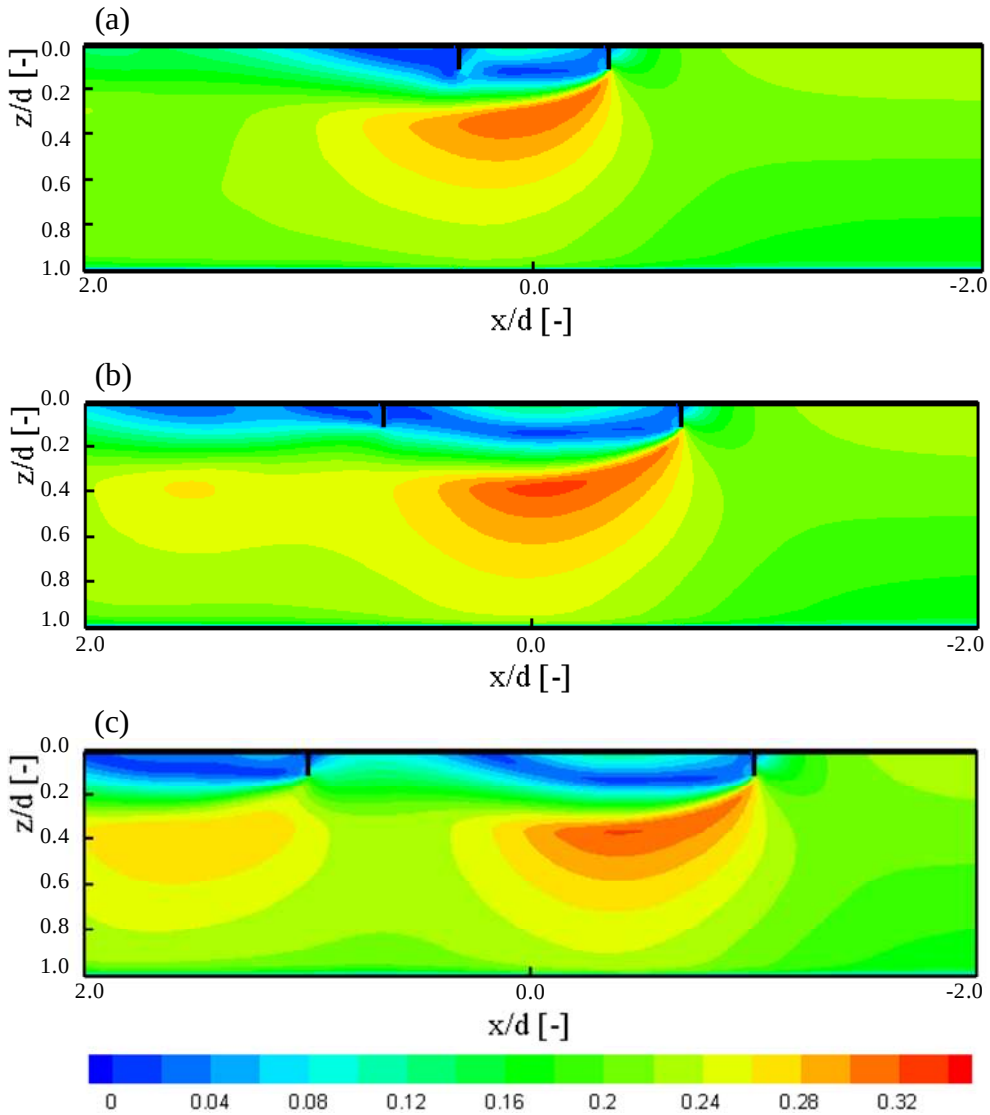

Figure 5.14: Contours of velocity magnitude in the vicinity of double rigid barriers with 10 *cm* draft: (a) barriers at 60 *cm* distance; (b) barriers at 120 *cm* distance; (c) barriers at 180 *cm* distance; mean flow velocity is 20 cm/s; velocities in m/s

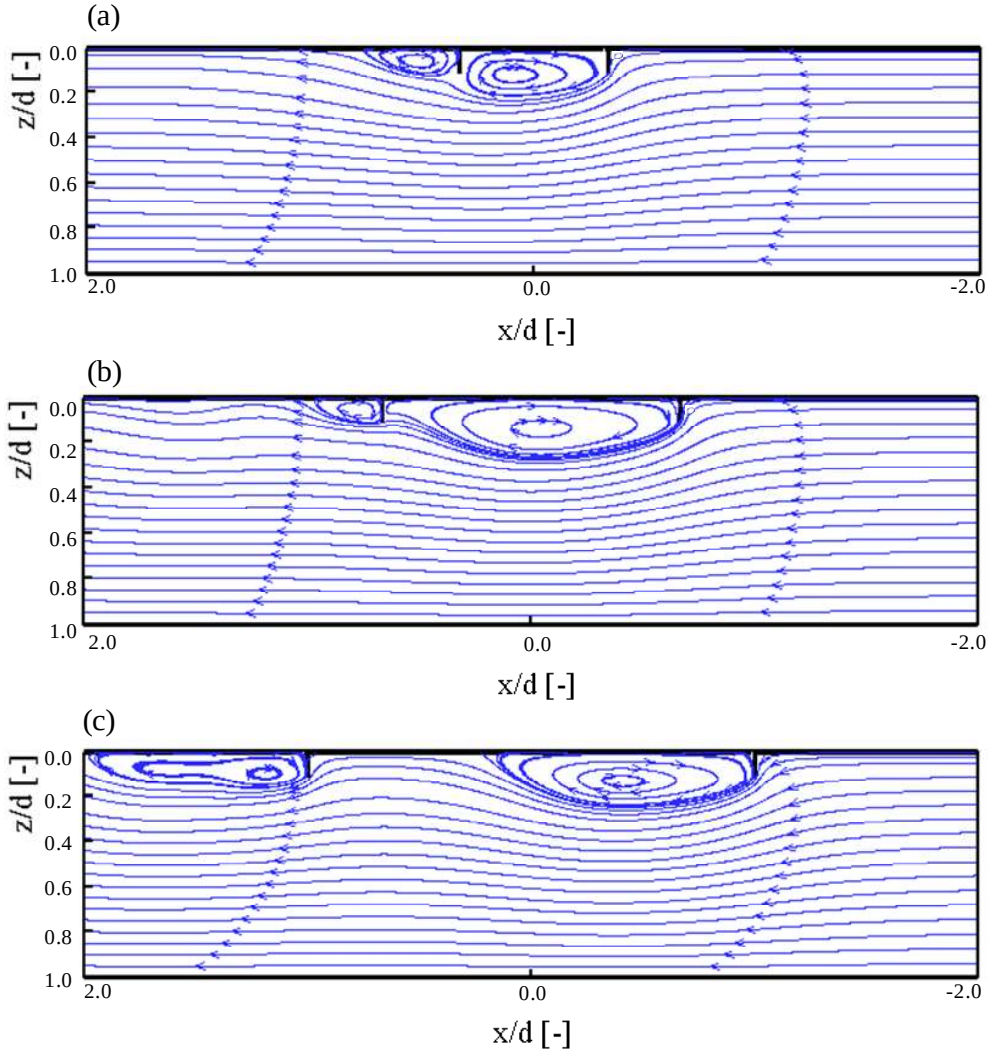

Figure 5.15: Streamlines in the vicinity of double rigid barriers with 10 *cm* draft: (a) barriers at 60 *cm* distance; (b) barriers at 120 *cm* distance; (c) barriers at 180 *cm* distance; mean flow velocity is 20 cm/s

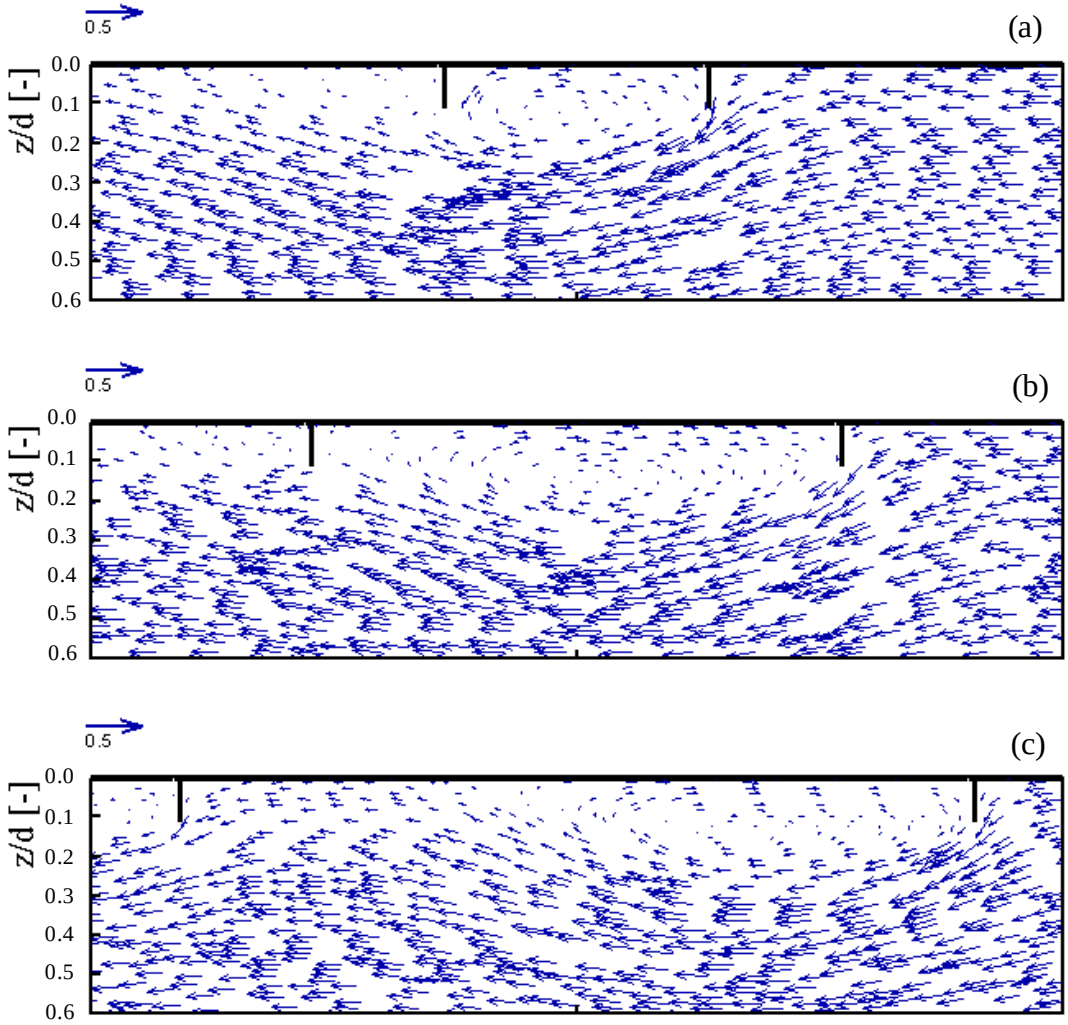

Figure 5.16: Velocity vectors in the close proximity of double rigid barriers with 10 *cm* draft: (a) barriers at 60 *cm* distance; (b) barriers at 120 *cm* distance; (c) barriers at 180 *cm* distance; mean flow velocity is 20 cm/s

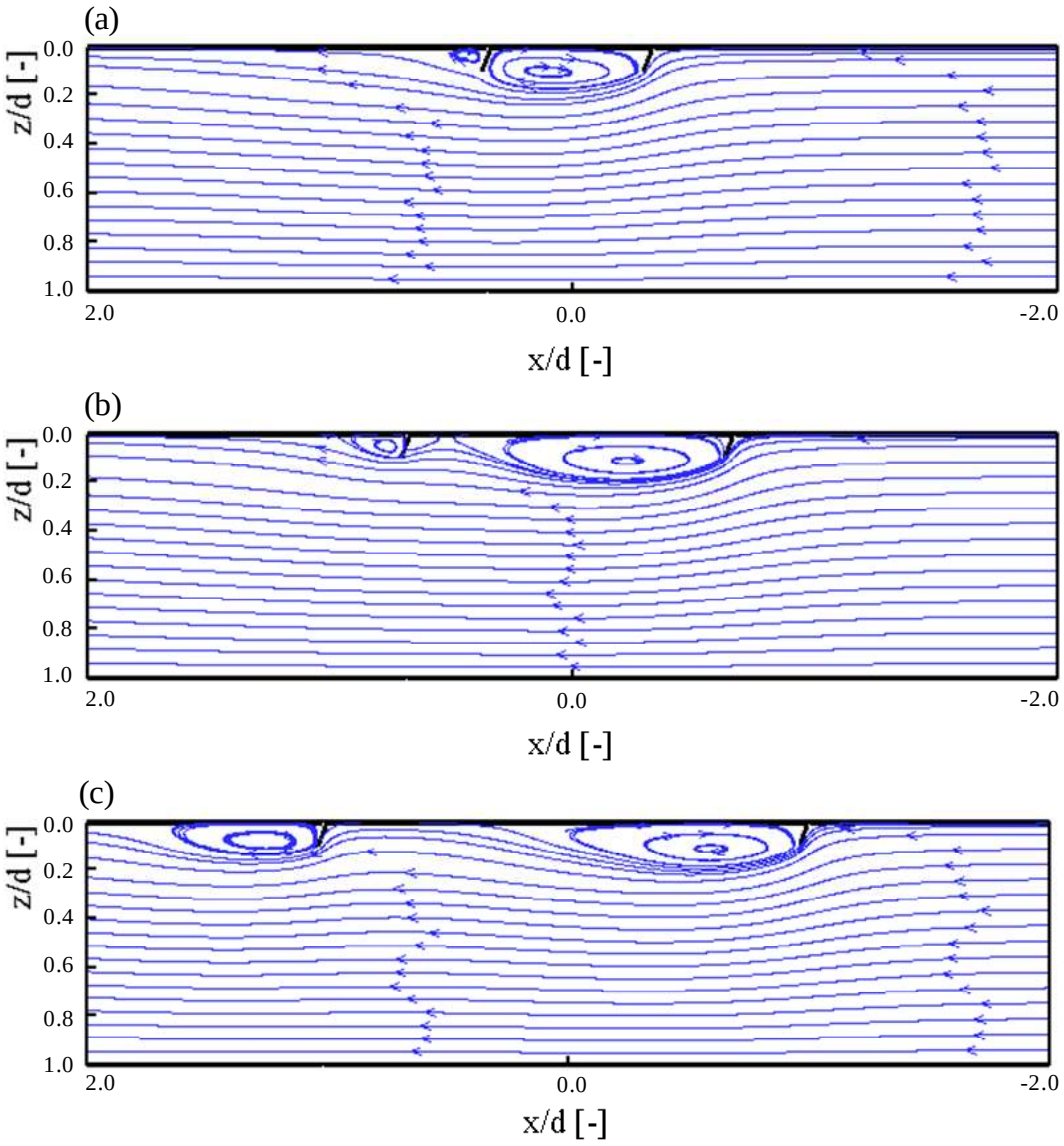

Figure 5.17: Streamlines in the vicinity of double flexible barriers with 10 *cm* draft: (a) barriers at 60 *cm* distance; (b) barriers at 120 *cm* distance; (c) barriers at 180 *cm* distance; mean flow velocity is 20 cm/s

5.4 Numerical model of barrier with oil

To investigate the effect of contained oil on the velocity field behind the barrier, same models as in the Sec. 5.3 were built up in presence of oil. The flow in the flume was modeled, and once the flow was fully established the oil was released into the model as a thin layer over water surface upstream of the barrier.

The oil volume was 0.2 m^3/m, and it had properties similar to rapeseed oil: density $\rho_o = 0.91\ gr/cm^3$, viscosity $\nu_o = 88.8\ cSt$, and oil-water interfacial tension, $\sigma_{ow} = 30\ mN/m$. To model the oil cohesion correctly, the molecular weight of 700 (the same as rapeseed oil) was also specified. To model the multiphase flow, the Volume of Fraction model (VOF) was used.

5.4.1 Numerical model characteristics

The VOF model can model two or more immiscible fluids by solving a single set of momentum equations and tracking the volume fraction of each of the fluids throughout the domain. It is a surface-tracking technique applied which is designed for two or more immiscible fluids where the position of the interface between the fluids is of interest. Typical applications include the motion of large bubbles in a liquid, the motion of liquid after a dam break, and the steady or transient tracking of any liquid-gas interface.

The VOF formulation relies on the fact that two or more fluids (or phases) are not interpenetrating. For each additional phase that is added to the model, a variable is introduced: the volume fraction of the phase in the computational cell. In each control volume, the volume fractions of all phases sum to unity. The fields for all variables and properties are shared by the phases and represent volume-averaged values, as long as the volume fraction of each of the phases is known at each location. Therefore, the variables and properties in any given cell are either purely representative of one of the phases, or representative of a mixture of the phases, depending upon the volume fraction values.

5.4.2 Modeling conditions

For simulations including oil slick, the geometry was the same as simulations without oil. The model was unsteady, and a $k - \epsilon$ model was applied for the turbulence. It was intended that the simulation be conducted for three phases, i.e. air, water, and oil. Hence, the air over the flume was also simulated in earlier models. This gave the possibility to take into account the wind effect as well as oil-air interfacial tension.

To verify the influence of ignoring air phase, two simulations with the same conditions were done with and without air. In the present study that wind effect is not considered, the advantage of simulating air phase was thus, a more realistic shape for headwave, as it is shown in Fig. 5.18. Additionally, accounting for oil-air interfacial tension in three-phase model results in a more realistic slick length. However, the difference in slick length for two-phase and three-phase models was less than 5%. On the other hand, running a three-phase model took

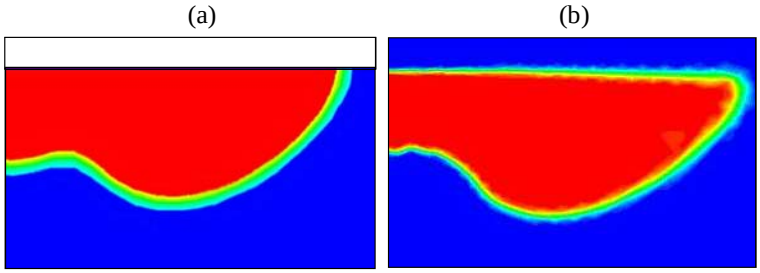

Figure 5.18: Slick headwave in: (a) two-phase, (b) three-phase models

an enormous time comparing to a two-phase (water-oil) model. Therefore, it was decided to make simulations with two-phase water-oil fluid.

The mesh should be fine enough to be capable of capturing the interface. Therefore, a finer mesh was used for the upstream region where the oil slick forms.

5.4.3 Boundary conditions

Following conditions were set at each boundary of the model:

- **Free-surface:** Slip wall condition with no shear was considered for oil-water model. However, for three-phase simulations the "open flow" was selected. FLUENT can model the effects of open channel flow using the VOF formulation and the open channel boundary condition. These flows involve the existence of a free surface between the flowing fluid and fluid above it, generally the air.

- **Bottom:** No slip wall condition was applied.

- **Inlet:** The velocity distribution was linear and horizontal, decreasing along the depth with a mean flow velocity of 20 cm/s as for simulations without oil. Volume of oil per unit length of the barrier was prescribed and the transient boundary condition at the inlet for oil volume fraction was programmed. The program calculates the time that a certain oil volume needs to enter the model with the same velocity as water, and during that time oil gets into the model.

- **Outlet:** The outflow boundary condition was considered.

- **Barrier:** No-slip wall condition was applied.

5.4.4 Results of models with oil

The intrusion of oil into the model and the evolution of slick shape is shown in Fig. 5.19. When oil enters the model it approaches the barrier and after reaching the barrier it is reflected. Although the shape in the first moments of

accumulation of oil behind the barrier does not correspond exactly to experiments, after a while the slick gets to an equilibrium condition and then the shape does not change anymore.

The velocity contours for rigid and flexible barriers are shown in Fig. 5.20 and Fig. 5.21 respectively. In these figures the volume fraction of oil and the corresponding slick shape in experimental model at the same flow velocity are also illustrated. Same as in the experiment, the headwave was formed at upstream end of the slick. Comparing the results with those of Sec. 5.3 indicates that the presence of oil could change the velocity filed significantly. Without oil slick, the barrier functions as a bluff edge in the flow. However, oil slick causes the gradual narrowing of the flume in the proximity of the barrier, and the headwave deviates the streamlines. A local zone with high velocity can be seen near to headwave. This phenomenon has been also evidenced in UVP measurements (see Sec. 4.4.2).

Fig. 5.22 shows the streamlines in the middle part of the flume where barrier is containing the oil slick. It can be seen that the presence of oil can significantly change the flow pattern downstream of the barrier, specially if the barrier draft is not too big in comparison with the oil thickness. Different flow pattern and turbulence wake size, in comparison to simulations without oil, can lead up to different pressure distributions on the skirt.

The circulation in the oil phase could also be modeled as illustrated in Fig. 5.22. As it can be seen in Fig. 5.20 and 5.21, the velocity magnitude in oil is only few centimeters which is in agreement with UVP measurements.

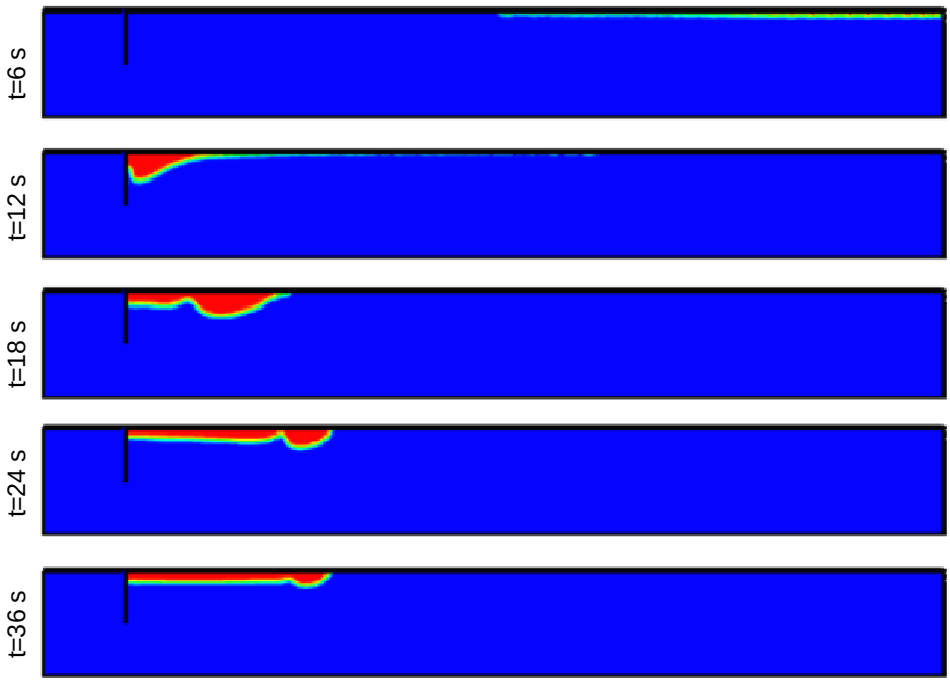

Figure 5.19: Intrusion of oil into the model and slick shape evolution behind a rigid barrier with 20 cm draft; mean flow velocity is 20 cm/s; oil starts to get into the model at $t = 0$ s

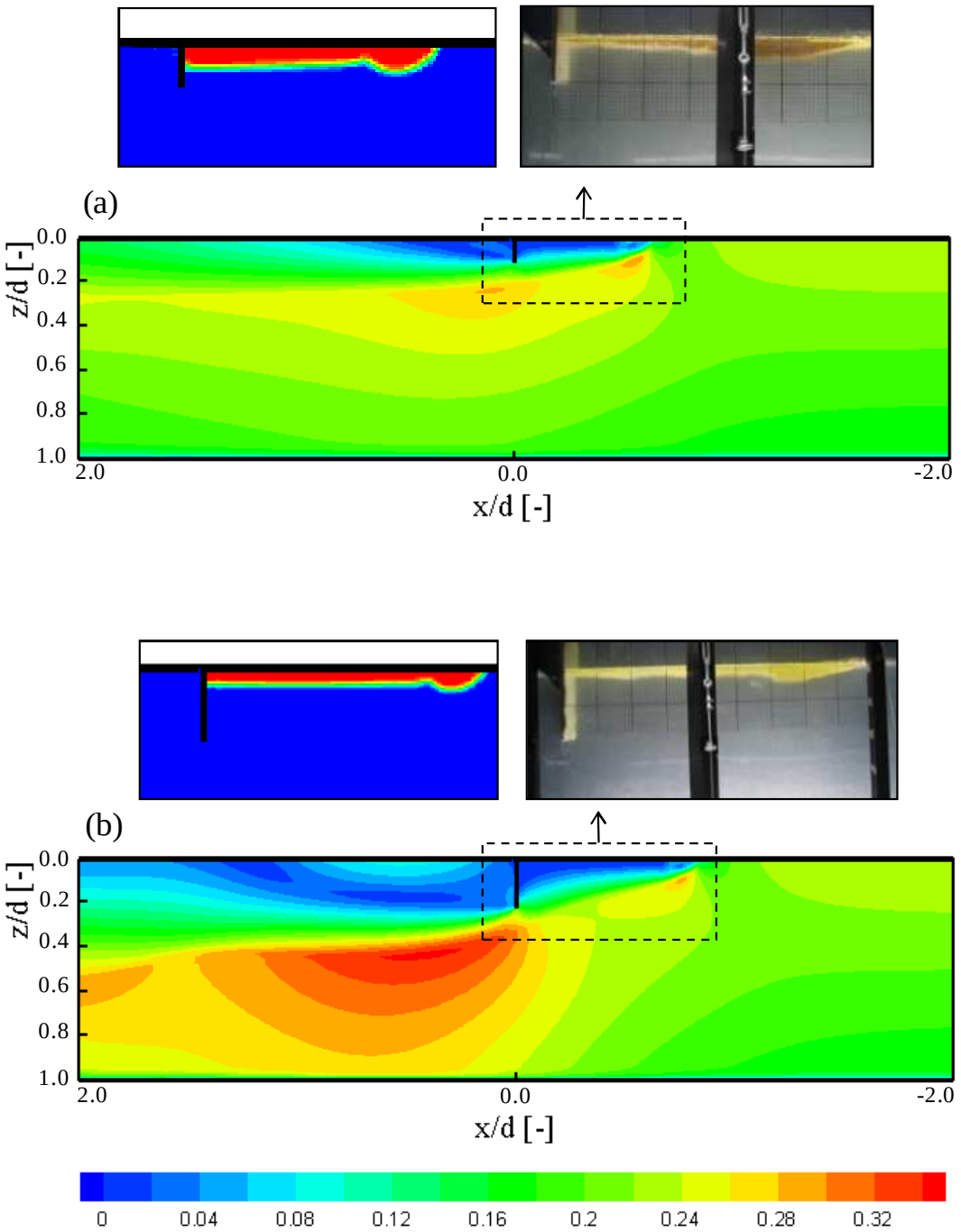

Figure 5.20: Contours of velocity magnitude in the middle of the flume for rigid barriers containing 20 lit/m oil: (a) barrier with 10 cm draft, (b) barrier with 20 cm draft; mean flow velocity is 20 cm/s; slick shape in numerical and experimental models are compared

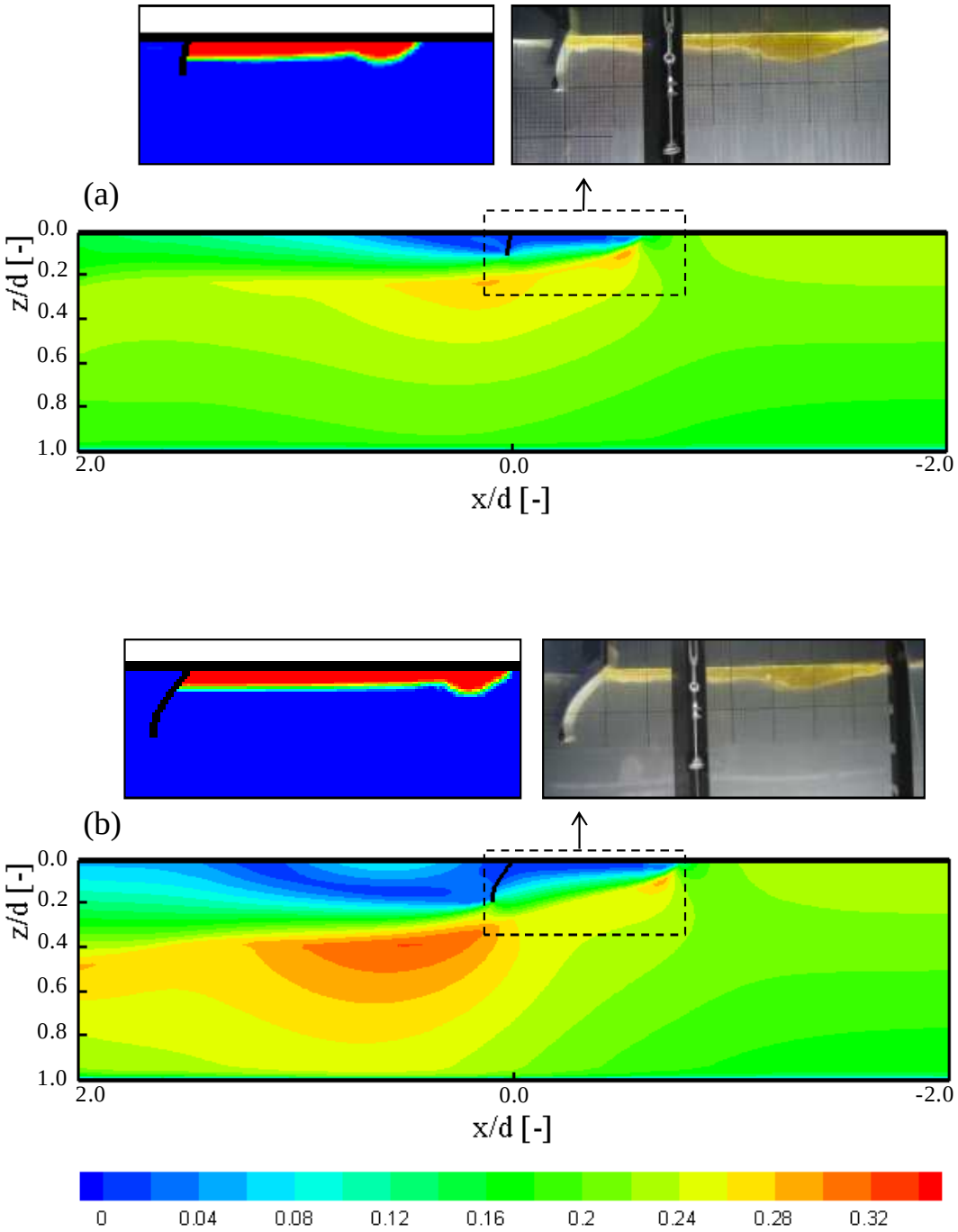

Figure 5.21: Contours of velocity magnitude in the middle of the flume for flexible barriers containing 20 lit/m oil: (a) barrier with 10 cm draft, (b) barrier with 20 cm draft; mean flow velocity is 20 cm/s; slick shape in numerical and experimental models are compared

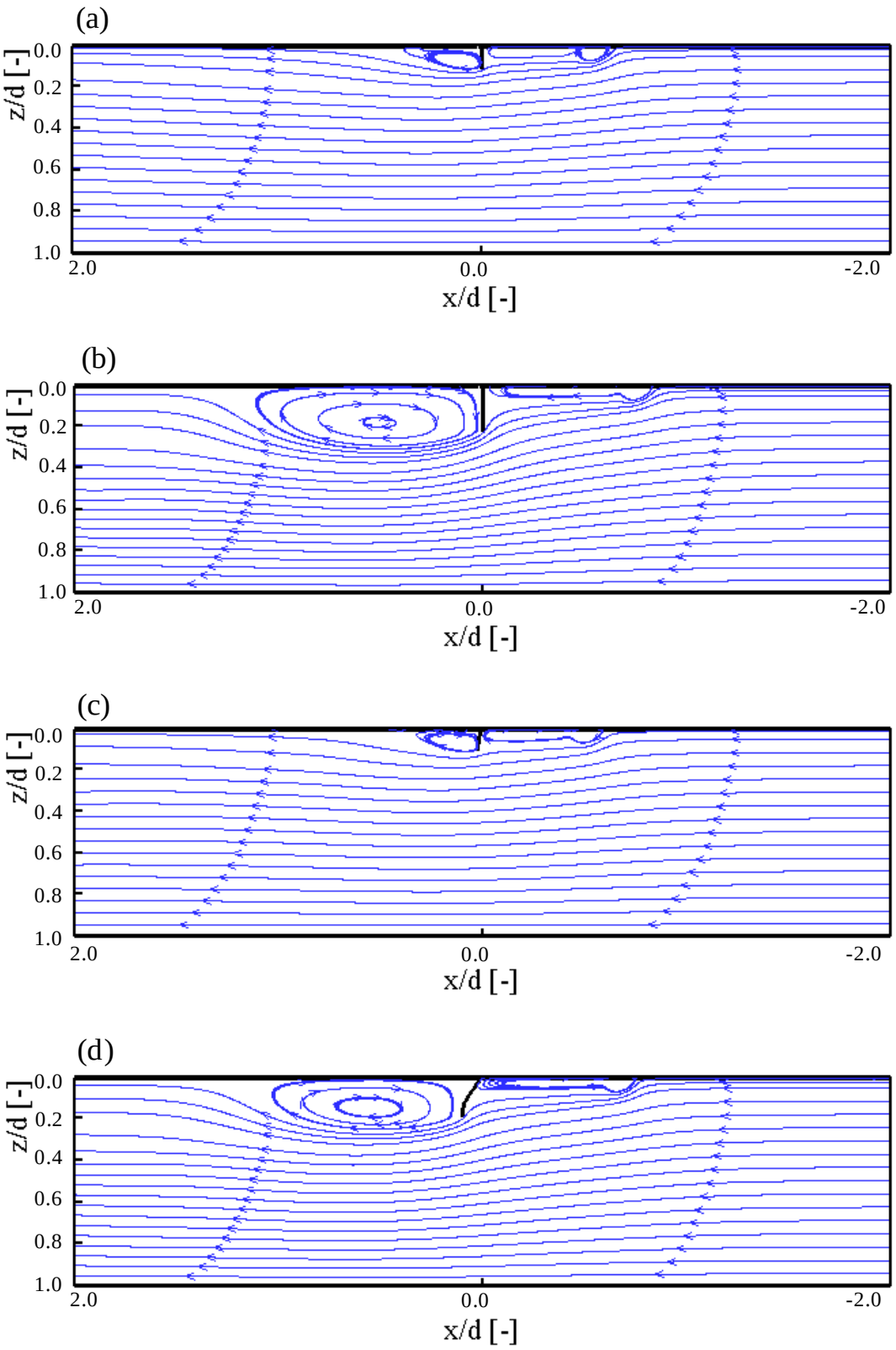

Figure 5.22: Streamlines in the middle of the flume for flexible barriers containing 20 lit/m oil: (a) rigid barrier with 10 cm draft; (b) rigid barrier with 20 cm draft; (c) flexible barrier with 10 cm draft; (d) flexible barrier with 20 cm draft; mean flow velocity is 20 cm/s

5.5 Simulation of real size booms

The purpose of simulation of real size booms was to estimate the forces imposed on the barriers in reality.

The force exerted on a body moving in a medium like air or water depends in a complex way upon the square of the velocity of the body relative to the medium, the viscosity and density of the medium, the shape of the body, and the roughness of its surface. Two objects of the same frontal area moving at the same speed through a fluid will experience a drag force, F_d, proportional to their drag coefficient, C_d:

$$F_d = \frac{1}{2}\rho_w U^2 C_d A \tag{5.5}$$

where ρ is the water density, U is the towing velocity, A is the frontal profile and represents the front projection length of the barrier, and C_d is the drag coefficient.

The drag coefficient, C_d, is not constant. It depends upon the velocity of the body, viscosity of the medium, the shape of the body, and the roughness of the body's surface. When the flow is turbulent ($Re > 1000$), the drag coefficient, C_d, is approximately constant (Batchelor, 1967).

Flow patterns and consequently drag forces can change when the barrier deforms. Therefore, understanding the flow pattern is essential to calculate or approximate the forces and moments acting on bodies in the flow. In this section, the drag force on the barrier is computed and the results for drag coefficient, C_d, are discussed.

5.5.1 Modeling and boundary conditions

To assure that the pressure on the barrier is not influenced by model boundaries, two-dimensional full scale models (first mode of skirt deformation) were built up with water depth 10 times and the barrier distance to inlet and outlet 20 times the barrier draft. Since the inlet boundary is at a considerable distance from the key area, i. e. near oil slick, the choice of velocity profile at the inlet is not important (Fang and Johnston, 2001a). Hence, the water flow is considered a horizontal uniform flow.

As it was concluded from the experimental study, the maximum towing velocity seldom pass 0.3 m/s in real cases. Therefore the imposed forces on the barrier are derived from the numerical simulations for the maximum velocity that barrier can experience, i. e. 0.3 m/s. However, to study the effect of barrier flexibility on drag force at different velocities, some simulations were done with lower towing velocities. Finally a series of simulations were carried out for a flexible, 2 m draft barrier containing oil slicks with different volumes. The simulation conditions are summarized in Table 5.1. The boundary conditions were defined same as in Sec. 5.3.

Table 5.1: Conditions of full scale numerical models

Group	**Draft** $[m]$	**Ballast weight** $[kg/m]$	**Towing velocity** [m/s]	**Oil volume** $[m^3/m]$
Rigid barrier,	1.0	-	0.30	-
No oil	1.5	-	0.30	-
	2.0	-	0.30	-
Flexible barrier,	2.0	10	0.20	-
No oil	2.0	10	0.25	-
	2.0	10	0.30	-
Flexible barrier,	2.0	10	0.30	1.0
With oil	2.0	10	0.30	2.0
	2.0	10	0.30	3.0
	2.0	10	0.30	4.0

5.5.2 Results of simulations of real size booms

FLUENT provides the possibility of calculating the pressure distribution on the barrier and obtaining the pressure force. The pressure and viscose forces along the specified force vector $\vec{a}$ on a wall zone is computed by summing the dot product of the pressure and viscose forces on each face with the specified force vector. Forces applying in the flow direction and resisting the movement of a solid object through a fluid are called drag forces (forces in direction perpendicular to the flow are lift). Drag is made up of friction forces, F_v (viscous drag), and pressure forces, F_d (shape drag). By choosing the direction of $\vec{a}$ in the directional of the fluid, both viscose and shape drag forces can be computed on barrier front and rear faces. The net drag force can then be obtained by summation of front and rear forces.

A maximum value for the contribution of viscous drag per unit width on a flat plate aligned with the flow can be estimated by the following expression (Batchelor, 1967):

$$F_v = 1.33\rho_w U^2 L Re^{-1/2} \tag{5.6}$$

where L is the characteristic length (barrier draft), U is the flow/towing velocity, and ρ_w and Re are water density and the Reynolds number respectively. For the parameters involved here, this value is at least two order of magnitude below the total drag, thus shape drag predominates and the viscose force is negligible in comparison to the pressure force. Hence in this study, only the shape drag force, F_d, is considered.

In the present study, on the basis of barrier length, flow velocities, and

Table 5.2: Drag force and drag coefficient for rigid barriers at mean flow velocity of 0.3 m/s

Draft $[m]$	**Drag force per unit length** $[N/m]$	$\boldsymbol{C_d}$ [-]
1.0	84.6	1.88
1.5	128.9	1.91
2.0	172.6	1.92
		$\bar{C}_d$ =1.90

water viscosity, the Reynolds number is typically large, in the range of 30'000 to 60'000. The classical theory of flow with such a high Re number predicts that a moving rigid object experiences a drag proportional to the square of its speed (Batchelor, 1967).

The computed drag force applied on rigid barriers and the value of drag coefficient, C_d, are shown in Table 5.2. As it is given, the drag coefficient varies between 1.88 to 1.92 for rigid barriers, with a mean value of 1.90.

5.5.2.1 Effect of barrier flexibility on drag force

For flexible barriers, unlike the rigid ones, as the flow velocity is increased the body changes its shape by bending and so presents a smaller frontal profile to the flow. Performing experiments with fibers of different flexibility in a soap film flow, Alben et al. (2002) showed that the deformation of flexible fiber lead to a reduced growth of drag with flow speed. In other words, the drag induced by a nearly rigid fiber was well-approximated by U^2 growth, while the drag for a flexible fiber showed a decreased drag approximated by $U^{4/3}$.

The numerical simulations in the present study also showed a decrease in drag force for flexible barriers. The values of computed drag force for a flexible barrier with 2 m draft and 10 kg/m ballast weight are presented in Table 5.3. The value of classic drag coefficient, $C_d = 2F_d/U^2\rho A$ was also calculated and is presented in the same table. As it is given, the value of C_d decreases for flexible barrier which is a result of shape deformation of flexible barriers. For the studied case, the results showed the drag to be approximated by $U^{5/3}$:

$$F_d = \frac{1}{2}\rho_w U^{5/3} C_f D \tag{5.7}$$

where the characteristic length is the barrier draft, D, instead of the frontal area, A. A new drag coefficient, called C_f, is then proposed which was equal to 1.0 for the studied case.

To find the value of C_f as a function of ballast weight, more simulations with different ballast weights should be conducted.

Table 5.3: Drag force and coefficient for a flexible barrier with ballast weight per length, B, equal to 10 kg/m, and barrier's draft, D, equal to 2 m at different flow velocities

Towing velocity $[m/s]$	**Frontal profile** $[m]$	**Drag force per unit length** $[N/m]$	$\boldsymbol{C_d}$ [-]
0.20	1.88	71.4	1.90
0.22	1.79	81.4	1.88
0.25	1.74	98.1	1.81
0.27	1.68	110.0	1.80
0.30	1.63	130.2	1.78

Comparison between the drag force on a rigid barrier with 2 m draft towed by a velocity of 0.3 m/s in Table 5.2 with those of a flexible barrier with the same draft and towing velocity in Table 5.3 (numbers in box) reveals that the forces on the skirt could be appreciably reduced by allowing the flexibility.

5.5.2.2 Effect of contained oil volume on drag force

Since the presence of oil slick can modify the flow pattern (compare Fig. 5.12 and Fig. 5.22), it was expected that it can influence the drag force as well. Fig. 5.23 shows the variation of drag force by increasing the contained oil volume. Due to change in streamlines, the drag force reduces by adding oil to the model for oil volumes less than 2 m^3/m. However, for oil volume more than 2 m^3/m, the slick length increases and the headwaves locates further to the barrier. Therefore, the flow pattern close to the barrier, and consequently the drag force do not change considerably.

5.5.2.3 Forces in towing cable

To estimate the towing force in the cables which are used to moor the Cavalli system the pressure distribution in the plan should be estimated by means of a three-dimensional model. However a simple approach is to apply empirical equations as it is described below.

The calculated force using Eq. 5.7 gives the drag force at centerline of the towed reservoir, i.e. section m-m in Fig. 5.24a. It is assumed that the towing force, T, is mainly for overcoming the drag force on the catenary shape part of the reservoir, as it is shown in Fig. 5.24b, and a towing force equal to $T/2$ is needed to tow the system. Performing full-scale experiments Milgram (1973), found a dimensionless parameter, so- called tension parameter τ, that gives an estimation of the pressure distribution for the catanary shape:

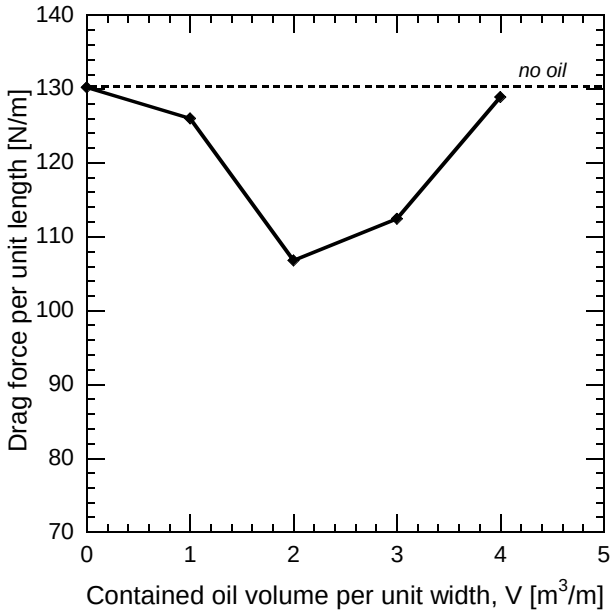

Figure 5.23: Effect of contained oil volume on drag force for a flexible barrier with 2 m draft and 10 kg/m ballast weight

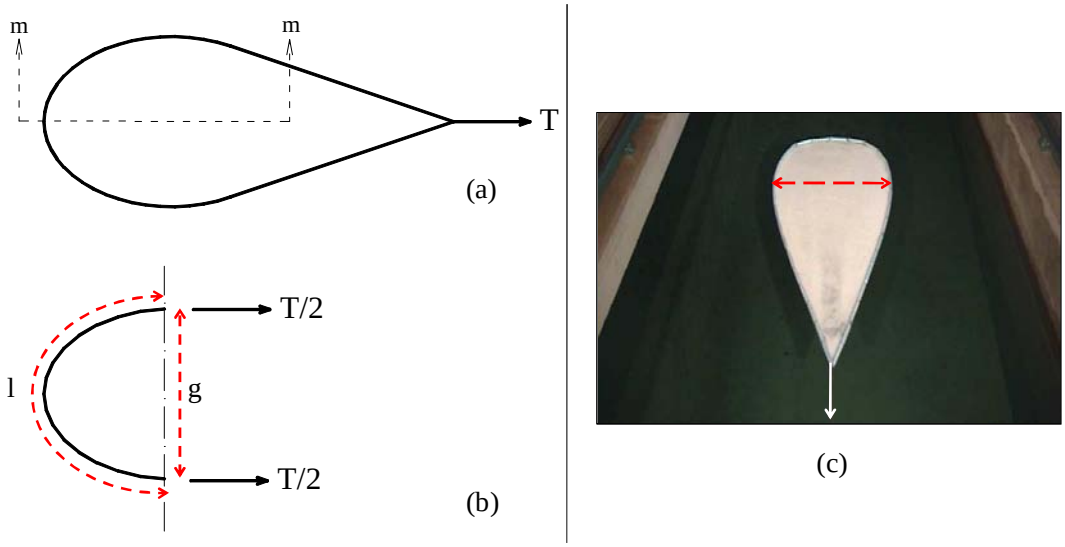

Figure 5.24: Schematic drawing of the towed Cavalli system (left), and experimental model of Cavalli system in the towing tank (right) (Sayah et al., 2004)

$$\frac{T}{2} = \tau l F_d \tag{5.8}$$

The value of τ depends on the gap ratio parameter of the catanary shape, i.e. the opening, g, divided by total barrier length, l, as previously presented in Fig. 2.9. Experiments in a towing tank held by Sayah et al. (2004) for Cavalli system (Fig. 5.24c) showed the barrier to exhibit a semi circle at its end, thus the gap ratio is $2/\pi$. Fig. 2.9 give a tension parameter, τ equal to 0.2.

5.6 Conclusions

Numerical simulations helped in comparing the velocity field in the vicinity of barriers of different types (rigid or flexible) and with different drafts. The simulated velocity field was in good agreement with LSPIV and UVP measurements. The extension of turbulence wake upstream of the barrier was obtained for different barriers. It was shown that for rigid barriers the stagnation point is at a distance of about 8 to 10 times the barrier draft from the barrier; whereas, for flexible barriers this distance is 6 to 8 times the barrier draft.

Two rigid barriers located at a certain distance from each other were subject of some numerical simulations. It was shown that when barriers are close to each other, the velocities in the space between two barriers are very low. By increasing the barriers distance, the velocities become more considerable. Hence, if two parallel barriers are located in a small distance from each other, they can be very efficient to protect a trapped slick. However, if two parallel barriers are supposed to work as tandem booms, the distance should be more than 12 time the barrier draft in a way that the downstream barrier locates after the turbulence wake of the upstream one.

To model the oil slick containing by the barrier, the VOF method was used. the results show good agreement with UVP measurements. The slick shape was the same as experiments with a headwave at upstream end. It was concluded that the presence of oil can significantly change the flow pattern downstream of the barrier. The circulation in oil phase was successfully modeled and the velocity magnitude was very low as it was measured by UVP device.

Computations proposed a drag coefficient, C_d, of 1.90 for rigid barriers. Moreover, results of numerical computations pointed out that for flexible barriers a constant value for the drag coefficient cannot be attributed, since it deforms and does not have similar shape at different velocities.

Chapter 6

Concluding summary, Recommendations, and Outlook

6.1 Summary and conclusion

6.1.1 Oil spill problem and clean-up technique

Oil spills are of major environmental concern in coastal regions. The movement of the oil slicks can pollute the coastal environment and damage marine life. Most oil spills occur during operational discharges of ships in the vicinity of marine oil platforms as well as from accidental tankers collision and grounding.

Experience shows that even best efforts cannot prevent the occasional occurrence of major accidents at sea. The need to confine spilled oil to a small area as quickly as possible, in relatively thick layers, is a practical necessity. Practically, many competitive methods are available; but, they are mainly associated with adverse side effects. Containment and physical removal is recognized to be the most desirable methods of oil spill cleanup. Mechanical oil barriers, or "booms", are used to contain or divert oil spills on water and are key tools in oil spill response. Booms are the most commonly used techniques to collect and contain oil on the sea surface, or to protect specific areas against slick spreading.

A new anti-pollution system has been designed by Cavalli in 1999. The aim was to trap the spilled oil in a floating reservoir and to improve the removal process by increasing the oil layer thickness. It can be used around or in close proximity to tankers and offshore platforms. The floating reservoir is made of several self-inflating curtain booms, made of Kevlar with a ballast at the end point. As a first step, oil spill is confined by a reservoir, avoiding its spreading over water surface. The reservoir can then be subdivided into two or four circles, in order to decrease its surface and increase the oil layer thickness. This improves the pumping operation by reducing the amount of water drawing up.

The Cavalli system is supposed to be carried by oil tankers and be deployed around the slick during the first hours after accident, when the oil in not yet weathered or emulsified. Hence, it will mainly deal with fresh crude oils with a viscosity less than 1'000 cSt (Delvigne, 1989).

Several mechanisms can cause the oil booms to fail. There are three main

failure mechanisms: entrainment, drainage, and critical accumulation failures. For oils with a viscosity in the order of less than 1'000 cSt, droplet entrainment failure occurs at a lower velocity than does drainage failure, so the former failure mechanism dictates the limits for effective containment.

Entrainment failure occurs when a high relative oil-water velocity causes interfacial waves to form and oil droplets to be entrained from the oil-water interface and pass beneath the barrier (Wicks, 1969; Milgram and Van Houten, 1978; Fannelop, 1983; Delvigne, 1989; Lee and Kang, 1997).

Oil spill removal and control in open seas is seldom conducted in calm conditions, so the effects of waves and turbulence on the performance of oil spill equipment must be faced. However, only few researchers studied the wave effect on containment efficiency (Fang and Johnston, 2001a,b,c).

On the other hand, although the flexible barriers become more and more common as a cleanup facility, the knowledge about their behavior is lacking. An extensive literature review showed that almost all existing research, either physical or numerical, has been done for rigid barriers.

The main motivation for introducing the present research project is to study the efficiency and operational limits of the Cavalli system. However, the objectives are not constrained to this particular case. The present investigation focuses on the behavior of flexible barriers containing spilled oil. Previous researches of containment booms, even for the case of rigid barriers, have been mainly carried out in calm water. Accordingly, the main concentration is devoted to the response of a flexible barrier in presence of sea waves, which had not yet been revealed previously. The study was conducted using both experimental and numerical modeling.

6.1.2 Description of experimental set-up and conditions

Experiments were conducted in a 12 cm wide, 6.5 m long and 1.2 m deep laboratory flume, with both rigid and flexible barriers, and in absence and presence of waves.

Fabricating a flexible barrier that can deform under flow conditions, and at the same time, is tight enough so that oil can be contained behind it without leakage from the sides, was the key challenge. This has been achieved using a slitted side skirt on the boom where it faces the lateral wall of the flume (Fig. 3.8).

The *rapeseed* oil was chosen for experimental study. The viscosity is 88.8 cSt and the density is 0.91 gr/cm^3 at room temperature. For such an oil the dominant failure mode was found to be entrainment failure.

The formation of droplets is caused by unstable waves (Kelvin-Helmholtz instability) on the interface. The interfacial waves and instabilities are influenced only by three oil parameters: density difference between oil and water, $\Delta\rho$, viscosity, ν, and interfacial tension, σ_{ow}. Hence, using real oil allowed doing full scale experiments to model droplet entrainment failure.

To investigate the wave effects, experiments were taken out in presence of five different experimental waves (see Table 3.4), where Froude similarity rule

could be considered using Eq. 3.4a and 3.4b. To generate experimental waves a pneumatic wave generator was used.

6.1.3 Physical properties of flow and contained slick in the vicinity of the barrier

The evolution of the slick shape upstream the barrier, due to increase of flow velocity, was subjected to some observations and measurements. The fluctuations at oil-water interface started at a mean flow velocity of about 12 cm/s. The Kelvin-Helmholtz threshold instability velocity, U_{KH}, for rapeseed oil and water was calculated to be 14.7 cm/s using Eq. 2.2. As it was explained by Hogan and Ayyaswamy (1985), the threshold velocity could be smaller than in the classical KH instability by factor $\sqrt{\rho_o/(\rho_w + \rho_o)}$ because of important viscosity contrast of the two fluids. Multiplying this latter factor to the classical KH instability velocity yields a velocity of 10.8 cm/s for the instability initiations, which is in a good agreement with the observed threshold velocity of instability.

For low flow velocities (< 18 cm/s), the oil slick formed a monotonous layer over the water surface. At a flow velocity of about 18 cm/s, a small headwave was formed at the upstream end of the slick, that approached the barrier by increasing the flow velocity and consequently decrease of the slick length. The interfacial waves became more significant at the headwave and propagated toward the barrier.

At higher flow velocities, the interfacial waves broke up on the headwave, causing droplets to be shed into the flowing water. The velocity at which droplets started to form was 24 to 26 cm/s in the present study. This is in quite good agreement with the value predicted by Wilson (1977) who proposed a minimum flow velocity of $1.55U_{KH}$ =22.8 for droplet shedding from the headwave.

Before reaching the failure velocity, the droplets detached and immediately rejoined the slick. At initial failure velocity, U_f, a part of detached droplets passed beneath the barrier, while the other part coalesced the slick. By increasing the flow velocity, a bigger part of droplets passed the barrier and loss rate increased. The length of slick decreased by increasing the mean flow velocity, while its thickness, particularly at the headwave, increased.

The waves could change the containment limits and conditions. On the one hand, in presence of waves a thicker and shorter slick formed upstream of the barrier; on the other hand, waves provoked instabilities in oil-water interface and consequently reduced the initial failure velocity. Like experiments without waves, the failure mode was entrainment failure. Nevertheless, for some experiments a type of drainage failure, namely surging drainage, was observed. The failure occurred when waves caused increase of oil layer thickness and interfacial wave height, and consequently led to occasional drainage under the barrier.

Accurate velocity measurements in oil and water were performed using UVP and LSPIV methods:

– UVP measurements provided precise results of horizontal velocity in oil-water two-phase fluid. The obtained results were useful to evaluate the

physics of oil slick, particularly the headwave region.

The headwave at upstream end of the oil slick was compared, in detail, to those of a gravity current. It was concluded that despite geometrical similarities, these two phenomena are quite different. Comparison between results of measurements with and without oil slick confirmed the noticeable influence of oil on velocity field behind the barrier.

The capability of UVP measurements in detecting the oil-water interface was approved and it was shown that the location of maximum ultrasonic echo intensity can be representative for the interface. Furthermore, the velocity profiles in each phase were derived and it could be revealed that the friction layer is located in the water, since water is less viscose and the energy dissipation is less in it.

– Measurements by means of LSPIV method helped in investigating the velocity fields and flow patterns in the vicinity of barriers with different conditions. The extension of zone with high velocity beneath the barrier with different types and drafts was investigated, and later used to calibrate the numerical model.

To improve the understanding of the mechanisms associated with oil containment failure, numerical models were built up to simulate the oil slick behind different barriers. The extension of turbulence wake downstream of the barrier was obtained for different barriers. It was shown that the for rigid barriers the stagnation point is at a distance of about 8 to 10 times the barrier draft from the barrier; whereas for flexible barriers, the distance is 6 to 8 times the barrier draft. Furthermore, to model the oil slick contained by the barrier, the Volume of Fraction (VOF) method was used and the effect of oil slick on flow pattern and velocity field was evaluated.

6.1.4 Oil slick geometrical characteristics

Slick length:

The slick length upstream of the barrier depended mainly on the oil volume. The only part of slick whose thickness and consequently its length was affected by the barrier draft or shape, due to the formation of a circulation cell upstream of the barrier, was the near-boom region. This region contains a small volume of the slick compared to the other parts, and it was observed to be extended about one times the draft upstream of the boom in numerical models. Therefore, the barrier geometry did not affect the slick length significantly.

An empirical relationship was proposed in Eq. 4.2 to estimate the length of oil slick, L_s, as a function of involved parameters:

$$L_s = V^{2/3}[-11.7 \ln U - \frac{2}{\sqrt{D}}]$$

The equation gives the value of slick length, L_s, in m, where initial oil volume, V, is in m^3/m, mean flow velocity, U, is in m/s, and barrier draft, D, in m.

Waves affect the slick length significantly by pushing the slick to accumulate behind the barrier. The decay of slick length as a result of increasing velocity, $\Delta L/L_s$, in presence of waves with steepness s, could be predicted by Eq. 4.10 as:

$$\frac{\Delta L}{L_s} = 19.35\ \sqrt{s}\exp\left(7.56U\right)$$

where $\Delta L = L_s - L_{sw}$ and U is the mean flow velocity in m/s.

Headwave:

The instability at oil-water interface starts from the headwave. The barrier type (flexible or rigid) and its draft were shown to have no significant influence on the headwave thickness. Increasing the flow velocity caused the increase of headwave thickness with a linear trend. The proportion of headwave thickness to the equivalent thickness of the slick (oil volume divided by the area it occupies) varied between 1.5 to 2.5. Considering results of experiments with both rigid and flexible barriers, Eq. 4.3 was obtained to calculate the headwave thickness, t_h:

$$t_h = 1.4\sqrt{V}U$$

The equation gives the thickness in m, where oil volume, V, is given in m^3/m and the mean flow velocity, U, is in m/s. In presence of waves, the headwave was more unstable and its thickness was increased as the wave steepness increased.

It should be noticed that the empirical equations for predicting the oil slick length and the headwwave thickness are only valid for rapeseed oil, or oils with similar characteristics, and for mean flow velocities less than 30 cm/s.

6.1.5 Containment failure

Initiation of entrainment failure:

It is generally stated that loss initiates for oil booms at a flow velocity of 0.5 to 1 *knot* (25 to 50 cm/s) (Cormark, 1999). Experiments with rigid and flexible barriers showed the initial failure velocity to be 31 ∓ 2 cm/s for all types of examined barriers when no wave exists. The initial failure velocity was somehow dependent on the barrier draft and it increased slightly by increasing the draft. Therefore, based on the equation proposed by Lee and Kang (1997), an empirical equation, Eq. 4.5, was suggested to predict the initiation of entrainment failure, U_f:

$$U_f = 1.98U_{KH} + 0.08\sqrt{g\Delta D}$$

where U_{KH} is the Kelvin-Helmholtz stability threshold velocity derived from Eq. 2.2 in m/s, Δ is relative oil density calculated from Eq. 2.5, and D is the barrier draft in m. This equation includes the properties of water and oil and can be applied for all low-viscous oils in case of entrainment failure. The initial failure velocity was nearly the same for rigid and flexible barriers, because the

droplet detachment starts at headwave and depends on the oil-water relative velocity, and a flexible barrier does not change significantly the velocity field at headwave.

Effect of different wave parameters on initiation of failure was studied. Increase of wave height reduces the initial failure velocity. However for small wave heights, this reduction was not noticeable. For a prototype, the effect of wave height on initial failure reduction starts at a wave height of about 0.5 m.

By decreasing the wave period (increasing the frequency), interfacial waves became more aggressive and consequently, failure initiated at a lower velocity. Flexible barriers were more sensitive to variations of wave period. Applying the time scale, a critical wave period of 5.8 s can be proposed for the prototype.

It was found that the wave steepness is a representative parameter to reveal the effect of waves, since it includes the effect of both wave height and period. For experiments with a rigid barrier, wave steepness of less than 0.01 could not affect the failure initiation, whereas flexible barriers due to its deformability were more sensitive to presence of waves, and even waves with low steepness could cause a decrease in initial failure velocity.

To take into account the effect of waves Eq. 4.9 can be used for prediction of failure initiation:

$$U_f = 1.98U_{KH} + 0.08\sqrt{gD\Delta} - \frac{5}{3}s$$

This equation gives the failure velocity, U_f, in m/s, where the draft, D, is introduced in m, and can be applied for low-viscous oils in presence of waves with steepness up to 0.04.

Loss rate due to entrainment failure:

In absence of waves it was observed that a longer draft can change the loss rate considerably, and Eq. 4.8 was proposed to assess the loss rate,q_E:

$$q_E = 122.79\ D\ V^{2/3} \exp\left(22.65\ I_U\right) + \frac{2.43\ I_U}{D^3\ V^{7/3}} - 0.74$$

where q_E is the loss rate in $cm^3/m/s$, I_U is the increment of the flow velocity in m/s comparing to the initial failure velocity, V is the initial oil volume in m^3/m and D is the barrier draft in m. Since the entrainment phenomenon was modeled at full scale, the equation can be used directly for the prototype, such as all other proposed equations.

Moreover in presence of waves, it was noticed that the loss rate increased more rapidly for experiments with stronger waves (s >0.01). In the case of a steep wave, the loss rate augmented very rapidly after initiation of failure. The loss rate was almost the same for experiments without waves and for experiments with weak waves (s <0.01).

Drainage failure:

Although main part of the study was dedicated to investigating effective parameters on entrainment failure, two cases with drainage failure were also

considered. Drainage failure happens when oil plunges under the boom and escapes with the passing water (Cross and Hoult, 1971; Wilkinson, 1972a; Lau and Moir, 1979; Ertekin and Sundararaghavan, 1995).

1. LECA experiments provided qualitative understanding of drainage failure in absence of waves. The occurrence and rate of drainage failure was highly dependent on the barrier characteristics. As a result, LECA experiments were important due to their role in investigating the effect of a flexible barrier.

   The obtained results concerning the barrier flexibility, highlighted the necessity of conducting experiments that are aimed to study drainage failure with flexible barriers, since it could modify the results significantly.

2. The surging drainage failure occurred when waves caused increase of oil layer thickness and interfacial wave height, which led to occasional drainage under the barrier. Large wave heights and frequencies increased the fluctuations in velocities near the bottom of the barrier, which provoked oil to drain. As a result, the effect of waves became more crucial, when the oil layer thickness was more and the oil water interface was located closer to the bottom of the barrier.

   Therefore, a key factor in occurrence of drainage failure, is the oil thickness. The equivalent thickness t_{eq}, previously defined in Eq. 4.1, was used to study the effect of the oil thickness and consequently oil volume. Another effective factor was the barrier depth. In fact, what provoked the drainage failure, is a high ratio of the equivalent thickness, t_{eq}, to the barrier draft, D. This ratio, called δ, is defined as t_{eq}/D in Eq. 4.11.

   The drainage happened when the wave height to draft ratio, H/D, was more than $0.0015\delta^{17/4}$. It was seen that by increasing the relative oil thickness, δ, the drainage can happen for lower wave height to draft ratios.

   Since the wave height to draft ratio, H/D, and relative oil thickness, δ, are both dimensionless parameters, the results can be directly used for prototype. As a rough estimation, for an oil layer thickness more than 25% barrier draft, the surging drainage can happen at relatively low wave height to barrier ratios, even about 0.1.

6.1.6 Trapped oil

Experiments with oil trapped between two rigid barriers demonstrated that the oil layer is highly influenced by the wake formed downstream of the first barrier. Induced fluctuations made a surging motion in the oil layer, which led to oil leakage underneath the second barrier. However, a trapping reservoir could increase the initial failure velocity to more than 45 cm/s, if the distance between two parallel barriers was less than 6 times the barrier draft. As a result, while using Cavalli system, in the case of a small slick, the towing velocity can be increased about 50%.

Two rigid barriers located at a certain distance from each other were subject of some numerical simulations. It was shown that when barriers are close to each other the flow velocities in the zone between two barriers are very low. By increasing the distance between barriers the velocities become more considerable. Hence, as it as shown by experimental and numerical models, if two parallel barriers are located in a short distance from each other (less than 6 times the barrier draft) , they can be very efficient to protect a trapped slick.

However, if two parallel barriers are supposed to work as tandem booms, the distance should be more than 12 times the barrier draft in a way that the downstream barrier locates after the turbulence wake of the upstream one.

6.1.7 Forces acting on the barrier

Numerical simulations of a full-scale barrier proposed a drag coefficient, C_d, of 1.90 for rigid barriers to calculate the drag force on unit width of the barrier using Eq. 5.5:

$$F_d = \frac{1}{2}\rho_w U^2 C_d A$$

where A is the frontal profile of the barrier. For flexible barriers, unlike the rigid ones, as the flow velocity is increased the body changes its shape by bending and so presents a smaller frontal profile to the flow. Additionally, the flow patterns and the drag force can change with the barrier.

The numerical simulations in the present study also showed a decrease in drag force for flexible barriers.

It was shown by results of numerical computations that for flexible barriers a constant value for the drag coefficient cannot be attributed, since it deforms and does not have similar shape at different velocities. For the 2 m draft barrier bearing a 10 kg/m ballast weight, the results showed the drag to be approximated by $U^{5/3}$:

$$F_d = \frac{1}{2}\rho_w U^{5/3} C_f D$$

where the characteristic length is the barrier draft, D, instead of the frontal area, A. A new drag coefficient, called C_f, is then proposed which was equal to 1.0 for the studied case.

Comparing the drag force on a rigid barrier with that of a flexible barrier towed by the same velocity pointed out that the forces on the skirt could be appreciably reduced by allowing the flexibility.

Since the presence of oil slick can modify the flow pattern, it was expected that it can influence the drag force as well. Due to change in streamline, the drag force reduces by adding oil to the model for oil volumes less than 2 m^3/m. However, for oil volume more than 2 m^3/m the slick length increases and the headwaves locates further to the barrier. Therefore, the flow pattern close to the barrier, and consequently the drag force, do not change considerably.

6.2 Recommendations for real case

Considering obtained results in the scope of the present study, following points are recommended in case of low-viscosity oil spill containment.

- Influence of the barrier draft to the entrainment initial failure velocity is not considerable. However, in presence of waves or for increasing the towing velocity of a reservoir trapping spilled oil, a deeper draft can increase the efficiency of containment. Regarding all studied aspects, a draft of 1.5 to 2 m is recommended for a flexible barrier.

- The towing velocity should be low enough that no entrainment initiates. Otherwise the loss rate may increase exponentially by increasing the towing velocity. This is more crucial in presence of waves with steepness more than 0.01.

- It is not recommended to tow the reservoir if the wave steepness is more than 0.01. In such a case, the oil can remain trapped by the reservoir on water surface and towing can start later when the waves become weaker.

- In dividing the Cavalli system into smaller circles, in order to increase the oil layer thickness, one should pay attention that oil thickness does not exceed 25% the barrier draft to avoid surging drainage failure in low wave steepness.

- To protect a trapped slick by a closed reservoir and tow it with higher velocities, the diameter of the reservoir should not be more than 6 times the barrier draft.

- If two parallel barriers are used as tandem booms, the distance between them should be more than 12 times the barrier draft.

- For drag force calculations, it is not necessary to account for oil, since the presence of oil leads to smaller drag forces.

- The drag force acting on the unit length of the barrier for a two-dimensional case can be obtained using equations of Sec. 5.5. For an estimation of force in towing cables the diagram of Fig. 2.9 can be applied.

6.3 Suggestions for further research

The following point are suggested to be addressed in a possible follow up of the present research:

- Three-dimensional experiment in wave and towing tanks for a flexible barrier containing oil to evaluate the response of Cavalli system in more realistic circumstances.

- Experiments with other kinds of oil to investigate drainage and critical accumulation failure modes with a flexible barrier. Particularly experimental investigations concerning the drainage failure should be held with a flexible barrier.
- Three-dimensional numerical simulations to assess the pressure distribution and drag force along the barrier.
- Extensive Fluid Structure Interaction (FSI) numerical simulations to take into account the rigidity of the barrier and the ballast weight for achieving a more accurate formulation to assess drag force.
- Conducting full-scale experiments or in-situ measurements to evaluate the results derived from experimental and numerical models.

References

Agrawal, R. K. and Hale, L. A. (1974). A new criterion for predicting head-wave instability of an oil slick retained by a barrier. In *Offshore Technology Conference*, pages 461–466, Texas, USA.

Alben, S., Shelley, M., and Zhang, J. (2002). Drag reduction through self-similar bending of a flexible body. *Nature*, 420:479–481.

Allen, A. A. and Dale, D. H. (1997). Oil slick classification: A system for the characterization and documentation of oil slicks. In *15th International Oil Spill Conference*.

Amini, A., Bollaert, E., Boillat, J.-L., and Schleiss, A. (2004). Preliminary design criteria for oil spill confinement booms. In *Coastal Environment V, incorporating Oil Spill Studies*, pages 411–420, Spain.

Amini, A., Bollaert, E., Boillat, J.-L., and Schleiss, A. (2006a). Experimental investigation of oil spill containment behind a flexible barrier. In *1st Conference on Application of Physical Modelling to Port and Coastal Protection*, pages 71–74, Porto, Portugal.

Amini, A., De Cesare, G., and Schleiss, A. (2006b). Interface tracking and velocity profile in an oil-water two-phase flow. In *5th International Symposium on Ultrasonic Doppler Methods for Fluid Mechanics and Fluid Engineering, ISUD 5*, pages 125–128, Switzerland.

Amini, A., Mahzari, M., Bollaert, E., and Schleiss, A. (2005). Fluid-structure interaction analysis applied to oil containment booms. In *19th International Oil Spill Conference*, Florida, USA.

Amini, A., Schleiss, A., and Mahzari, M. (2006c). Numerical modeling of floating granules containment behind a rigid barrier in a flume. In *7th International Conference on Hydroinformatics*, pages 99–106, Nice, France.

An, C. F., Brown, H. M., Goodman, R. H., and Clavelle, E. (1996). Animation of boom failure processes. *Spill Science & Technology Bulletin*, 3(4):221–224.

ANSYS (2007). www.ansys.com.

ASCE Task Committee (1996). State-of-the-art review of modeling transport and fate of oil spills. *Journal of Hydraulic Engineering-ASCE Task Committee on Modeling of Oil Spills of the Water Resources Engineering Division*, 122(11):594–609.

ASTM (2004). Water and environmental technology: Standard specification for oil spill response boom connection. In *Annual Book of ASTM Standards*, volume 11.04, F962. American Society for Testing and Materials.

Badesha, S. S., Hunt, J., and Wenck, E. (1993). Structural analysis of oil containment booms. In *13th International Oil Spill Conference*, pages 595–603.

Batchelor, G. K. (1967). *An introduction to fluid dynamics*. Cambridge Univ. Press.

Benjamin, T. B. (1968). Gravity currents and related phenomena. *Journal of Fluid Mechanics*, 31:209–248.

Berteaux, H. O. (1976). *Buoy engineering*. New York: Wiley.

Britter, R. E. and Simpson, J. E. (1978). Experiments on dynamics of a gravity current head. *Journal of Fluid Mechanics*, 88(2):223–240.

Brown, H. M., Goodman, R. H., An, C. F., and Bittner, J. (1996). Boom failure mechanisms: Comparison of channel experiments with computer modelling results. *Spill Science & Technology Bulletin*, 3(4):217–220.

Cavalli, U. (1999). Réservoir flottant souple et contractile: Dimensionnement théorique préalable. Unpublished report, Elec-Engineering S.A.

Chandrasekhar, S. (1961). *Hydrodynamics and Hydromagnetic Stability*. Oxford.

Chang, K. A. and Liu, P. L. F. (1998). Velocity acceleration and vorticity under a breaking wave. *Physics of Fluids*, 10(1):327–329.

Chao, X. B., Shankar, N. J., and Cheong, H. F. (2001). Two- and three-dimensional oil spill model for coastal waters. *Ocean Engineering*, 28(12):1557–1573.

Chao, X. B., Shankar, N. J., and Wang, S. S. Y. (2003). Development and application of oil spill model for singapore coastal waters. *Journal of Hydraulic Engineering-ASCE*, 129(7):495–503.

Cho, I. H. and Cho, B. W. (1995). Developement of an optimal oil boom in waves. In *14th International Oil Spill Conference*.

Collins, D. J., Mackey, G. D. M., and Wong, K. T. (1976). The analysis of an emulsified oil slick. In *Eighth Offshore Technology Conference*, pages 889–899.

Cormark, D. (1999). *Response to Marine Oil Pollution - Review and Assessment*, volume 2 of *Environmental Pollution*. Kluwer Academic Publishers.

Cross, R. H. and Hoult, D. P. (1971). Collection of oil slicks. *Journal of the Waterways, Harbors and Coastal Engineering Division, ASCE*, 97(May):313–322.

De Cesare, G. (1999). Use of UVP monitor in applied hydraulics. In *XVI Symposium on Anemometry*, pages 12–13, Czech Republic.

De Cesare, G. and Schleiss, A. (1999). Turbidity current monitoring in a physical model flume using ultrasonic doppler method. In *2nd International Symposium on Ultrasonic Doppler Methods for Fluid Mechanics and Fluid Engineering*, pages 61–64, Switzerland.

Delvigne, G. A. L. (1984). Laboratory experiments on oil spill protection of a water intake. Technical report, Delft Hydraulics Laboratory.

Delvigne, G. A. L. (1989). Barrier failure by critical accumulation of viscous oil. In *11th International Oil Spill Conference*, pages 143–148.

Delvigne, G. A. L. (1991). On scale modeling of oil droplet formation from spilled oil. In *12th International Oil Spill Conference*.

Di Pietro, N. D. and Cox, R. G. (1980). Containment of an oil-slick by a boom placed across a uniform stream. *Journal of Fluid Mechanics*, 96(Feb):613–640.

Drazin, P. G. (1970). Kelvin-Helmholtz instability of finite amplitude. *Journal of Fluid Mechanics*, 42:321– 335.

Drazin, P. G. and Reid, W. H. (2004). *Hydrodynamic Stability*. Cambridge University Press, second edition.

Ertekin, R. C. and Sundararaghavan, H. (1994). Potential and viscous flows past an oil boom: the instability problem. In *13th International Conference of Offshore Mechanics and Arctic Engineering, ASME*, volume I, pages 189–197.

Ertekin, R. C. and Sundararaghavan, H. (1995). The calculation of the instability criterion for a uniform viscous-flow past an oil boom. *Journal of Offshore Mechanics and Arctic Engineering-Transactions of the ASME*, 117(1):24–29.

Fang, F. (1999). *Viscous oil containment under open sea conditions*. PhD thesis, James Cook University.

Fang, F. and Johnston, A. J. (2001a). Oil containment by boom in waves and wind. I: Numerical model. *Journal of Waterway Port Coastal and Ocean Engineering-ASCE*, 127(4):222–227.

Fang, F. and Johnston, A. J. (2001b). Oil containment by boom in waves and wind. II: Waves. *Journal of Waterway Port Coastal and Ocean Engineering-ASCE*, 127(4):228–233.

Fang, F. and Johnston, A. J. (2001c). Oil containment by boom in waves and wind. III: Containment failure. *Journal of Waterway Port Coastal and Ocean Engineering-ASCE*, 127(4):234–239.

Fang, J. and Wong, K. F. V. (2001). Optimization of an oil boom arrangement. In *17th International Oil Spill Conference*, pages 1367–1374.

Fannelop, T. K. (1983). Loss rates and operational limits for booms used as oil barriers. *Applied Ocean Research*, 5(2):80–92.

FLUENT (2007). www.fluent.com.

Giustolisti, O. and Savic, D. A. (2003). Evolutionary Polynomial Regression (EPR): Development and applications. Technical report, School of of Engineering, Computer Science and Mathematics, Centre for Water System, University of Exeter.

Goodman, R. H., Brown, H. M., An, C. F., and Rowe, R. D. (1996). Dynamic modeling of oil boom failure using computational fluid dynamics. *Spill Science & Technology Bulletin*, 3(4):213–216.

Grilli, S. T., Fake, T., and Spaulding, M. L. (2000a). Numerical modelling of oil containment by a boom/barrier system: Phase III. Technical report, Department of Ocean Engineering, University of Rhode Island.

Grilli, S. T., Fake, T., and Spaulding, M. L. (2000b). Slickmap: An interactive computer model of oil containment by a boom. In *23rd International Arctic and Marine Oil Spill Program Technical Seminar*, pages 953–986.

Hogan, J. M. and Ayyaswamy, P. S. (1985). Linear stability of a viscous-inviscid interface. *Physics of Fluids*, 28(9):2709–2715.

ITOPF (2006). www.itopf.com.

Johnston, A. J., Fitzmaurice, M. R., and Watt, R. G. M. (1993). Oil spill containment: Viscous oils. In *13th International Oil Spill Conference*, pages 89–94.

Jones, W. T. (1972). Instability at an interface between oil and flowing water. *Journal of Basic Engineering*, 94(4):874–878.

Kamphuis, J. W. (2000). *Introducton to Coastal Engineering and Management*, volume 16 of *Advanced Series on Ocean Engineering*. World Scientific Publishing Co. Pte. LTD.

Kantoush, S. A., Bollaert, E., De Cesare, G., Boillat, J.-L., and Schleiss, A. (2006). Flow investigation in a rectangular shallow reservoir using uvp, lspiv and numerical model. In *5th international symposium on Ultrasonic Doppler Methods for Fluid Mechanics and Fluid Engineering*, pages 129–133, Zurich, Switzerland.

Kim, M. H., Muralidharan, S., Kee, S. T., Johnson, R. P., and Seymour, R. J. (1997). Seakeeping performance of a containment boom section in random waves and currents. *Ocean Engineering*, 25(2-3):143–172.

Kordyban, E. (1982a). Laboratory study of oil thickness on water-waves. *Journal of the Waterway Port Coastal and Ocean Division-ASCE*, 108(2):220–224.

Kordyban, E. (1982b). Oil thickness variation on wavy water in the presence of wind. *Journal of Fluids Engineering-Transactions of the ASME*, 104(1):81–87.

Kordyban, E. (1992). The effect of waves on the oil-slick at a retention boom. *Journal of Energy Resources Technology-Transactions of the ASME*, 114(1):31–37.

Lau, Y. L. and Moir, J. (1979). Booms used for oil slick control. *Journal of the Environmental Engineering Division-ASCE*, 105(2):369–382.

Lee, C. M., Han, D. G., Kang, K. H., and Lee, S. J. (2004). Investigation of the effectiveness of tandem oil fences under currents. *Marine Science and Technology*, 8:117–125.

Lee, C. M. and Kang, K. H. (1997). Prediction of oil boom performance in currents and waves. *Spill Science & Technology Bulletin*, 4(4):257–266.

Lee, C. M., Kang, K. H., and Cho, N. S. (1998). Trapping of leaked oil with tandem oil fences with lagrangian analysis of oil droplet motion. *Journal of Offshore Mechanics and Arctic Engineering-Transactions of the ASME*, 120(1):50–55.

Lehr, W. J. (1984). A new technique to estimate initial spill size using a modified fay-type spreading formula. *Marine Pollution Bulletin*, 15:326–329.

Leibovich, S. (1975a). Hydrodynamic problems in oil spill control and removal. In *Offshore Technology Conference*, pages 527–544.

Leibovich, S. (1975b). Natural limit to containment and removal of oil spills at sea. *Ocean Engineering*, 3(1):29–36.

Leibovich, S. (1976). Oil slick instability and entrainment failure of oil containment booms. *Journal of Fluids Engineering-Transactions of the ASME*, 98(1):98–105.

Lindenmuth, W. T., Miller, E. R., and Hsu, C. C. (1970). Studies of oil retention boom hydrodynamics. *US Coast Guard Report*, (714102/A/008).

Lo, J. M. (1996). Laboratory investigation of single floating booms and a series of booms in the prevention of oil slick and jellyfish movement. *Ocean Engineering*, 23(6):519–531.

Maraghei, A. R., Zaker, H., and Allahdadi, M. N. (2002). Wave measurements and analysis in khowr-e-musa, north of persian gulf. In EUROCOAST, editor, *Littoral 2002, The Changing Coast*, pages 311–317, Portugal.

Met-Flow (2005). UVP monitor, User's guide. Technical report, Met-Flow.

Milgram, J. H. (1971). Forces and motion of a flexible floating barrier. *Journal of Hydronautics*, 5(2):41–51.

Milgram, J. H. (1973). Physical requirements for oil pollution control barriers. In *3rd International Oil Spill Conference*, pages 375–381.

Milgram, J. H. and Van Houten, R. J. (1978). Mechanics of a restrained layer of floating oil above a water current. *Journal of Hydronautics*, 12(3):93–108.

Nakamura, H., Kondo, M., and Kukita, Y. (1998). Simultaneous measurement of liquid velocity and interface profiles of horizontal duct wavy flow by ultrasonic velocity profile meter. *Nuclear Engineering and Design*, 184:339–348.

Nash, J. H. and Molsberry, D. D. (1995). The performance of booms in an offshore environment. In *14th International Oil Spill Conference*, pages 578–581.

Oebius, H. U. (1999). Physical properties and processes that influence the clean up of oil spills in the marine environment. *Spill Science & Technology Bulletin*, 5(3-4):177–289.

Oil Spill Response Catalog (2005). World catalog of oil spill response products.

Oppenheim, A. V., Wilsky, A. S., and Young, I. T. (1983). *Signals and systems*. Prentice-hall international edition.

Raffel, M., Willert, C. E., and Kompenhans, J. (1998). *Particle Image Velocimetry: A practical guide*. Berlin-Springer.

Rasmussen, D. (1985). Oil spill modelling - A tool for cleanup operation. In *9th International Oil Spill Conference*, pages 243–249.

Sayah, M. S. (2006). *Efficiency of brushwood fences in shore protection against wind-wave induced erosion*. PhD thesis, No. 3424, Ecole Polytechnique Fédérale de Lausanne.

Sayah, M. S., Boillat, J.-L., and Schleiss, A. (2004). Behavior of a contractile floating reservoir for the confinement and recovery of oil slicks. *Journal of Waterway, Port, Coastal and Ocean Engineering, ASCE*, 130(5):266–275.

Shields, A. (1936). Application of similarity principles and turbulence research to bed-load movement. *Mitteilungen der Preussischen Versuchsanstalt fur Wasserbau und Schiffbau*, 26:5–24.

Shin, J. O., Dalziel, S. B., and Linden, P. F. (2004). Gravity currents produced by lock exchange. *Journal of Fluid Mechanics*, 521:1–34.

Simpson, J. E. (1972). Effects of the lower boundary on the head of a gravity current. *Journal of Fluid Mechanics*, 53(4):759–768.

Simpson, J. E. (1997). *Gravity Currents: in the Environment and the Laboratory*. Cambridge University Press, 2nd edition.

Simpson, J. E. and Britter, R. E. (1979). The dynamics of the head of a gravity current advancing over a horizontal surface. *Journal of Fluid Mechanics*, 94(3):477–495.

Squire, H. B. (1933). On the stability of three-dimensional disturbance of viscous flow between parallel walls. In *Royal Society*, volume 142, pages 621–628, London.

Sundararaghavan, H. (2000). *Analysis of oil Containment Failure and Spreading*. PhD thesis, University of Hawaii.

Sundararaghavan, H. and Ertekin, R. C. (1997). Near-boom oil-slick instability criterion in viscous flows and the influence of free-surface boundary conditions. *Journal of Energy Resources Technology-Transactions of the ASME*, 119(1):26–33.

Swedberg, J. (2003). Report: Oil booms. *GFR magazine*, pages 28–31.

Takeda, Y. (1995). Velocity profile measurement by ultrasonic doppler method. *Experimental Thermal and Fluid Science*, 10(4):444–453.

Tkalich, P. and Chao, X. B. (2001). Accurate simulation of oil slicks. In *17th International Oil Spill Conference*, pages 1133–1137.

Tkalich, P., Huda, M. K., and Gin, K. Y. H. (2003). A multiphase oil spill model. *Journal of Hydraulic Research*, 41(2):115–125.

Van Dyck, R. L. and Bruno, M. S. (1995). Effect of waves on containment boom response. In *14th International Oil Spill Conference*.

Van Rijn, L. C. (1993). *Principles of sediment transport in rivers, estuaries and coastal seas*. Aqua Publications.

Versteeg, H. K. and Malalasekera, W. (2007). *An Introduction to Computational Fluid Dynamics: The Finite Volume Method*. Pearson-Prentice Hall, second edition.

Von Karman, T. (1940). The engineer grapples with nonlinear problems. *Bulletin of the American Mathematical Society*, 46:615–680.

Wicks, M. (1969). Fluid dynamics of floating oil containment by mechanical barriers in the presence of water currents. In *Conference on Preventation and Control of Oil Spills*, pages 55–106.

Wilkinson, D. I. (1972a). Discussion of "Collection of oil slicks". *Journal of the Waterways, Harbors and Coastal Engineering Division, ASCE*, 98(Feb):122–125.

Wilkinson, D. l. (1972b). Dynamics of contained oil slicks. *Journal of the Hydraulics Division-ASCE*, 98(HY6):1013–1030.

Wilkinson, D. l. (1973). Limitations to length of contained oil slicks. *Journal of the Hydraulics Division-ASCE*, 99(NHY5):701–712.

Wilson, M. P. (1977). Assessment of treated versus untreated oil spills. Technical report, College of Engineering, University of Road Island.

Wong, K. V. and Stewart, H. O. (2003). Oil spill boom design for waves. *Spill Science & Technology Bulletin*, 8(5-6):543–548.

Xu, Q. (1992). Density currents in shear flow- a two-fluid model. *Journal of the Atmospheric Sciences*, 49(6):511–524.

Xu, Q. and Moncrieff, M. W. (1994). density current circulation in shear flows. *Journal of the Atmospheric Sciences*, 51(3):434–446.

Yalin, S. (1971). *Theory of Hydraulic Models*. Mcmillan, first edition.

Yalin, S. (1977). *Mechanics of sediment transport*. Oxford: Pergamon Press, 2nd edition.

Zalosh, R. G. and Jenson, D. S. (1975). A numerical model of droplet entrainment from a contained oil slick. In *Symposium on Fluid mechanics in the Petroleum Industry, ASME*, pages 17–27.

Zapryanov, Z. and Tabakova, S. (1999). *Dynamics of Bubbles, Drops and Rigid Particles*, volume 50 of *Fluid Mechanics and its Applications*. Kluwer Academic Publishers.

Zhu, S. P. and Strunin, D. (2001). Modelling the confinement of spilled oil with floating booms. *Applied Mathematical Modelling*, 25(9):713–729.

Zhu, S. P. and Strunin, D. (2002). A numerical model for the confinement of oil spill with floating booms. *Spill Science & Technology Bulletin*, 7(5-6):249–255.

Acknowledgment

This thesis is the outcome of a wonderful four-years experience at the magnificent Laboratory of Hydraulic Constructions (LCH) in Ecole Polytechnique Fédérale de Lausanne (EPFL).

First and foremost, I would like to express my gratitude to my supervisor, Prof. Anton Schleiss, for his support and guidance without which this study would not have been possible. I would like to thank him for having confidence in my abilities, for supporting this work with his ideas, for his integral view on research, and of course, for providing me the opportunity to visit this beautiful country.

I gladly acknowledge my debt to Dr Jean-Louis Boillat. His overly enthusiasm in discovering new horizons, his optimistic point of view, and his rich experience in conducting experimental research was really helpful to me during these years. My gratitude also goes to Dr Erik Bollaert, for his constant friendship, encouragement and advice.

This dissertation was funded by Swiss Petroleum Union (grant No. 4'09'02). My thanks are due to Dr A. Heitzer for following this project and for his positive attitude and encouraging interest.

I'm indebted to Prof. Y. Takeda and Dr G. De Cesare, who have shared with me their remarkable knowledge in accurate flow measurements. I would like to thank Olivier Marriete from Met-Flow for providing technical support for conducting UVP measurements. I appreciate also the precious help of Sameh Kantoush in conducting PIV measurements.

I am grateful for the highly responsive support from my teacher and friend Maziar Mahzari, who collaborated in developing the numerical model, during his visit as an academic guest at LCH-EPFL, and was always available for further scientific discussions. I would also like to thank Babak Hejazi for his relevant help in launching the numerical simulations, and to Ali Tolou for providing me with technical support to run the simulations on the Pleiades cluster.

I am deeply thankful to Dr F. Fang, who always was available when I needed her advises, and has accepted to attend my PhD committee. I would also like to thank the other members of my PhD committee, Prof. A. Lejeune and Prof. A. Wüest, who have honored me by accepting to review and evaluate this thesis, and Prof. J.-L. Scartezzini for accepting to be the president of my PhD thesis jury.

It is a pleasure for me to acknowledge my friends and colleagues at LCH for being the surrogate family during these past years. I'm proud and happy of making wonderful friendships with: Stephanie, Pedro, Selim, Fréd, Philippe,

Burkhard, Tobias, Jolanda, Sameh, Alexandre, Rémi, Javier, Marcelo, Sabrina, Soleyman, Peyman and Matteo. Also special thanks to Caroline Etter and Martine Tiercy who helped me at several occasions.

Doing an experimental project is not possible without a strong technical support; my thanks are, therefore, addressed to Louis Schneiter, Eric Pantillon, and Michel Teuscher for preparing experimental set-up, even if it was the most polluting set-up at LCH. I have also benefited from my multilingual friends: special thanks to Jolanda for the "Zusammenfassung", and Rémi for the "Résumé".

I wish to express my warmest thanks to my beloved parents, Eftekhar and Hossein; my sisters, Sheyma, Zahra, and Yasaman; my brothers in law, Ali and Timo; as well as Azad's parents and brothers, who gave me the extra strength, motivation and love necessary to get things done. My sincere gratitude to my eternal sunshine, Azad, for his persistent love, continuous support, and enormous patience.

Appendix A

Oil classification and properties

Group 1

Specific Gravity < 0.8 (°API > 45)

B Viscosity cSt @ 15°C: 0.5 - 2.0
C % boiling below 200°C: 50 - 100%
D % boiling above 370°C: 0%

	B	C	D
Gasolene	0.5	100	0
Naptha	0.5	100	0
Kerosene	2.0	50	0

Group 2

Specific Gravity 0.8 – 0.85 (°API 35 - 45)

A Pour Point °C
B Viscosity cSt @ 15°C
C % boiling below 200 °C: 19 - 48% Average 33%
D % boiling above 370 °C: 12 - 50% Average 31%

High pour point >5° C

	A	B	C	D
Amna	18	S	25	30
Argyll	9	11	29	39
Arjuna	27	S	37	15
Auk	9	9	33	35
Bach Ho	35	S	21	47
Bass Straight	15	S	40	20
Beatrice	12	32	25	35
Bintulu Neat	17	S	24	34
Bunyu	18	S	29	12
Cormorant	12	13	32	38
Dunlin	6	11	29	36
Es Sider	6	11	28	42
Escravos	10	9	35	15
Gippsland Mix	15	S	40	20
Lalang	33	S	19	49
Lucina	16	S	26	41
Nigerian Light	9	S	35	27
Qua Iboe	15	7	29	32
Rio Zulia	27	S	34	30
San Joachim	24	S	43	20
Santa Rosa	10	4	34	27
Sarir	24	S	24	39
Seria	18	S	37	15
Soyo	17	S	20	50
Thistle	9	9	35	38
Zuetina	9	9	35	30

Low pour point

	B	C	D
Abu Dhabi	7	36	31
Arabian Super Light	3	26	39
Berri	9	36	35
Beryl	9	35	34
Brass River	4	45	17
Brega	9	38	32
Brent Blend	6	30	38
Ekofisk	4	46	25
Kirkuk	1	35	36
Kole Marine	1	34	35
Lower Zakum		34	35
Marib Light		40	20
Montrose	7	36	31
Murban	7	32	34
Murchison	7	36	20
Olmeca		32	32
Oseberg	10	28	39
Palanca		30	35
Qatar Land	9	36	33
Sahara Blend	4	48	27
Sirtica	7	44	27
Gas Oil	5		

High pour point oils would only behave as Group 2 at ambient temperatures well above their pour points. At lower temperatures treat as Group 4 oils.

Group 3

Specific Gravity 0.85 – 0.95 (°API 17.5 - 35)

A Pour point °C
B Viscosity cSt @ 15°C
C % boiling below 200°C: 14 - 34% Average 22%
D % boiling above 370°C: 28 - 50% Average 46%

High Pour Point >5° C

	A	B	C	D
Bakr	7	1,500	14	60
Belayim	15	S	22	55
Bonny Light	12	25	30	30
Cabinda	17	S	18	56
Dai Hung	25	S	30	33
Djeno	6		16	61
Duri	21	S	5	74
Mandji	9	70	21	53
Morgan	7	30	25	47
Nile Blend	36	S	13	59
Soyo Blend	15	S	21	48
Suez Mix	10	30	24	49
Trinidad	14	S	23	28
Zaire	15	S	18	55

Low Pour Point

	B	C	D
Arabian Heavy	55	20	56
Arabian Light	14	24	45
Arabian Medium	25	22	51
Basrah Light		26	45
Bonny Medium		14	39
Buchan	14	31	39
Champion Export	18	15	28
Escravos		30	32
Flotta	11	34	26
Forcados	12	17	37
Forozan		24	49
Forties	8	32	36
Gullfaks	13	21	40
Hout	15	24	48
Iranian Heavy	25	24	48
Iranian Light		26	43
Khafji	80	21	55
Kuwait Export	30	23	52
Leona		14	56
Loreto		17	50
Maya	500	17	61
Miri Light		25	25
Nigerian Medium	40	14	40
Oman		23	45
Qatar Marine		29	39
Santa Maria	250	22	54
Siberian Light		24	52
Sov. Export Blend	15	27	24
Tia Juana Light	2,500	24	45
Upper Zakum		26	44
Medium Fuel Oil (IFO 180)	1,500-3,000		

High pour point oils would only behave as Group 3 at ambient temperatures well above their pour points. At lower temperatures treat as Group 4 oils.

Group 4

Specific Gravity > 0.95 (°API < 17.5) or Pour Point > 30°C
A Pour point °C
B Viscosity cSt @ 15°C: 1500 - Solid
C % boiling below 200°C: 3 - 24% Average 10%
D % boiling above 370°C: 33 - 92% Average 65%

	A	B	C	D
Bachequero	-20	5,000	10	60
Bascan	15	S	4	80
Bu Attifil	39	S	19	47
Cinta	43	S	10	54
Cyrus	-12	10,000	12	66
Daquing	36	S	12	66
Gamba	23	S	11	54
Handil	35	S	23	33
Heavy Lake Mix	-12	10,000	12	64
Jatibarang	43	S	14	65
Merey	-18	7,000	7	70
Minas	37	S	14	57
Panuco	2	S	3	76
Pilon	-4	S	2	92
Quiriquire	-29	1,500	3	88
Shengli	21	S	9	70
Taching	35	S	12	49
Tia Juana Pesado	-1	S	3	78
Wafra Eocene	-29	3,000	11	63
Widuri	46	S	7	70
Heavy Fuel Oil (IFO 380)		5,000-30,000		

Figure A.1: Classification of oils according to their specific gravity, (ITOPF, 2006)

Appendix B

Characteristics of experimental waves

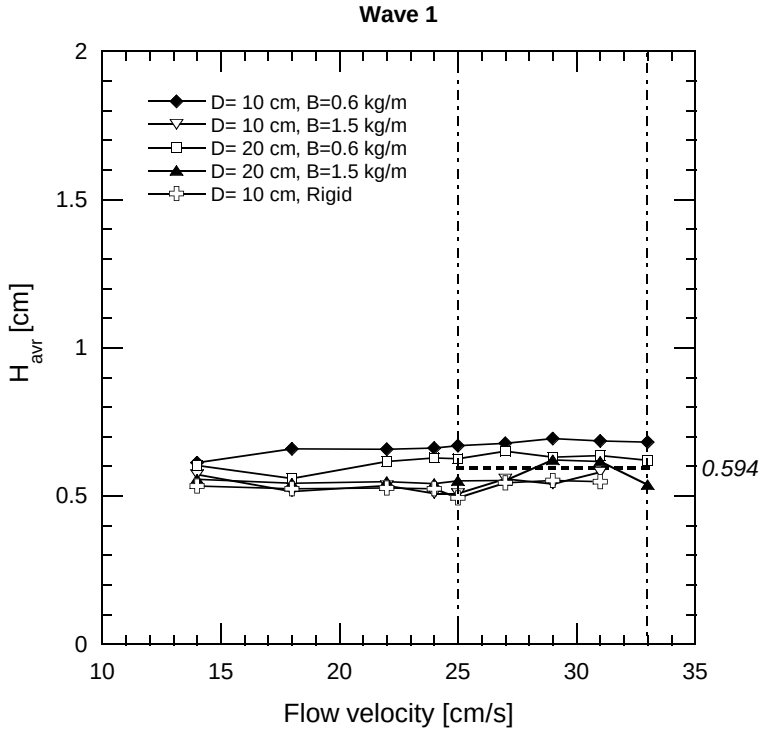

Figure B.1: Average wave height, H_{avr}, of Wave 1 measured at different velocities; dashed line shows the mean value of H_{avr}; dot dashed lines shows the range of failure velocity for wave 1

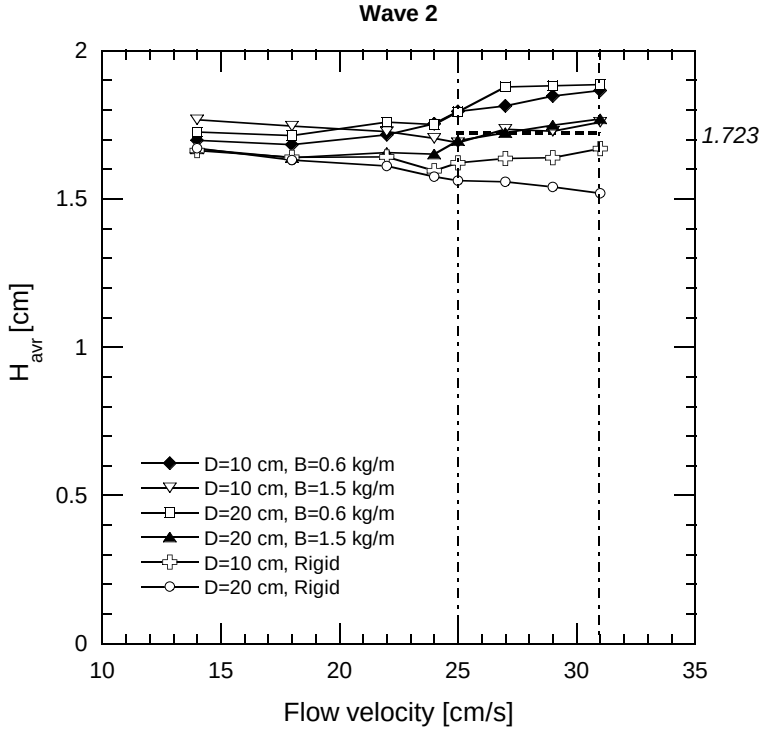

Figure B.2: Average wave height, H_{avr}, of Wave 2 measured at different velocities; dashed line shows the mean value of H_{avr}; dot dashed lines shows the range of failure velocity for wave 2

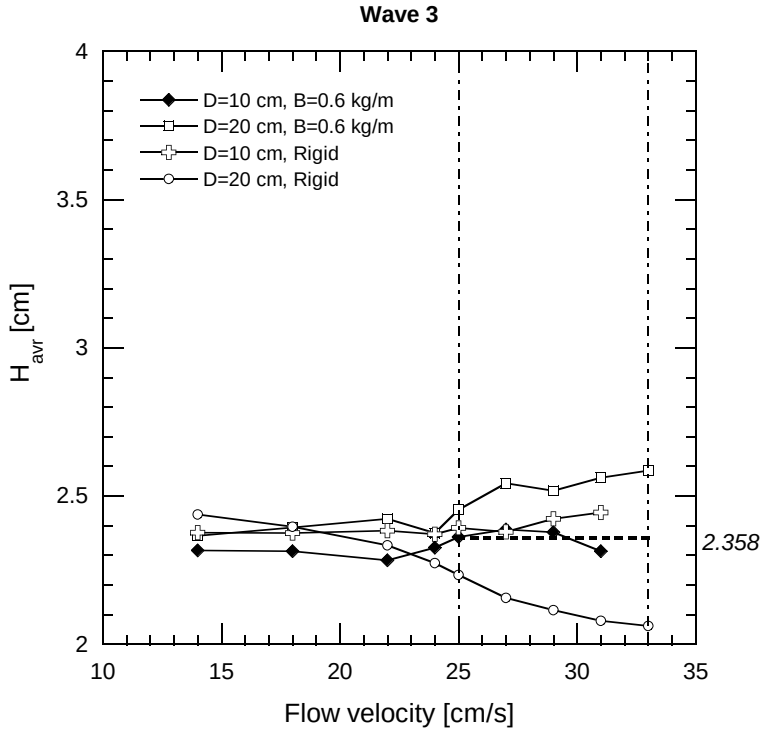

Figure B.3: Average wave height, H_{avr}, of Wave 3 measured at different velocities; dashed line shows the mean value of H_{avr}; dot dashed lines shows the range of failure velocity for wave 3

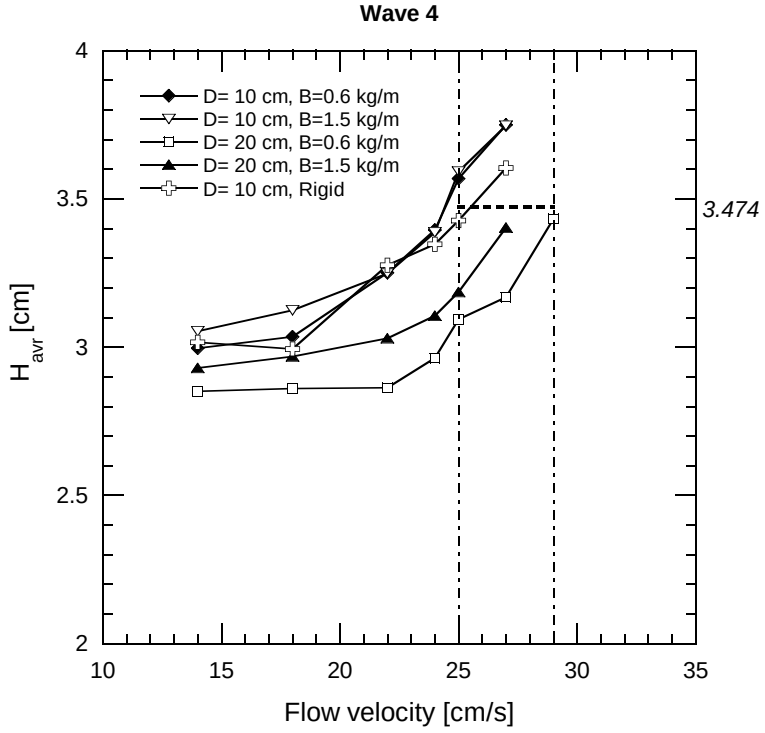

Figure B.4: Average wave height, H_{avr}, of Wave 4 measured at different velocities; dashed line shows the mean value of H_{avr}; dot dashed lines shows the range of failure velocity for wave 4

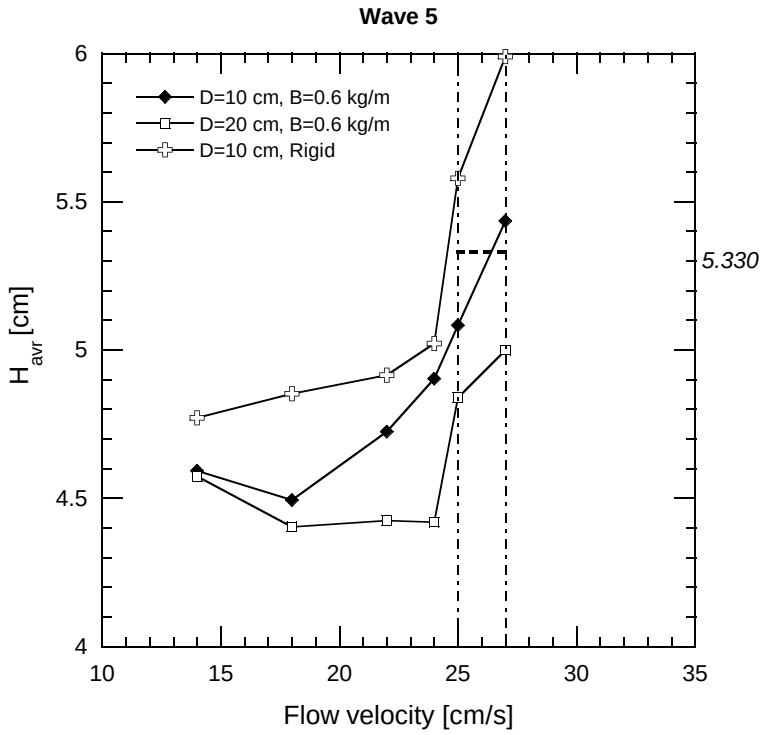

Figure B.5: Average wave height, H_{avr}, of Wave 5 measured at different velocities; dashed line shows the mean value of H_{avr}; dot dashed lines shows the range of failure velocity for wave 5

Appendix C

Shear stress analysis of LECA granules motion using Shields' diagram

To define the initiation of motion for sediment transportation in rivers or channels, Shields' diagram is commonly used. Particle movement will occur when the instantaneous fluid force on a particle is just larger than the instantaneous resisting force related to the particles submergence and friction. The initiation of movement of individual grains is dependent on a variety of factors, both deterministic (e.g. drag and submerged gravity forces) and random (e.g. turbulence). As a result, it is difficult to establish a relationship between the shear stress and initiation of motion (Van Rijn, 1993). Shields (1936) was the first to propose a relationship between the particle Reynolds number, Re_p, and the critical shear stress (Shields parameter, τ) in order to predict the initiation of motion. In the Shields' diagram the axes are defined as:

$$X = Re_p = \frac{\upsilon_* D_s}{\nu_w} \tag{C.1}$$

$$Y = \tau = \frac{\tau_0}{\gamma_s - \gamma_w} \tag{C.2}$$

where D_s is the typical particle size (usually d_{50}), ν_w is the kinematic viscosity of water and γ_w and γ_s are specific weights of water and solid particle respectively. The shear stress, τ_0, and shear velocity, υ_*, are defined as:

$$\tau_0 = \gamma_w J R_h \tag{C.3}$$

$$\upsilon_* = \sqrt{\frac{\tau_0}{\rho_w}} = \sqrt{gJR_h} \tag{C.4}$$

where J and R_h are the energy slope and the hydraulic radius respectively. the Shield's curve represents the incipient motion and no sediment movement occurs for the points under it.

A modified relationship based on Shields' diagram is presented by Yalin (1977). In the modified diagram the shear stress is presented as a function of a

nondimensinal parameter E:

$$E = \sqrt[3]{\frac{X^2}{Y}} = D_s \sqrt[3]{\frac{\gamma_s}{\rho_w \nu_w^2}} \tag{C.5}$$

E parameter represents the influence of the solid phase (density and diameter) and the liquid phase (density and viscosity) and does not change as a function of flow conditions. Using this parameter the relation $Y_{cr} = \Psi(E)$ can be solved explicitly on whole range of E, as presented in Eq. C.6:

$$Y_{cr} = \Psi(E) = 0.13E^{-0.392}\exp(-0.015E^2) + 0.045(1 - \exp(-0.068E)) \tag{C.6}$$

The idea in the present study, is to use the Shields' modified curve for predicting the LECA granules movement applying Eq. C.2 to Eq. C.6. Contrary to the case of sediment transportation, particles are suspending over water surface and that is the buoyancy force which keeps a particle in contact with the mass, acting as resisting force. Hence, the gravity difference should be considered as $\gamma_s - \gamma_w$.

Another parameter to be modified is the shear stress, τ. Accumulated LECA particles behind the barrier form a triangle with a certain longitudinal slope, β. The effect of this slope can be considered as the effect of up sloping flow in sediment transportation problem and modify the shear parameter of Eq. C.3, as follows:

$$\tau_b = k_\beta \tau_0 \tag{C.7}$$

where

$$k_\beta = \frac{sin(\varphi + \beta)}{sin\varphi} \tag{C.8}$$

In the former equation φ is the reposing angle of LECA, measured to be 28 degrees. The slope angle, β is measured for each experiment and varies between 10 to 22 degrees.

The energy slope was calculated based on measured head loss in the flume using Bernoulli equation. Fig. C.1 illustrates the measured and calculated parameters. The upstream depth, z_1, and downstream depth, z_2, are firstly measured at the upstream end of the slick and 10 cm after the barrier respectively. Then the Bernoulli's equation (Eq. C.9) is used to calculate the global loss:

$$h = z_1 - z_2 + \frac{U_1^2 - U_2^2}{2g} \tag{C.9}$$

This head loss is due to energy slope along the slick as well as local losses corresponding to narrowing and widening the flow. The head loss along the slick, h_s, can be obtained by Eq. C.10.

$$h_s = h - h_n - h_w \tag{C.10}$$

where h_n and h_w are local head losses due to narrowing and widening respectively. The head loss due to narrowing, h_n, was assumed to be negligible. However, widening may cause a significant head loss:

$$h_w = \zeta_w \frac{U_1^2}{2g} \tag{C.11}$$

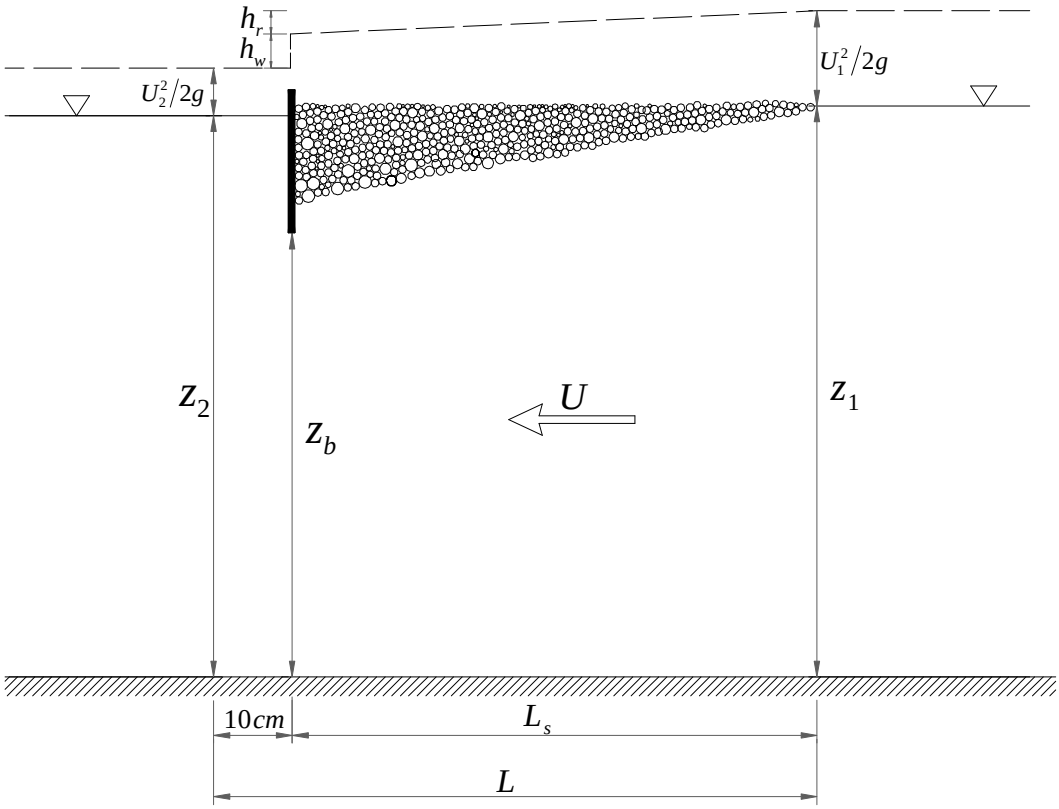

Figure C.1: Schematic drawing and energy line of LECA experiments

where

$$\zeta_w = (1 - \frac{A_b}{A_2})^2 \tag{C.12}$$

In this equation, A_b and A_2 are the flow surface under the barrier and $10cm$ downstream of it. As a result, a mean value of energy slope along the LECA slick can be obtained using the following equation:

$$J = \frac{h_s}{L} \tag{C.13}$$

where L represents the distance between two measurement points (Fig. C.1)

To define a critical shear stress, complexity is mainly caused by the lack of a clear criterion of initiation of motion (Van Rijn, 1993). In this study, the initiation of motion is attributed to the frequent particle movement at many locations.

To verify the application of the Shields' diagram for suspended granules, a supplementary experiment was undertaken. The goal was to test another material than LECA to achieve a different value for the material parameter, E. The experiment was then carried out with plastic particles (Eraclene MP 90) with $\rho_s = 0.96\ gr/cm^3$ and $D_s = 2.6\ mm$.

Obtained points corresponding to LECA and plastic granules for a rigid barrier with 10 cm draft and initial volume of 20 lit/m are shown in Fig. C.2. It indicates the capability of Shields' diagram in prediction of incipient motion

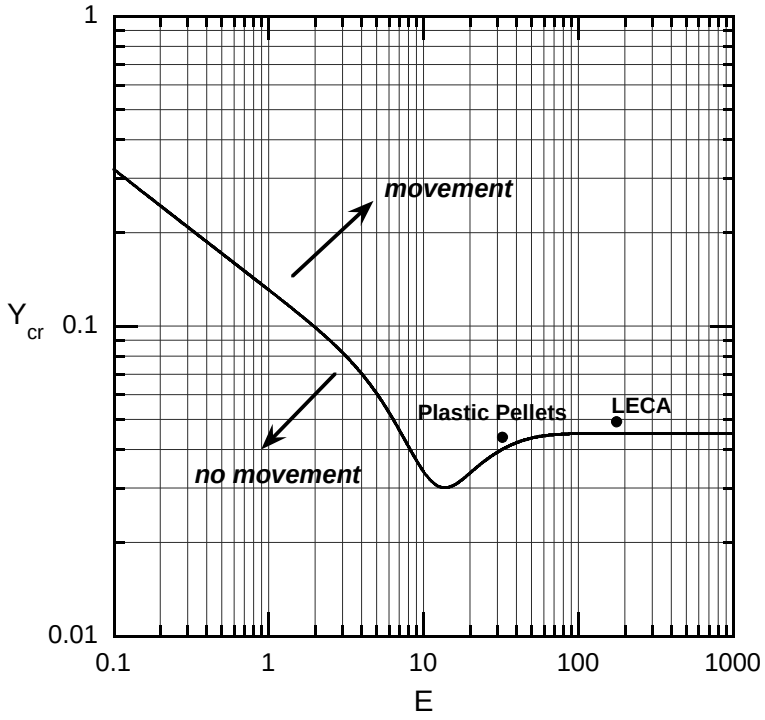

Figure C.2: Modified Shields' diagram applied for the case of polymer pellets and LECA containment behind a barrier with 10 *cm* draft

for suspending granules. Thereby, Shields' diagram was used to predict granules movement for experiments with different conditions.

Fig. C.3 shows the critical shear stress for two flexible barriers with different ballast weights and a rigid barrier, all with 10 *cm* draft and containing 20 lit/m LECA slick. The movement starts at a lower calculated shear stress values for a flexible barrier than a rigid one. This can be explained by the difference in velocity fields and streamlines in the vicinity of rigid and flexible barriers, and the fact that the shear stress was calculated using the mean flow velocity, instead of precise local velocity at interface. This is also the case for experiments with a rigid barrier of different barrier draft as it is shown in Fig. C.4.

As a result, it can be concluded that with appropriate assumptions, Shiled's diagram is capable in predicting the movement initiation in a suspended slick of granules. Difference in critical shear stress obtained for flexible and rigid barriers with different drafts seems to be due to the effect of the barrier type and draft on the velocity field upstream of the barrier. Hence, it is on crucial importance to use the precise local velocity at interface, to achieve acceptable results.

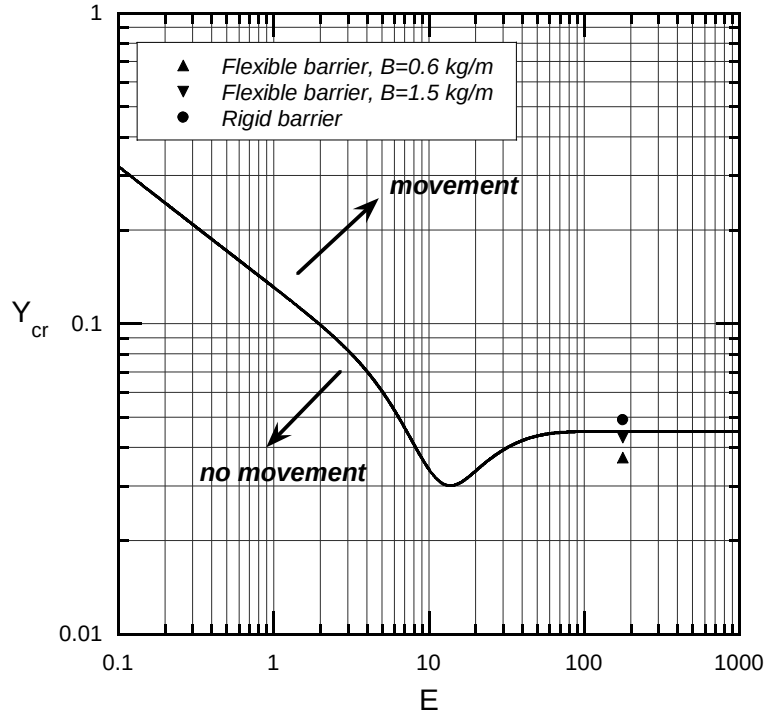

Figure C.3: Modified Shields' diagram applied for barriers with 10 *cm* draft with different types: two flexible barriers with different ballast weights and one rigid barrier

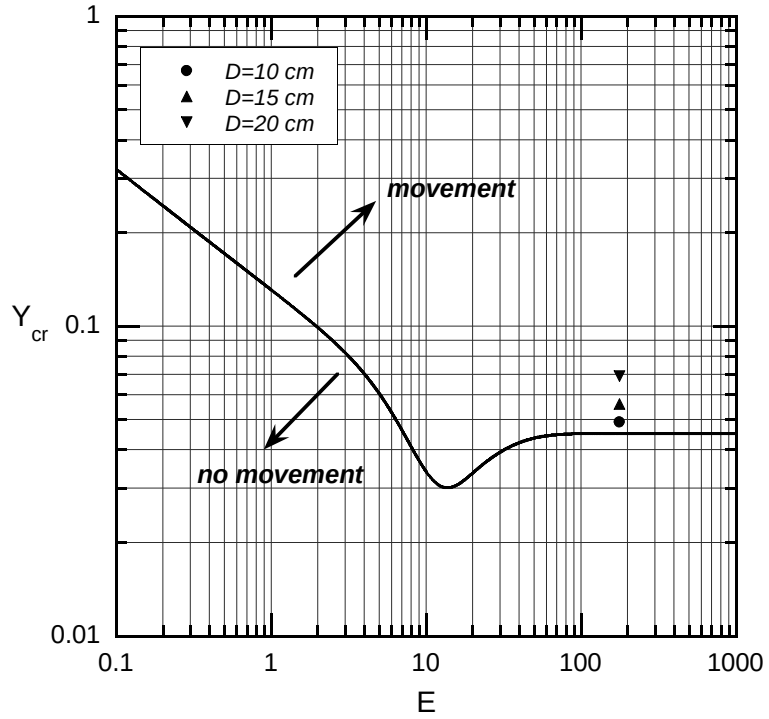

Figure C.4: Modified Shields' diagram applied for rigid barriers with different drafts

Appendix D

UVP measurements

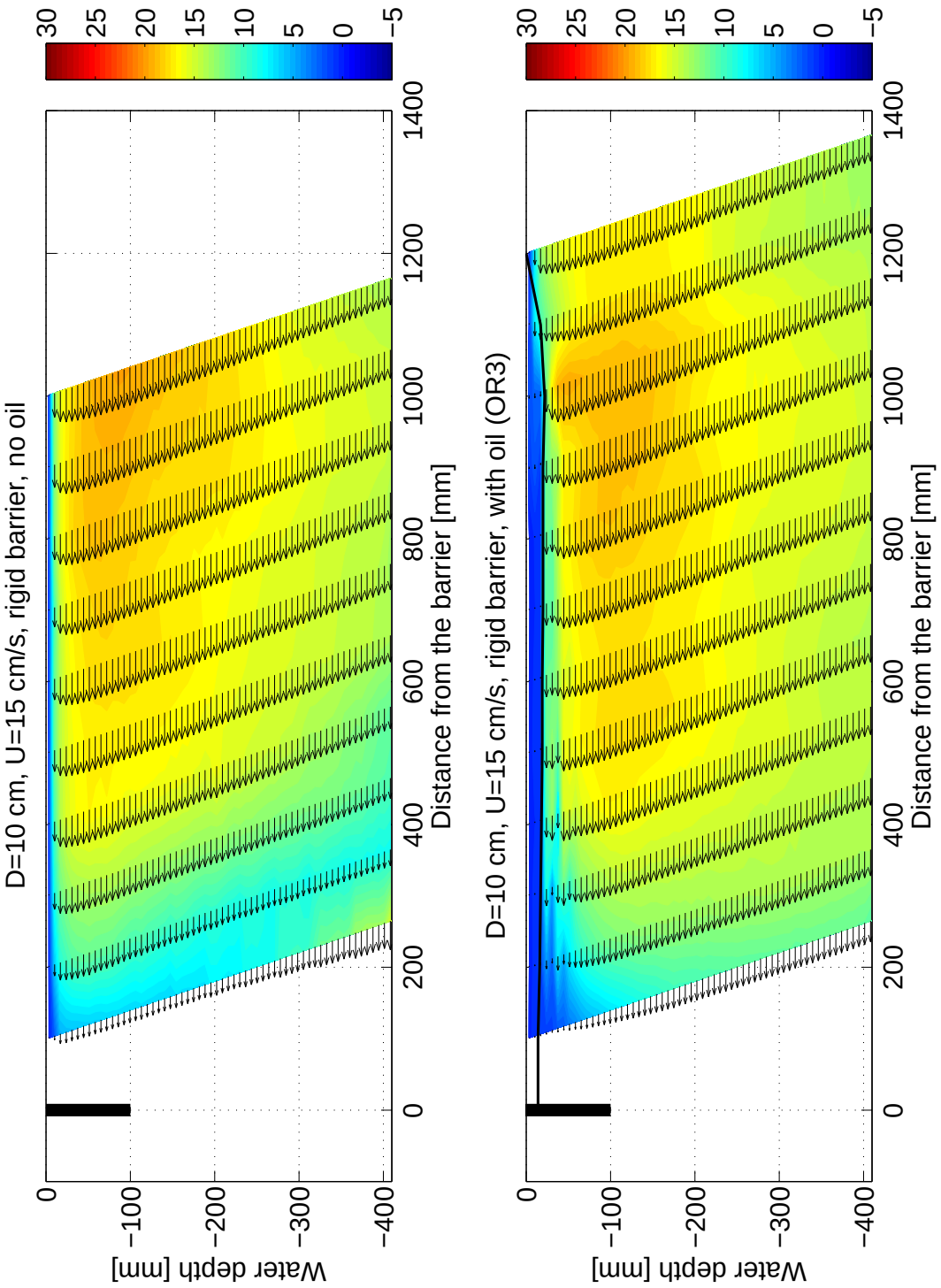

Figure D.1: UVP measurements of U_x for a rigid barrier with 10 cm draft and mean flow velocity of 15 cm/s, color bar shows the velocity in cm/s

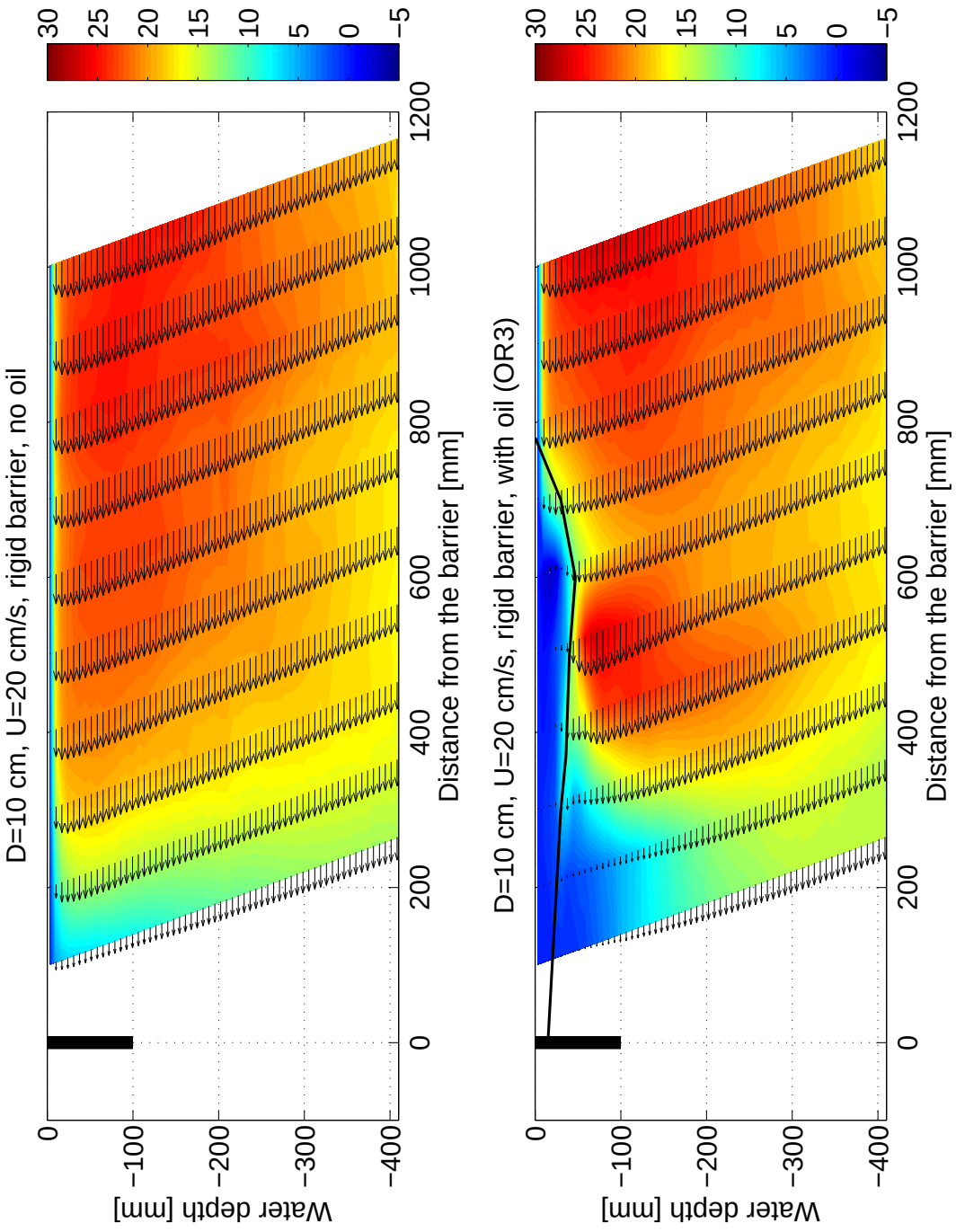

Figure D.2: UVP measurements of U_x for a rigid barrier with 10 cm draft and mean flow velocity of 20 cm/s, color bar shows the velocity in cm/s

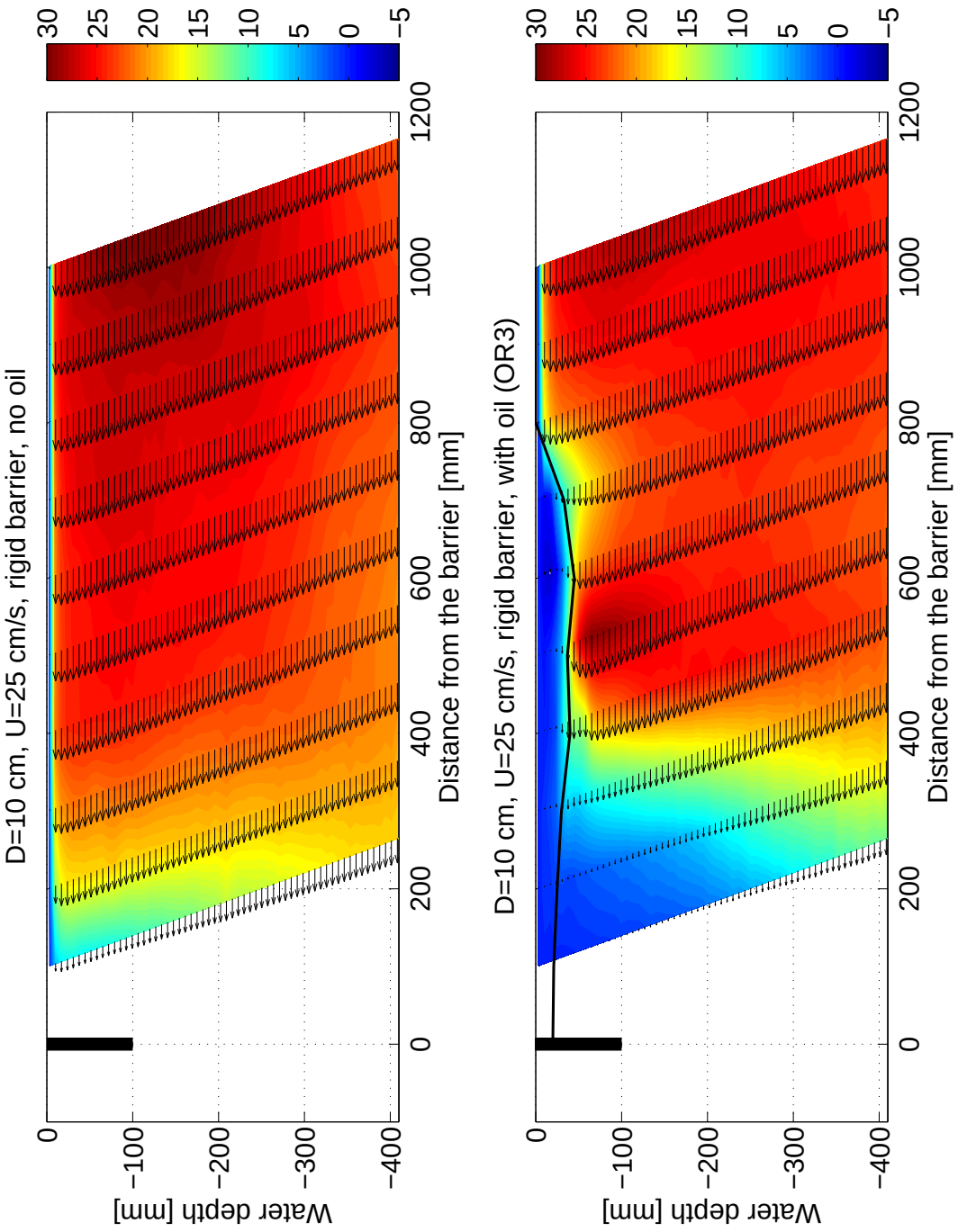

Figure D.3: UVP measurements of U_x for a rigid barrier with 10 cm draft and mean flow velocity of 25 cm/s, color bar shows the velocity in cm/s

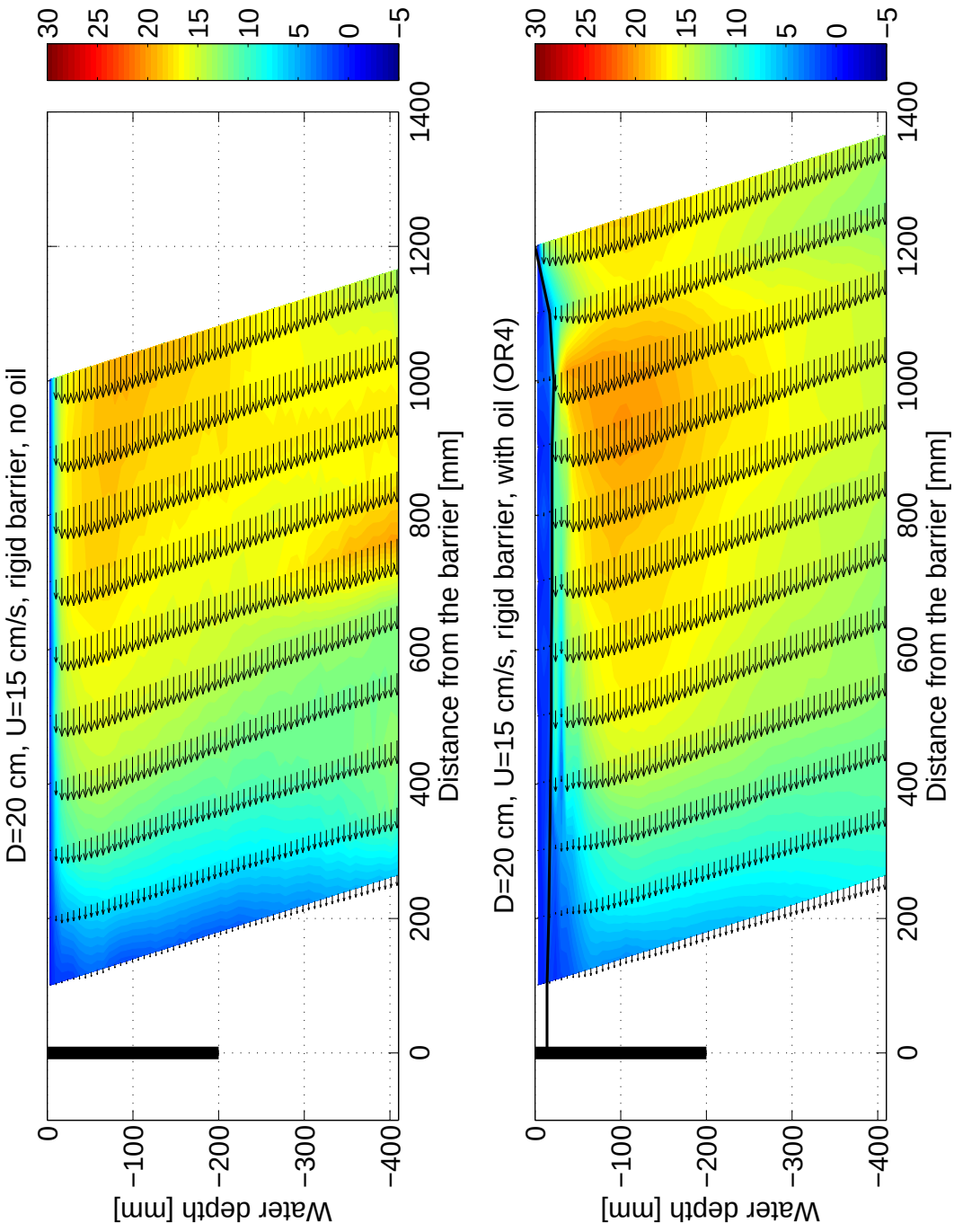

Figure D.4: UVP measurements of U_x for a rigid barrier with 20 cm draft and mean flow velocity of 15 cm/s, color bar shows the velocity in cm/s

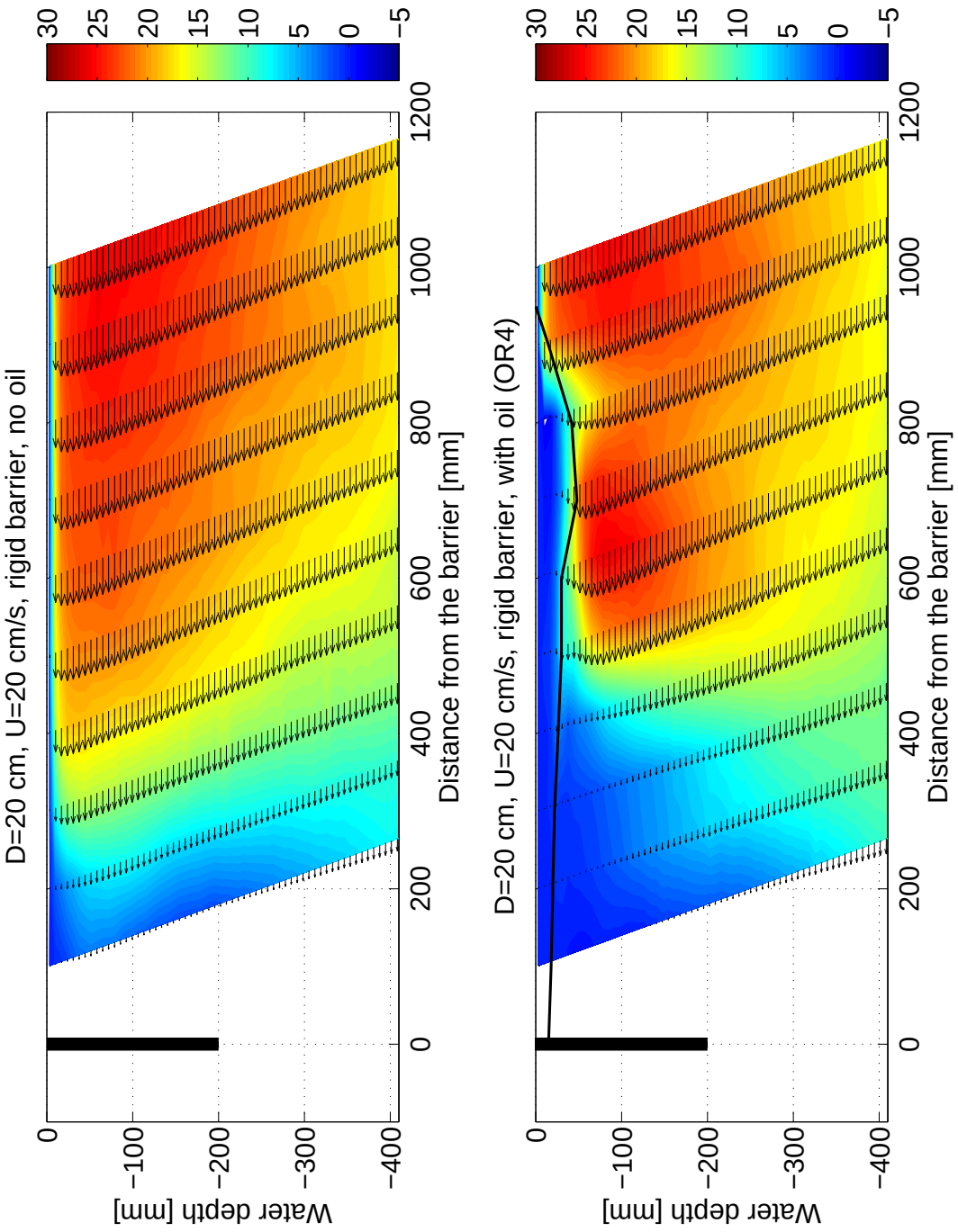

Figure D.5: UVP measurements of U_x for a rigid barrier with 20 cm draft and mean flow velocity of 20 cm/s, color bar shows the velocity in cm/s

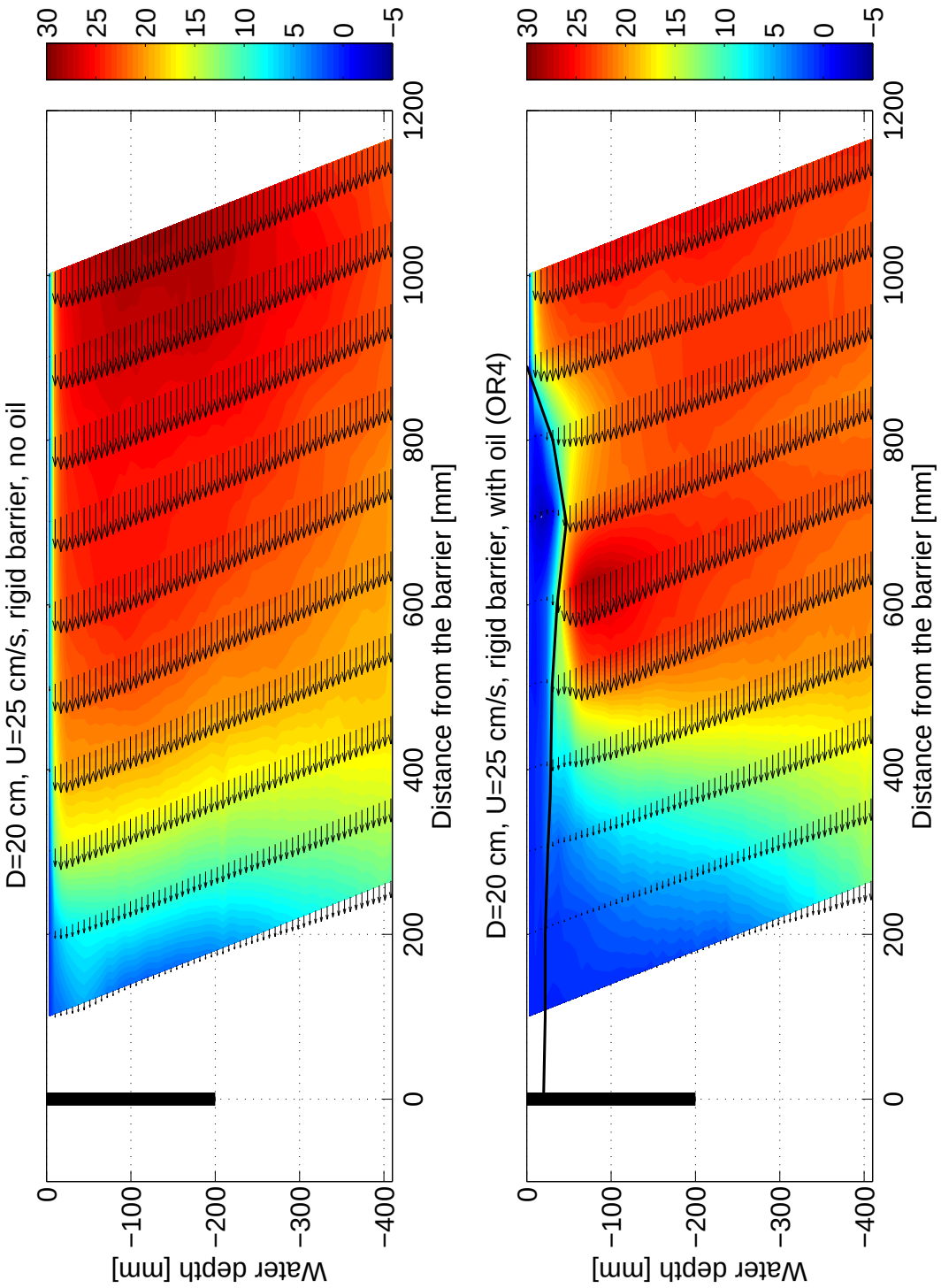

Figure D.6: UVP measurements of U_x for a rigid barrier with 20 cm draft and mean flow velocity of 25 cm/s, color bar shows the velocity in cm/s

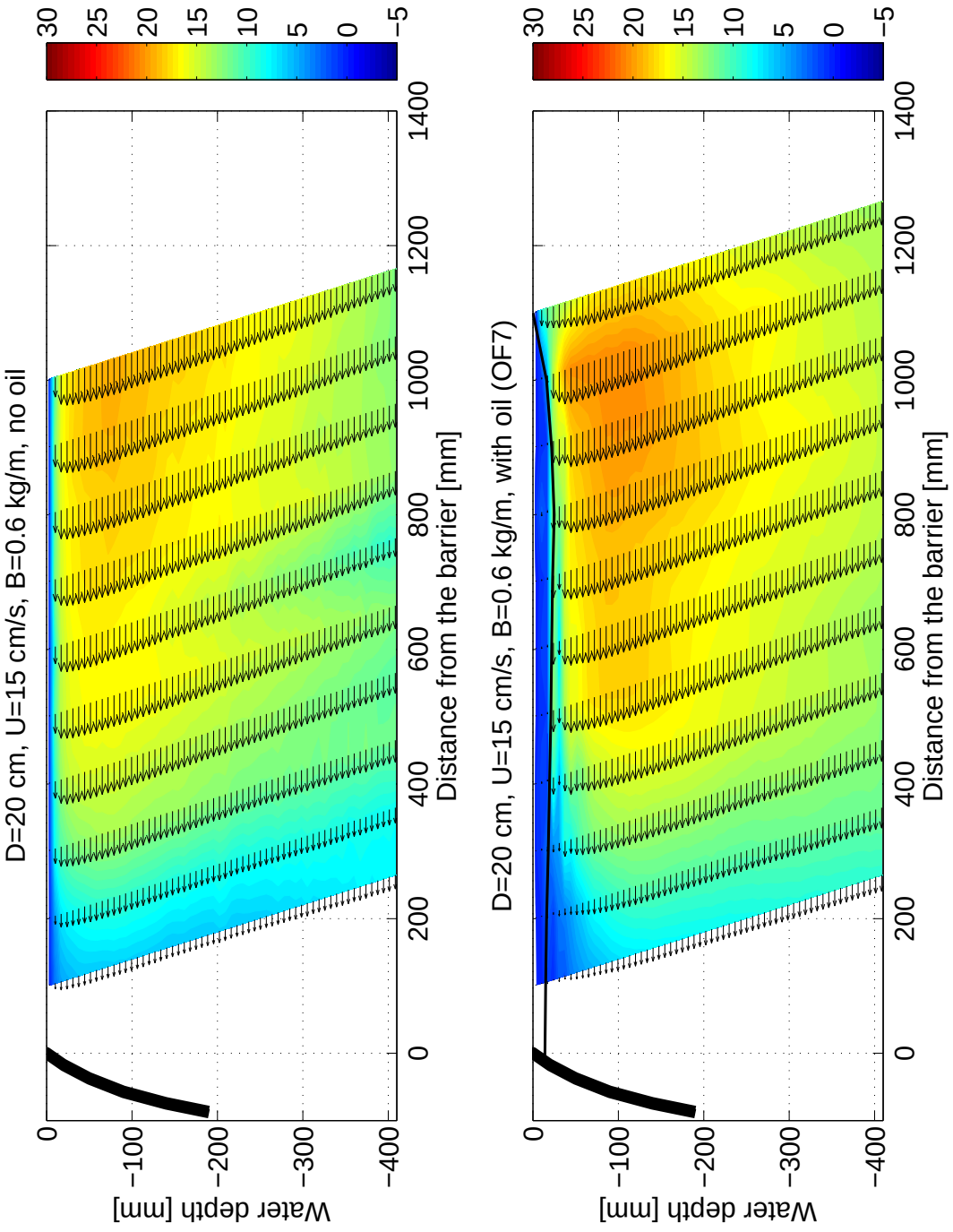

Figure D.7: UVP measurements of U_x for a flexible barrier with 20 cm draft and mean flow velocity of 15 cm/s, color bar shows the velocity in cm/s

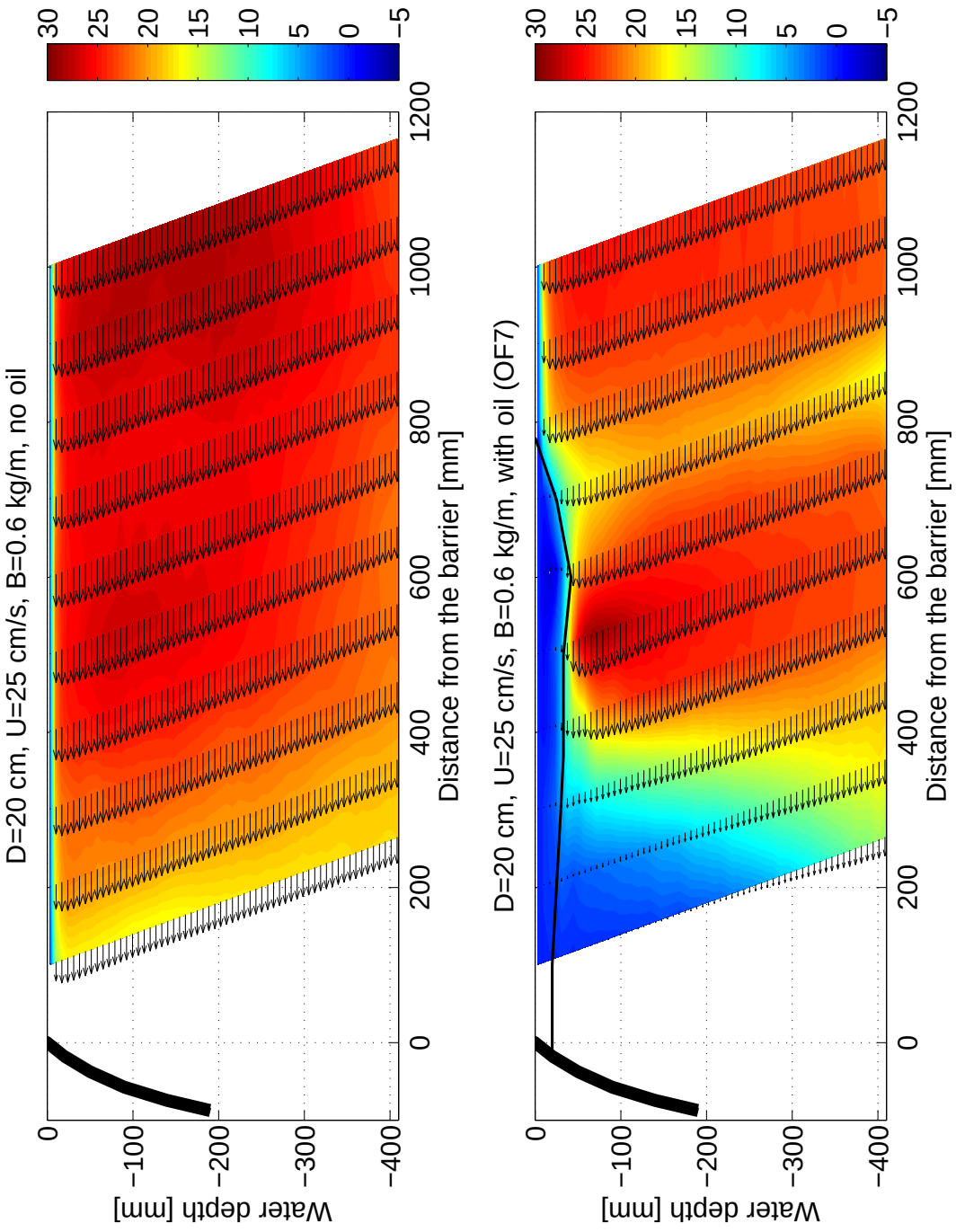

Figure D.8: UVP measurements of U_x for a flexible barrier with 20 cm draft and mean flow velocity of 25 cm/s, color bar shows the velocity in cm/s

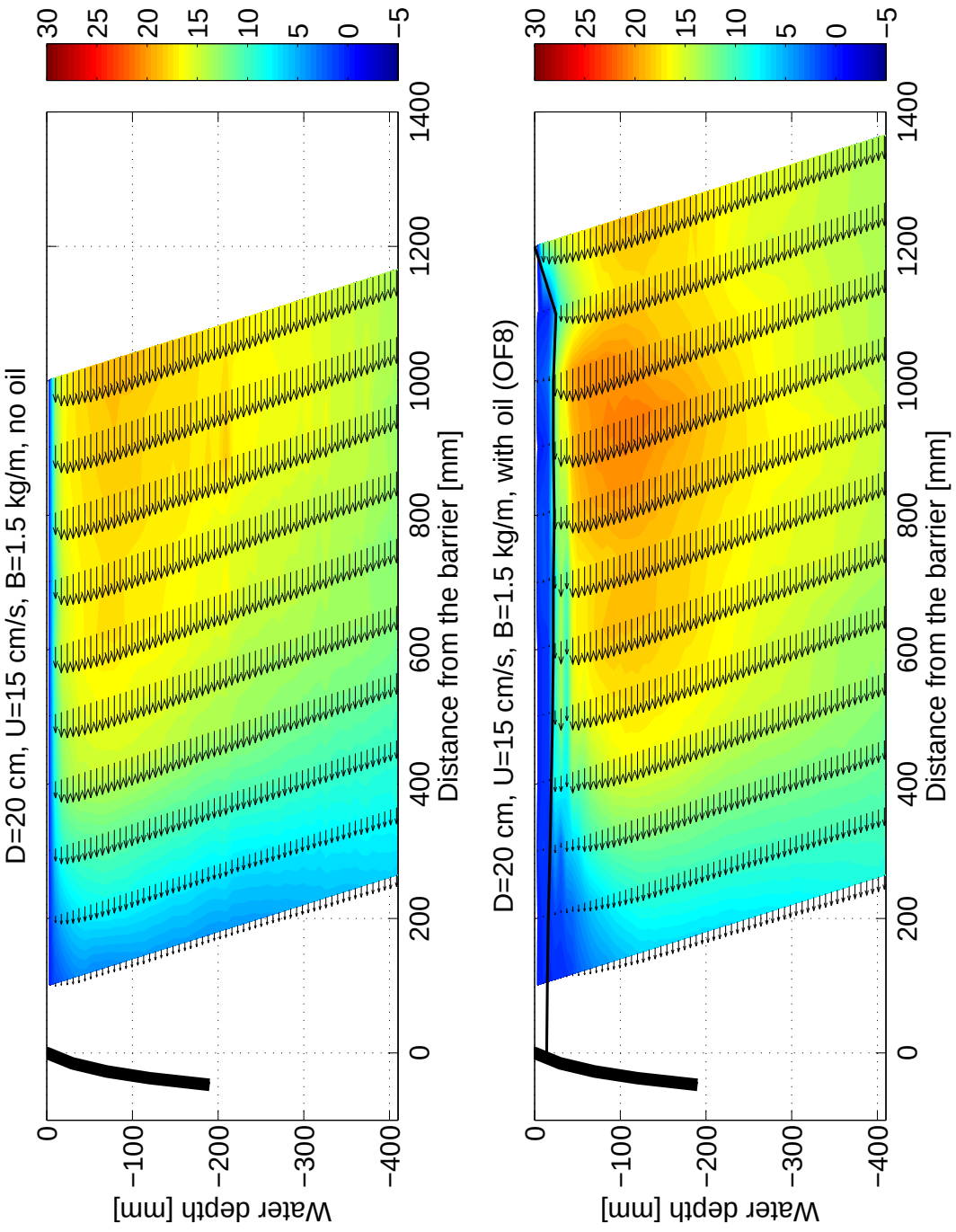

Figure D.9: UVP measurements of U_x for a flexible barrier with 20 cm draft and mean flow velocity of 15 cm/s, color bar shows the velocity in cm/s

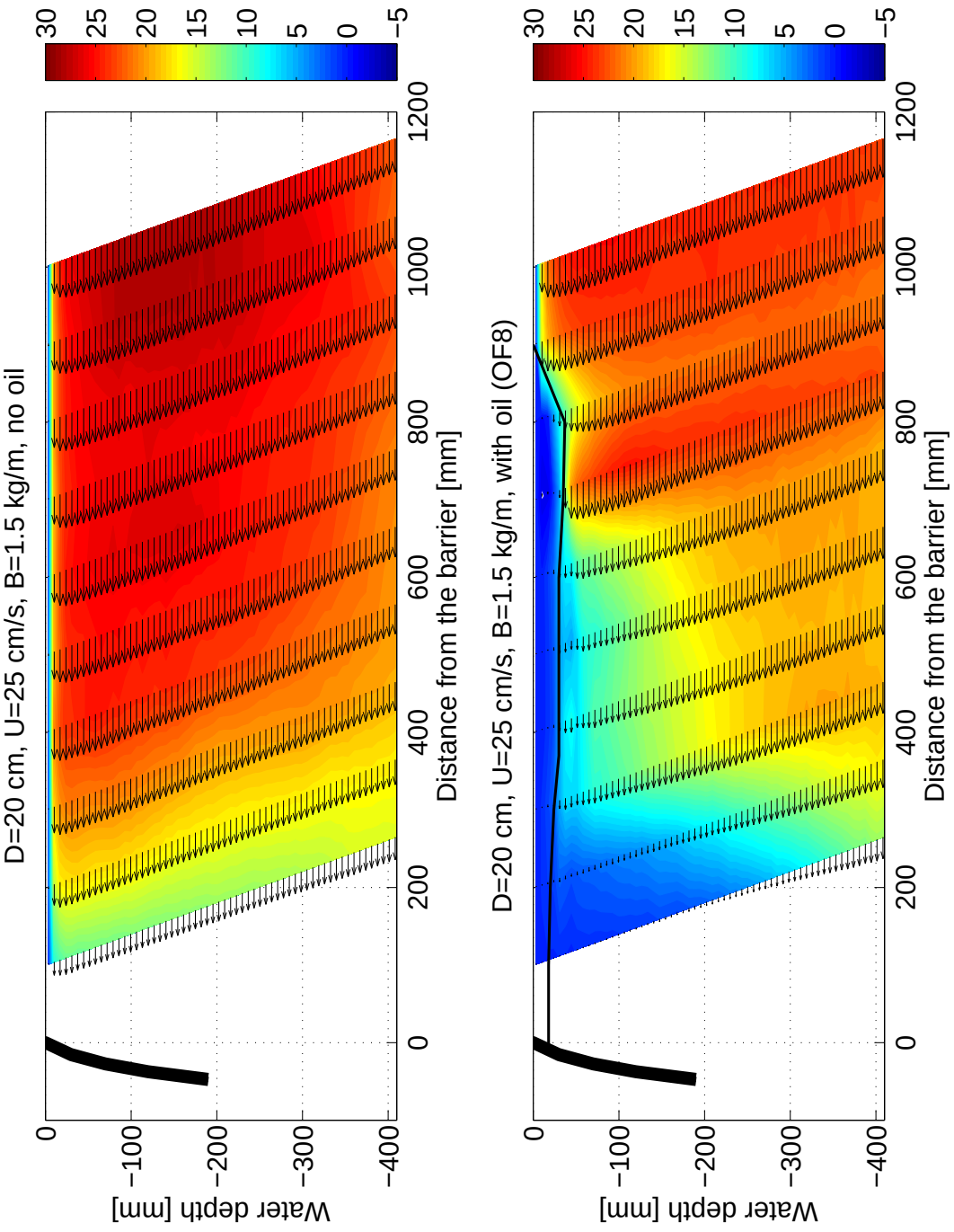

Figure D.10: UVP measurements of U_x for a flexible barrier with 20 cm draft and mean flow velocity of 25 cm/s, color bar shows the velocity in cm/s

Appendix E

LSPIV measurements

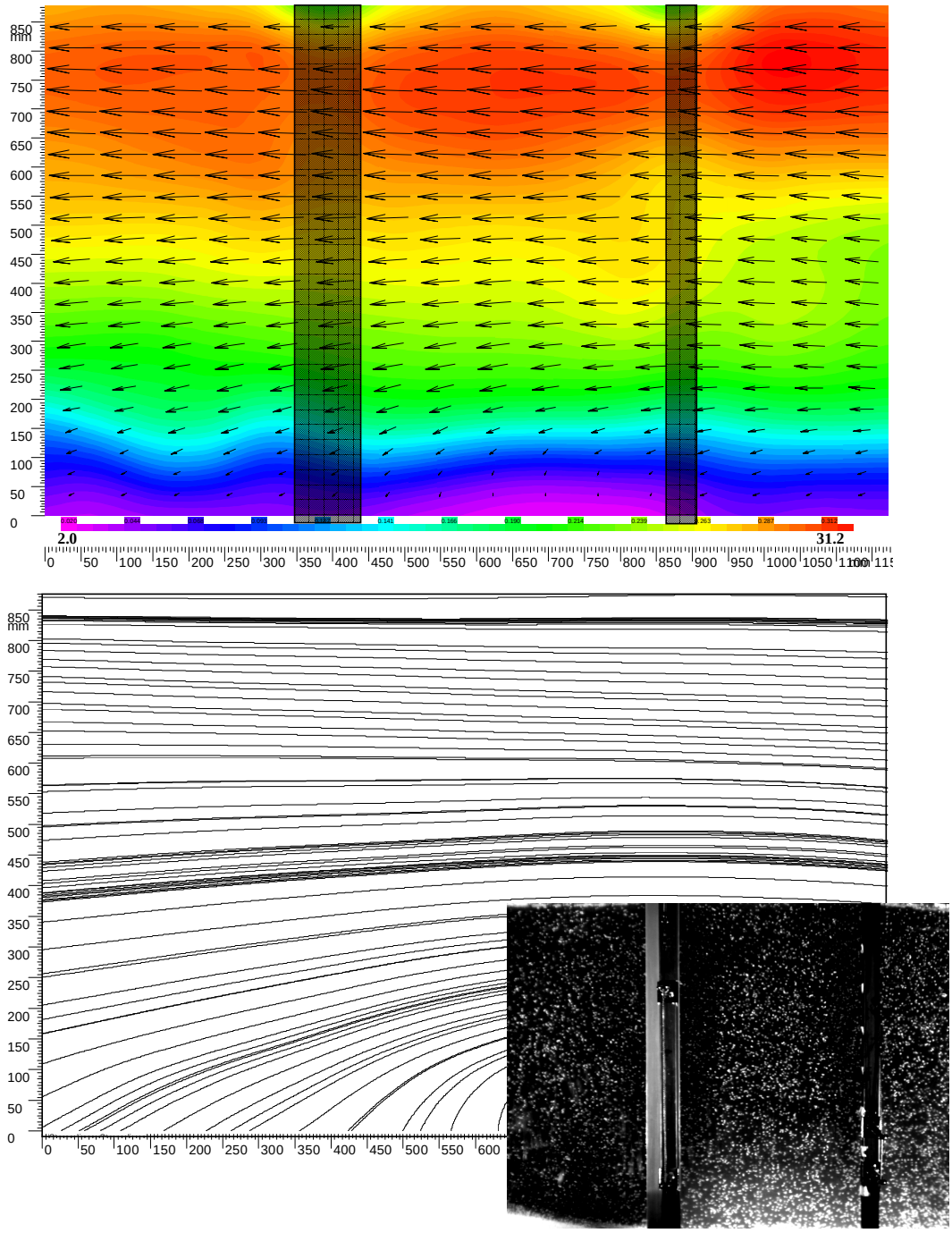

Figure E.1: Results of LSPIV measurements in the laboratory flume with no barrier

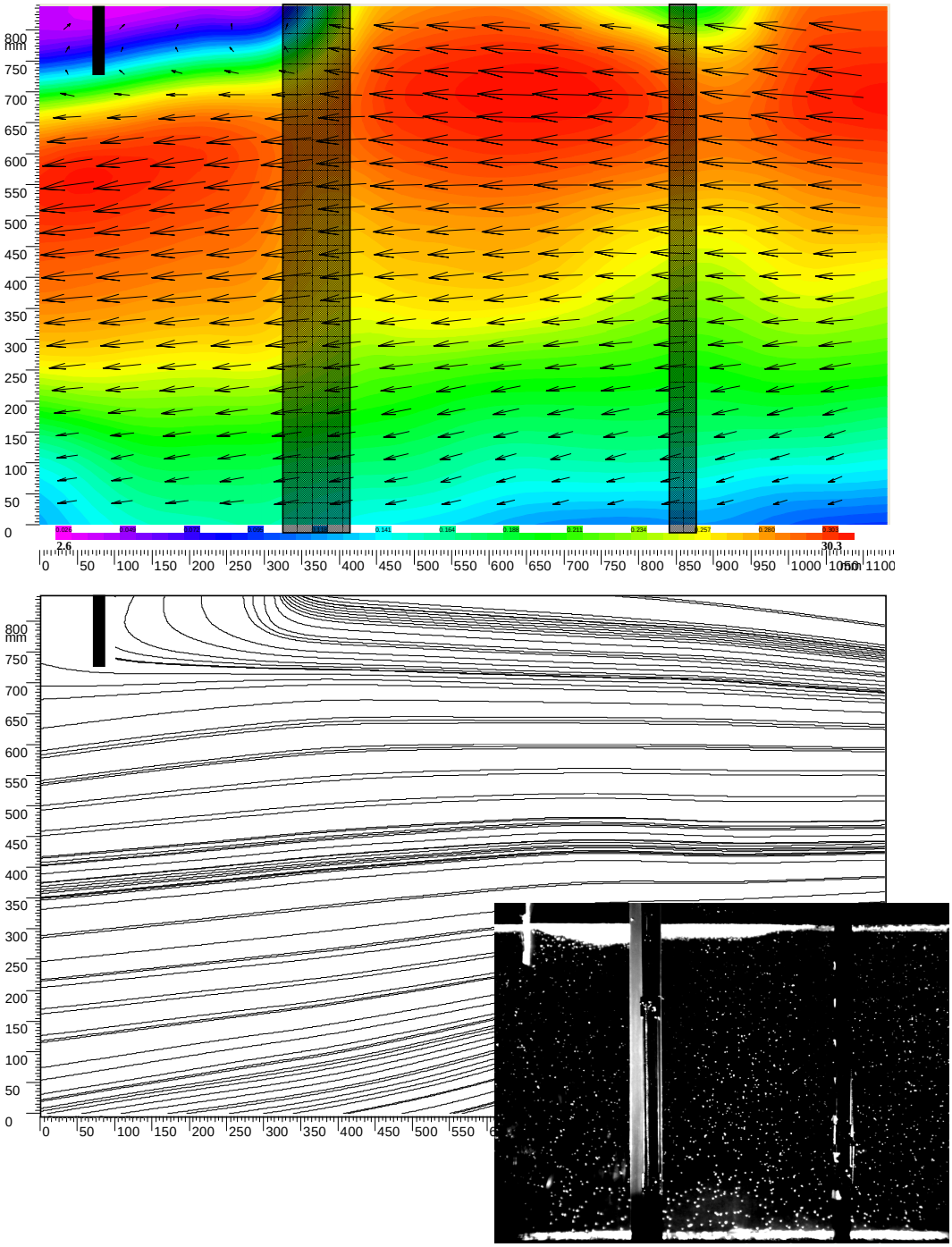

Figure E.2: Results of LSPIV measurements for a rigid barrier with 10 cm draft and mean flow velocity of 20 cm/s; barrier is in the corner of the measurement window

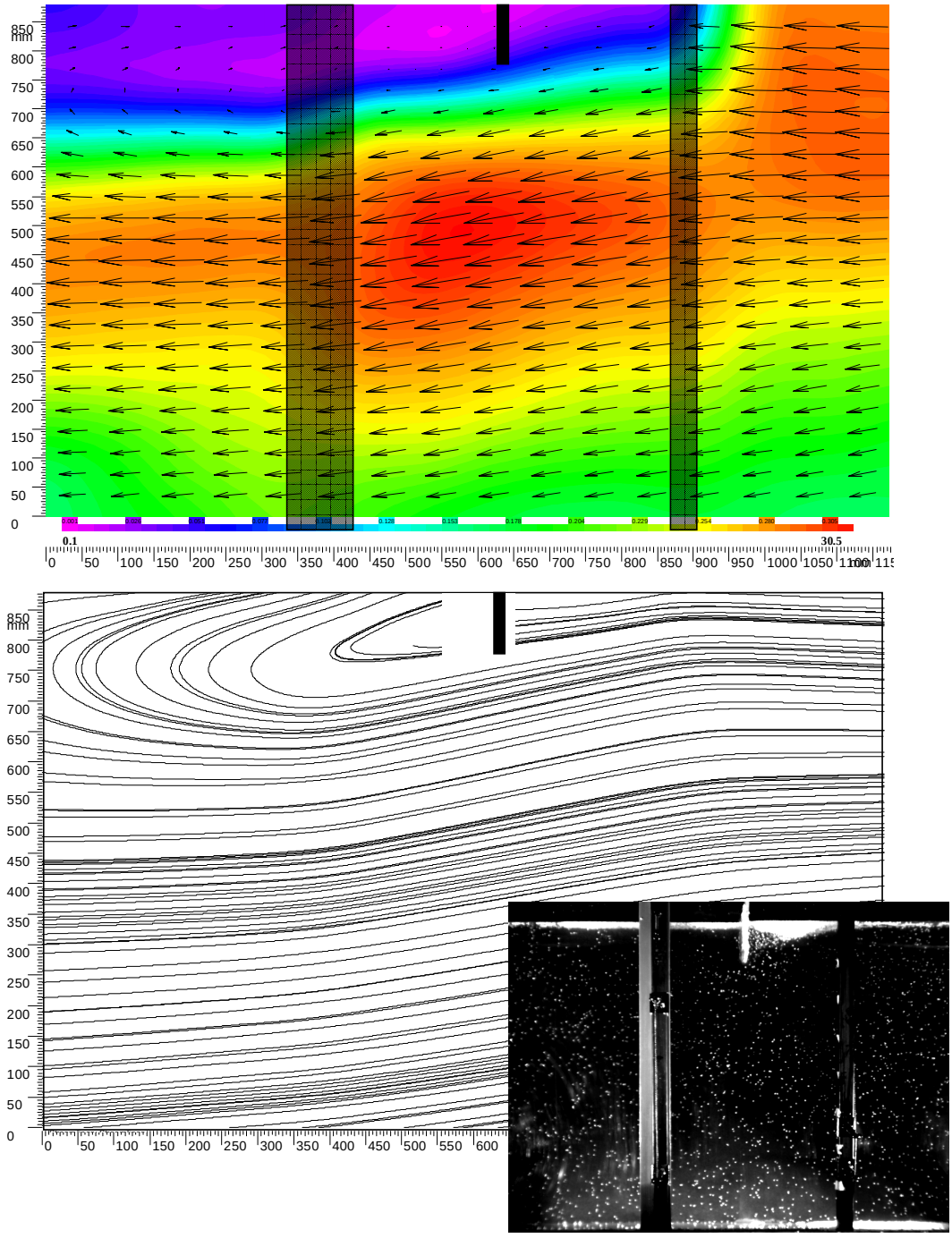

Figure E.3: Results of LSPIV measurements for a rigid barrier with 10 cm draft and mean flow velocity of 20 cm/s; barrier is in the middle of the measurement window

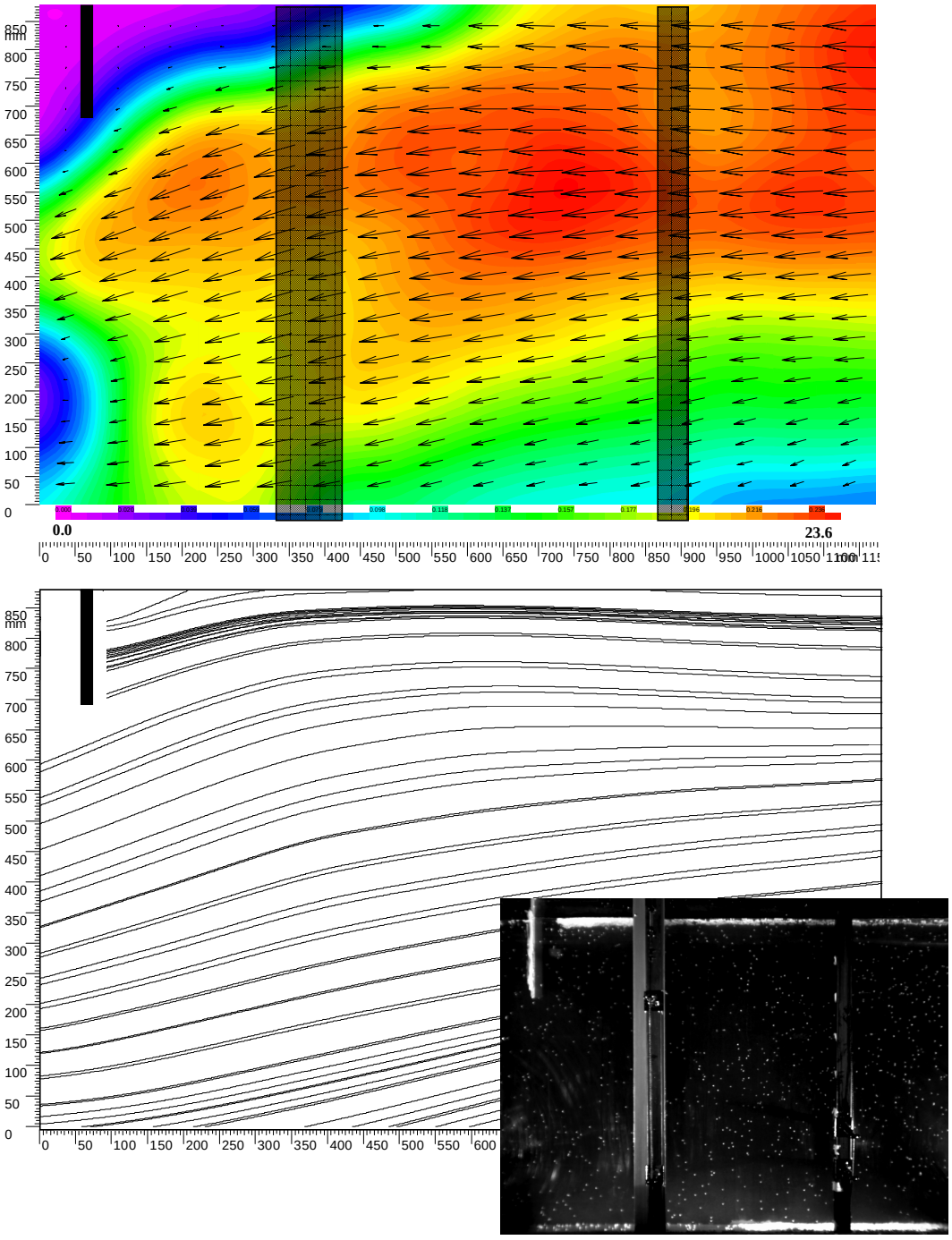

Figure E.4: Results of LSPIV measurements for a rigid barrier with 20 cm draft and mean flow velocity of 20 cm/s; barrier is in the corner of the measurement window

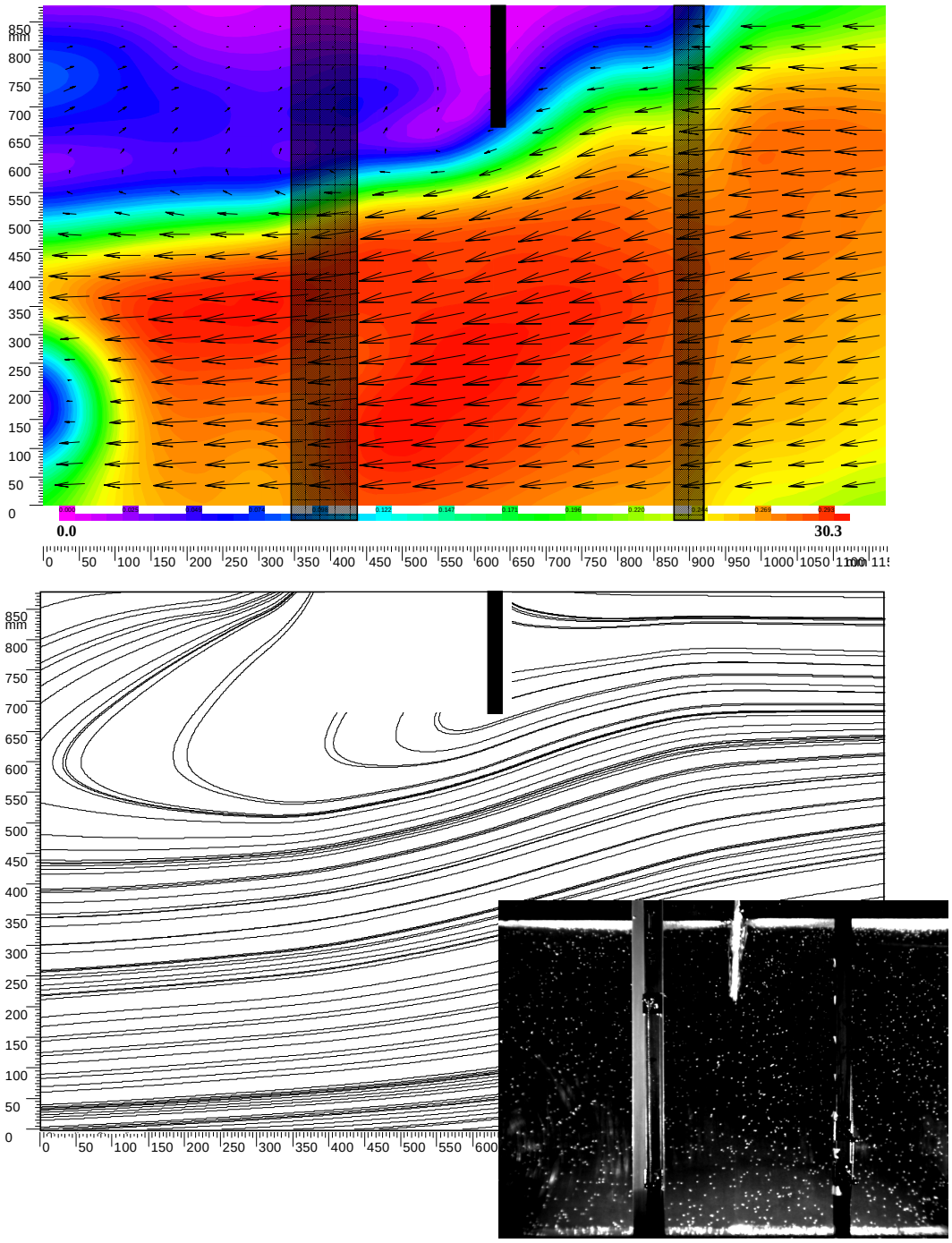

Figure E.5: Results of LSPIV measurements for a rigid barrier with 20 cm draft and mean flow velocity of 20 cm/s; barrier is in the middle of the measurement window

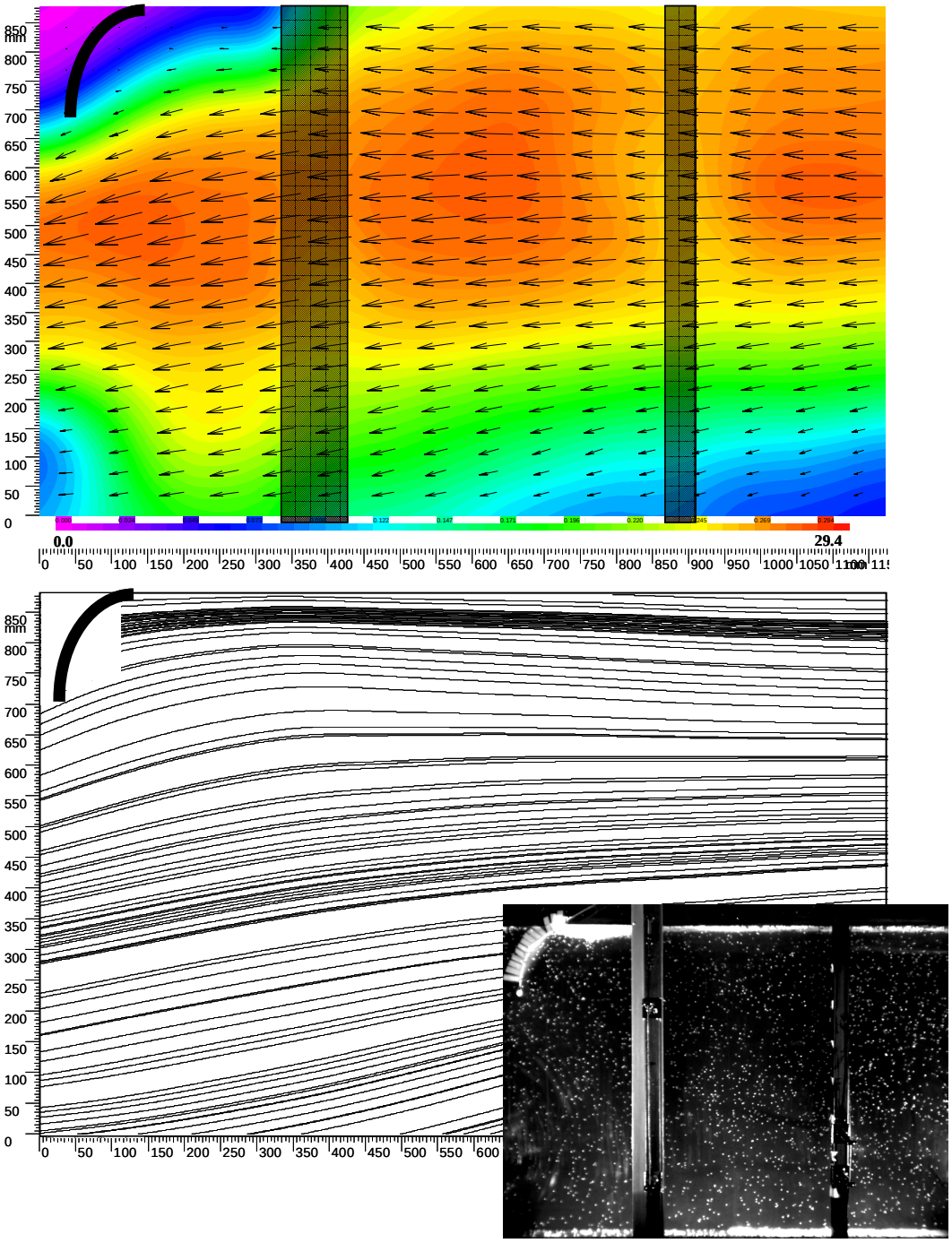

Figure E.6: Results of LSPIV measurements for a flexible barrier with 20 *cm* draft and mean flow velocity of 20 cm/s; barrier is in the corner of the measurement window

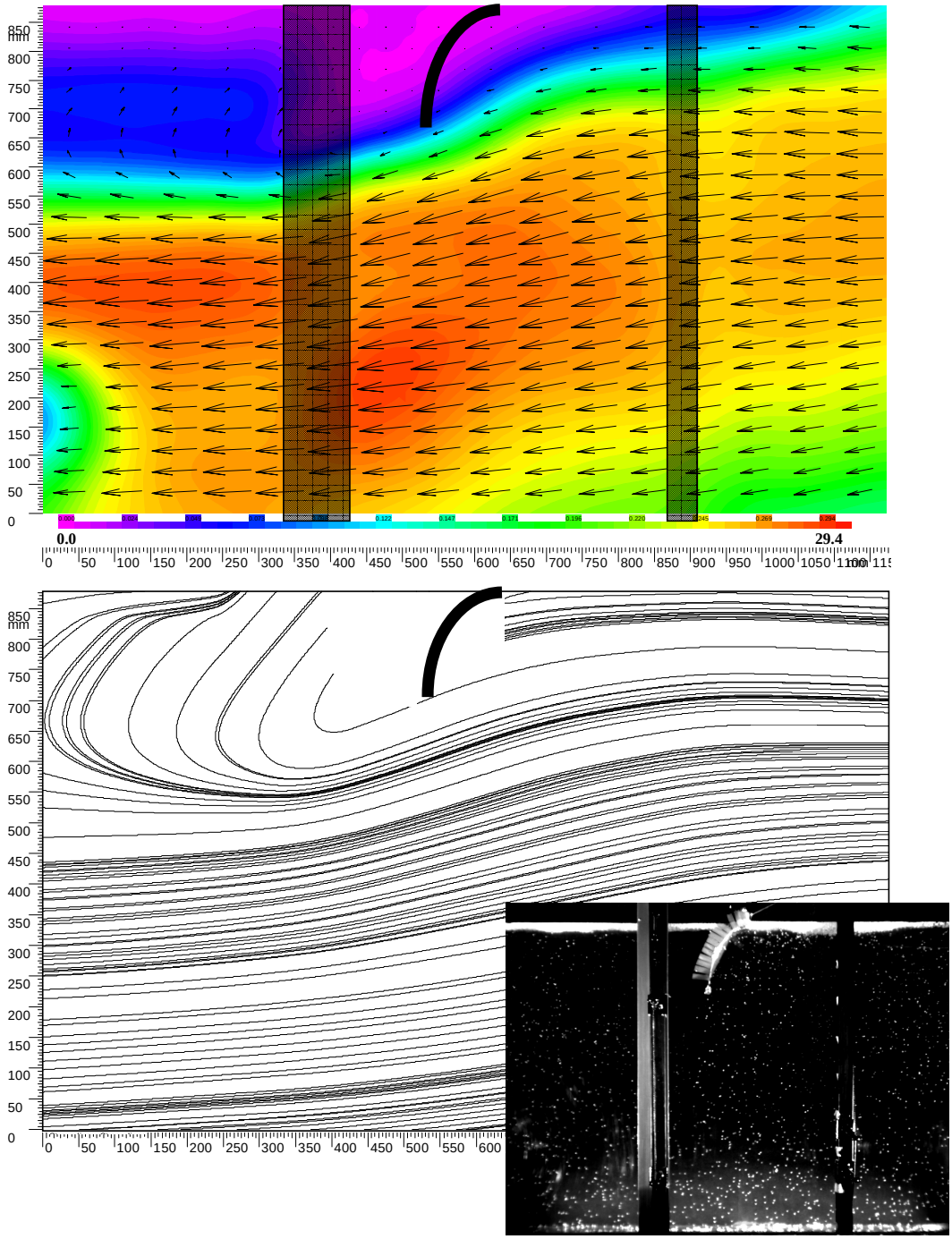

Figure E.7: Results of LSPIV measurements for a flexible barrier with 20 *cm* draft and mean flow velocity of 20 cm/s; barrier is in the middle of the measurement window

Appendix F

Hydrostatic analysis of oil spill containment booms

This appendix is dedicated to analyze the hydrostatic equilibrium of oil spill containment barriers. It concerns the simple hydrostatic calculations, which are necessary for a better understanding of a containment system response.

For a given oil slick thickness, the floating position of the barriers is affected by the float radius and the total system weight. Different cases for position of an oil containment boom floating on water are presented in Fig. F.1. These cases can be classified into two groups. In the first group, the float is in contact with water on one side and with both oil and water on the other side as shown in Fig. F.1 a, b, and c. In the second group, the float is in contact with water on one side and only with oil on the other side (Fig. F.1 d, e and f). For each of these two groups, three different situations have been considered:

- center of the float is located above both oil and water levels (Fig. F.1a, d)
- center of the float is located under oil but above water level (Fig. F.1b, e)
- center of the float is located under both oil and water levels (Fig. F.1c, f)

A sufficient freeboard for the floating reservoir has to be provided in order to avoid oil splashing over. Therefore, the conditions in which the oil or water level are above the float center are not plausible, the equations have been developed only for “a” and “d” positions.

To study the vertical equilibrium of floating barriers, the only considered forces are the weight and the buoyancy. The total weight is the sum of the weights of the float, the skirt, and the ballast, while the total buoyancy is derived from the submerged volume of the float in oil and water. These two forces acting in opposite directions should be in equilibrium to achieve a stable position of the floating barrier.

Accordingly, the involved parameters are the float radius, which influences the buoyancy of the system, the densities of spilled oil and water, which influence the water and oil level difference between reservoir sides, the oil layer thickness, and finally the total weight of the system. For “a” and “d” conditions shown in Fig. F.1, the vertical equilibrium equations are mathematically developed,

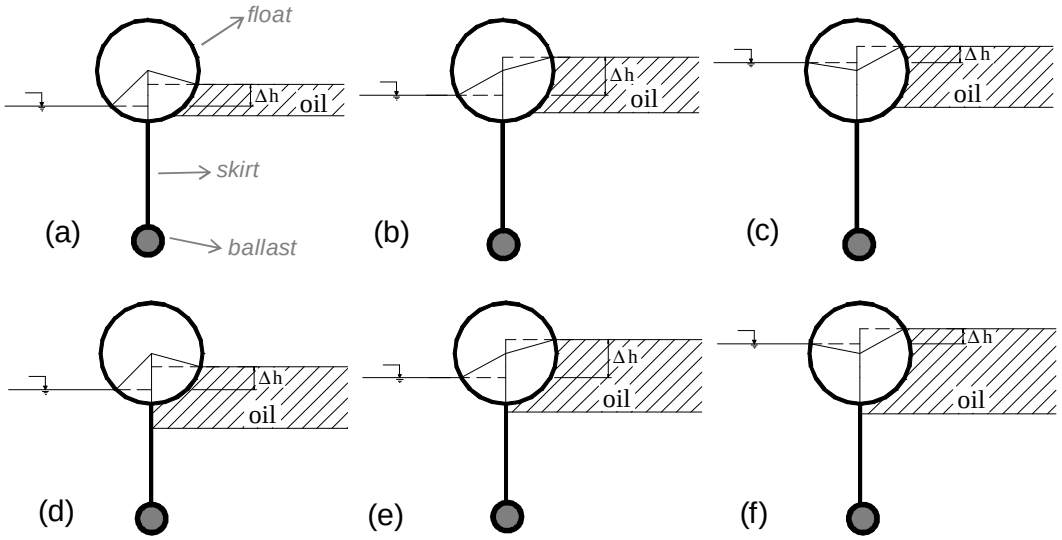

Figure F.1: Vertical float position; first row: oil is not in contact with the skirt; second row: oil is in contact with the skirt

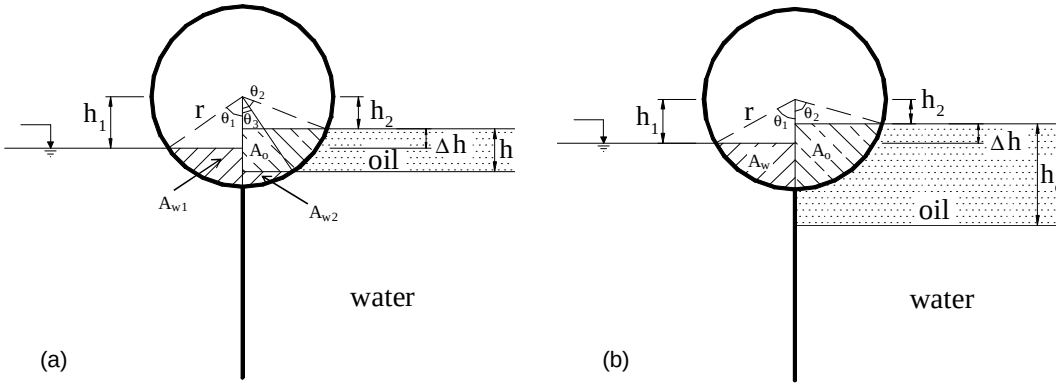

Figure F.2: Buoyancy conditions of the boom: (a) oil above the float bottom; (b) oil below the float bottom

regarding the float geometry (see Fig. F.2) and its submerged parts in water and oil, as follows.

First condition: Oil has no contact with the skirt

If the oil layer is not too thick to touch the skirt (Fig. F.2 a), the equilibrium of vertical forces can be written as:

$$A_{w1}\gamma_w + A_{w2}\gamma_w + A_o\gamma_o = W_{tot} \tag{F.1}$$

where γ_o and γ_w are the densities of oil and water respectively. A_w is the area of that part of the float that is submerged in water(A_{w1} and A_{w2} correspond to A_w on both sides of the barrier) and A_o is the area of that part of the float that is submerged in oil, and are calculated as follows:

$$A_{w1} = \frac{1}{4}r^2(2\theta_1 - Sin\ 2\theta_1) \tag{F.2a}$$

$$A_{w2} = \frac{1}{4}r^2(2\theta_3 - Sin\ 2\theta_3) \tag{F.2b}$$

$$A_o = \frac{1}{4}r^2(2\theta_2 - Sin\ 2\theta_2) - A_{w2} \tag{F.2c}$$

where,

$$\theta_1 = ArcCos(\frac{h_1}{r}) \tag{F.3a}$$

$$\theta_2 = ArcCos(\frac{h_2}{r}) \tag{F.3b}$$

$$\theta_3 = ArcCos(\frac{h_2 + h}{r}) \tag{F.3c}$$

In these equations, h_1 and h_2 stand for distance of float center to water and oil surface respectively (see Fig. F.2 a). On the other hand the water and oil level difference, Δh, can be calculated as:

$$\Delta h = h_1 - h_2 = h(1 - \frac{\gamma_o}{\gamma_w}) \tag{F.4}$$

where h is the oil layer thickness. Eq. F.1 can hence be written as:

$$\begin{aligned}
&\gamma_w \left[ArcCos(\frac{h_1}{r}) - \frac{h_1}{r}\sqrt{1 - \left(\frac{h_1}{r}\right)^2} \right] + \\
&\gamma_o \left[ArcCos(\frac{h_2}{r}) - \frac{h_2}{r}\sqrt{1 - \left(\frac{h_2}{r}\right)^2} \right] + \\
&(\gamma_w - \gamma_o) \left[ArcCos(\frac{h_2 + h}{r}) - \frac{h_2 + h}{r}\sqrt{1 - \left(\frac{h_2 + h}{r}\right)^2} \right] = \frac{2W_{tot}}{r^2}
\end{aligned} \tag{F.5}$$

By replacing h_2 from Eq. F.4 in Eq. F.3c:

$$\theta_3 = ArcCos\left(\frac{h_1 + h(\gamma_o/\gamma_w)}{r}\right) \tag{F.6}$$

As a result, Eq. F.5 can now be written as a function of h_1:

$$\gamma_w \left[ArcCos(\frac{h_1}{r}) - \frac{h_1}{r}\sqrt{1-\left(\frac{h_1}{r}\right)^2} \right] +$$
$$\gamma_o \left[ArcCos(\frac{h_1-\Delta h}{r}) - \frac{h_1-\Delta h}{r}\sqrt{1-\left(\frac{h_1-\Delta h}{r}\right)^2} \right] +$$
$$(\gamma_w-\gamma_o) \left[ArcCos(\frac{h_1+h(\gamma_o/\gamma_w)}{r}) - \frac{h_1+h(\gamma_o/\gamma_w)}{r}\sqrt{1-\left(\frac{h_1+h(\gamma_o/\gamma_w)}{r}\right)^2} \right]$$
$$= \frac{2W_{tot}}{r^2} \tag{F.7}$$

Knowing the properties of the spilled oil (h, γ_o) contained by a reservoir with a particular float radius, r, h_1 remains the only unknown parameter in Eq. F.7.

Second condition: oil is in contact with the skirt

In second condition, the float is fully submerged in oil on one side (Fig. F.2b). The vertical equilibrium can be achieved when:

$$A_{w1}\gamma_w + A_o\gamma_o = W_{tot} \tag{F.8}$$

By replacing the respective equations, Eq. F.8 can be presented as:

$$\gamma_w \left[ArcCos(\frac{h_1}{r}) - \frac{h_1}{r}\sqrt{1-\left(\frac{h_1}{r}\right)^2} \right] +$$
$$\gamma_o \left[ArcCos(\frac{h_2}{r}) - \frac{h_2}{r}\sqrt{1-\left(\frac{h_2}{r}\right)^2} \right] = \frac{2W_{tot}}{r^2} \tag{F.9}$$

This latter can be written as a function of h_1:

$$\gamma_w \left[ArcCos(\frac{h_1}{r}) - \frac{h_1}{r}\sqrt{1-\left(\frac{h_1}{r}\right)^2} \right] +$$
$$\gamma_o \left[ArcCos(\frac{h_1-\Delta h}{r}) - \frac{h_1-\Delta h}{r}\sqrt{1-\left(\frac{h_1-\Delta h}{r}\right)^2} \right] = \frac{2W_{tot}}{r^2} \tag{F.10}$$

Thereby, for an oil layer thickness that does not exceed the depth of the float, the vertical static stability of the floating boom is governed by Eq. F.7. If the oil thickness increases, it will exceed the float depth and the governing equation has to be replaced by Eq. F.10. Using these two equations, dimensionless

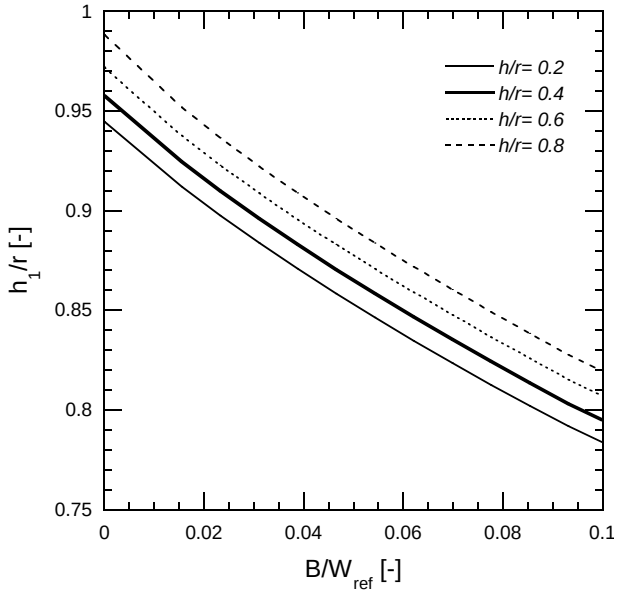

Figure F.3: Influence of non-dimensional ballast weight (B/W_{ref}) on the relative freeboard above water (h_1/r)

graphs have been derived that illustrate the equilibrium position of the system as a function of ballast weight and oil spill thickness. The vertical equilibrium position of the structure is expressed by the differences between float center and water level, h_1, and float center and oil level, h_2. The non-dimensional equivalents (h_1/r) and (h_2/r) represent the relative freeboard above water and oil, respectively (see Fig. F.2)

Effect of the ballast weight

Fig. F.3 illustrates the effect of increasing the ballast weight per unit length of barrier, B, on relative relative freeboard above water, h_1/r, for different oil thicknesses. The increase of ballast weight, causes the barrier to descend into the water by the same rate for different oil thicknesses. In this graph, the ballast weight has been divided by a reference weight (W_{ref}), which is the weight of water that can fill half of the float volume per unit length ($\pi r^2/2$). The relationship shows a non-linear trend.

Effect of the oil thickness

Fig. F.4 shows the effect of oil thickness increase on vertical position of the barrier according to oil and water surfaces. As can be seen, the increase of oil thickness leads to a decrease of h_1 and an increase of h_2, which means that the whole system moves up. The reason is that the density of oil is less than density of water and the added oil replaces less water in order to achieve the same upward force to balance weight. The ultimate states for the increase of oil thickness happens when h_1 becomes equal to the float radius, or when h_2 becomes zero, which means that oil level reaches the center of float.

The effect of oil thickness increase on the relative freeboard above water (h_1/r) for different ballast weights is shown in Fig. F.5. As mentioned before,

by increasing oil thickness, the governing equation changes from Eq. F.7 to Eq. F.10. That is the point of full submergence of the float in oil on one side, which turns the non-linear curve into a linear one.

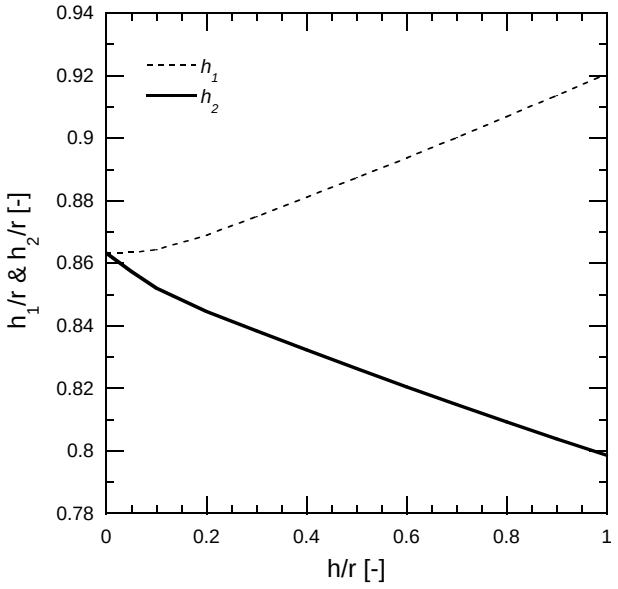

Figure F.4: Effect of the relative oil thickness (h/r) on the relative freeboard above water (h_1/r) and relative freeboard above oil (h_2/r) for a non-dimensional weight equal to 0.06

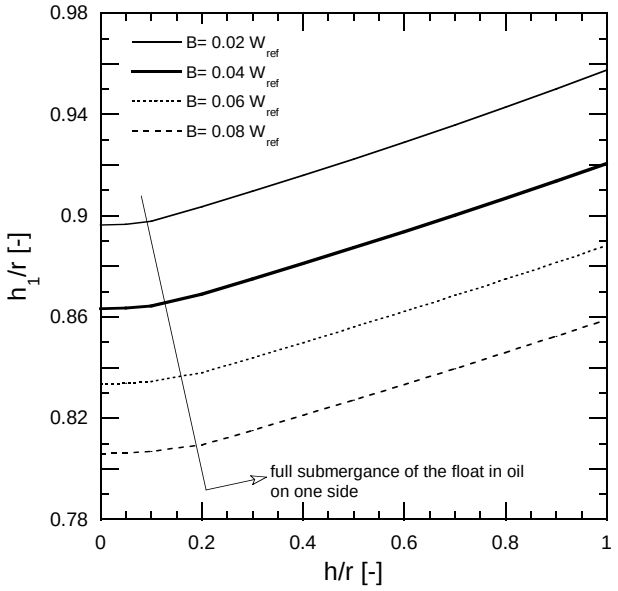

Figure F.5: Effect of the relative oil thickness (h/r) on the relative freeboard above water (h_1/r) for different ballast weights

Communications du Laboratoire de Constructions Hydrauliques ISSN 1661-1179
Ecole Polytechnique Fédérale de Lausanne
Editeur: Prof. Dr A. Schleiss

N° 24 2006 S. Sayah
Efficiency of brushwood fences in shore protection against wind-wave induced erosion

N° 25 2006 P. Manso
The influence of pool geometry and induced flow patterns in rock scour by high-velocity plunging jets

N° 26 2006 M. Andaroodi
Standardization of civil engineering works of small high-head hydropower plants and development of an optimization tool

N° 27 2006 Symposium érosion et protection des rives lacustres
Bases de dimensionnement des mesures de protection des rives lacustres

N° 28 2007 A. Vela Giró
Bank protection at the outer side of curved channels by an undulated concrete wall

N° 29 2007 F. Jordan
Modèle de prévision et de gestion des crues - Optimisation des opérations des aménagements hydroélectriques à accumulation pour la réduction des débits de crue

N° 30 2007 P. Heller
Méthodologie pour la conception et la gestion des aménagements hydrauliques à buts multiples

N° 31 2007 P. Heller
Analyse qualitative des systèmes complexes à l'aide de la méthode de Gomez & Probst

N° 32 2007 J. García Hernández, F. Jordan, J. Dubois, J.-L. Boillat
Routing System II - Modélisation d'écoulements dans des systèmes hydrauliques

N° 33 2007 Symposium - Flussbauliche Massnahmen im Dienste des Hochwasserschutzes, der Umwelt, Gesellschaft und Wirtschaft / Mesures d'aménagement des cours d'eau pour la protection contre les crues, l'environnement, la société et l'économie

N° 34 2007 B. Rosier
Interaction of side weir overflow with bed-load transport and bed morphology in a channel

N° 35 2007 A. Amini
Contractile floating barriers for confinement and recuperation of oil slicks

ISSN 1661-1179

Prof. Dr A. Schleiss
Laboratoire de constructions hydrauliques - LCH
EPFL, Bât. GC, Station 18, CH-1015 Lausanne
http://lchwww.epfl.ch
e-mail: secretariat.lch@epfl.ch